Measurements of π^0-jet correlations in $\sqrt{s} = 7$ TeV pp collisions and in $\sqrt{s_{\mathrm{NN}}} = 2.76$ TeV central Pb-Pb collisions at ALICE experiment

Daisuke Watanabe

February 2016

Measurements of π^0-jet correlations in $\sqrt{s} = 7$ TeV pp collisions and in $\sqrt{s_{\mathrm{NN}}} = 2.76$ TeV central Pb-Pb collisions at ALICE experiment

Daisuke Watanabe
Doctoral Program in Physics

Submitted to the Graduate School of
Pure and Applied Sciences
in Partial Fulfillment of the Requirements
for the Degree of Doctor of Philosophy in
Science

at the University of Tsukuba

Abstract

Quarks and gluons are confined in a hadron by the strong interaction described by Quantum Chromodynamics (QCD). However, at high temperature, the quarks and gluons move freely beyond the boundary of hadrons. Such state is called Quark-Gluon Plasma (QGP) and believed to exist at a few micro second after the Big Bang of the universe. The ultra relativistic heavy ion collision is unique tool to create the QGP state on the earth.

Several results indicates a creation of QGP state by the ultra relativistic heavy ion collisions. One of them is the suppression of high momentum particles (jet quenching) which is observed by the two particle correlation measurements at the Relativistic Heavy Ion Collider (RHIC) and di-jet measurements at the Large Hadron Collider (LHC). This modification is caused by the energy loss of the partons in the QGP.

Jets are produced from the two body scattering of partons with large momentum transfer. In theoretical approach, it is indicated that the energy loss of jets in QGP is related to the properties of QGP particularly gluon density and initial temperature of the QGP. Therefore, jet measurements play a critical role in probing the QGP matter created in heavy ion collisions through parton energy loss via the observation of the jet structure modification or jet suppression.

The energy loss of energetic partons also depends on the path length in the QGP matter. For example, jet pairs with a large energy asymmetry in the final states can be produced due to the difference of path-length between leading jet and sub-leading jet. While leading jets escape mostly from the surface in the medium, recoil jets traverse in the matter with losing its energy in a hot and dense matter. We use this surface bias to acquire deeper insights into the matter properties. The stronger the surface bias, the larger the path length in the QGP for the recoiling jet at the opposite azimuth. By measuring jets directly rather than measuring inclusive high transverse momentum (p_{T}) hadrons as is done in the previous study, we can perform more comprehensive and direct study of jet interactions in the matter.

In this thesis, we report measurements of neutral pion and charged jet correlations in pp collisions at $\sqrt{s} = 7$ TeV and in central Pb-Pb collisions at $\sqrt{s_{\mathrm{NN}}} = 2.76$ TeV from the LHC-ALICE experiment. The LHC at CERN is the largest energy accelerator in the world. The ALICE detector was built to exploit the unique physics in nucleus-nucleus interactions at the LHC and is capable of studying jet quenching effects via jet reconstruction and particle identification.

For the neutral pion identification, we use an electro-magnetic calorimeter (EMCal) in ALICE. In addition, EMCal is used as a trigger detector to enrich the high p_{T} neutral pion sample. The opening angle of two photons decayed from the neutral pion become smaller, when the neutral meson energy is high due to the Lorentz boost. In order to identify π^0 at higher p_{T} range, we use the cluster splitting method which identifies a single cluster as a neutral meson via the parameter λ_0. This parameter is the length of long axis of the ellipse with two overlapping showers on the surface of calorimeter. We can identify π^0 from 8 up to 40 GeV/c by using the cluster splitting method.

Jets are reconstructed by using charged particles which are measured by the Inner Tracking System (ITS) and Time-Projection Chamber (TPC) with jet constituents $p_{\mathrm{T,ch}} > 0.15$ GeV/c, with jet resolution parameter $R = 0.4$. Underlying event backgrounds are subtracted by the event-by-event background subtraction method which takes into account the event plane dependence of the background coming from the event anisotropy. The measured p_{T} range of the jets is from 10 to 80 GeV/c.

Azimuthal correlations between trigger π^0's and reconstructed jets have been measured at $\sqrt{s} = 7$ TeV pp collisions as a baseline, and at $\sqrt{s_{\mathrm{NN}}} = 2.76$ TeV Pb-Pb central $0-10$ % collisions to see a modification of jet in heavy ion collisions. We observe jet-like peaks in near and away side in pp and Pb-Pb collisions, and the away side peak becomes sharp with increasing p_{T} of the associated jets in pp collisions. This result indicates that the high p_{T} π^0 production is strongly associated with a jet production.

Next we take a ratio of per trigger yields I_{AA} which is ratio between per trigger yield in Pb-Pb and that in pp. We measure an enhancement for near side jet for jet $p_{\mathrm{T,ch.jet}} > 40$ GeV/c, and a suppression for all measured jet $p_{\mathrm{T,ch.jet}}$ range for away side. Triggering higher p_{T} π^0 would select near side jets produced close to the surface in a medium, while the path-length of its away side jets become longer than the near side jets. In the near and away side widths measurement, we observe an indication of a jet broadening effect in the near-side with requiring the lower p_{T} of trigger π^0 lower p_{T} leading particle in a jet in Pb-Pb collisions. This effect decreases with increasing p_{T} of the leading particle in a jet. These results may suggest a possible jet broadening effect in central Pb-Pb collision at the LHC energy depending on the path-length of a initial parton in a medium.

Contents

List of Figures

Acknowledgment

I would like to start thanking my appreciation to Prof. Yasuo Miake, he gave me many comments and suggestions to improve the results in this thesis. I also would like to express my appreciation to Prof. ShinIchi Esumi, he also gave me a lot of advises and suggestions on my analysis. I also would like to express my deepest appreciation to Prof. Tatsuya Chujo for giving me continuous encouragements and supporting my activities in my college life. I learned many things from him. I am very grateful to the staffs in University of Tsukuba, Prof. M. Inaba, Prof. H. Masui, Mr. S. Kato and Ms. H. Sakai for my college life.

Many thanks to the colleagues in University of Tsukuba. In particular, I would like to thank Dr. D. Sakata, Mr. H. Yokoyama, Mr. N. Tanaka, Mr. H. Nakagomi, Mr. S. Horiuchi, Ms. K. Gunji, Ms. T. Nakajima for their supports and friendships in my college life. I would like to express my great thanks to Mr. M. Sano, Dr. T. Niida, Dr. T. Todoroki, Dr. B. Jihyun, Mr. S. Kubota, Mr. Y. Kondo, Mr. H. Nakazato, Mr. R. Funato, Mr. T. Kobayashi, Mr. K. Kihara, Mr. K. Oshima, Ms. H. Ozaki, Mr. T. Nonaka, Mr. K. Yodogawa, Mr. H. Watanabe, Mr. W. Sato, Mr. R. Hosokawa, Mr. R. Aoyama, Mr. J. Lee, Ms. I. Sakatani, Mr. T. Shioya, Mr. M. Hirano, Mr. H. Yamamoto, Mr. T. Sugiura, Mr. K. Ito, Mr. B.C. Kim, Ms. S, Kudo, Ms. M. Chang, and Mr. Y. Fukuda for their advice, suggestions and discussions.

I am very grateful to the staffs and students of the University of Tokyo and Hiroshima University, especially thank to Mr. S. Hayashi, Mr. S. Yano, Ms. Y. Sekiguchi, Mr. K. Terasaki, Mr. T. Ookubo and Mr. D. Sekihata for their supports and friendships in my CERN like.

I would like to many thanks to the ALICE Collaboration. I also would like to thanks to the physics working group for photon and jet measurements and the EMCal group in ALICE, especially Prof. Christian Klein-Boesing, Prof. Marco Van Leeuwen, Prof. Gustavo Conesa Balbastre, Prof. Jana Bielcikova, Prof. Oliver Busch, Prof. Terry Awes and Prof. David Silvermyr for their helps in my analysis and detector work.

I would like to express many thanks to Prof. H. En'yo for helping me through the Junior Research Associate program.

Chapter 1

Introduction

In this chapter, we present theoretical background in jet physics in high energy heavy-ion collisions and recent results for jet modification as introduction to understand physics motivation of this thesis.

1.1 Quark Gluon Plasma (QGP)

Quarks and gluons are in a hadron at a normal temperature. Quarks and gluons are confined in a hadron due to a nature of the strong force in Quantum Chromodynamics (QCD). By increasing temperature and density, a deconfinement of quarks and gluons occurs, and a such state is called "Quark-Gluon Plasma (QGP)". In order to create such state, there are two methods, one is to heat up a matter, and the other is putting a matter under the extremely high density condition. When we create high energy or density state by using the two methods, hadrons start to overlap each other, and then the quarks and gluons in hadrons can move freely beyond the boundary of hadrons. Fig.1.1.1 shows a schematic view of the QCD phase diagram that can be reached in high energy heavy-ion collisions by the high energy accelerators. In nature, matters are composed by proton and neutron at a normal temperature and normal baryon density. However if we apply heat and pressure to matter, a phase transition from hadronic phase to QGP phase can happen. Experimentally, we can create a hot QGP by using high energy nuclear collisions, and it is also believed to create a dense matter QGP at high baryon density at the lower beam energy for example at AGS energy ($\sqrt{s_{\rm NN}} \sim 5$ GeV) and a such state can might exist also interior of a neutron star. The energy density ε of an equilibrated ideal gas is given by the following equation,

$$\varepsilon = n_{dof}\frac{\pi^2}{30}T^4 \tag{1.1.1}$$

where n_{dof} is a degree of freedom of the matter, and T is a temperature. $n_{dof} = 16$ when the state has only gluons, 37 the state is with two flavors (up and down) and 47.5 with three flavors (up, down, and strangeness). Fig.1.1.2 shows the energy density divided by T^4 as function of temperature calculated by a Lattice QCD at non-zero chemical potential and resonance gas model. According to the most recent lattice QCD calculation[2], there is a cross over phase transition near zero chemical potential at the critical temperature $T_c = 155\pm9$ MeV.

1.2 High energy nucleus-nucleus collision

High energy nucleus-nucleus collision is powerful and unique tool to study a high temperature and energy density matter in a larger volume compared to those in proton-proton collisions. In this section, we describe a formation of QGP in a high energy nucleus-nucleus collisions, in particular the collision geometry, time evolution and particle production.

Table.1.2.1 shows the list of high energy heavy-ion accelerator in the world.

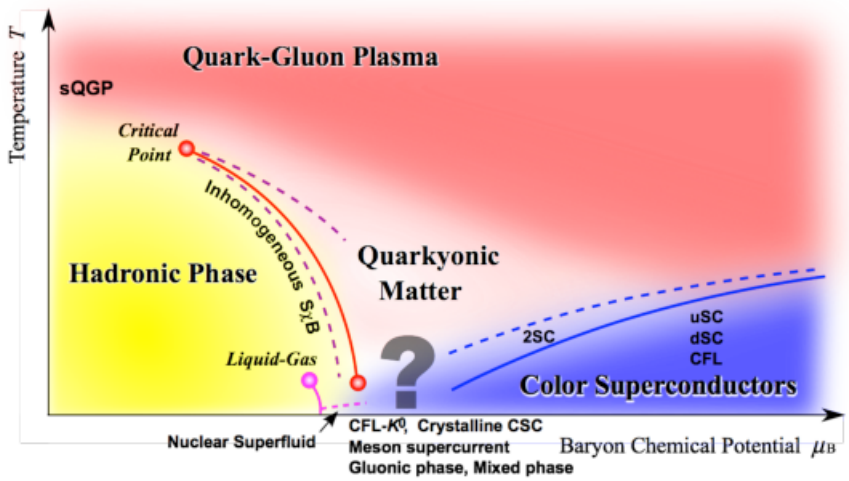

Fig. 1.1.1: Schematic view of QCD phase diagram as function of temperature and net baryon density[1]. High energy nucleus-nucleus collisions such as those at the to RHIC and LHC energies, could create a hot and baryon free QGP on the earth.

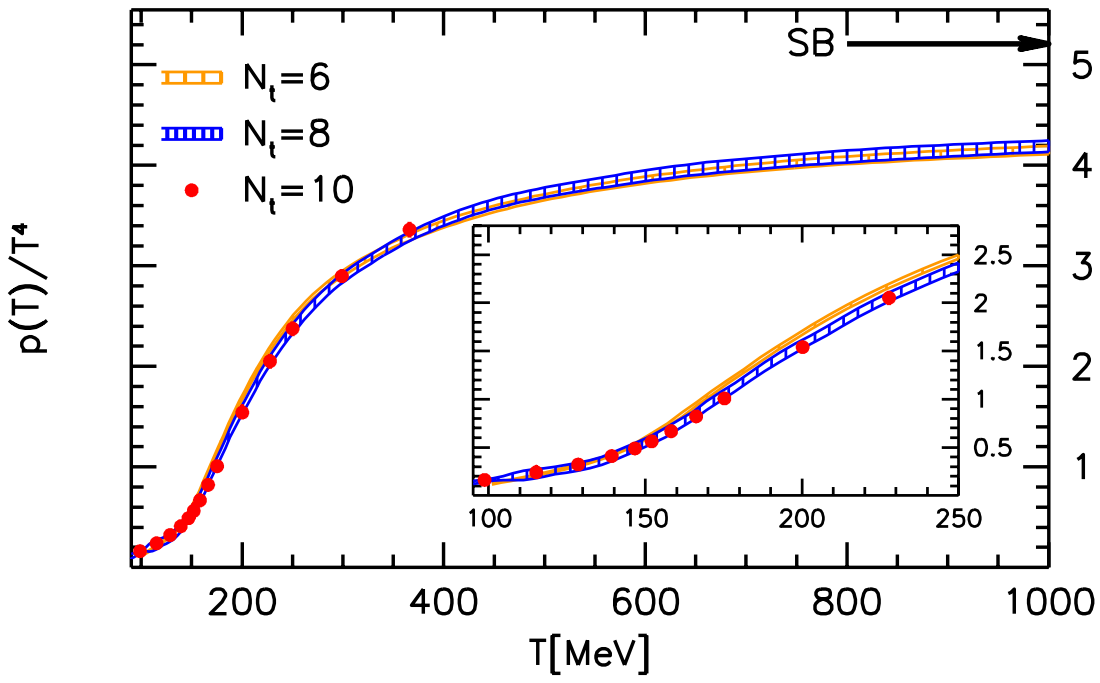

Fig. 1.1.2: The pressure normalized by T^4 as a function of the temperature on $N_t = 6$, 8 and 10 lattices. The Stefan-Boltzmann limit $p_{SB}(T) \approx 5.209 \cdot T^4$ is indicated by an arrow. For our highest temperature $T = 1000$ MeV the pressure is almost 20% below this limit[7]

.

Accelerator	Laboratory	Year	Nucleus	Collision energy $\sqrt{s_{\rm NN}}$ (GeV/c)
SPS	CERN	1986	^{16}O, ^{28}Si	19.4 (fixed target)
		1994	^{208}Pb	17.4 (fixed target)
RHIC	BNL	2000	^{197}Au	130
		2001	^{197}Au	200
LHC	CERN	2010	^{208}Pb	2760
		2011	^{208}Pb	2760
		2015	^{208}Pb	5500

Table 1.2.1: List of high energy heavy-ion accelerator in the world.

The first heavy ion experiments above $\sqrt{s_{\rm NN}} = 10$ GeV is at the Super Proton Synchrotron (SPS) using fixed target, starting from a light ion collisions (O and Si beams) and a heavy-ion collisions (Pb beam) at CERN to create for a new state of matter. Several hadronic observable shows strong non-linearity dependence with respect to the number of nucleons which participate in collisions. The Relativistic Heavy Ion Collider (RHIC) is the first colliding-beam accelerator instead of a fixed-target accelerator, and measured many kinds of signatures that indicates a creation of new state of matter, QGP. However the equation of state of QGP still remains unknown. To access property of the exact matter need to perform the experiments at higher collision energy, because rare probes such as jets were statistically limited. Since 2010, new experiments have been started at the Large Hadron Collider (LHC) at the energy of about 10 times higher ($\sqrt{s_{\rm NN}} = 2.76$ TeV) than at RHIC energy. The new experiments are expected to provide signals from QGP with long life time. Therefore the heavy-ion experiments at LHC allows us to study a significant qualitative improvement for measurements to draw out properties of QGP.

1.3 Collision Geometry

A collision geometry is one of the important and basic ingredients to understand the heavy-ion collisions at high energies. Fig.1.3.1 shows the example of collision geometry along the beam direction, before (left) and after (right) a nucleus-nucleus collisions at a high energy.

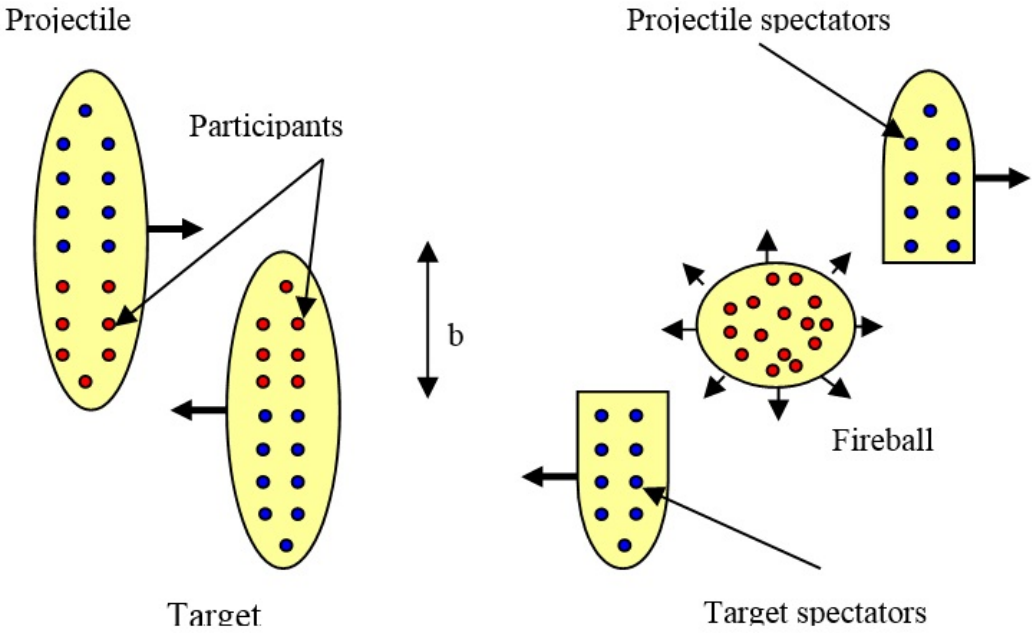

Fig. 1.3.1: Simple picture of Before and after collision of high energy nucleus-nucleus

The collision geometry in a heavy-ion collision is mainly constructed by number of nucleons in projectile nucleus (A), collision energy ($\sqrt{s}$) and distance between center of two nucleons, called an impact parameter (b). Differential cross section with inelastic total cross section of nucleon $\sigma^{in}_{\rm NN}$ is described as following equation

$$\frac{d^2\sigma^{in}_{\rm AA}}{d^2b}(b,\sqrt{s_{\rm NN}}) = 1-(1-\frac{1}{A^2}T_{AB}(b)\sigma^{in}_{\rm NN}(\sqrt{s_{\rm NN}})^{A^2}. \tag{1.3.1}$$

In the case same nuclei collide each other, overlap function $T_{AB}(b)$ should be described as

$$T_{AB}(b) = \int ds^2 T_A(s)T_A(s-b) \tag{1.3.2}$$

where $T_A(s)$ is thickness of nuclei where are penetrated the other nuclei defended as function of nucleon density $\rho_A(r)$ (normalized nucleon density ρ_{nm}) and radius in transverse plane s

$$T_A(s) = \int dz\rho_A(z,s), \rho_A(r) = \frac{\rho_{nm}}{1+exp\left((r-R_A)/a\right)}. \tag{1.3.3}$$

The nucleons in high energy nucleus-nucleus collisions are divided into two regions. One is the "participant" which is the overlapped region in a collision, and other is the "spectator" region. A nucleus-nucleus collision have all of assumption by the Glauber Model[12].

In the Glauber model, we can calculate number of participant nucleons N_{part}, and number of nucleon-nucleon collisions N_{binary} as following equations,

$$N_{part}(b) = \int d^2sT_A(s)(1-exp(-\sigma^{in}_{\rm NN}T_A(s)) + \int d^2sT_A(s-b)(1-exp(-\sigma^{in}_{\rm NN}T_A(s)), \tag{1.3.4}$$

$$N_{binary}(b) = \int d^2s\sigma^{in}_{\rm NN}T_A(s)T_B(s-b). \tag{1.3.5}$$

1.4 Time Evolution

Another important aspect of heavy-ion collisions at high energies is the space-time evolution of a created system, because the system is dynamical, and the properties also change as a function of time. Fig.1.4.1 shows the schematic diagram of time evolution for the produced matter by a high energy nucleus-nucleus collision in the Bjorken picture[3].

After a nucleus-nucleus collision, it is consider that a produced matter is developed by taking the following steps as a function of time.

Initial collision and pre-equibiliation ($0 < \tau < \tau_0$) : A central high energy nucleus-nucleus collision is a process of huge entropy production. This entropy production be constructed from the incoherent models and the coherent models[4]. The incoherent models is minijet production from partons generated by semi-hard process. Such partons are difficult to separate with partons generated by soft parton production. And they also interact with each other. The process could contribute to from an equilibrated parton plasma. The coherent models is the color string braking model which is the formation of color strings and ropes between two projectile nuclei. Then many quark pairs and gluon pairs are generated in color electric field in participant region. In short time scale, equilibrated parton plasma are produced by partons in exited fields[5].

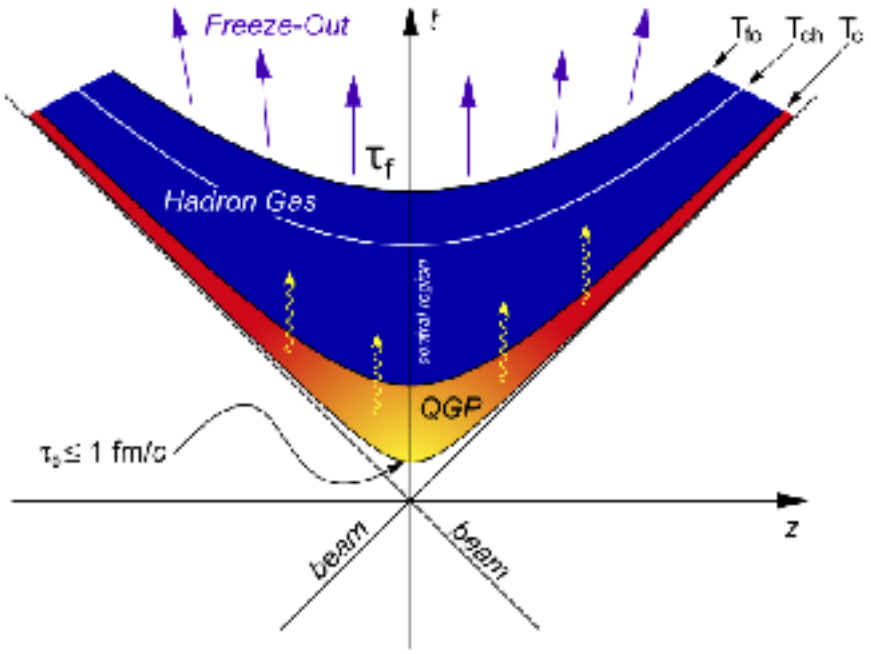

Fig. 1.4.1: The schematic diagram of time evolution of a nucleus-nucleus collision as functions of the beam direction and time after a collision.

QCD phase transition and hydrodynamical evolution stage ($\tau_0 < \tau < \tau_f$) : After the local thermal equilibrium is achieved, we can use the relativistic hydrodynamical model to describe the expansion of the system to longitudinal and transverse direction. The results of experiments at the RHIC indicate that transverse expansion can be described by a nearly perfect fluid. If a thermal matter expands on approximated hydrodynamics by a perfect fluid, the evolution of a fluid can be parameterized by a local energy density ε and the local pressure P. The energy-momentum tensor $T^{\mu\nu}$ and the baryon number current j_B^μ of the perfect fluid with fluid four velocity u^μ is given by

$$T^{\mu\nu} = (\varepsilon + P)u^\mu u^\nu - g^{\mu\nu}P, \partial_\mu < T^{\mu\nu} >= 0, \tag{1.4.1}$$

$$j_B^\mu = n_B u^\mu, \partial_\mu < j_B^\mu >= 0. \tag{1.4.2}$$

Freeze out stage ($\tau_f < \tau$) : After a phase transition to QGP, the matter gets cooling down due to an expansion of the system. Then the quark-gluon matter will become hadron gas again on hypersurface and the number of hadron is frozen. We call this stage a chemical freeze-out, where all inelastic scattering stop and the particle ratios are fixed. And then the elastic scatting stop by the further cooling of the system, and the kinematics for all hadron (e.g. momentum) are fixed. We call this stage as "kinetic freeze-out or thermal freeze-out".

1.5 Jet production and parton energy loss in the medium

A jet is a shower of hadrons from the fragmentation of hard parton which is produced by high energy collisions with large momentum transfer Q and produced back-to-back direction due to a momentum conservation. The left figure in Fig.1.5.1 shows the sketch of jet production in a single proton-proton collision.

According to the results of nucleus-nucleus collisions of experiments at the RHIC and LHC, the

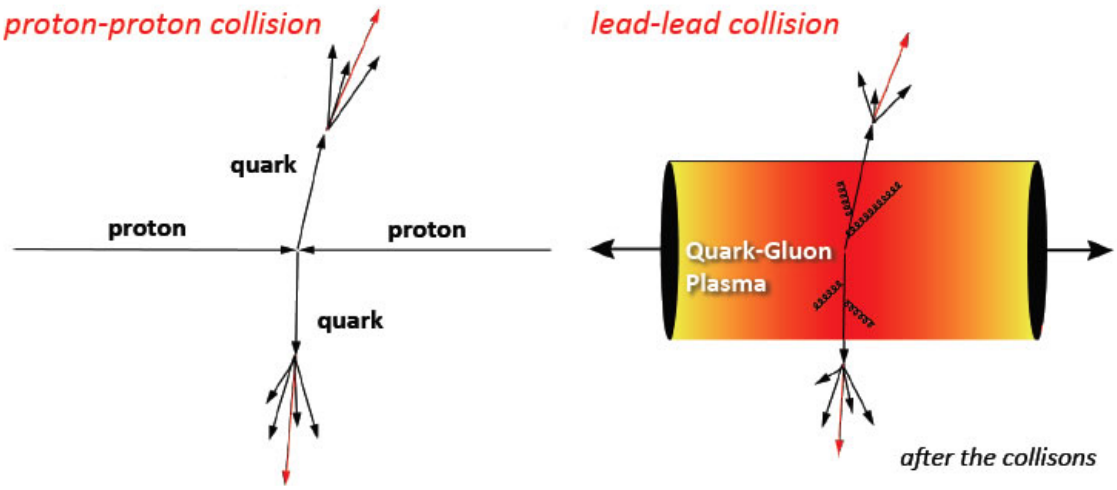

Fig. 1.5.1: Energy loss of parton in QGP

particle yield produced by a hard scattering is suppressed compared with the yield of pp collisions[22]. The right figure in Fig.1.5.1 shows an idea how a produced jet loses its energy in a medium created by heavy ion collisions. According to an energy loss model[6], we can describe amount of energy loss of a parton ΔE using parton position l, path length L, scattering probability density $dP(l)/dl$ and mean free path λ in general,

$$\Delta E = \int_0^L dl \frac{dP(l)}{dl} \lambda(l) \frac{dE(l,E)}{dl}, \frac{dP(l)}{dl} = \frac{1}{\lambda(l)} exp\left(\frac{-l}{\lambda(l)}\right). \tag{1.5.1}$$

It is considered that there are two mechanisms. The first one is collisional energy loss when the parton lose their energy colliding constituents partons of QGP. Latter one is radiative energy loss when the parton radiate gluons.

Thus, Eq.1.5.1 can be describe by sum of energy loss as follows,

$$\Delta E = \Delta E_{collisional} + \Delta E_{radiative} \tag{1.5.2}$$

At LHC energies, the energy loss by the gluon radiation (ΔE radiative) is dominated.

1.6 Experimental results of high p_T physics

Now, we show current experimental results about jet modification measured at RHIC and LHC.

1.6.1 High p_T physics of heavy ion collisions at the RHIC

At RHIC energy, there are two highlighted results using high p_{T} particles; 1) a strong suppression of yields in Au+Au central collisions at high p_{T} (nuclear modification factor $R_{\mathrm{AA}} < 1$) and 2) a disappearance of away-side jet peak measured by the two particle hadron correlations.

Nuclear modification factor R_{AA} :

High momentum particles and jets are produced from hard parton scattering with large momentum transfer at the initial state in a collision. Such probes are the strong tool to measure the properties of the medium. At first, the results by using hard probes were measured as suppression of high p_T particle at the RHIC. These suppression was quantified by the two analysis methods, one is the nuclear modification factor R_{AA} and another is two particle correlation measurement. The nuclear

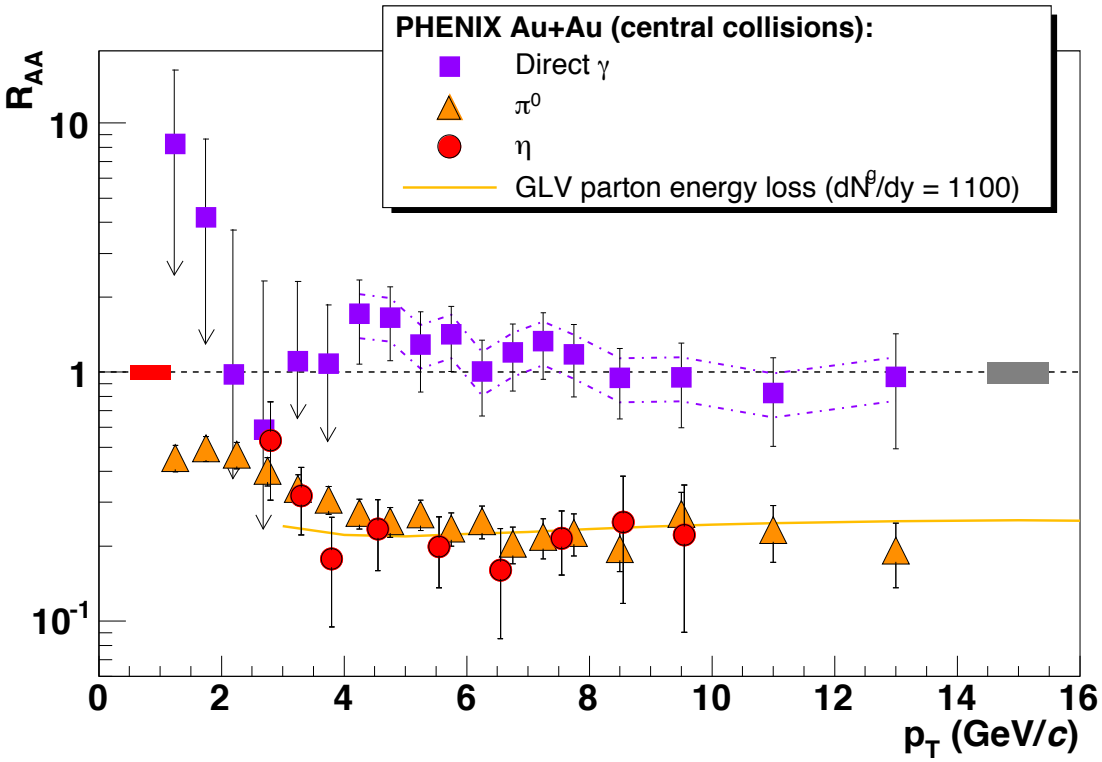

Fig. 1.6.1: Nuclear modification factors of π^0, η, direct γ as functions of p_T in central Au+Au collisions at $\sqrt{s_{\rm NN}} = 200$ GeV/c[22]. The solid yellow curve is a parton energy loss prediction for a medium with density $dN^g/dy = 1100$.

modification factor $R_{\rm AA}$ is the ratio of yields of heavy-ion collisions that in pp collisions and can be given by,

$$R_{\rm AA} = \frac{\frac{1}{N_{event}^{\rm AA}} \frac{d^2 N_{ch}^{\rm AA}}{dp_T d\eta}}{< N_{coll} > \frac{1}{N_{event}^{pp}} \frac{d^2 N_{ch}^{pp}}{dp_T d\eta}} \tag{1.6.1}$$

where the number of binary nucleon-nucleon collisions $< N_{coll} >$ is estimated by the product of the nuclear overlap function $T_{\rm AA}$ obtained from the Glauber model, and the inelastic NN cross-section $\sigma_{inel}^{\rm NN}$.

Fig.1.6.1 shows the nuclear modification factor $R_{\rm AA}$ as function of p_T for η, π^0 and direct γ in central Au+Au collisions at $\sqrt{s_{\rm NN}} = 200$ GeV measured by the PHENIX collaboration. Direct γ in high p_T region are generated from hard scattering process with high momentum transfer process. And, direct γ is not suppressed due to neutral color charge, which means that they do not interact a QGP matter strongly. On the other hands, the yields of η and π^0 in Au+Au collisions are strongly suppressed compared with the yields of pp collisions.

Suppression of away side peak :

Fig.1.6.2 shows the azimuthal yields of the associated charged particles yields with respect to the trigger particle ($4 < p_{\rm T}^{\rm trig} < 6$ GeV/c, $2 < p_{\rm T}^{\rm asso} < p_{\rm T}^{\rm trig}$ GeV/c). The bottom figure of Fig.1.6.2 is the comparison of azimuthal yields of pp, d+Au and Au+Au collisions. The azimuthal yields of pp and d+Au collisions show two clear jet like peaks, while the away-side peak in Au+Au collisions are strongly suppressed relative to pp and d+Au collisions. These result indicate that suppression of away-side peak is caused by jet modification effect in a medium. On the other hand, near side peaks for all three collision systems look similar, and it indicates one can put a similar surface bias for three collision systems by requiring high $p_{\rm T}$ trigger hadron on the near-side.

1.6.2 High p_T physics of heavy ion collisions at the LHC

Next we summarize the experimental highlights of jet measurements at LHC. The first one is the di-jet energy asymmetry and the second one is the direct measurement of jet quenching by the study of single jet spectrum in pp and Pb-Pb collisions at 2.76 TeV. The experiments at LHC started direct measurements for jet and jet modification.

Di-jet energy asymmetry A_j :

Fig.1.6.3 shows an asymmetry of di-jet distribution on $\varphi - \eta$ plane in an event of Pb-Pb $\sqrt{s_{\rm NN}} =$ 2.76 TeV from the CMS collaboration at LHC[26]. The two jets are reconstructed from charged particles and neutral particles. The leading jet is seen sharp peak with large transverse momentum ($p_{\rm T}^{\rm leading} = 205.1$ GeV/c), while the sub-leading jet is seen smaller peak and transverse momentum ($p_{\rm T}^{\rm sub-leading} = 70.0$ GeV/c) compared with the leading jet.

Fig.1.6.4 shows the di-jet energy asymmetry parameter A_j distributions (top figures) and di-jet open angle distributions as function of centrality with $p_{\rm T}^{\rm leading} > 120$ GeV/c, $p_{\rm T}^{\rm sub-leading} > 50$ GeV/c and $\Delta\varphi_{\rm leading,sub-leading} > 2\pi/3$. Di-jet asymmetry parameter A_j can be given by

$$A_j = \frac{p_{\rm T}^{\rm leading} - p_{\rm T}^{\rm sub-leading}}{p_{\rm T}^{\rm leading} + p_{\rm T}^{\rm sub-leading}}. \tag{1.6.2}$$

The shape of A_j distributions in Pb-Pb collisions is modified with respect tor the distribution in pp and increasing A_j value. The $\Delta\varphi$ distributions show that the leading and sub-leading jets distribute primarily back-to-back direction in all centrality. However, a small increase are seen in the rate of sub-leading jets at large angle with increasing centrality.

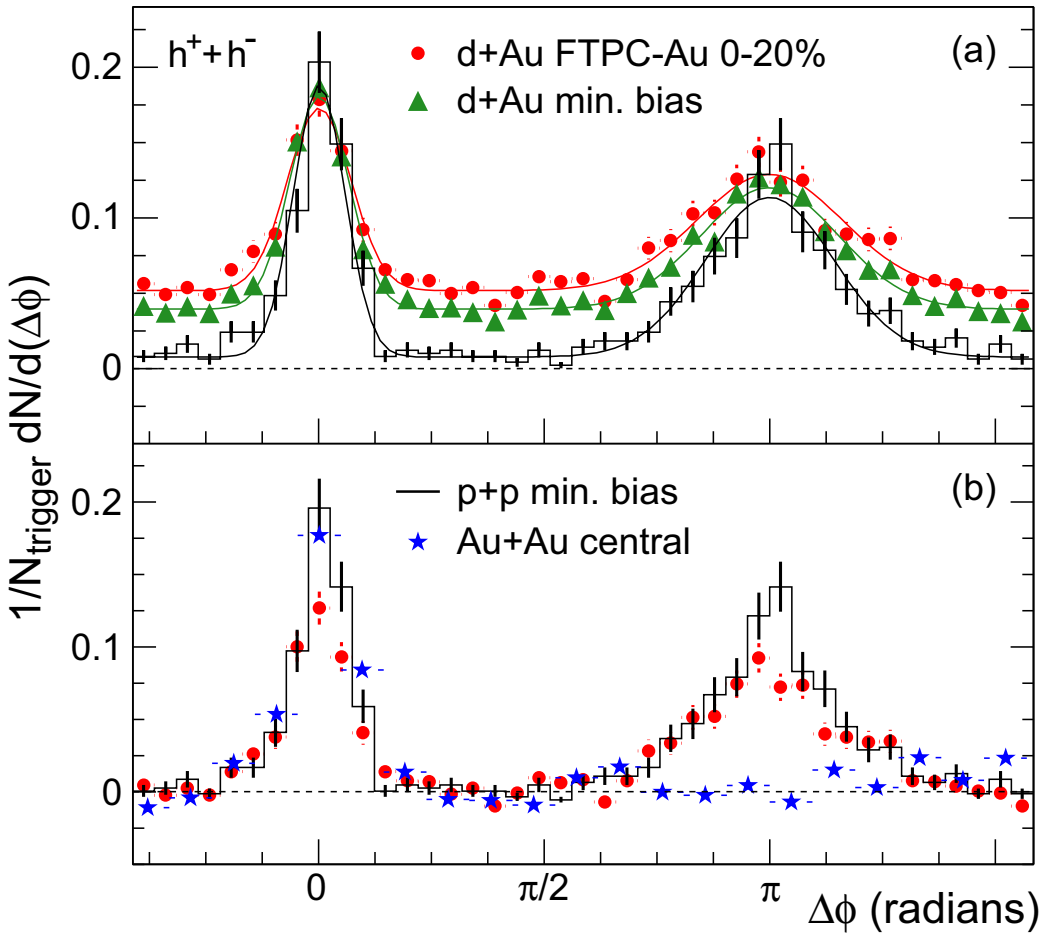

Fig. 1.6.2: (a) Two-particle azimuthal distributions for minimum bias and central d+Au collisions and for pp collisions. (b) Comparison of two-particle azimuthal distributions for central Au+Au collisions and d+Au collisions and pp collisions [25].

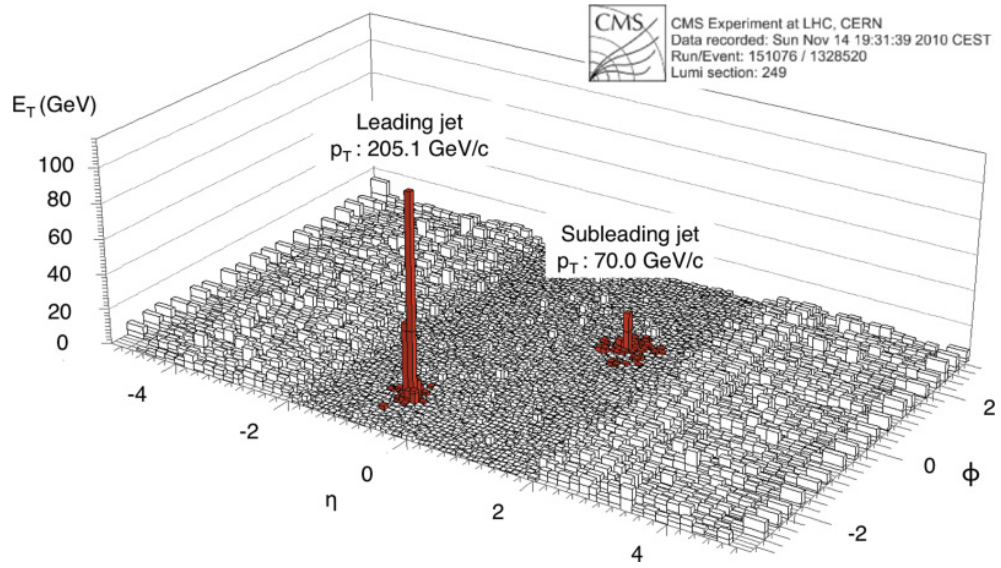

Fig. 1.6.3: Leading and sub-leading jet p_T on transverse plane in an event of Pb-Pb at $\sqrt{s_{NN}} = 2.76$ TeV from CMS[26].

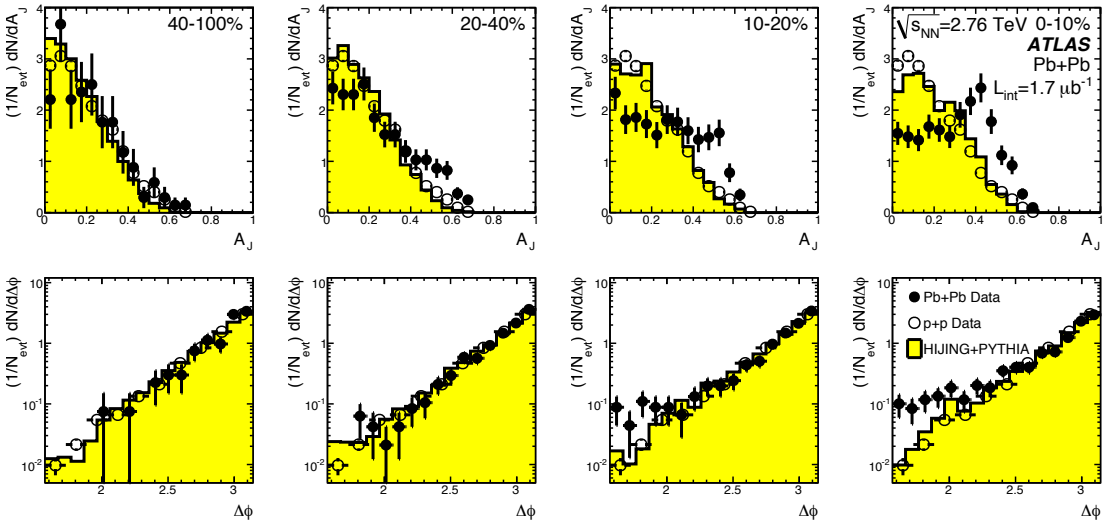

Fig. 1.6.4: The top figures are comparison of Di-jet energy asymmetry parameter A_j of pp, central Pb-Pb collisions and HIJING simulation embedded PYTHIA events[26]. The bottom figures show Distributions of the azimuthal angle between leading and sub-leading jets as function of centrality.

Nuclear modification factor of charged jets :

Fig.1.6.5 shows the nuclear modification factor of charged jets as function of p_T in Pb-Pb col-

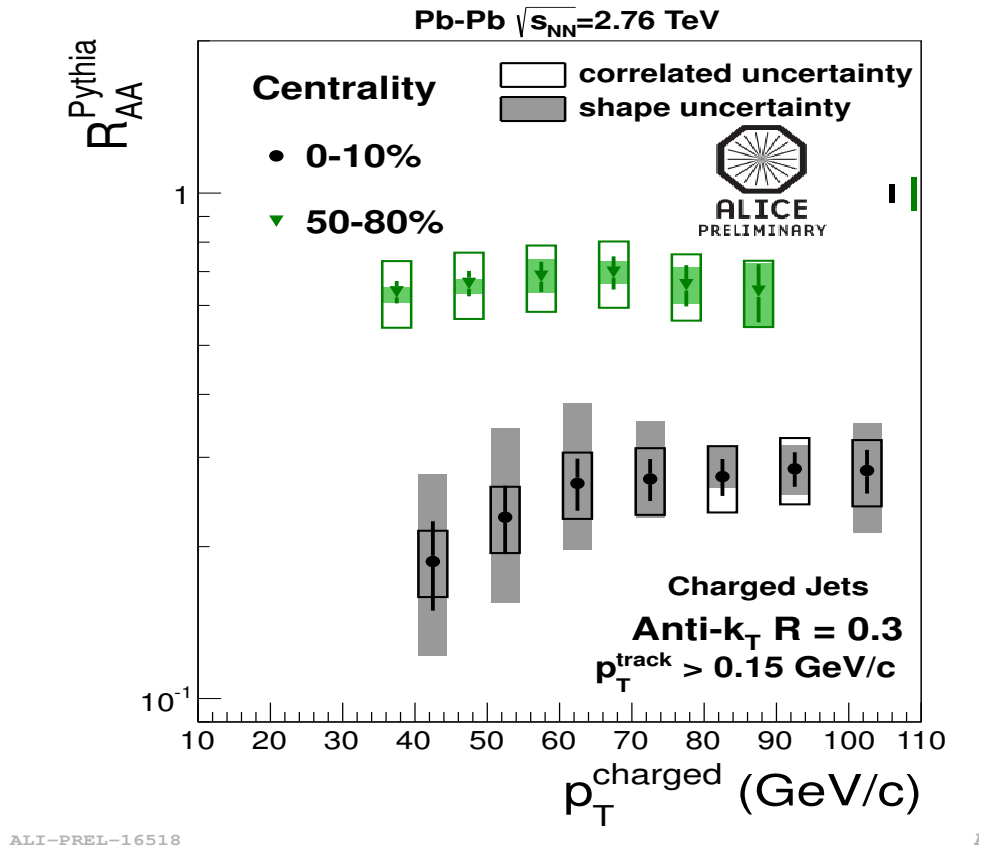

Fig. 1.6.5: Nuclear modification factors of charged jet as function of p_T in Pb-Pb collisions at $\sqrt{s_{\rm NN}} = 2.76$ TeV from the ALICE experiment[24].

lisions at $\sqrt{s_{\rm NN}} = 2.76$ TeV from the ALICE experiment[24]. The reference jet yields are taken from PYTHIA calculation instead of the jet yields from experimental data. A strong suppression is seen in jet $R_{\rm AA}$ in measured $p_{\rm T}$ range, and the magnitude of suppression and $p_{\rm T}$ dependence of of suppression pattern is similar to the single particle analysis.

1.7 Suppression of high $p_{\rm T}$ particles and surface bias

In general, the hard scattering of initial partons with high momentum transfer dominates at $p_{\rm T} > 2$ GeV/c. Fig.1.7.1 shows the nuclear modification factors of charged particles as function of p_T in central Pb-Pb collisions at $\sqrt{s_{\rm NN}} = 2.76$ TeV from ALICE and CMS experiments at LHC. This figure indicates that most of high momentum hadrons in heavy-ion collisions are strongly suppressed at $p_{\rm T} > 2$ GeV/c, and then absorbed into a medium or shifted towards the low momentum region. Thus, the part of high momentum hadrons which is not suppressed are produced at the surface in a medium. This effect is called “surface bias”.

1.8 π^0-jet correlations

As mentioned in the previous section, high momentum hadrons in heavy-ion collisions mainly come from the surface of a medium by the surface bias. This fact suggests that the medium path-length of jets

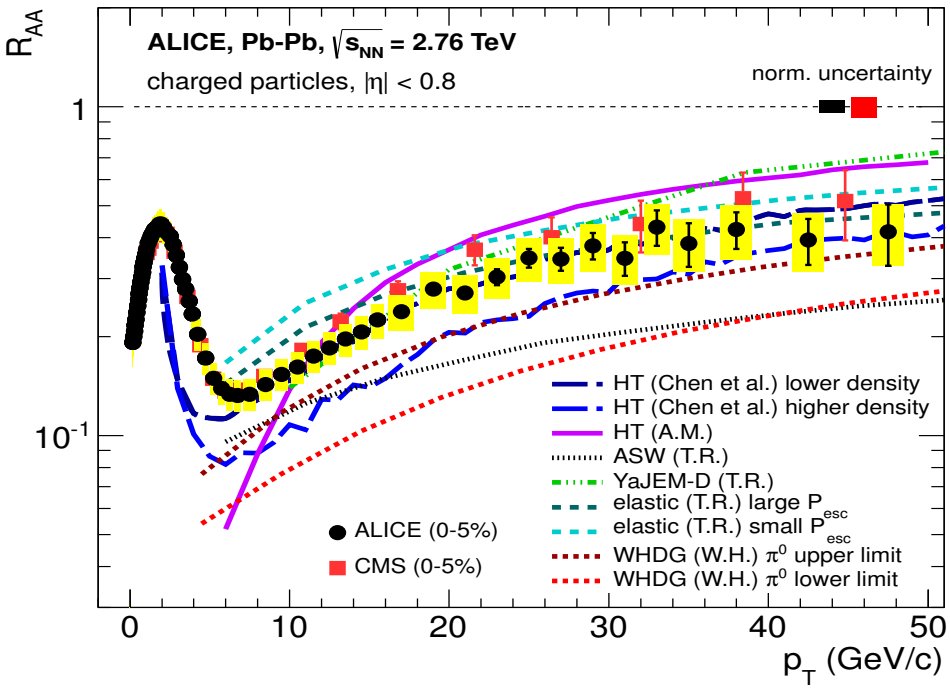

Fig. 1.7.1: Nuclear modification factors of charged particles as function of p_T in central Pb-Pb collisions at $\sqrt{s_{\rm NN}} = 2.76$ TeV from ALICE and CMS experiments[23].

emitted to the opposite side can be maximized by selecting high momentum hadrons as trigger. Thus, we can control the path-length of jets by changing $p_{\rm T}$ of trigger hadron.

Fig.1.8.1 shows the geometry of a trigger π^0 and its recoil jet in transverse plane. A hard scattering point is indicated as solid star, where a di-jet is produced back to back. A trigger π^0 goes to the right with traversing length L1 in the matter, while its recoil jet goes to the left with traversing length L2. Fig.1.8.2 shows the path-length bias of the trigger π^0 with various $\hat{q}$ (energy loss per unit path-length) and trigger π^0 energy threshold which is generated by qPYTHIA. Assuming no in medium energy loss per unit path length ($\hat{q}$ = 0 GeV^2/fm), the distribution follows the unbiased distribution of hard scattering, whereas for a large $\hat{q}$ values (in this case $\hat{q} = 20$ and 50 GeV^2/fm) with high energy trigger π^0, it is strongly biased towards the surface in a medium. In fact, the path-length of away-side jets become longer than the near-side jets by the surface bias. In addition, we can make an artificial bias on the production points of near and away-side jets towards at the surface in a medium by requiring the high momentum leading particle in a jet. Fig.1.8.3 shows an idea of leading particle bias effect and the expected $p_{\rm T}$ dependence. If we require high momentum leading particle in a near and away-side jet, the path-length of near and away-side jets become shorter than the other.

Fig.1.8.4 shows the ratio of per trigger yields $I_{\rm AA}$ in near and away-side as a function of the associated particle $p_{\rm T}$ with the di-hadron correlations in central and peripheral Pb-Pb collisions measured by the ALICE collaboration. The enhancement of jet-like yields are observed in near-side, while the suppression of jet-like yields is observed in away-side by the surface bias. The enhancement in near-side is caused by the effect of 1) a change of the fragmentation function and 2) a possible change of the quark/gluon jet ratio in the final state[29].

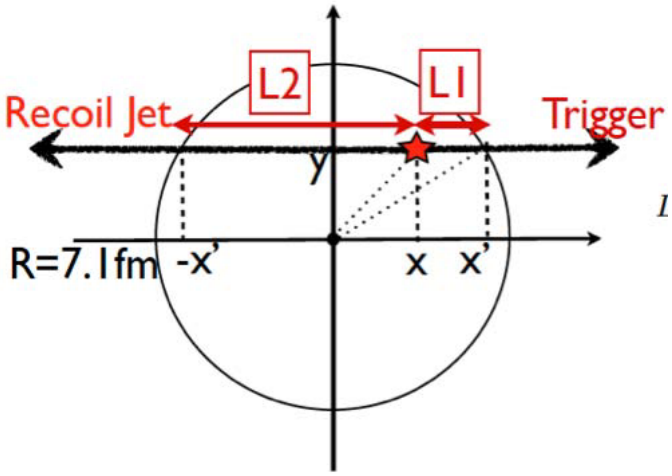

Fig. 1.8.1: Geometry of trigger π^0 and its recoil jet in transverse plane[28].

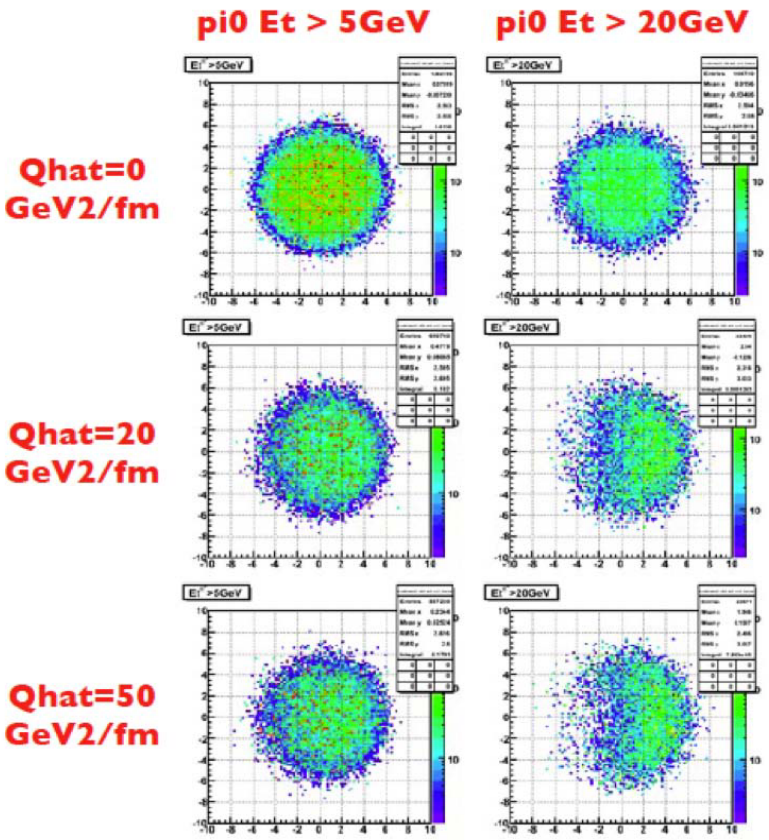

Fig. 1.8.2: Trigger π^0 energy dependence of hard scattering point distribution in transverse plane with trigger pions moving to the right[28].

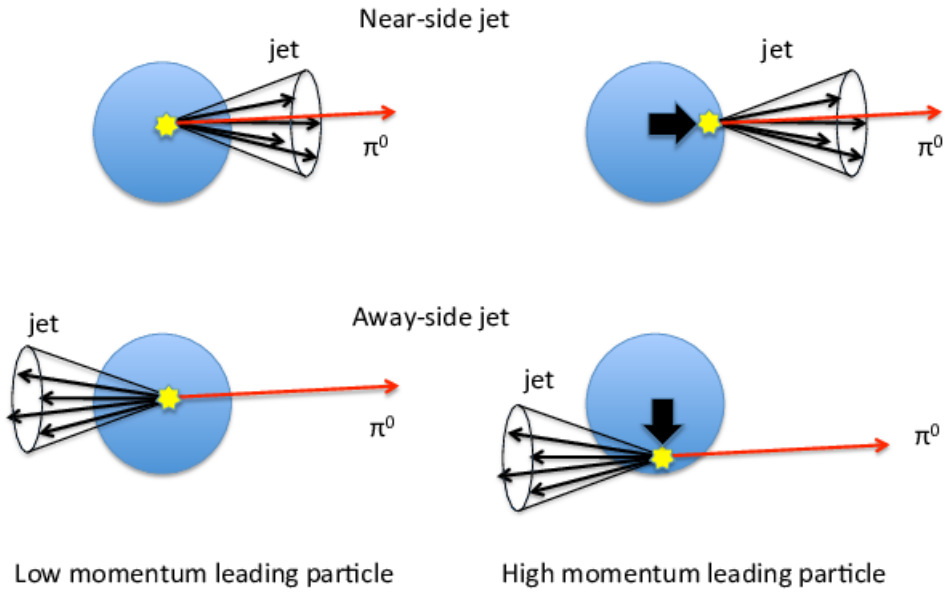

Fig. 1.8.3: Momentum dependence of the leading particle in a jet of the surface bias in near (top) and away-side (bottom). The left two figures are required a low momentum leading particle, the right figures are required a high momentum leading particle.

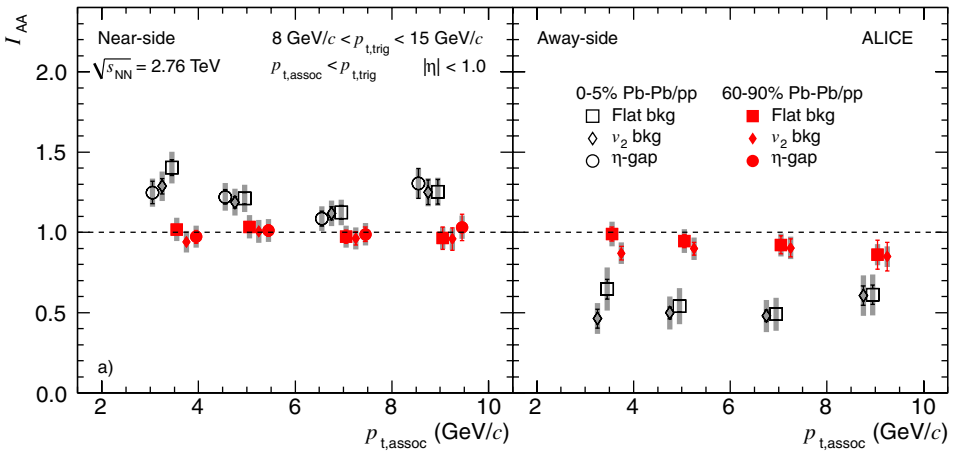

Fig. 1.8.4: Ratio of per trigger yields I_{AA} in near and away-side as a function of the associated particle p_T with the di-hadrons correlation in central (black) and peripheral (red) Pb-Pb collisions at $\sqrt{s_{NN}} = 2.76$ TeV from LHC-ALICE[29].

1.9 Physics motivation

According to the results of from the RHIC and LHC, jet modifications are measured a suppression of high p_{T} particles. Di-jet energy asymmetry and suppression of jet and high p_{T} particle in away-side with respect to triggered high p_{T} hadron indicate that a medium created in heavy-ion collisions at RHIC and LHC is opaque and a large amount of energy is deposited the medium.

The RHIC experiments have measured particle yield ratios of nucleus-nucleus collisions and pp collisions by using nuclear modification factor and modification of away-side particle yields in two particle correlation measurements. They give us knowledge of jet modification in medium. However, it is difficult to reconstruct jets due to lower jet cross section at the RHIC that at the LHC. Thus, we can not extract information of jet modification directory. The LHC experiments have measured the back-to-back di-jet energy asymmetry and suppression of recoil jet yields with triggered high p_{T} charged hadron in heavy-ion collisions. However, these measurements does not give enough information of path-length of leading and sub-leading jets and near-side jet modification due to auto-correlation. We need more detail differential measurements on jets.

According to the jet quenching model, hadron-jet correlation measurements allow us to control the medium path length of the parton that is reconstructed as jet in away-side of measured hadron, by selecting high transverse momentum hadrons as trigger that mainly come from the surface of the medium. In addition, selecting π^0 as trigger particle instead of charged hadron, we can ignore a trivial auto-correlation between trigger particles and charged jets, since the trigger π^0 is not directly a part of charged jet, although the auto-correlation from other physics processes are all include in the measured correlation, that is also a motivation of this analysis.

In this thesis we report the measurement of neutral pion-charged jet correlation in pp $\sqrt{s} = 7$ TeV and central Pb-Pb collisions at $\sqrt{s_{\mathrm{NN}}} = 2.76$ TeV. In particular, we report the azimuthal correlations between high momentum π^0 and charged jet, the ratio of per trigger yields I_{AA} and Gaussian widths in near and away-side as function of trigger π^0 and associated jet momentum. These measurements could address the following physics points using π^0-jet angular correlation;

- Correlation between high momentum neutral particle production and jet production
- Effect of the surface bias of jet production in the medium at high p_{T} region.
- Path-length dependence jet energy loss by changing p_{T} of trigger π^0.
- Possible modification of jet shape which exhibit in widths of azimuthal distributions of jet in near and away sides by a comparison between pp and Pb-Pb collisions, different trigger p_{T} for π^0 and leading particles.

In particular, we measure the enhancement of near-side jets and suppression of away-side jet by the surface bias at high p_{T} region above jet p_{T} larger than 10 GeV/c for the first time.

1.10 My contribution

- obtain the preliminary results of π^0-jet correlation measurements in pp collisions at $\sqrt{s} = 7$ TeV in the ALICE experiment.
- EMCal/DCal commissioning works for the Run 2.

Chapter 2

Experimental Apparatus

As mentioned in the previous section, we use the high energy heavy-ion collisions for research of QGP matter. In this section, we describe the overview of the Large-Hadron Collider (LHC) and the sub-detectors used in this analysis in the ALICE detector.

2.1 Large Hadron Collider (LHC)

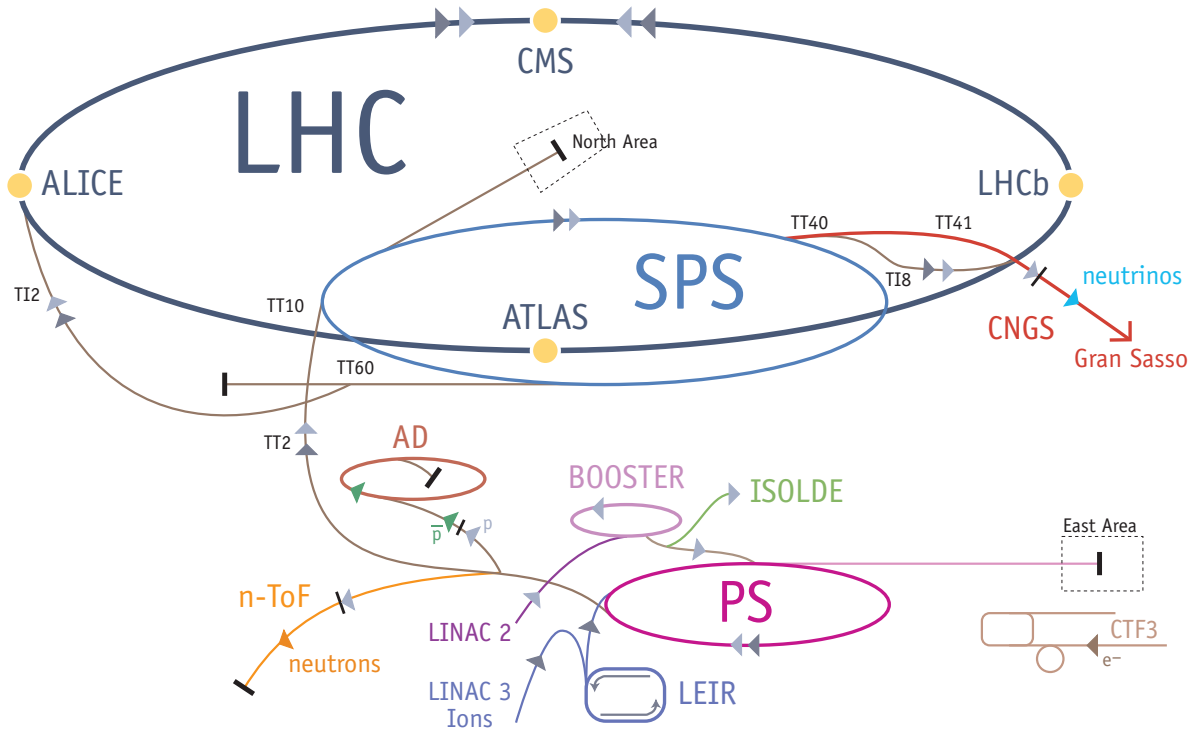

Fig. 2.1.1: Large Hadron Collider (LHC)[30]

The Large Hadron Collider (LHC)[30] is located at CERN laboratory of Geneva in Switzer-land and was built for research high energy particle and nuclear physics. It first started up on 10 September 2008. The first physics run for Pb-Pb collisions started since end of 2010. The collision energy of LHC is the

highest energy in the world with proton-proton collisions $\sqrt{s} = 14$ TeV and Pb-Pb collisions at $\sqrt{s_{\rm NN}} =$ 5.5 TeV as the maximum design energy. The LHC is constructed the two rings which had 27 km long circumference, and the Super Proton Synchrotron (SPS) and Proton Synchrotron (PS) is used as the booster accelerators to inject proton and lead beams to the LHC. There are four major experiments at LHC: ATLAS[31], CMS[32], ALICE[33] and LHCb[34].

Table.2.1.1 shows the LHC beam parameters for proton beam operation. LHC can fill bunches with 25 ns interval in full bunches operation, and accelerate proton to 7 TeV from injection energy 450 GeV.

		Injection	Collision
Beam Data			
Proton Energy	(GeV)	450	7000
Relativistic gamma		479.6	7461
Number of particles per bunch		1.15×10^{11}	
Number of buches		2808	
Longitudinal emittance (4σ)	(eVs)	1.0	2.5
Transverse normalized emittance	(μm rad)	3.5	3.75
Circulating beam current	(A)	0.582	
Stored energy per beam	(MJ)	23.3	362
Peak Luminosity Related Data			
RMS bunch length	(cm)	11.24	7.55
RMS beam size at the IP1 and IP5	(μm)	375.2	16.7
RMS beam size at the IP2 and IP8	(μm)	279.6	70.9
Geometric luminosity reduction factor F		-	0.836
Peak luminosity in IP1 and IP5	($\mathrm{cm}^{-2}\mathrm{sec}^{-1}$)	-	1.0×10^{34}
Peak luminosity per bunch crossing in IP1 and IP5	($\mathrm{cm}^{-2}\mathrm{sec}^{-1}$)	-	3.56×10^{30}

Table 2.1.1: LHC beam parameters relevant for the luminosity lifetime for protons.

2.2 ALICE detector

The ALICE detector(Fig.2.2.1)[35] was built to exploit the unique physics potential of nucleus-nucleus interactions at the LHC and is capable of studying jet quenching effects via particle identification and jet reconstruction. The ALICE detector is constructed by the 14 sub-detectors which is divided into three kinds of detector class, Global detectors, Central detectors and Forward detectors. Table.2.2.1 shows the overview of geometrical properties of sub-detectors in the ALICE detector. In latter section, we will describe more detail of sub-detectors in the ALICE detector.

2.2.1 VZERO

The V0 detector[36] is constructed from 32 scintillator counters in 4 rings and installed on both side of the ALICE interaction point. The detector of A side is named V0A, the detector of C side is named V0C. Fig.2.2.3 shows the segmentation of the V0 detector. This detector was designed for three purposes, 1) to provide minimum-bias trigger for the central detectors in pp and Pb-Pb collisions, 2) to determine centrality in Pb-Pb collisions and 3) to determine event plane angle in Pb-Pb collisions.

2.2.2 Inner Tracking System (ITS)

The Inner Tracking System (ITS)[37] is consists of 6 cylindrical layers of silicon detector. The pair of each two layers are called the Silicon Pixel Detector (SPD), Silicon Drift Detector (SDD) and Slicon Strip Detector (SSD) from the interaction point. The main purposes of the ITS are,

– reconstruction of primary vertex and secondly vertex from a heavy flavor decay,

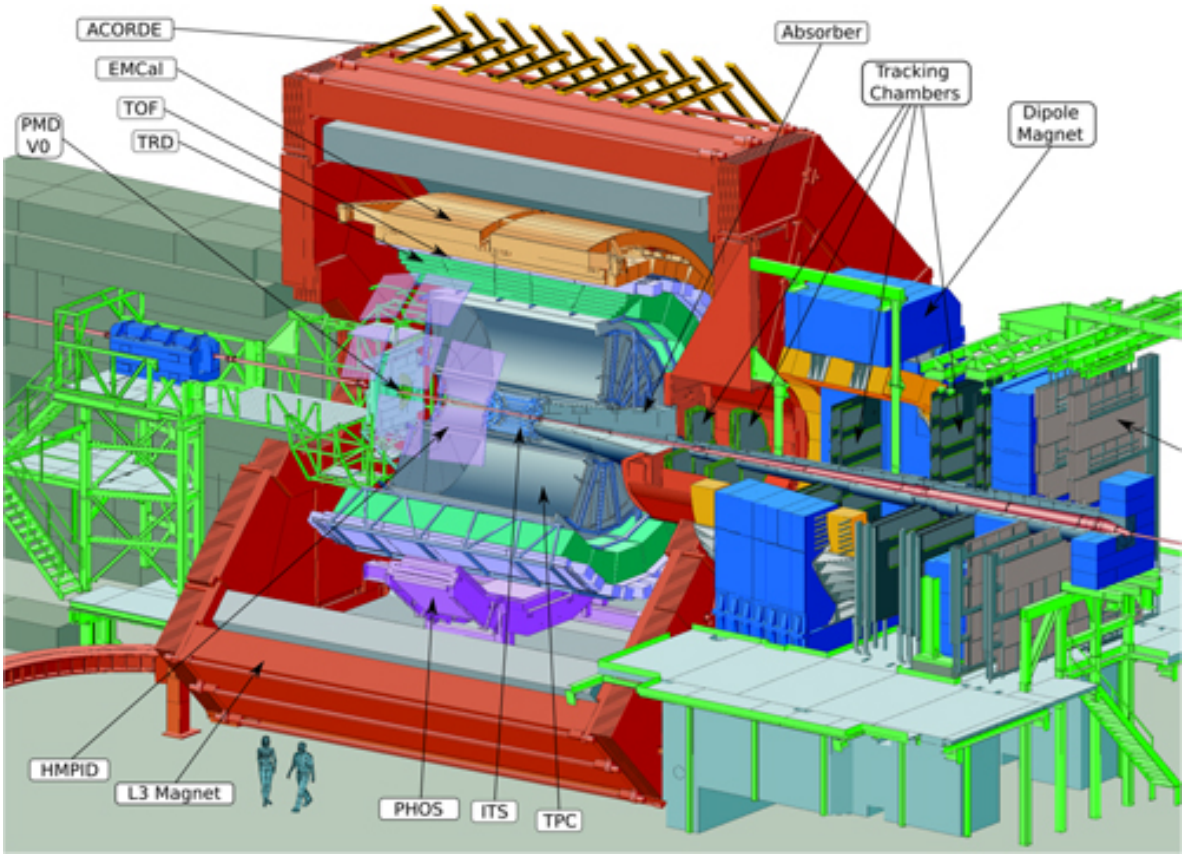

Fig. 2.2.1: ALICE detector

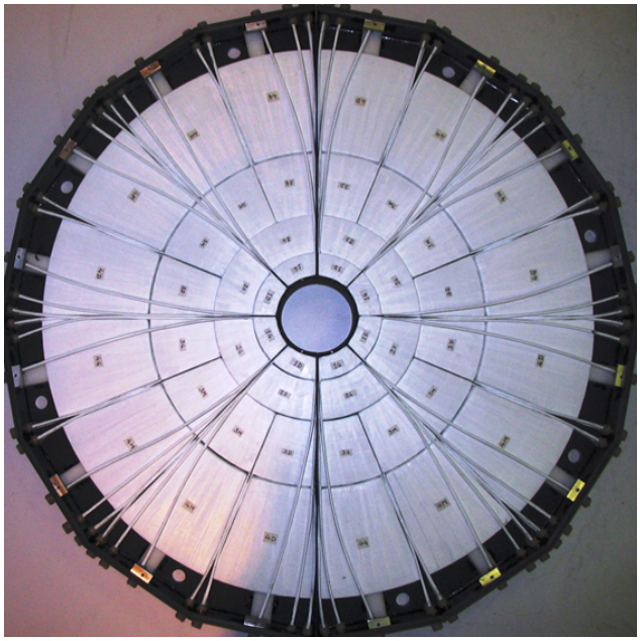

Fig. 2.2.2: V0 detector

Detector	Radius	Rapidity	Azimuthal Range	Technology	Purpose
Global detectors					
T0	z = 370 cm	$4.6 < \eta < 4.9$	full	quartz	time, vertex
	z = -70 cm	$-3.3 < \eta < -3.0$	full	quartz	time, vertex
V0	z = 329 cm	$2.8 < \eta < 5.1$	full	scint.	charged particles
	z = -88 cm	$-3.7 < \eta < -1.7$	full	scint.	charged particles
ZDC	z = $\pm$113 cm	$\lvert\eta\rvert > 8.8$	full	W+quartz	forward neutrons
	z = $\pm$113 cm	$6.5 < \eta < 7.5$	$\lvert\phi\rvert < 10^\circ$	W+quartz	forward neutrons
Central detectors					
SPD	r = 3.9 cm	$\lvert\eta\rvert < 2.0$	full	Si pixel	tracking, vertex
	r = 7.6 cm	$\lvert\eta\rvert < 1.4$	full	Si pixel	tracking, vertex
SDD	r = 15.0 cm	$\lvert\eta\rvert < 0.9$	full	Si drift	tracking, PID
	r = 23.9 cm	$\lvert\eta\rvert < 0.9$	full	Si drift	tracking, PID
SSD	r = 38.0 cm	$\lvert\eta\rvert < 1.0$	full	Si strip	tracking, PID
	r = 43.0 cm	$\lvert\eta\rvert < 1.0$	full	Si strip	tracking, PID
TPC	$85 < r/cm < 247$	$\lvert\eta\rvert < 0.9$	full	Ne drift+MWPC	tracking, PID
TRD	$290 < r/cm < 368$	$\lvert\eta\rvert < 0.8$	full	TR+Xe drift+MWPC	tracking, $e^{\pm}$ id
TOF	$370 < r/cm < 399$	$\lvert\eta\rvert < 0.9$	full	MRPC	PID
EMCal	$430 < r/cm < 455$	$\lvert\eta\rvert < 0.7$	$80^\circ < \phi < 187^\circ$	Pb+scint.	photons and jets
PHOS	$460 < r/cm < 478$	$\lvert\eta\rvert < 0.12$	$220^\circ < \phi < 320^\circ$	PbWO_4	photons
HMPID	r = 490 cm	$\lvert\eta\rvert < 0.6$	$1^\circ < \phi < 59^\circ$	C_6F_{14} RICH+MWPC	PID
Forward detectors					
FMD	z = 320 cm	$3.6 < \eta < 5.0$	full	Si strip	charged particles
	z = 80 cm	$1.7 < \eta < 3.7$	full	Si strip	charged particles
PMD	z = 367 cm	$2.3 < \eta < 3.9$	full	Pb+PC	photons
MCH	$-14.2 < z/m < -5.4$	$-4.0 < \eta < -2.5$	full	MWPC	muon tracking
MTR	$-17.1 < z/m < -16.1$	$-4.0 < \eta < -2.5$	full	RPC	muon trigger

Table 2.2.1: Information of sub-detectors in ALICE detector

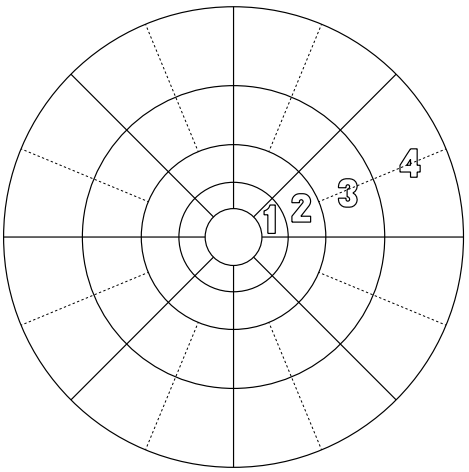

Fig. 2.2.3: Segmentation of the V0 detector[36]

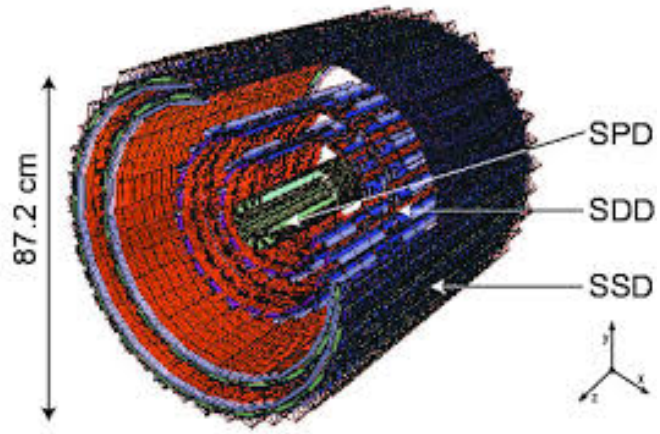

Fig. 2.2.4: Schematic view of Inner Tracking System (ITS)

– particle identification and reconstruction of low-momentum particle,

– improvement of the momentum and angle measurements from the TPC.

Fig.2.2.5 shows vertex resolution in z axis (beam direction) as a function of particle density in η and indicates that this detector contribute to a better z vertex resolution in heavy-ion collisions.

The ALICE is used the method based on the Kalman filter algorithm to reconstruct charged par-

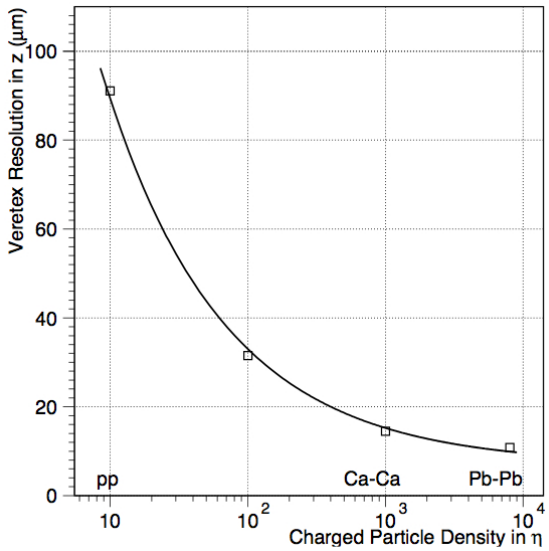

Fig. 2.2.5: Vertex resolution in z axis as a function of particle density in η[37].

ticles. The left figure in Fig.2.2.6 shows ITS stand-alone efficiency and fake track rate as a function of transverse momentum and the right figure shows angular resolution as function of transverse momentum. We obtain 90 % tracking efficiency with less than 10 % fake track rate above 2 GeV/c in p_{T}, and angle resolution is less than 1 mrad at 2 GeV/c.

Momentum of charged particles are reconstructed by combining the ITS and TPC, because it is difficult to estimate curvature factor in high momentum region. Fig.2.2.7 shows the comparison of momentum resolution between only ITS and ITS+TPC as a function of transverse momentum. Momentum

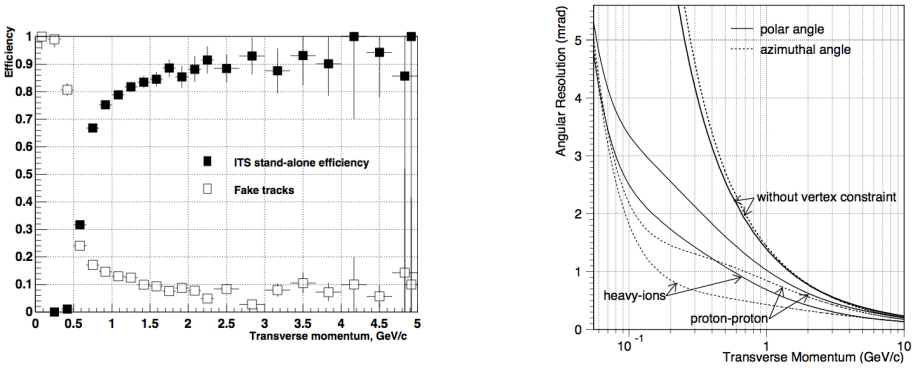

Fig. 2.2.6: Left figure: ITS stand-alone efficiency and fake track rate as a function of transverse momentum. Right figure :Angle resolution as function of transverse momentum[37].

resolution get better by sorting and refitting for TPC tracks to ITS tracks in high momentum region.

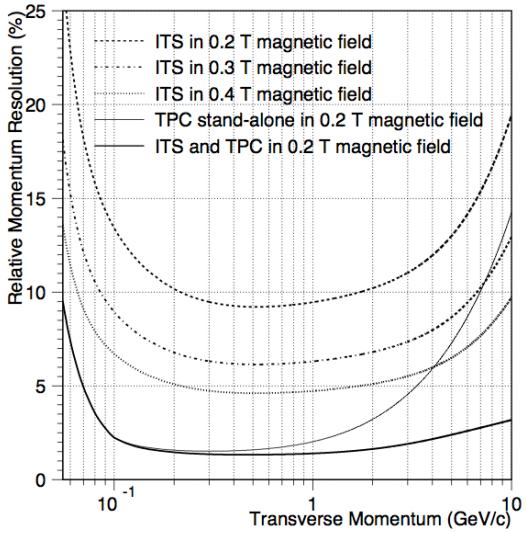

Fig. 2.2.7: Comparison of momentum resolution between only TPC and combining ITS+TPC as a function of transverse momentum[37].

2.2.3 Time Projection Chamber (TPC)

The Time Projection Chamber (TPC)[38] is the most important sub-detector which is installed in the ALICE experiment to reconstruct charged particles and tracking. The TPC is a drift chamber with MWPC (Multi-Wire Proportional Chamber) for three dimensional charged particles reconstruction with a good resolution and less materials. The TPC can detect transverse trajectory as track of induced charge on a pad and longitudinal trajectory as difference of drift time. The main purposes of the TPC are;

- Charge particle momentum measurement with the ITS.
- Particle identification and primary, secondly vertex reconstruction with a good momentum resolution.

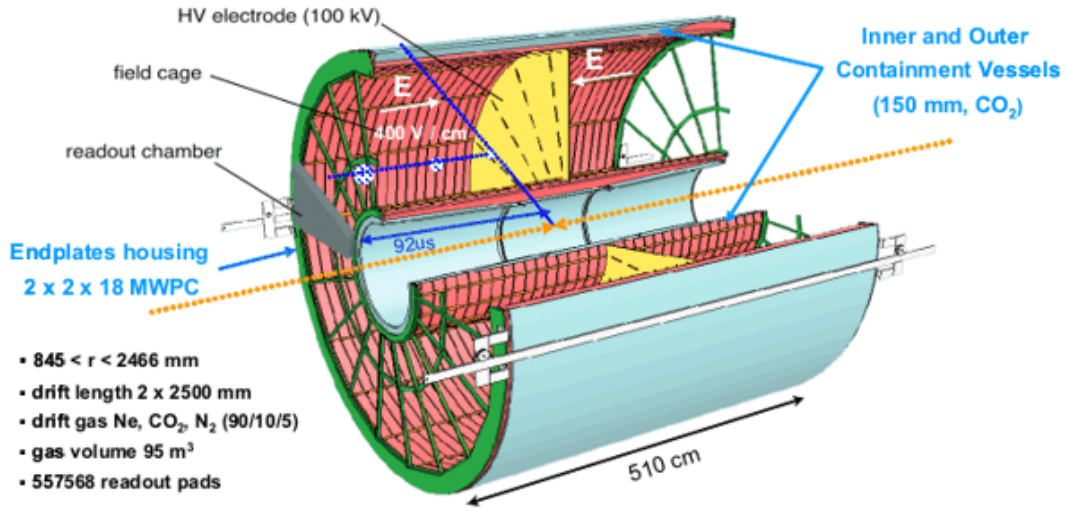

Fig. 2.2.8: Schematic view of Time Projection Chamber (TPC)

– Two track separation and dE/dx resolution to study about hadronic and leptonic signals in the region $p_T < 10$ GeV/c and the acceptance $|\eta| < 0.9$.

– charged particle identification using dE/dx.

2.2.4 Electromagnetic Calorimeter (EMCal)

The Electro-Magnetic Calorimeter (EMCal)[39] in the ALICE detector is the Pb-scintillator sampling calorimeter with a longitudinal pitch of 1.44 mm Pb and 1.76 mm scintillator and constructed from the 12,288 towers of the 12 super-modules2.2.9. The EMCal is designed to measured electrons and photons with large acceptance for high momentum physics and also used as the photon and jet trigger detector.

Energy resolution of EMCal is given by,

$$\frac{\sigma_E}{E} = \sqrt{\left(\frac{b}{\sqrt{E}}\right)^2 + c^2} \tag{2.2.1}$$

where b is the stochastic term and c is the constant term.

Fig.2.2.10 shows the energy resolution as function of electron energy measured from PS and SPS test beam line in CERN compared with the simulation results calculated from GEANT 3 indicated as the dashed carve.

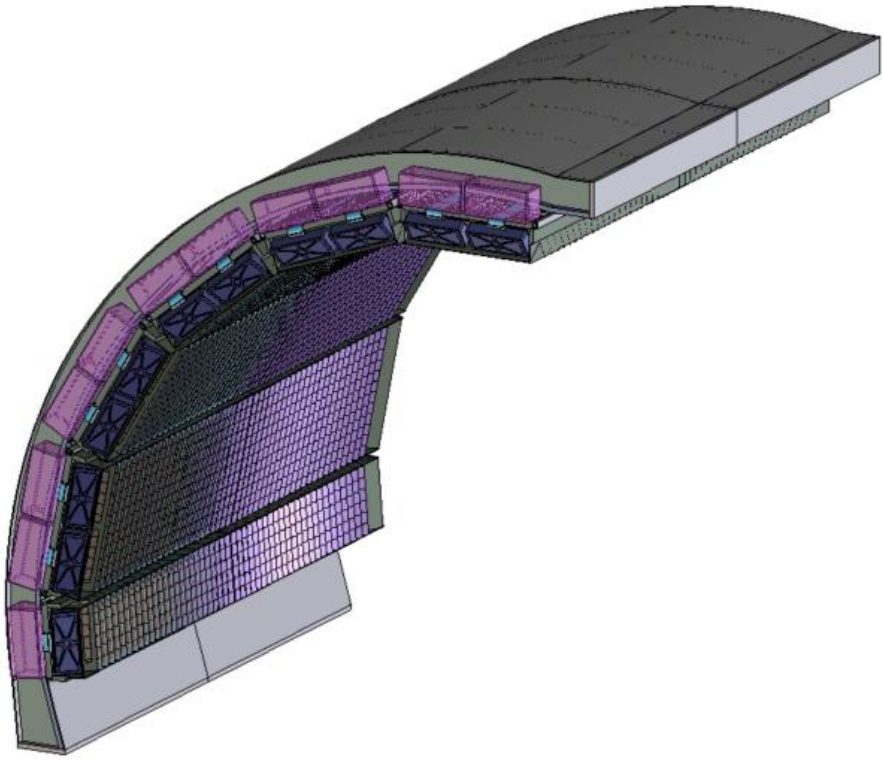

Fig. 2.2.9: Schematic view of Electro-magnetic Calorimeter (EMCal)

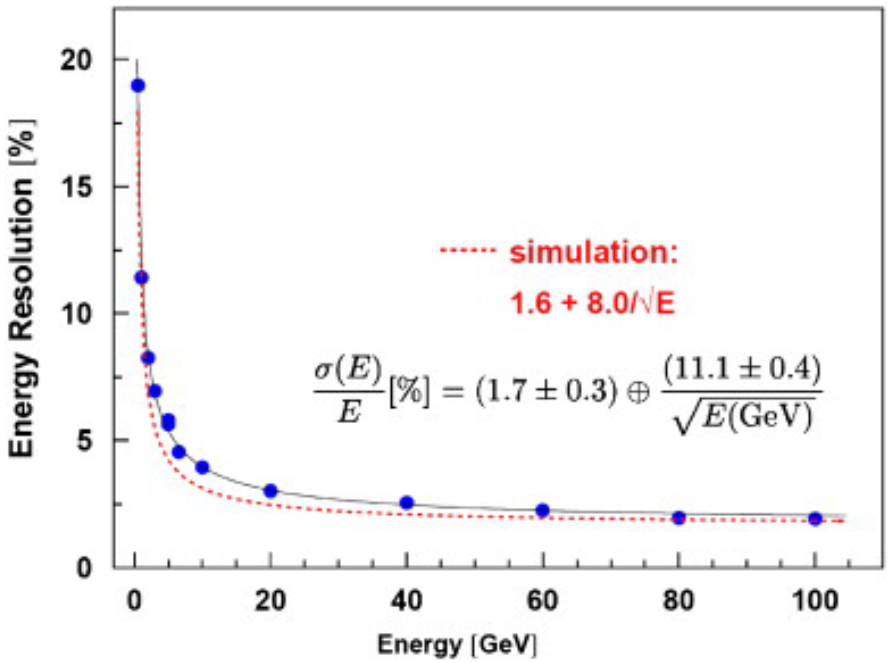

Fig. 2.2.10: Energy resolution of EMCal as a function of electron energy with fitting by Eq.2.2.1

Chapter 3

Analysis

In this chapter, we describe details of the procedure of this analysis to study π^0-jet correlation. At first, we present the event selection for this analysis, and then describe hot to reconstruct high momentum π^0's and charged jets.

3.1 Data set

The pp collision data used in this analysis were measured in 2011 LHC pp collisions at $\sqrt{s}$ = 7 TeV with EMCal triggered events and the Pb-Pb data used in this analysis were measured in 2011 LHC central (centrality: 0-10 %) Pb-Pb collisions at $\sqrt{s_{\rm NN}}$ = 2.76 TeV with EMCal triggered events (Table.3.1.1), because the statistics of pp collisions at $\sqrt{s} = 2.76$ TeV and mid-central and peripheral Pb-Pb collisions are not enough for this analysis.

The Pb-Pb collisions data used in this analysis are divided in two categories,

Year	Collision	Energy	Number of event
2011	pp collisions	$\sqrt{s} = 7$ TeV	7 M
2011	Pb-Pb collisions	$\sqrt{s_{\rm NN}} = 2.76$ TeV	12 M

Table 3.1.1: Information of data used in this analysis.

- Good TPC runs : A run is qualified as "good" if and when the TPC has been functioning fully during data taking, resulting in a flat distribution of tracks in η, φ plane. The analysis on this data-set is done in full azimuth.
- Semi-good TPC runs : In these runs, the inner read-out chamber's (IROC C13) voltage was lowered resulting in a loss of tracking efficiency. Since azimuthal acceptance of the semi-good TPC runs is not uniform.

The run list of the two kinds of runs are putted on Appendix.

3.2 Event selection

3.2.1 Vertex cut

The following reconstructed z-vertex cut is used to select a primary collisions.

- Primary vertex is reconstructed by the SPD.

– Number of tracklets contributing to the primary vertex is larger than 0.

– Vertex position in z direction: $|z_{vertex}| < 10$ cm

3.2.2 Event trigger

This analysis are used the three kinds of trigger class, minimum bias trigger (Pb-Pb collisions), EMCal L0 trigger (pp collisions) and EMCal L1-gamma trigger (Pb-Pb collisions). The definition and purpose of those triggers are as follows.

– Minimum bias trigger : The minimum bias trigger in the ALICE experiment is used to select the low multiplicity events and the diffractive events with fine beam background (beam-gas, beam-halo interaction), efficiently. The hits from the three detectors are used to define the minimum bias trigger, V0A (A side), V0C (C side) and SPD as following,

– EMCal L0 and L1-gamma trigger : The EMCal photon trigger in the ALICE experiment is used to measured the high momentum photons efficiently and based on the energy deposition in 2×2 adjacent tiles. If the energy deposited in the 4 tiles was above the values mentioned previously, the event was recorded. The main difference between the L0 and the L1-gamma trigger is that the tiles in the L0 cannot be a combination of adjacent tiles in 2 adjacent EMCal super-modules and the fact that the threshold has to be fixed and not depend on V0 multiplicity (Fig.3.2.1). The data of pp collisions used in this analysis is the trigger threshold from 4.5 to 5.5 GeV. In order to enhance the high p_{T} photon clusters relative to the minimum bias events.

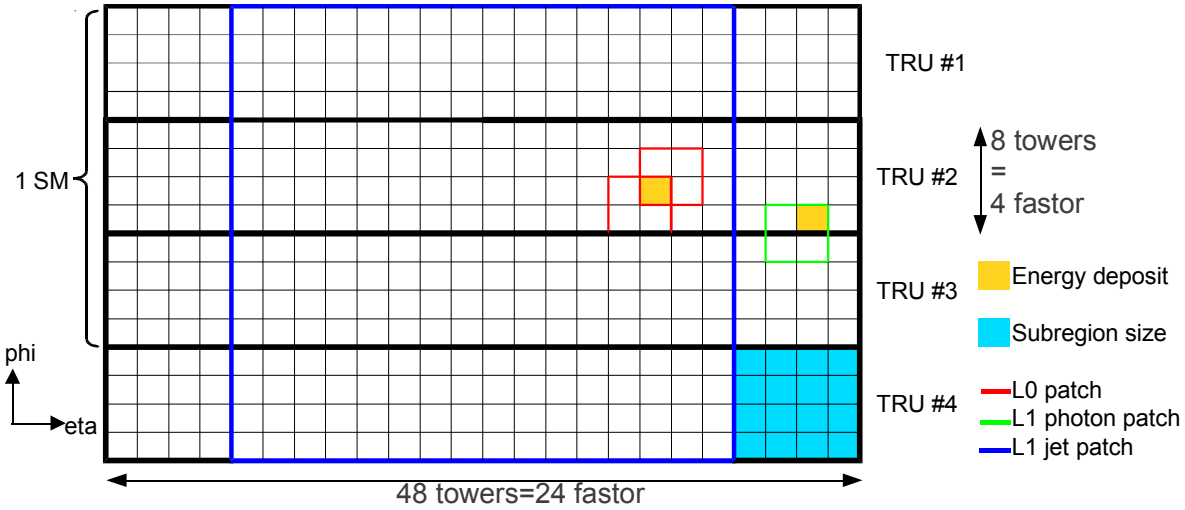

Fig. 3.2.1: Comparison of different possible L0,L1-gamma and L1-jet trigger patches [40].

3.2.3 Centrality

The Pb-Pb collision events is characterized by the collision geometry, and we use the centrality calculated from the Monte Carlo Glauber model instead of the impact parameter. The ALICE experiment estimates the centrality using the V0 detector amplitude, and then we obtain a good centrality resolution in the all centrality region. The resolution is from 0.5 % (central) to 2 % (peripheral). Fig.3.2.2 shows the V0 detector amplitude distribution with data and Glauber model fitting (a high V0 amplitude corresponds to a central event (e.g. $0-10$ %), and low amplitude corresponds to peripheral event (e.g. $60-80$ %.

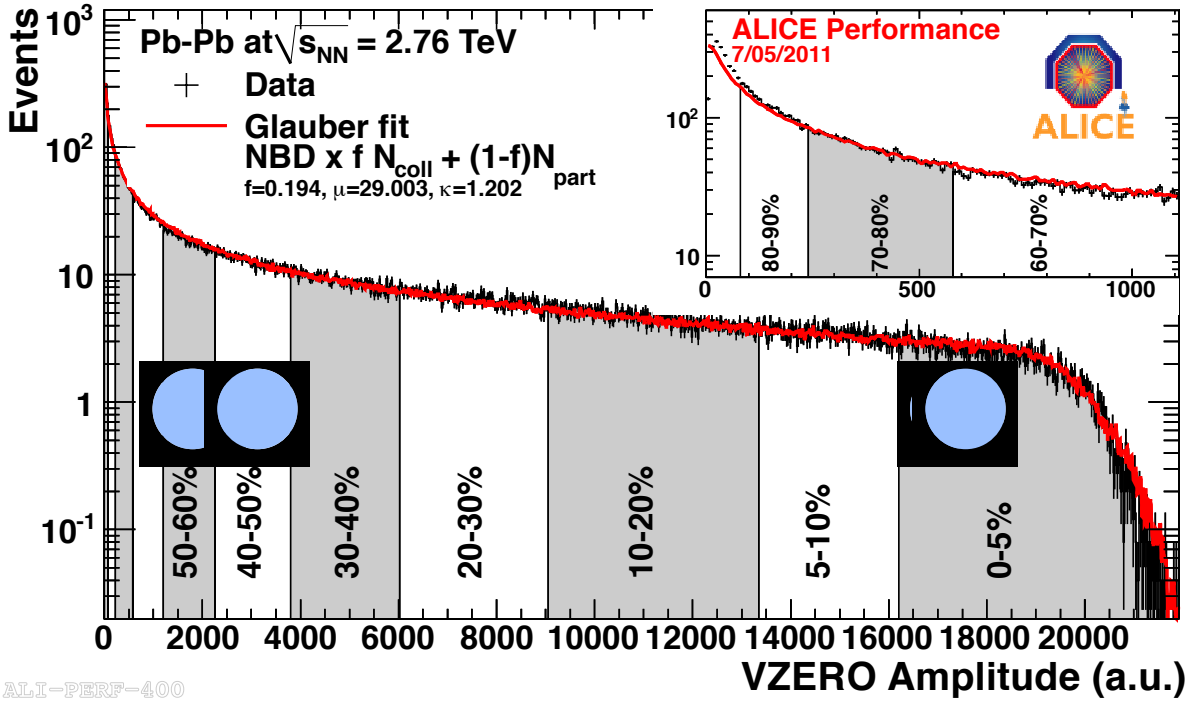

Fig. 3.2.2: V0 amplitude distribution with data and Glauber fitting.

3.3 π^0 identification with EMCal

This analysis uses the π^0 identification by using the cluster splitting method [42]. The invariant mass method identify a π^0 by calculated the invariant mass from 2 photon clusters when decaying from π^0. This method with V1 clusterizer (see Sec.3.3.1) is used to identify low energy π^0 ($1 \sim 15$ GeV/c). Another way to identify π^0 is via the cluster splitting method with V1 clustrizer that used the fact that π^0 decays form a single cluster instead of two in the calorimeter already at 6 GeV. When high energy π^0decaying into 2 photons with small opening angle, of the order of few calorimeter cells size (6 cm), it produces a large and elongated cluster of calorimeter cell. Checking the energy deposition in the cells, if there are local maxima cells, this cluster can be separated into two sub-clusters that should correspond to the original photons, when the particle showers are not too overlapped. When we have 2 local maxima, the split is relatively straight forward, just take the cells around the 2 maxima to form the 2 clusters, but when there are only 1 maxima or more than 2, careful studies are needed as described in the ALICE analysis note [42].

3.3.1 Clusterization

A calorimeter cluster consists of calorimeter cells. Clusters represent ideally the energy a given particle deposited in the calorimeter. There are several clustering methods for the ALICE-EMCal as follows.

- V1 clusterizer: Start the clusters selecting a seed cell with energy above a given threshold E_{seed}. Then, it aggregates to the cluster all cells with common side to the seed tower if their energy is above E_{min}. It continues aggregating towers with common side to the already aggregated ones if their energy is still larger than E_{min}. A cell cannot belong to more than one cluster.

- V2 clusterizer: Similar to V1 clusterizer but before aggregating a cell to the cluster, it checks if the energy of the cell to be aggregated is smaller than the energy of the cell that belongs already to

the cluster and is neighbor with common side. If the energy is larger, the cell is not added to this cluster and the clusterization stops. Default clusterizer in Pb-Pb and p-Pb collisions.

For the invariant mass mass method, we usually use the V2 clusterizer. For the cluster splitting method (current analysis), we use the V1 clusterizer, because V2 clusterizer can split clusters produced by several particles if the shower topology is appropriate.

The parameters of clusterizer in this analysis used E_{seed} and E_{min} and the cell time region.

- E_{seed} = 100 MeV
- E_{min} = 50 MeV.
- $425 < t < 825$ ns.

3.3.2 Cluster selection

The cuts for cluster selection in this analysis are listed here:

- $E_{cluster} > 6$ GeV (the cluster splitting method)
- Cell with highest energy in cluster must be 1 cell away from border of the calorimeter.
- Distance to a bad channel from the highest energy cell is larger than 2 cells.
- Rejected exotic clusters : Exotic clusters have cells with larger energy compared with its surrounding cells. In this analysis, we rejected clusters with 1-$E_{cross}/E_{cell}^{max} > 0.97$ as the exotic cluster. More details in Ref. [45].
- Timing cut : The cluster time is the time of the cell with highest energy in the cluster. It is not calibrated during the reconstruction. At the analysis level, a recalibration procedure has been implemented allowing to improve the time cell resolution and recenter the time distribution to 0 ns[42]. After recalibration, The cluster time was required window $|t| < 20$ ns, because recalibration procedure centers the cluster timing at 0 with a spread of $\pm$ 25 ns. At n*50 ns pile-up contribution can be clearly observed (Fig. 3.3.1).
- Charged particles veto : There are clusters which are generated by charged particles. In order to remove such clusters from the analysis, we apply a cut in the residual angular position between the clusters and the projection of the TPC tracks to the EMCal surface. We reject clusters with residuals in η and φ direction of $\Delta\eta < 0.025$ and $\Delta\varphi < 0.03$ (Fig. 3.3.2).

3.3.3 Number of Local Maxima in cluster

A local maxima cell in the cluster is defined as cell with higher energy than its adjacent cells defined as follows,

$$E(Local\,Max\,candidate) - E(ad\,jacent\,cell) > \Delta E_{LM} \tag{3.3.1}$$

when comparing to all the adjacent cells and with energy above a certain threshold $E_{LM-seed}$. In this analysis, $\Delta E_{LM-seed}$ = 30 MeV was used, like in the EMCal reconstruction code used for the unfolding procedure, and an energy threshold $E_{LM-seed}$ = 100 MeV in pp collisions.

The Number of Local Maxima, NLM, will be used later in the analysis to select the clusters, since the shape of the shower depends on this number. With the V1 clusterizer, photon clusters can have only NLM = 1 unless the suffered previously a conversion in the material in front of EMCal or they have a random contribution from other particles, and π^0 clusters will have a priory NLM = 2 at low energy and NLM = 1 at higher energy. The reason of more photons converted in the material in front of the calorimeter, producing at least two separated e^+e^- particles, or some spurious noise in the calorimeter.

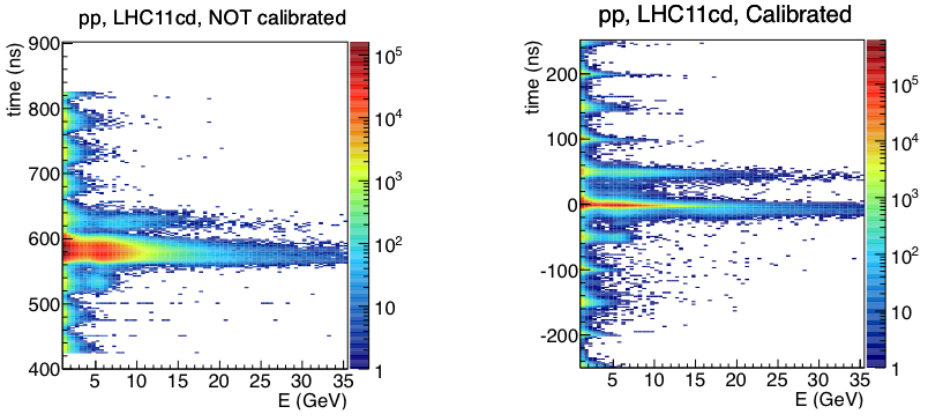

Fig. 3.3.1: Photon clusters ($0.1 < \lambda_0^2 < 0.27$) time before (left plot) and after (right plot) time recalibration in pp collisions at $\sqrt{s}$ = 7 TeV, real data triggered with EMCal.[42]

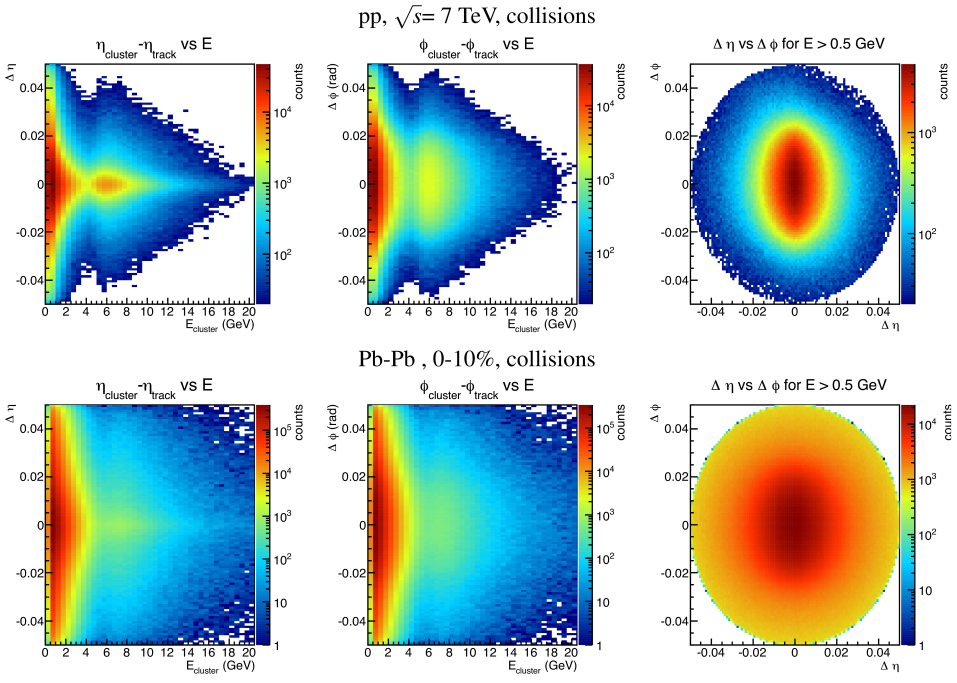

Fig. 3.3.2: Residual in η and φ between the cluster and projected track to the EMCal surface η or φ versus the cluster energy or versus each one, V1 clusters in pp collisions at $\sqrt{s}$ = 7 TeV.[42]

3.3.4 Shower shape

The shower shape of a cluster can be described using an ellipsoidal parametrization by the axis of the shower surface ellipse in the calorimeter towers. The ellipse parameters are denoted as λ_0^2 (long axis) and λ_1^2 (short axis). Fig. 3.3.3 shows the λ_0^2 and λ_1^2 distributions for photons and π^0 for a wide energy range from 8 to 30 GeV. Photons are peaked at $\lambda_0^2 = 0.25$ within a narrow range $0.1 < \lambda_0^2 < 0.3$ and independently of the energy. π^0's have a widely spread distribution, that changes with the energy, being closer to the photon region when increasing the π^0 energy. No clear dependency on the particle type and energy can be observed for λ_1^2.

A possible conclusion is that those V1 clusters with $\lambda_0^2 > 0.3$ can be considered as π^0, but the merging of photon clusters is not only reason to have large shower shape. The reasons why a cluster can have a large λ_0^2 or several local maxima are summarized below:

- Conversion photon in the material in front of EMCal produce the electronic magnetic shower earlier, instead of a photon there is a separated e^+e^- pair depositing in the calorimeter.
- Several particles from a jet produced in a close region.
- In heavy-ion collisions, the high multiplicity particle environment produces overlaps of random particles.
- Decay of different meson types like π^0 or η.
- Incidence angle of the particle in the calorimeter (negligible effect for particles coming from the interaction point).
- Hadronic interactions, neutrons, pion, etc, produce a broader shower compared to the electromagnetic particles.
- Overlap of clusters produced in different event, pile-up. Such contribution is not observed when looking to the time of the cells inside the cluster, no structures due to different bunch-crossings are observed.

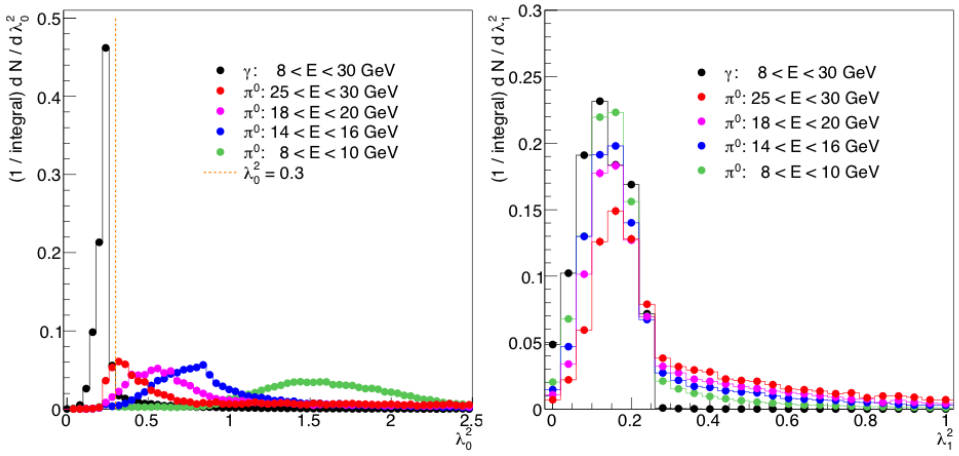

Fig. 3.3.3: λ_0^2 and λ_1^2 distributions for photon and π^0 clusters with the large cluster energy regions.[42]

3.3.5 Cluster splitting for π^0identification

For the illustration, Fig. 3.3.4 shows cluster splitting procedure, taken from the analysis note [42]. The briefly description of the cluster splitting is as follows.

1. Select EMCal clusters with track matching cut removed track matched clusters).
2. Find local maxima in the cluster
3. Split the cluster in new two sub-clusters by taking the two highest local maxima cells and aggregate all towers around them from 3×3 cluster.
4. Overlapped cell energy is re-calculated by weighting with respect the local maxima cell energy.
5. Obtain the two newly produced sub-clusters, and calculate the energy asymmetry and invariant mass from these new sub-clusters.

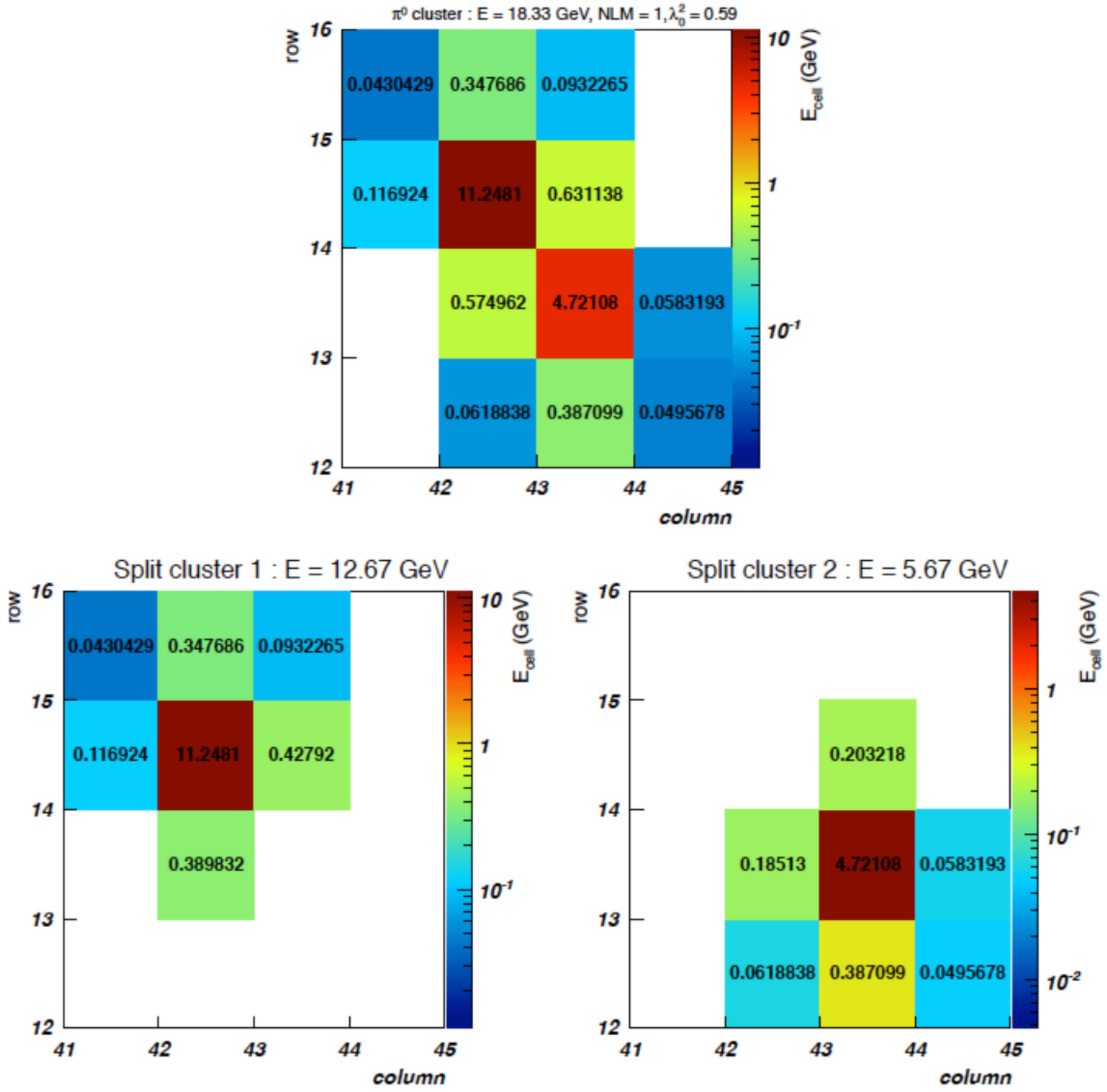

Fig. 3.3.4: Example of the cluster splitting method, taken from [42]. The squares represent the cells, and the value in the cell is the cluster energy in each cell, being the y and x axis the position within the super-module. Upper plot: V1 input cluster with NLM = 1 measured in real data, pp collisions $\sqrt{s} = 7$ TeV, coming likely from a π^0. Bottom plots: sub-clusters formed after splitting. Each plot contains the fraction of energy measured in a cell of the cluster. In this case the 2 selected maxima are in diagonal.

3.3.6 Shower shape long axis parameter (λ_0^2) cut

The shower shape parameter λ_0^2 of single photon clusters is below $\lambda_0^2 \leq 0.27$ and almost independent of the energy distribution, whereas the shower shape parameter λ_0^2 of π^0 clusters depends on the cluster energy and the NLM value. This analysis required λ_0^2 as a function of cluster energy and the different NLM value. Fig. 3.3.5, 3.3.6, 3.3.7 show the λ_0^2 distribution as function of the cluster energy with different NLM in the real data and simulation. We defined a minimum and maximum value of λ_0^2 as as shown in the black lines. Also the fixed minimum cut off value of $\lambda_0^2 = 0.3$ is used for all cases. The selected window has been chosen a bit broader from the comparisons of λ_0^2 distribution as function of cluster energy between π^0 clusters and other particle clusters. Written as:

$$\lambda^2_{0,max,min}(E) = e^{a+b*E} + c + d*E + e/E \tag{3.3.2}$$

The parameters can be found in Tab. 3.3.1 and are estimated by the simulation (PYTHIA and HIJING).

	a	b	c	d	e
NLM = 1,2 Min	2.135	-0.245	0	0	0
NLM = 1 Max	0.0662	-0.0201	-0.0955	$1.86\text{x}10^{-3}$	9.91
NLM = 2 Max	0.353	-0.0264	-0.524	$5.59\text{x}10^{-3}$	21.9

Table 3.3.1: The parameter of λ_0^2 cuts

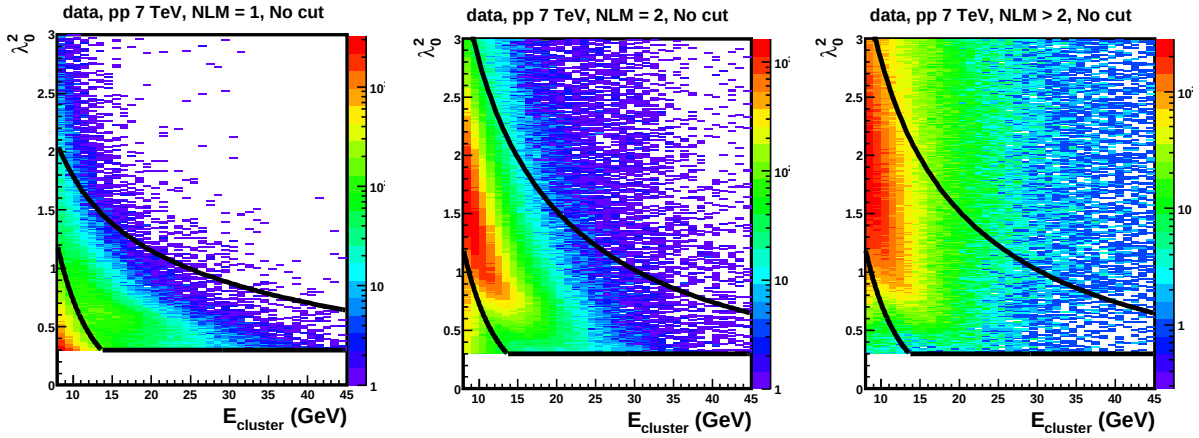

Fig. 3.3.5: λ_0^2 distributions as function of the cluster energy with three different NLM in pp collisions at $\sqrt{s}$ = 7 TeV. The two black lines show the selection windows defined in this section.

3.3.7 Energy asymmetry cut on split sub-cluster

The two photons coming from π^0 decay are the same energy, but in laboratory we observe an energy asymmetry defined as $|A| = |E1 - E2|/|E1 + E2|$, spanning from 0 to 1. The energy asymmetry is related to the opening angle that becomes smaller with increasing π^0 energy. Fig. 3.3.8, 3.3.9 and 3.3.10 show the energy asymmetry of the split sub-cluster as function of cluster energy with different NLM. Fig. 3.3.8 and 3.3.9 are used the real data (LHC11c,d and LHC11h), Fig. 3.3.10 is used the simulation data (LHC12f2a). The black line define the maximum value cut. This line is a polynomial fit of order 3:

$$A_{min}(E) = a + b*E + c/E^3 \tag{3.3.3}$$

The parameters can be found in Tab. 3.3.2 and are estimated by the simulation.

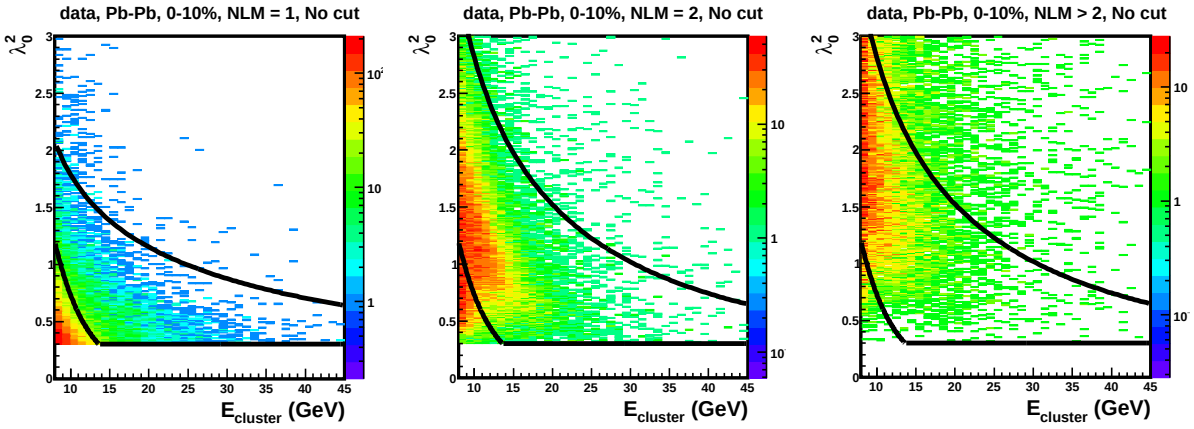

Fig. 3.3.6: λ_0^2 distributions as function of the cluster energy with three different NLM in central PbPb collisions at $\sqrt{s_{NN}}$ = 2.76 TeV with centrality 0−10 %. The black lines show the selection windows defined in this section.

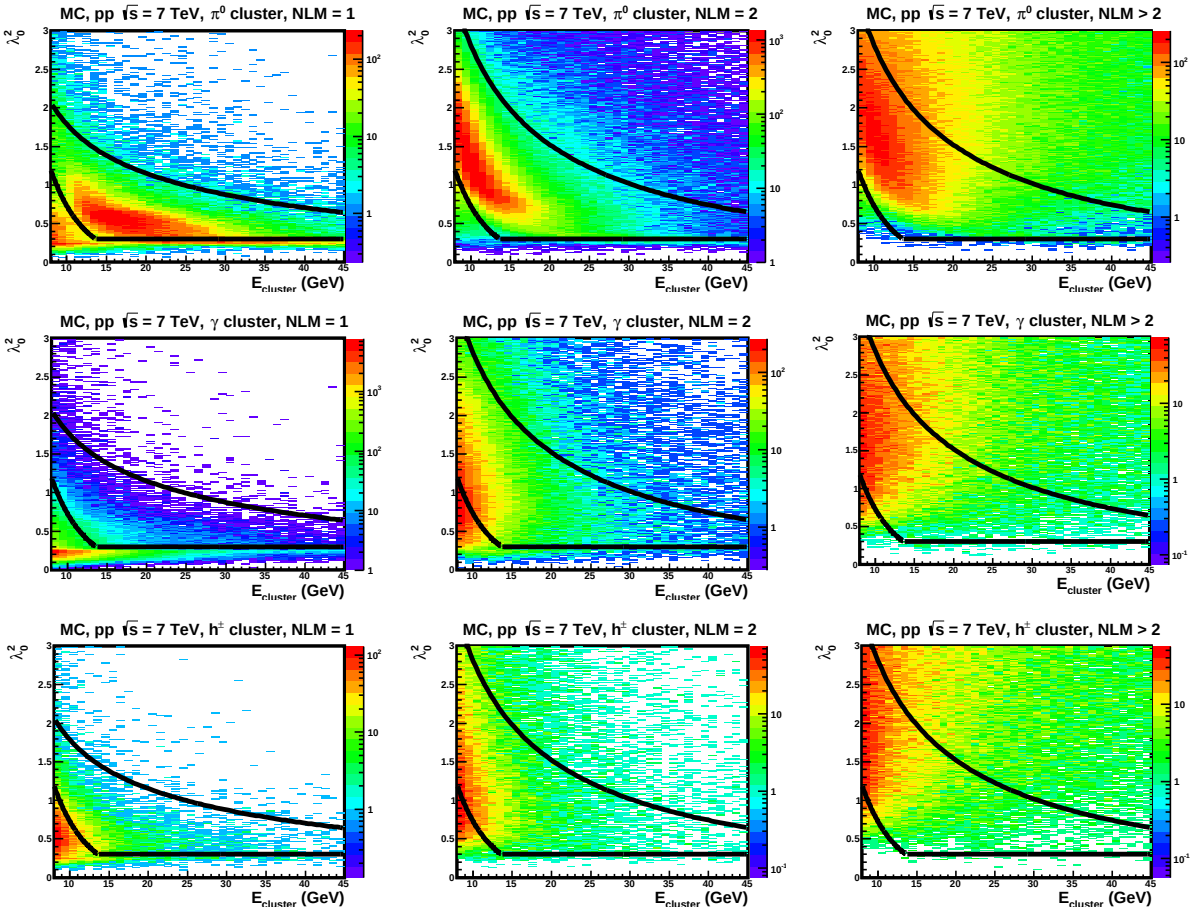

Fig. 3.3.7: λ_0^2 distributions as function of the cluster energy by using the simulation data (LHC12f2a). First row plots are generated by the π^0 clusters, second row plots are generated by the single photon clusters and third row plots are generated by the charged hadron clusters.

	a	b	c
NLM = 1	0.96	0.0	-879
NLM = 2	0.95	0.0015	-233

Table 3.3.2: The parameters of split sub-cluster energy asymmetry cut.

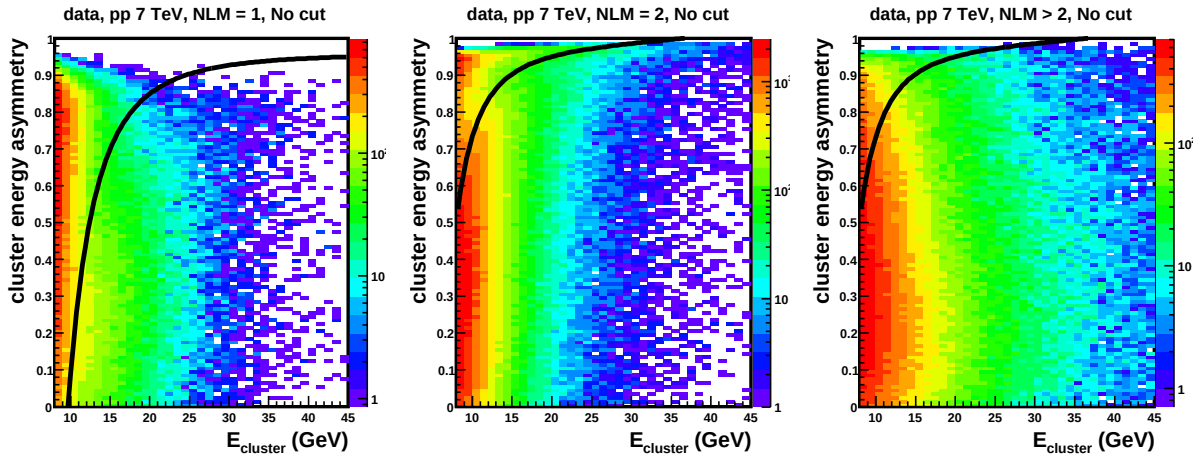

Fig. 3.3.8: The split sub-cluster energy asymmetry as function of cluster energy with three different NLM in pp collisions at $\sqrt{s}$ = 7 TeV. The black line shows the selection windows defined in this section.

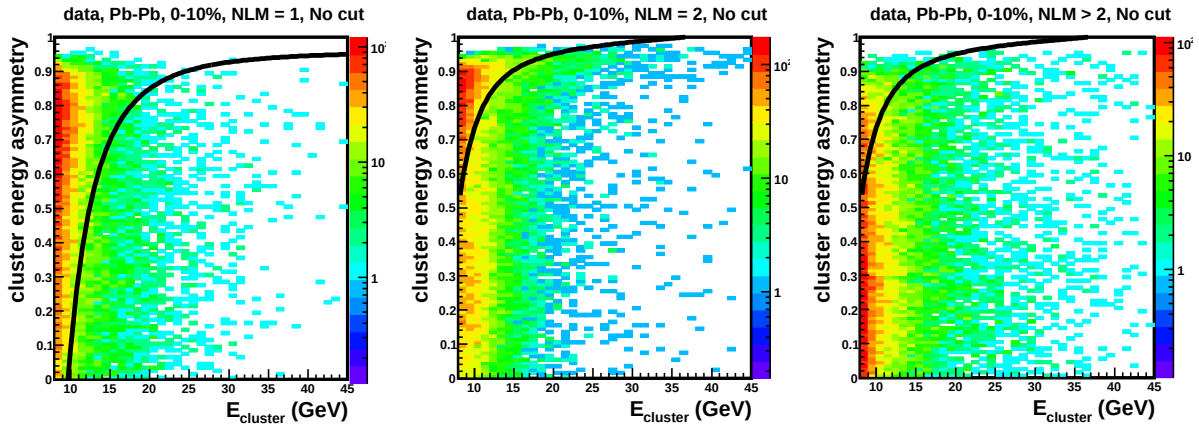

Fig. 3.3.9: The split sub-cluster energy asymmetry as function of cluster energy with three different NLM in PbPb collisions at $\sqrt{s_{\mathrm{NN}}}$ = 2.76 TeV. The black line shows the selection windows defined in this section.

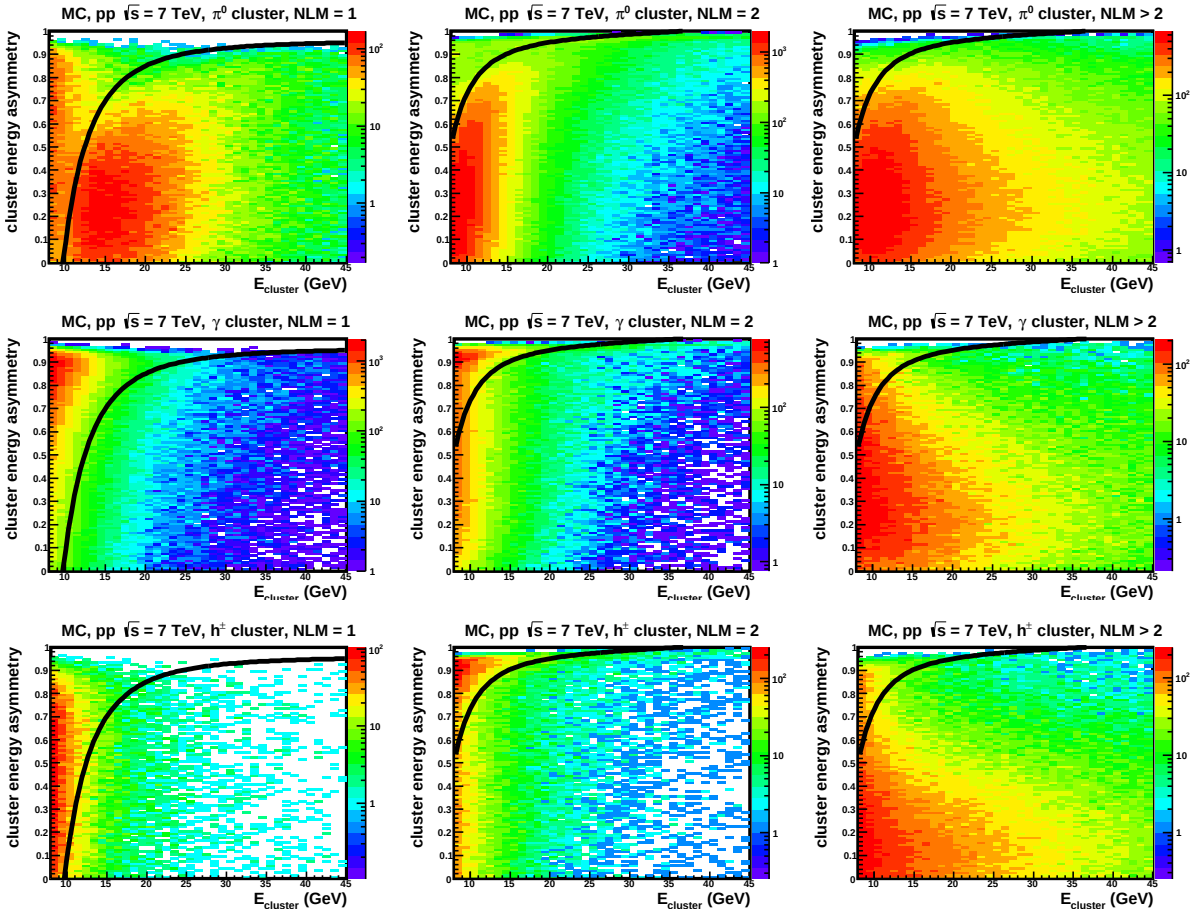

Fig. 3.3.10: The split sub-cluster energy asymmetry as function of cluster energy by using the simulation data (LHC12f2a). First row plots are generated by the π^0 clusters, second row plots are generated by the single photon clusters and third row plots are generated by the charged hadron clusters.

3.3.8 Invariant mass

Fig.3.3.11, 3.3.12 show the invariant mass distribution as function of cluster for different NLM.

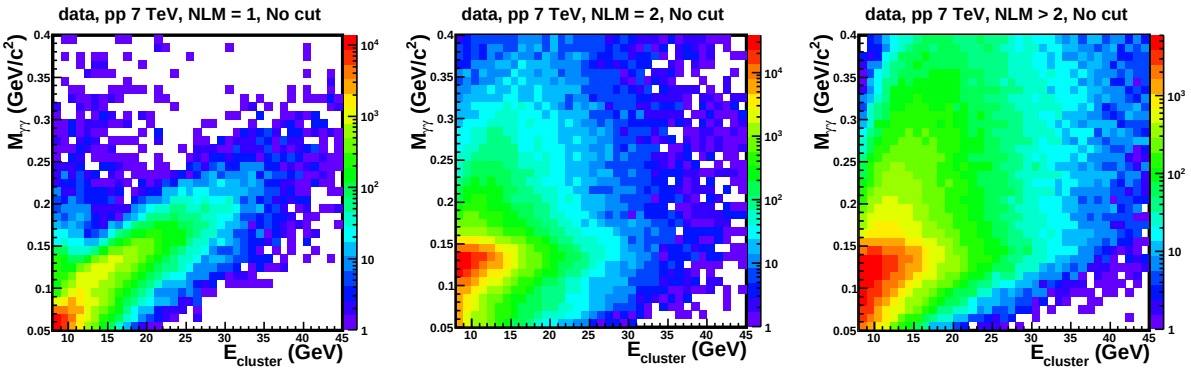

Fig. 3.3.11: Invariant mass $M_{\gamma\gamma}$ distributions as function of cluster energy with three different NLM in pp collisions at $\sqrt{s}$ = 7 TeV. These distributions are not applied λ_0^2, energy asymmetry and invariant mass cuts.

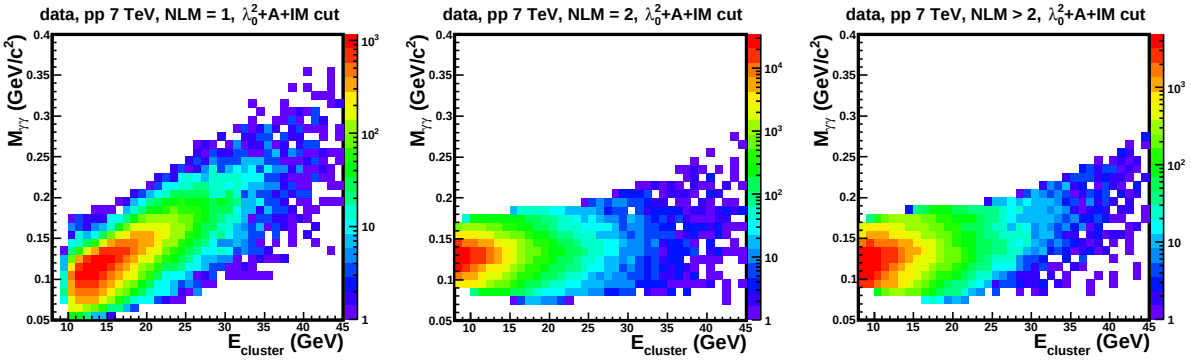

Fig. 3.3.12: Invariant mass $M_{\gamma\gamma}$ distributions as function of cluster energy with three different NLM in pp collisions at $\sqrt{s}$ = 7 TeV. These distributions are applied λ_0^2, energy asymmetry and invariant mass cuts.

Fig.3.3.15 and 3.3.16 are projections of the invariant mass distributions versus cluster energy after λ_0^2 and energy asymmetry cuts. Based on these observations from real data, a rough parametrization of the evolution of the mass and the width as a function of the cluster energy is found to be good and it will be used later to select the clusters falling at 3σ from the expected mass window. The data points in Fig. 3.3.17 were fitted with a polynomial function for the first order:

$$M(E), \sigma(E) = a + b * E \tag{3.3.4}$$

and the parameters can be found in Tab. 3.3.3. The parametrization is shown in the red lines displayed in Fig. 3.3.17. Fig. 3.3.19 shows π^0 raw transverse momentum spectra after applying λ_0^2, asymmetry and invariant mass window cuts. This result indicates that we can identify high momentum π^0's up to 40 GeV/c by using the cluster splitting method.

3.4 Charged jet reconstruction

3.4.1 Charged track selection

This analysis used the charged tracks reconstructed by ITS and TPC with the track momentum range $p_T > 0.15$ GeV/c and η range $|\eta| < 0.9$. In order to avoid the azimuthally-dependent efficiency due

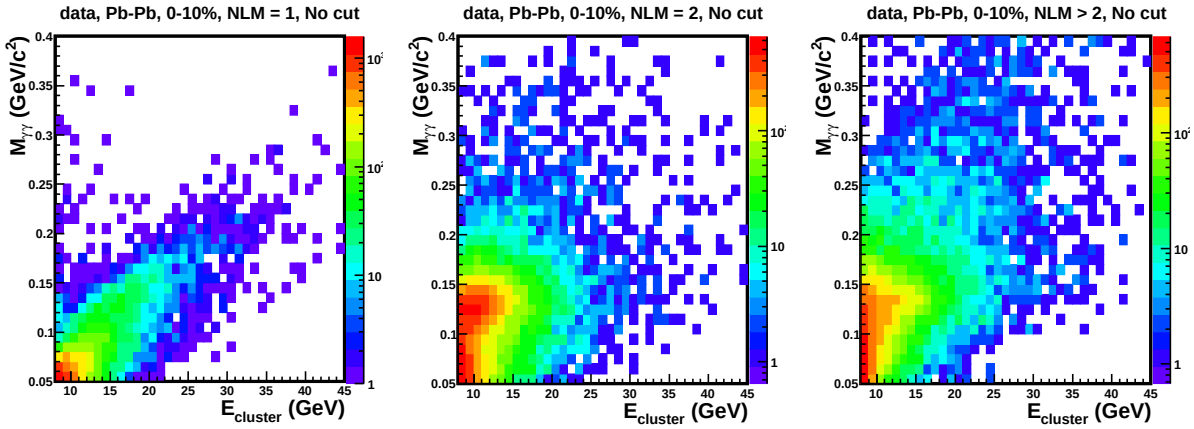

Fig. 3.3.13: Invariant mass $M_{\gamma\gamma}$ distributions as function of cluster energy with three different NLM in Pb-Pb collisions at $\sqrt{s_{\rm NN}}$ = 2.76 TeV. These distributions are not applied λ_0^2, energy asymmetry and invariant mass cuts.

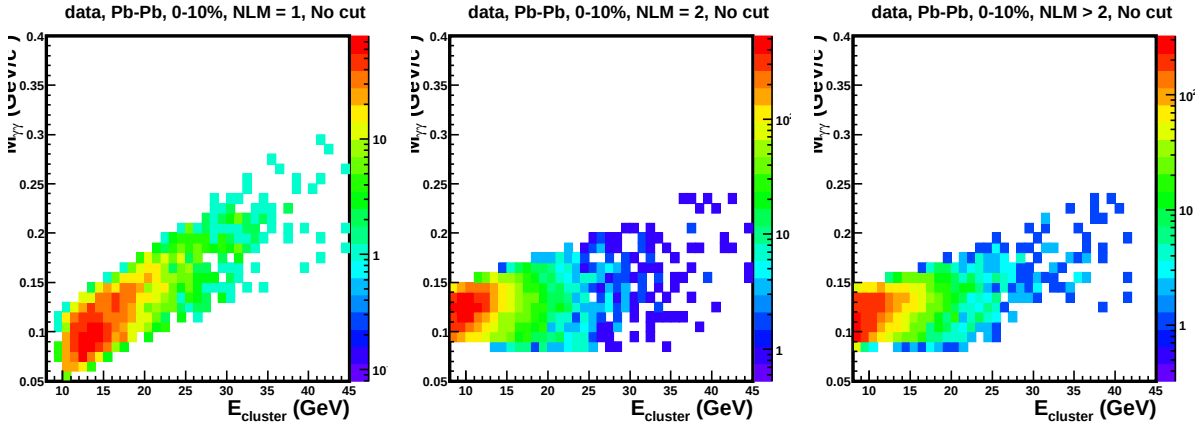

Fig. 3.3.14: Invariant mass $M_{\gamma\gamma}$ distributions as function of cluster energy with three different NLM in Pb-Pb collisions at $\sqrt{s_{\rm NN}}$ = 2.76 TeV. These distributions are applied λ_0^2, energy asymmetry and invariant mass cuts.

Function	NLM	E range(GeV)	a	b
M(E)	1	12-50	0.044	0.0049
M(E)	2	6-21	0.115	$9.6\text{x}10^{-4}$
M(E)	2	21-50	0.1	0.0017
σ(E)	1	12-19	0.012	0
σ(E)	1	19-50	0.0012	$6\text{x}10^{-4}$
σ(E)	2	6-10	0.009	0
σ(E)	2	10-50	0.0023	$6.7\text{x}10^{-4}$

Table 3.3.3: The parameters of mass mean and sigma.

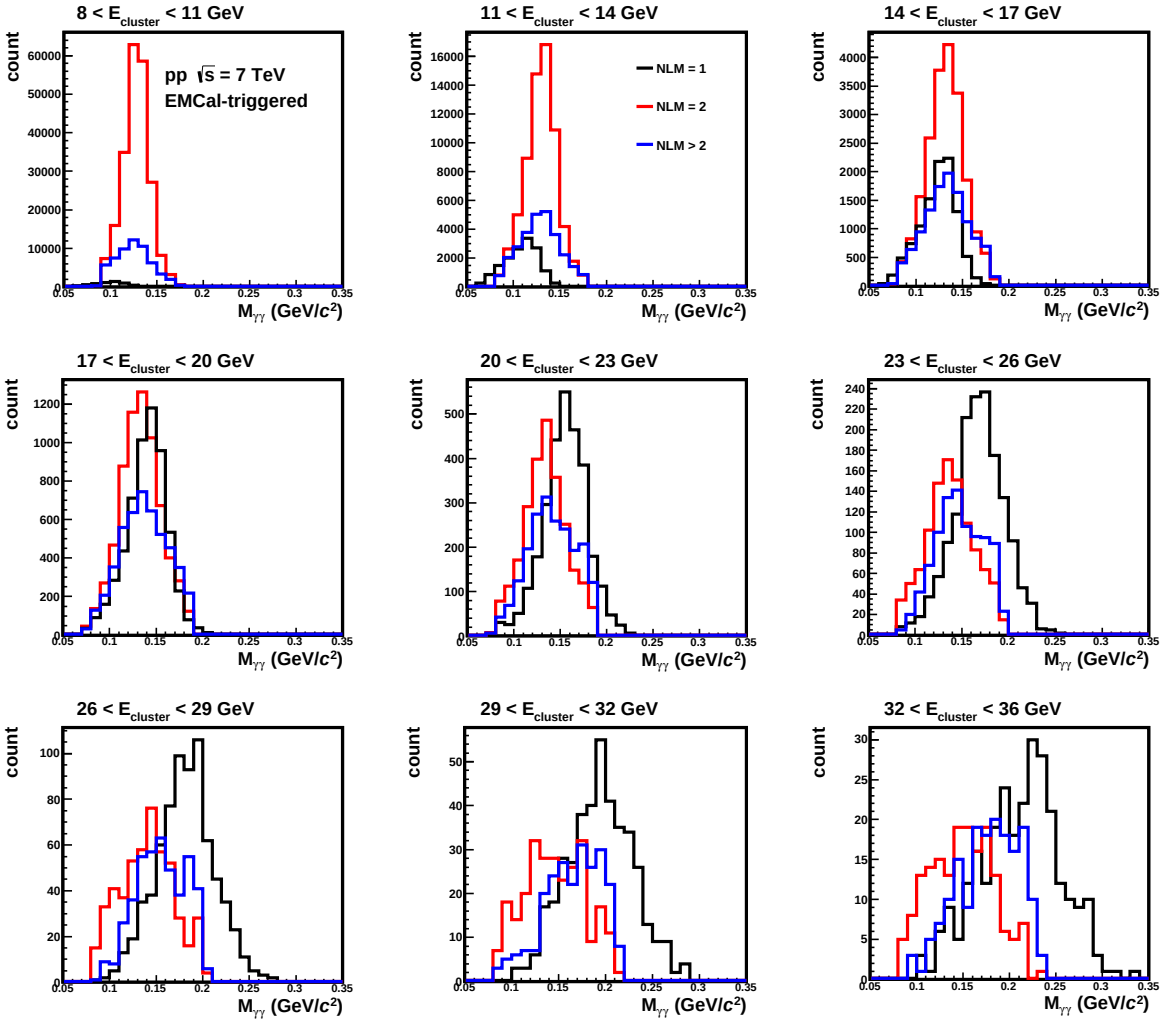

Fig. 3.3.15: Mass of split clusters in LHC11c and d, real data pp collisions at $\sqrt{s}$ = 7 TeV, after λ_0^2 and energy asymmetry cuts, for 9 cluster energy bins and different NLM.

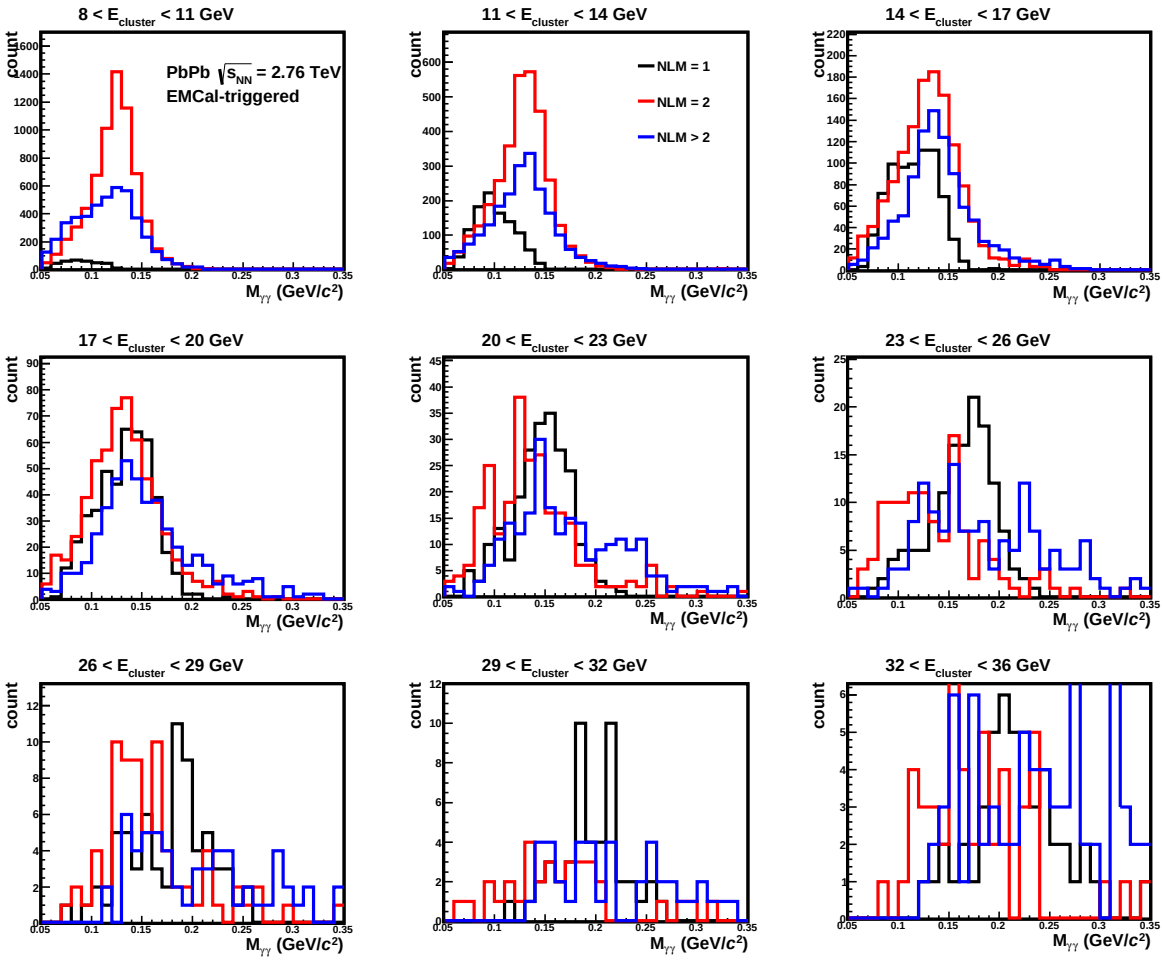

Fig. 3.3.16: Mass of split clusters in LHC11c and d, real data pp collisions at $\sqrt{s_{\rm NN}}$ = 2.76 TeV, after λ_0^2 and energy asymmetry cuts, for 9 cluster energy bins and different NLM.

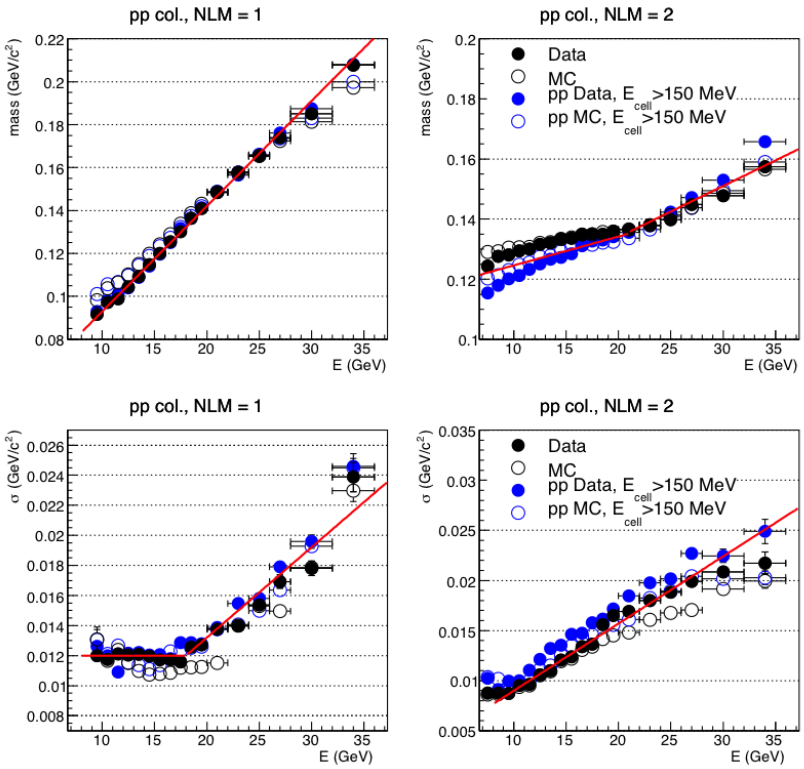

Fig. 3.3.17: Mean mass (upper) and width(lower) of split sub-clusters invariant mass distribution versus cluster energy, for different values of NLM from left to right: filled circles, pp collisions at $\sqrt{s} = 7$ TeV, LHC11c+LHC11d EMCal triggered.

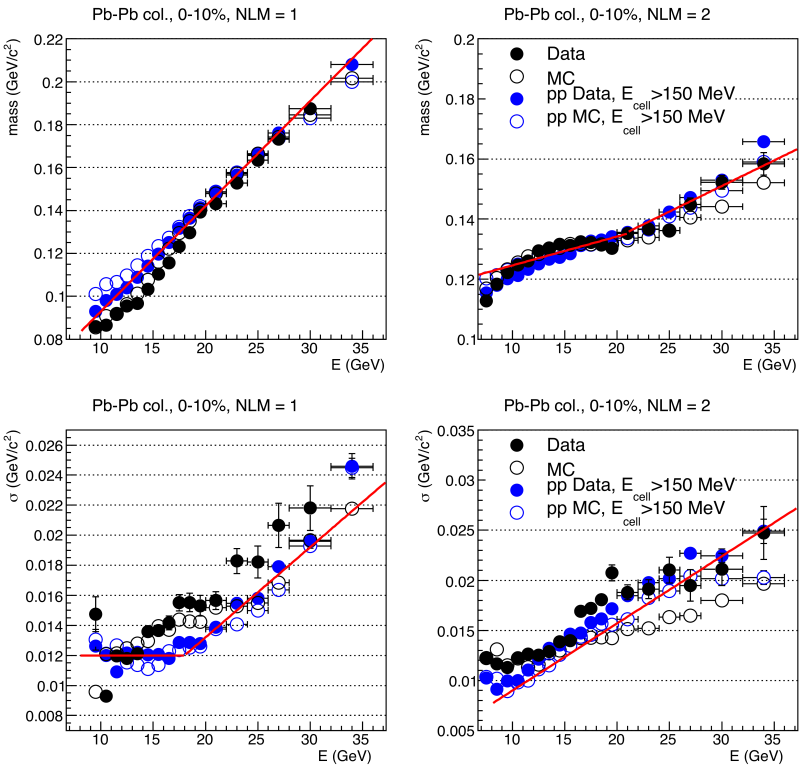

Fig. 3.3.18: Mean mass (upper) and width(lower) of split sub-clusters invariant mass distribution versus cluster energy, for different values of NLM from left to right: filled circles, PbPb collisions at $\sqrt{s_{\rm NN}}$ = 2.76 TeV, LHC11h EMCal triggered.

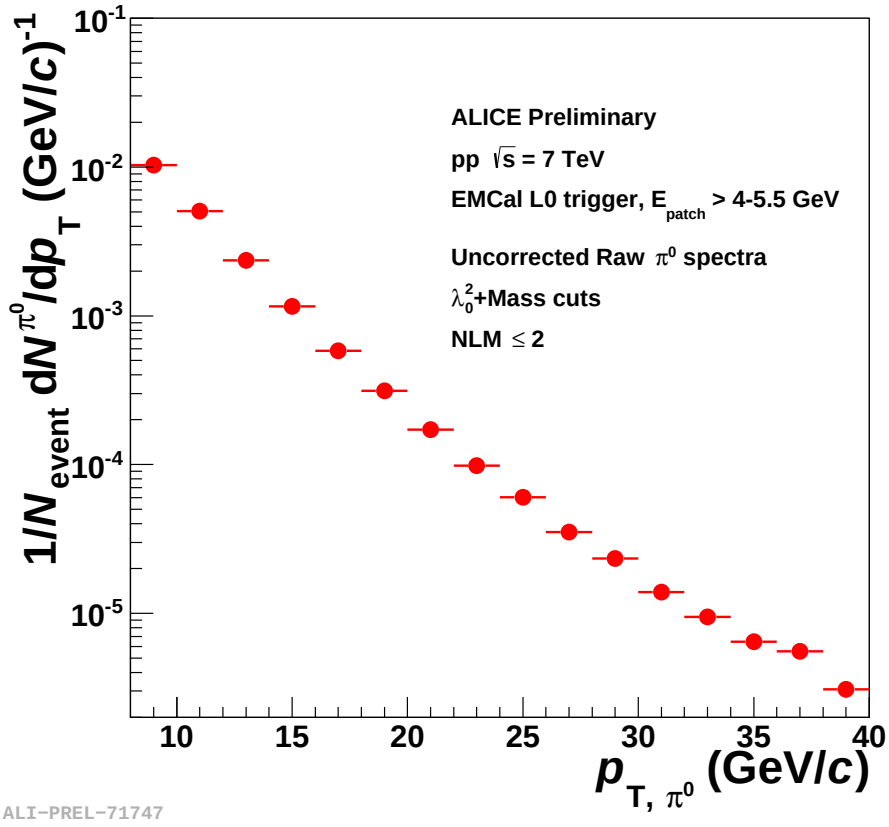

Fig. 3.3.19: $\pi^0 p_T$ distributions with three different NLM after applying λ_0^2, energy asymmetry and invariant mass window cuts.

to non-uniform response of the SPD, charged tracks were selected via the hybrid track selection. The hybrid track selection consists of two track classes (global and complementary tracks). For global tracks, at least one SPD hit is required, complementary tracks cover the regions without SPD response. In order to ensure a consistent momentum resolution in the event without the SPD hits, the complementary tracks are constrained to a primary vertex. These selection criteria are given in Table 3.4.1.

After applying the hybrid track cuts, we checked the φ and η distributions of charged tracks. The

`AliESDtrackCuts` function	Value	Comment
Global and complementary tracks		
`SetMinNClustersTPCPtDep`	$70 + 30/20 \cdot p_{\mathrm{T}}, 20$	linear rise from 70 ($p_{\mathrm{T}} = 0$) to 100 ($p_{\mathrm{T}} = 20\mathrm{GeV}/c$), 100 for $p_{\mathrm{T}} > 20\mathrm{GeV}/c$
`SetMaxChi2PerClusterTPC`	4	Maximum χ^2 per TPC cluster in the first iteration
`SetRequireTPCStandAlone`	`kTRUE`	Enable cut on TPC clusters in the first iteration
`SetAcceptKinkDaughters`	`kFALSE`	Reject tracks with kink
`SetRequireTPCRefit`	`kTRUE`	Require TPC refit
`SetMaxFractionSharedTPCClusters`	0.4	Maximum fraction of shared TPC clusters
`SetMaxDCAToVertexXY`	2.4	Maximum Distance of Closest Approach (DCA) to the main vertex in transverse direction
`SetMaxDCAToVertexZ`	3.2	Maximum DCA in longitudinal direction
`SetDCAToVertex2D`	`kTRUE`	Cut on the quadratic sum of DCA in XY- and Z-direction
`SetMaxChi2PerClusterITS`	36	Maximum χ^2 per ITS cluster
`SetMaxChi2TPCConstrainedGlobal`	36	Maximum χ^2 between global and TPC constrained tracks
`SetRequireSigmaToVertex`	`kFALSE`	No sigma cut to vertex
`SetEtaRange`	-0.9,0.9	Pseudorapidity cut
`SetPtRange`	0.15, 1E+15	Minimum $p_{\mathrm{T}} > 150\mathrm{MeV}/c$
Only for global tracks		
`SetClusterRequirementITS`	`AliESDtrackCuts::` `kSPD, kAny`	Require at least one hit in SPD
`SetRequireITSRefit`	`kTRUE`	Require ITS refit
Only for complementary tracks		
`SetRequireITSRefit`	`kFALSE`	No ITS refit

Table 3.4.1: The parameters of the hybrid track selection [47]

uniformity of track acceptance is important for the uniformity of reconstructed jet. Fig. 3.4.1 demonstrates the effect of hybrid track cuts. There is an uniformity in φ in hybrid track cuts in minimum bias

triggered events (left). We recover the uniformity in φ and η directions by using the hybrid track cuts.

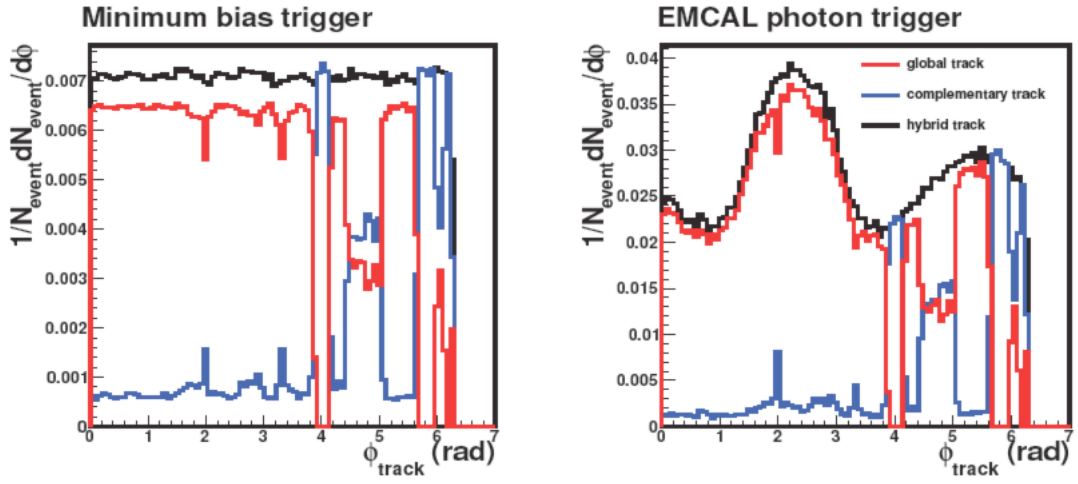

Fig. 3.4.1: φ distribution of global tracks, complementary tracks, and hybrid tracks for minimum bias trigger (left) and EMC gamma trigger (right) . The right plots are enhanced towards EMCal acceptance by EMCal photon trigger

3.4.2 Jet reconstruction

In order to reconstruct jets, this analysis used charged particles which are reconstructed by ITS+TPC with hybrid track cuts. We utilize anti-k_T algorithm in FastJet package[48] with jet cone radius R = 0.4, jet area A $>$ 0.4. Fig.3.4.2 shows transverse momentum $p_T^{jet,ch}$, azimuthal angle φ, rapidity angle η distribution in pp collisions at $\sqrt{s} = 7$ TeV.

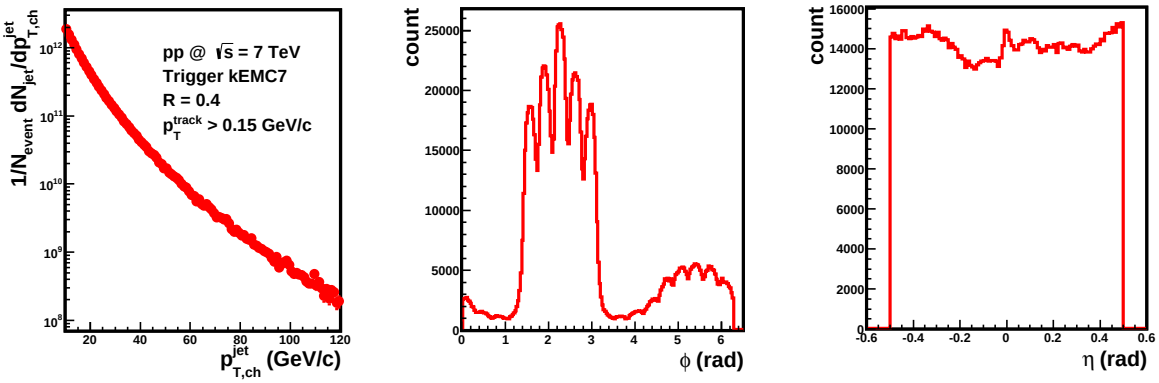

Fig. 3.4.2: Charged jet p_T, φ end η distributions with R=0.4, $A_{area} > 0.4$ and input track $p_T^{track} > 0.15$ (GeV/c), used EMCal triggered events.

3.4.3 Jet reconstruction in Pb-Pb collisions

The energy of a jet in Pb-Pb collisions includes the contributions of the hard process and the underlying event. In order to measure the true jet energy, we have to subtract the contribution of the underlying event on a jet-by-jet. Earlier ALICE studies have used an event averaged energy density per unit area

ρ, as an estimate of the jet background energy coming from the underlying event. In this section, this event averaged ρ, from here denoted as $\langle\rho\rangle$, will be described briefly, after which a 'local $\rho(\varphi)$' will be introduced in order to take into account the contribution of elliptic flow (v_2) and triangular flow (v_3) from the underlying event.

3.4.4 Event averaged energy density per unit area $\langle\rho\rangle$

The event averaged energy density per unit area $\langle\rho\rangle$ is estimated from the FastJet package [48] [49]. To subtract background energy calculated from event averaged energy density $\langle\rho\rangle$ and a jet's area A ($=\pi R^2$) is performed jet-by-jet,

$$p_T^{jet} = p_T^{raw} - \langle\rho\rangle \times A \tag{3.4.1}$$

where $\langle\rho\rangle$ is estimated by the median method of the distribution of k_T jets divided by their area

$$\rho = median\frac{p_{T,i}}{A_i} \tag{3.4.2}$$

as used in previous ALICE jet studies[50].

3.4.5 Local energy density $\rho(\varphi)$

The reconstructed jet momentum is biased not only by the centrality but also the event second order and third order. We need to subtract the background energy depended on the event plane second order and third order from the reconstructed jet energy in Pb-Pb collisions. The 'local' estimate, $\rho(\varphi)$, is obtained by fitting the first three terms of a Fourier expansion

$$\rho(\varphi) = \rho_0 \times (1 + 2\Big\{v_2^{obs} cos(2\Big[\varphi - \Psi_{EP,2}\Big]\Big\}) + v_3^{obs} cos(3\Big[\varphi - \Psi_{EP,3}\Big])\Big\}) \tag{3.4.3}$$

to the $\frac{d\Sigma p_T}{d\varphi}$ distribution - the distribution of total transverse momentum per $\Delta\phi$ window - of an event. In this equation, $\Psi_{EP,2}, \Psi_{EP,3}$ represent the second and third order event plane reconstructed by V0 detector. The event plane reconstruction procedure will be described in the next section. Fig.3.4.3 shows the $\frac{d\Sigma p_T}{d\varphi}$ distributions fitted by $\rho(\varphi)$ with three different centrality bins.

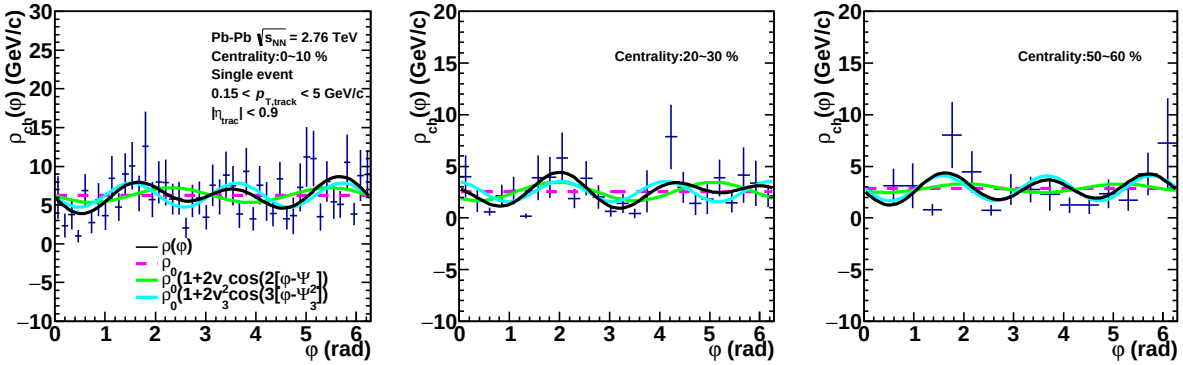

Fig. 3.4.3: $\frac{d\Sigma p_T}{d\varphi}$ distribution fitted by $\rho(\varphi)$, $\rho(\varphi)$ (total of local ρ) is the black lines, elliptic and triangular flow components are the green and blue lines and $\langle\rho\rangle$ is the dashed magenta lines, respectively.

3.4.6 Event plane reconstruction

In order to obtain a flat event plane distribution, we applied the two step corrections. The first correction is V0 gain equalization and the second correction is re-centering of the flow vector Q_n.

In this analysis, we do not consider the difference in rapidity and acceptance of each V0 ring and the gain equalization was performed separately for V0A and V0C according to equation,

$$M_i^{cor} = \frac{M_i}{\langle M_i \rangle \times M} \tag{3.4.4}$$

where M_i is the multiplicity of channel i in the analyzed event, $\langle M_i \rangle$ the mean multiplicity of channel i from all good events in the run, M a gain factor obtained by fitting with a degree 0 polynomial the mean multiplicity distribution of V0A/V0C. Fig. 3.4.4, 3.4.5 show the multiplicity distribution and its RMS of V0 detector before and after gain equalization as a function of channel number for run 167813. We can obtain the flat distribution of V0 multiplicity by applying the gain equalization.

The re-centering was performed for each centrality bin using the following equation,

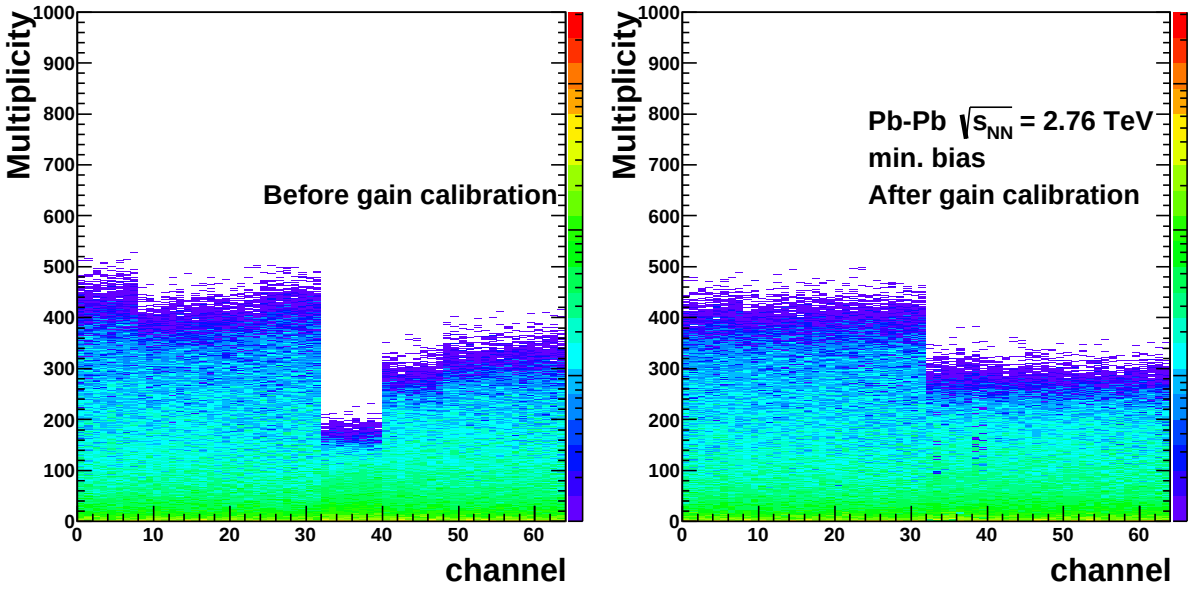

Fig. 3.4.4: Multiplicity distribution before (left) and after (right) gain equalization together with the main multiplicity as a function of channel number for run 167813. The steps around the channel 30 indicate the difference of distance from a interaction point of V0 A side and C side.

$$Q_{n,x}^{cor} = \frac{Q_{n,x} - \langle Q_{n,x} \rangle}{\sigma Q_{n,x}} \tag{3.4.5}$$

$$Q_{n,y}^{cor} = \frac{Q_{n,y} - \langle Q_{n,y} \rangle}{\sigma Q_{n,y}} \tag{3.4.6}$$

where the $\langle Q_n \rangle$ and σQ_n are the mean value and the width of the Q_x (Q_y) distribution from the full run under investigation. Then the event plane angle is calculated using the corrected Q_n,

$$\Psi_n^{cor} = \frac{atan2(Q_{n,y}^{cor}, Q_{n,x}^{cor})}{n} \tag{3.4.7}$$

Fig. 3.4.6 shows the V0 A+C side event plane distribution before (black) and after (red) the two corrections with three different centrality bins and indicates that we can obtain flat event plane distribution by the re-centering correction.

In order to check whether the event plane is reconstructed correctly, we compared the anisotropic

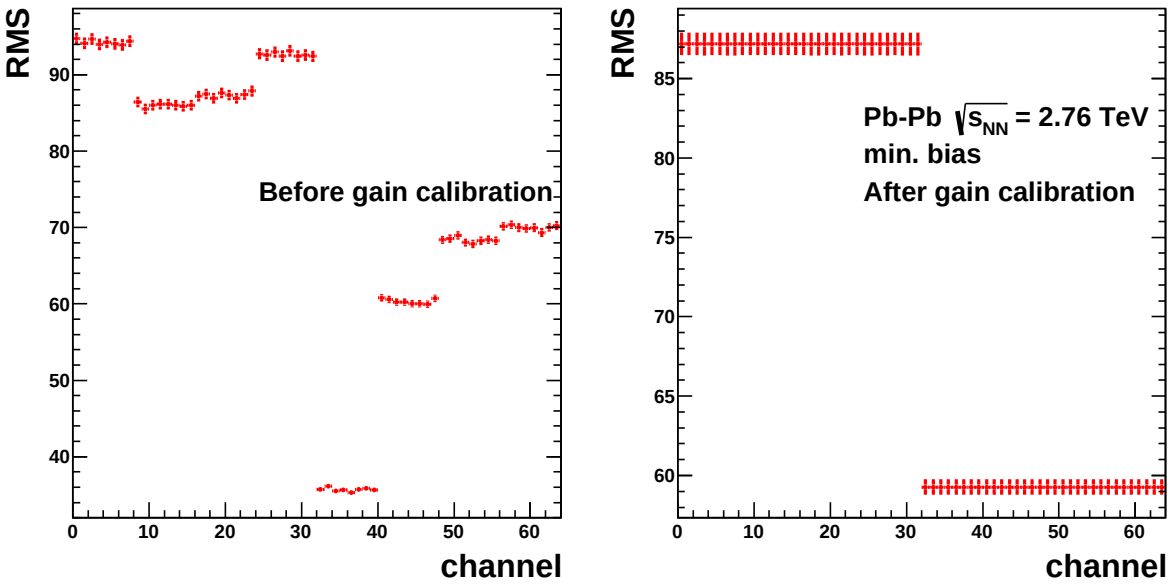

Fig. 3.4.5: RMS of the multiplicity distribution before (left) and after (red) gain equalization for run 167813

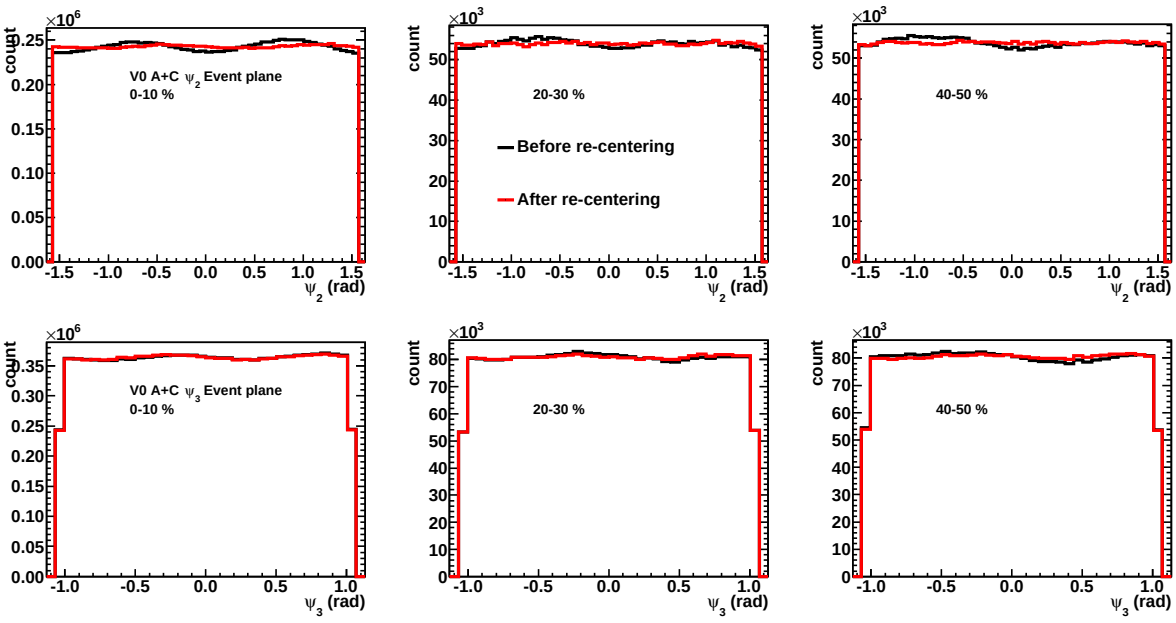

Fig. 3.4.6: The V0 A+C side event plane distribution before (black) and after (red) the corrections with three different centrality bins.

flow coefficients (v_2, v_3) with the ALICE published results.

The event plane resolution was estimated using the 3 sub-event method based on Ψ calculated from TPCA, TPCC, TPCAC, V0A, V0C, V0AC,

$$\langle cos(n(\Psi_n^a - \Psi_n)) \rangle = \sqrt{\frac{\langle cos(n(\Psi_n^a - \Psi_n^b)) \rangle \langle cos(n(\Psi_n^a - \Psi_n^c)) \rangle}{\langle cos(n(\Psi_n^b - \Psi_n^c)) \rangle}} \tag{3.4.8}$$

Fig. 3.4.7 shows the V0 event plane resolution from the 3 sub-event method for V0A (black), V0C (red) and V0AC (blue) as a function of centrality.

The observed v_n can be calculated as

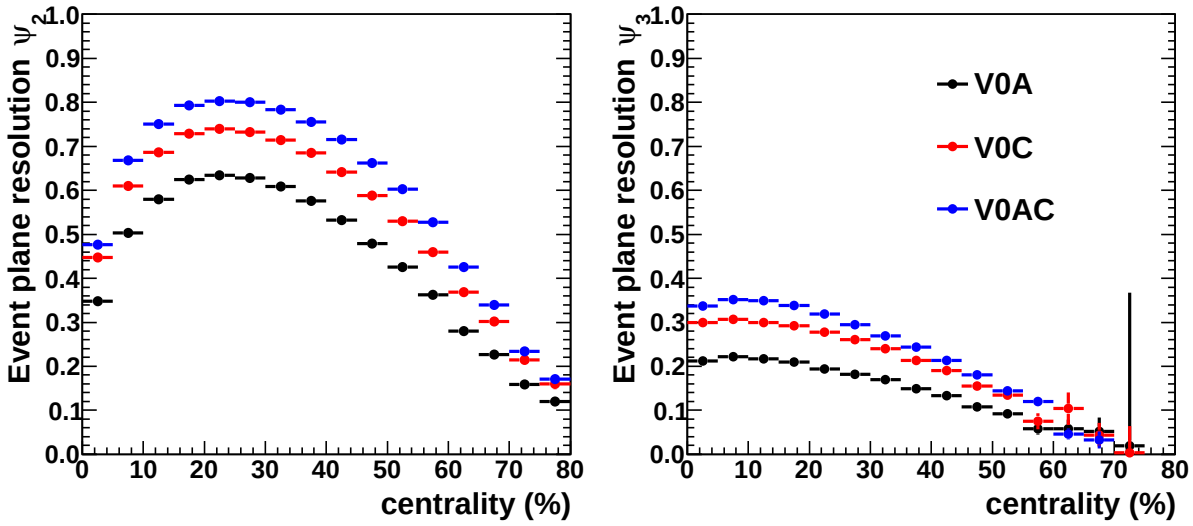

Fig. 3.4.7: The V0 event plane resolution from the 3 sub-event method for V0A (black), V0C (red) and V0AC (blue) as a function of centrality.

$$v_n^{obs} = \langle cos(n(\varphi_i - \Psi_n)) \rangle \tag{3.4.9}$$

where the angel brackets denote an average over all particles in all events. And then, the final flow coefficients are

$$v_n = \frac{v_n^{obs}}{R_n} \tag{3.4.10}$$

where R_n is the event plane resolution. Fig. 3.4.8, 3.4.9, 3.4.10 show the v_2, v_3 as a function of $p_{T,track}$ and centrality. The open markers are the ALICE published results[51].

The v_2 and v_3 results in this analysis are good agreement with the result published from the ALICE experiment, which mean the event plane in this analysis are reconstructed, exactly.

3.4.7 Fitting procedure

In order to obtain v_2 and v_3 value in Eq.3.4.3, we fitted a $\frac{d\sigma p_T}{d\varphi}$ distribution event-by-event by using Eq.3.4.3.

ρ_0 calculation

Parameter ρ_0 in Eq.3.4.3 which is the normalization of the Fourier expansion is calculated by the median method of the distribution of k_T jets with excluding two leading jet in a event. And then, this parameter is not fixed parameter and only used for the initial input. ρ_0 can be changed by the fitting results.

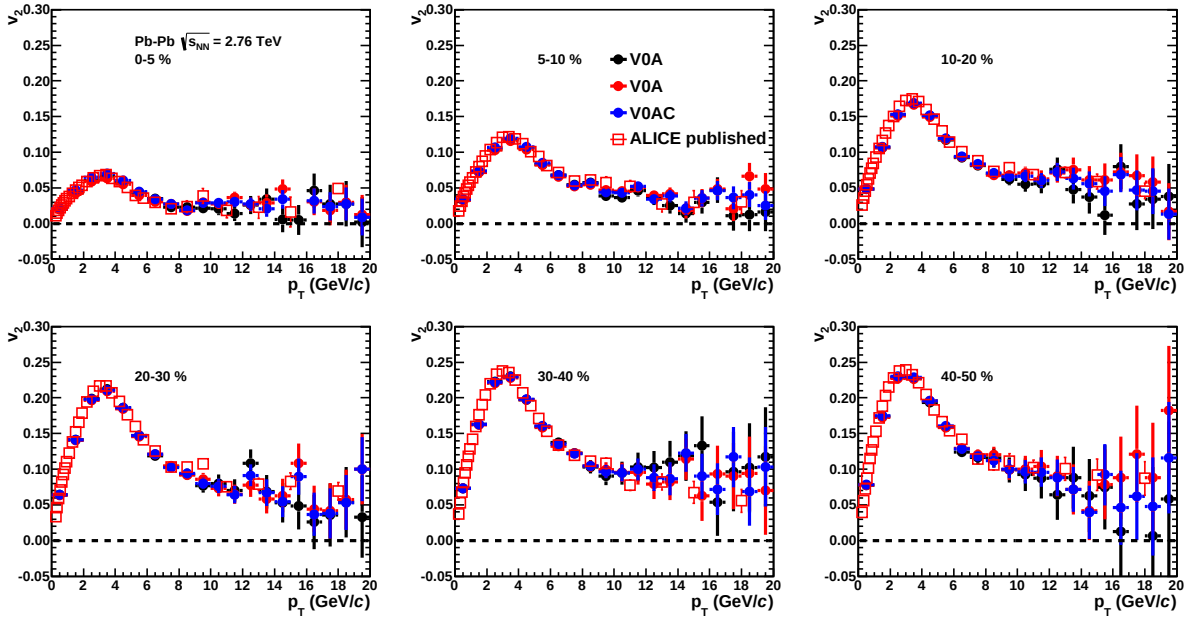

Fig. 3.4.8: v_2 as a function of $p_{T,track}$ with six centrality bins. The open markers are the ALICE published results[51].

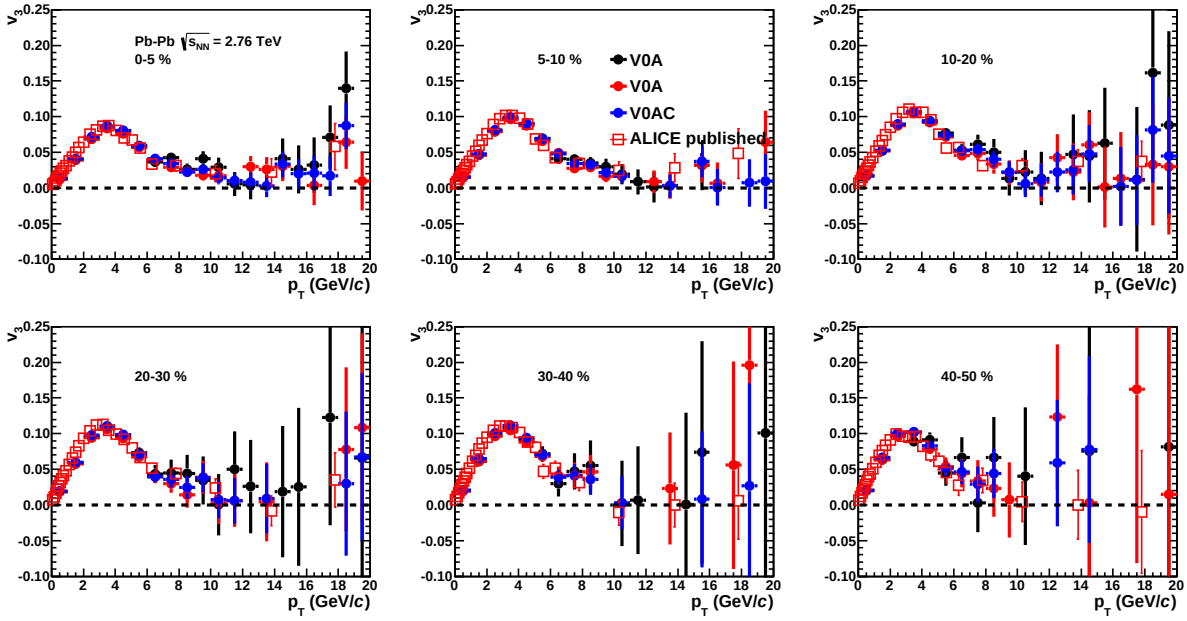

Fig. 3.4.9: v_3 as a function of $p_{T,track}$ with six centrality bins. The open markers are the ALICE published results[51].

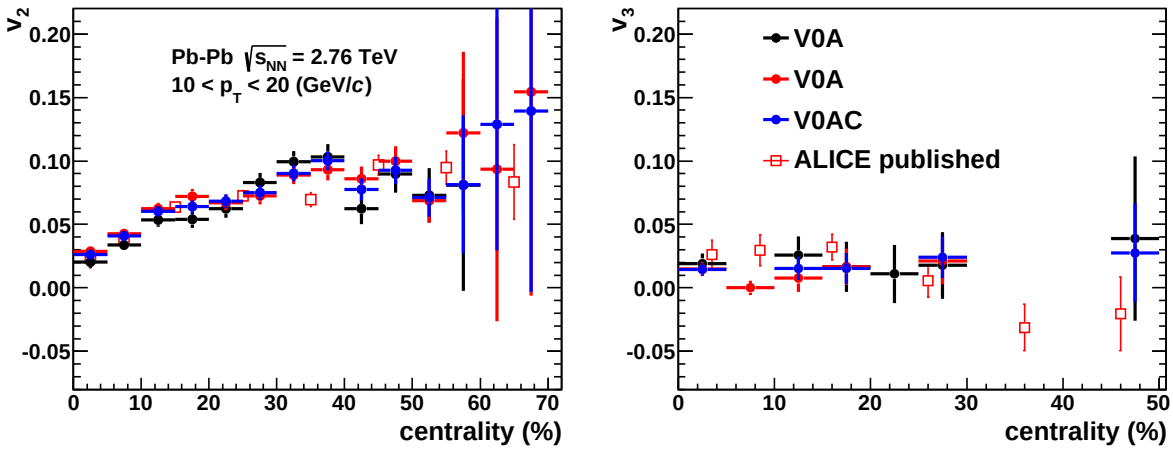

Fig. 3.4.10: v_2 (left), v_3 (right) as a function of centrality. The open markers are the ALICE published results[51].

Fit histogram

A $\frac{d\Sigma p_T}{d\varphi}$ distribution is obtained by filling of the φ value of tracks using for each track a weight of p_T, and then fitted by Eq.3.4.3 (see in Fig.3.4.3). p_T range of tracks filled to a $\frac{d\Sigma p_T}{d\varphi}$ distribution is from 0.2 to 5 Gev/c. Tracks that are part of the leading jet of an event excluded from the sample. All tracks within the same η region of the leading jet are rejected from the sample (i.e. a cut excluding all tracks $|\eta_{track} - \eta_{leading\,jet}| < R$ where R is the jet resolution parameter is performed). For the semi-good runs, tracks with an azimuthal angle $\varphi > 4$ are rejected to obtain uniform efficiency of the azimuthal region. In order to obtain the good fitting quality, the number of bins of a $\frac{d\Sigma p_T}{d\varphi}$ histogram is determined corresponding to the square root of the number of accepted tracks selected by the hybrid track cut. In case of the semi-good runs, the region $0 < \varphi < 4$ is divided into $\sqrt{N}$ bins.

Finally, we checked χ^2 value. We will describe more detailed how to check the fitting quality in the next section.

3.4.8 Fitting quality check

We can not obtain a better fitting result of the background density than $\langle\rho\rangle$, when φ dependence is either absent, ill-described poorly by Eq.3.4.3 or the fitting procedure is failed for some reason. If the fitting of Eq.3.4.3 is failed, the median method is taken to estimate the background density instead of the local $\rho(\varphi)$ method. We require to pass a number of quality checks to determine whether or not to use the local $\rho(\varphi)$ method.

- Negative values : The first check is the requirement that a minimum value of $\rho(\varphi)$ in an event is larger than or equal to 0, which mean that an event can not have a local energy density smaller than 0. This reason dominate in very peripheral events with a sparsely filled $\frac{d\sum p_T}{d\varphi}$.

- p-values and goodness of fit : The second check is a cut on the probability p value derived from the χ^2 static. The χ^2 static of the fit is given by,

$$\chi^2 = \sum_{n=0}^{i} \left(\frac{x_i - {\mu_i}^2}{\sigma_i} \right) \tag{3.4.11}$$

where x_i is the content of bin i, μ_i is the theorized value of the bin content and σ_i is the error on the measured point. The χ^2 method is used as the quality check which is taken into account the

estimates of the errors on the measurements when determining the goodness fit.
In a simple case, if the number of bins in the fitted histogram would be equal for each event, a goodness of fit quality could be imposed by cutting on the χ^2 or the reduced χ^2,

$$\tilde{\chi^2} = \frac{\chi^2}{k} \tag{3.4.12}$$

where k is the number of degrees of the freedom. However, an acceptable cut on $\tilde{\chi^2}$ depends on the multiplicity of accepted track, because the binning of the $\frac{d\sum p_T}{d\varphi}$ histogram varies from event to event. In order to obtain a goodness of fit which does not depend on the number of degrees of freedom, we calculate the p-value, which is the probability of finding a test statistic at least as extreme as the observed one in a χ^2 distribution of each fit. The p-value can be obtained from evaluating the cumulative distribution function (CDF) with the appropriate number of degrees of freedom k and χ^2 value:

$$CDF(k,\chi^2) = \frac{1}{\Gamma(\frac{k}{2})}\gamma(\frac{k}{2},\frac{x}{2}), \tag{3.4.13}$$

where Γ and γ are Gamma functions. The corresponding p-value of the fit is obtained from Eq.3.4.13 by

$$p = 1 - CDF. \tag{3.4.14}$$

The higher p-value is the confidence that the observed deviation from the null hypothesis is significant. Thus, the fit with the lower p-value should be rejected. Fig.3.4.11 shows the p-value and χ^2 as a function of centrality and the correlation between p-value and χ^2. In this analysis, the local

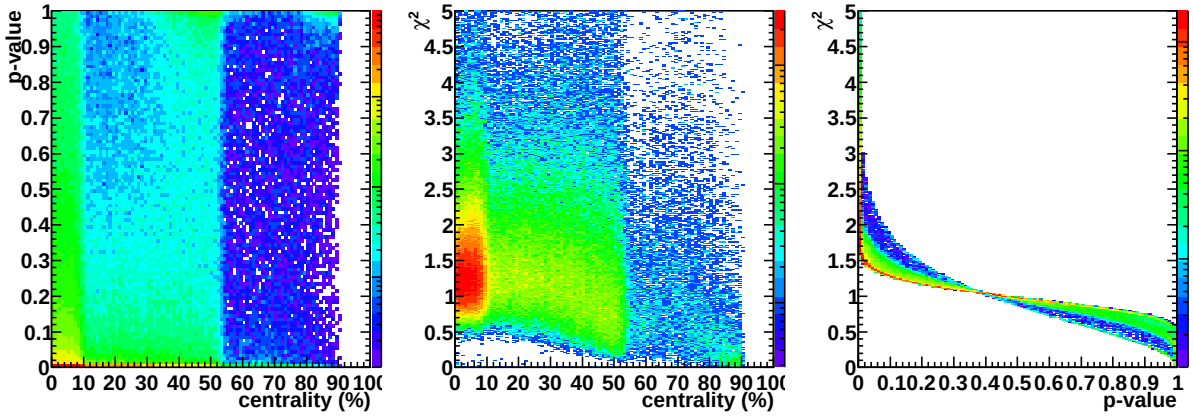

Fig. 3.4.11: p-value (left) and χ^2 (center) as a function of centrality and correlation between p-value and χ^2 (right).

$\rho(\varphi)$ is used when the p-value is larger than 0.01.

3.4.9 Comparison of background density estimation method between the median method and the local $\rho(\varphi)$ method

Fig.3.4.12 shows the Jet p_T distributions subtracted after background with the local $\rho(\varphi)$ method and the median method. The distributions subtracted background by the median method are biased towards a in-plane region, while the peak centers of the distributions subtracted background by the local method are seen no difference between the in-plane and out-plane regions.

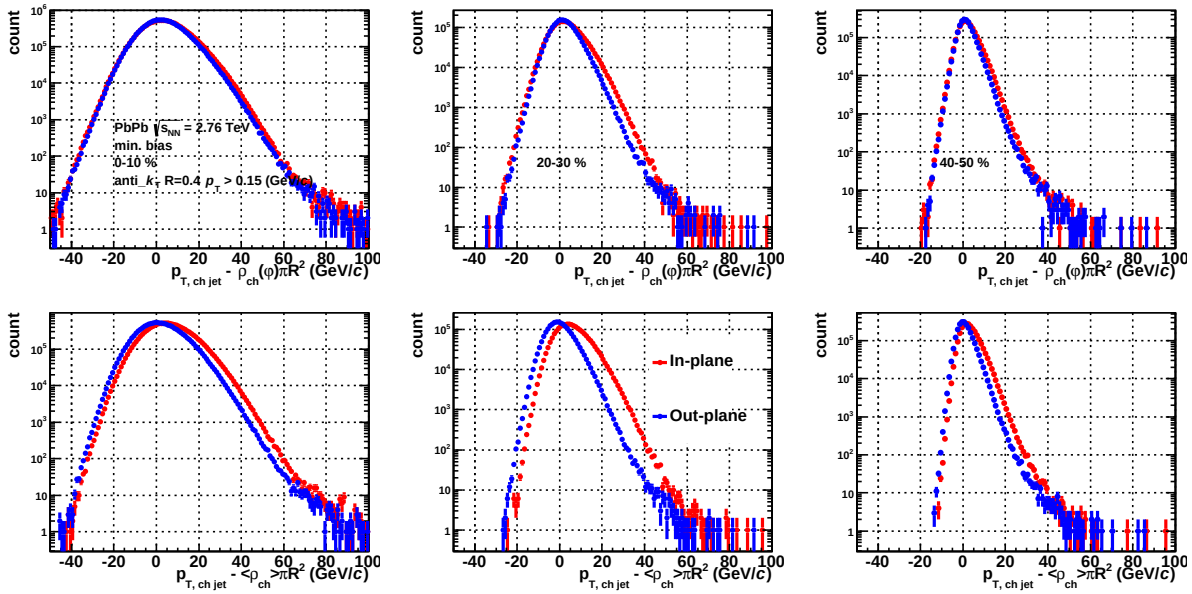

Fig. 3.4.12: Jet p_T distribution subtracted after background with the local $\rho(\varphi)$ method (upper 3 figures) and the median method (bottom 3 figures).

3.4.10 Leading particle momentum dependence of background fluctuation

Fig.3.4.13 shows the jet spectra after event-by-event subtraction of the background (mentioned in the previous sections) with the four different momentum thresholds of the leading particle in a jet. We observe the large fluctuations around zero, and it is removed by selecting jets with a high momentum leading particle.

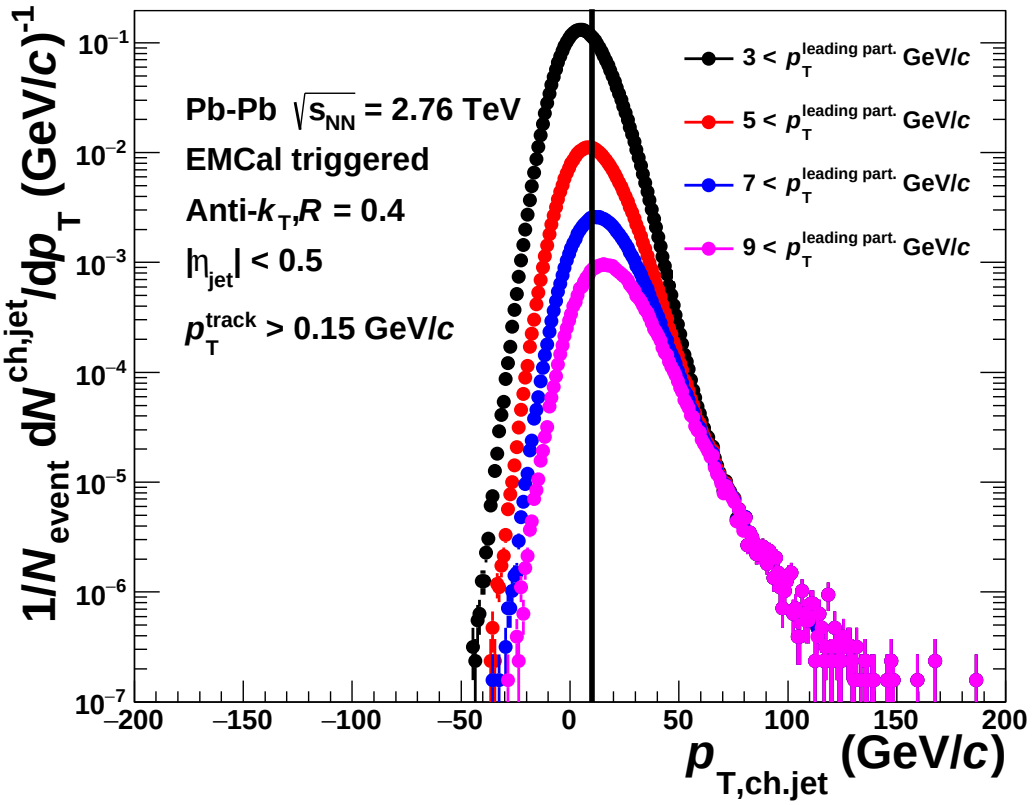

Fig. 3.4.13: Leading particle momentum dependence of the widths of background fluctuations in Pb-Pb collisions with the momentum thresholds of the leading particle in $p_{\mathrm{T}}^{\text{leading part.}} > 3$ GeV/c (black), $p_{\mathrm{T}}^{\text{leading part.}} > 5$ GeV/c (red), $p_{\mathrm{T}}^{\text{leading part.}} > 7$ GeV/c (blue) and $p_{\mathrm{T}}^{\text{leading part.}} > 9$ GeV/c (magenta). Jet p_T distribution subtracted after background with the local $\rho(\varphi)$ method (upper 3 figures) and the median method (bottom 3 figures).

Chapter 4

Corrections

In this analysis, the azimuthal correlations was calculated by the following function to obtain the associated par trigger yields as function of $\Delta\varphi = \varphi_{\pi^0} - \varphi_{jet}$.

$$\frac{dN_{jet}}{d\Delta\varphi} = \frac{1}{N^{\pi^0}_{trigger}} \frac{dN_{pair}}{d\Delta\varphi} \tag{4.0.1}$$

The azimuthal correlation is obtained in five different p_T bins for trigger π^0, and three different associated jet p_T bins. Trigger $\pi^0 p_{\rm T}$ regions were required [8-12] [12-16] [16-20] [20-24] [24-36] GeV/c, and associated jet $p_{\rm T}$ thresholds were require [$p^{jet}_{\rm T,ch} > 10$, 20, 30] GeV/c.

4.1 Event mixing

We selected trigger particles π^0 within EMCal acceptance, and associated jets within all azimuthal acceptance. In order to correct the effect of detector acceptance, this analysis is used event mixing method. We analyzed π^0-jet correlation with EMCal triggered events. Such events can not be used to construct the mixed event pool due to the limited EMCal acceptance and the trigger, which make most of the time the selected associated particles close to the trigger particle in the calorimeter. The conditions for the event mixing in pp and Pb-Pb are as follows.

pp $\sqrt{s}$ = 7 TeV

- 100 events in the pool
- z vertex divided by 2 cm step bin size (10 bins) from -10 cm to 10 cm
- Track multiplicity, 8 bins on multiplicity of hybrid tracks being : [0-5], [5-10], [10-20], [20-30], [30-40], [40-55], [55-70], [>70] (show in Fig.4.1.1)

Pb-Pb $\sqrt{s_{\rm NN}}$ = 2.76 TeV

- 100 events in the pool
- z vertex divided by 2 cm step bin size (10 bins) from -10 cm to 10 cm
- Centrality, 10 bins on centrality : [0-10], [10-20], [20-30], [30-40], [40-50], [50-60], [60-70], [70-80], [80-90], [90-100]

For mixed events we get $N^{same}_{pair}(p^{\pi^0}_T, \Delta\varphi)$ and $N^{mixed}_{pair}(p^{\pi^0}_T, \Delta\varphi)$. In order to get the final per-trigger yield, we calculate the following formula:

$$C(\Delta\varphi) = \frac{\int N^{mixed}_{pair}(p^{\pi^0}_T, \Delta\varphi) d\Delta\varphi}{\int N^{same}_{pair}(p^{\pi^0}_T, \Delta\varphi) d\Delta\phi} \cdot \frac{N^{same}_{pair}(p^{\pi^0}_T, \Delta\varphi)}{N^{mixed}_{pair}(p^{\pi^0}_T, \Delta\varphi)} \tag{4.1.1}$$

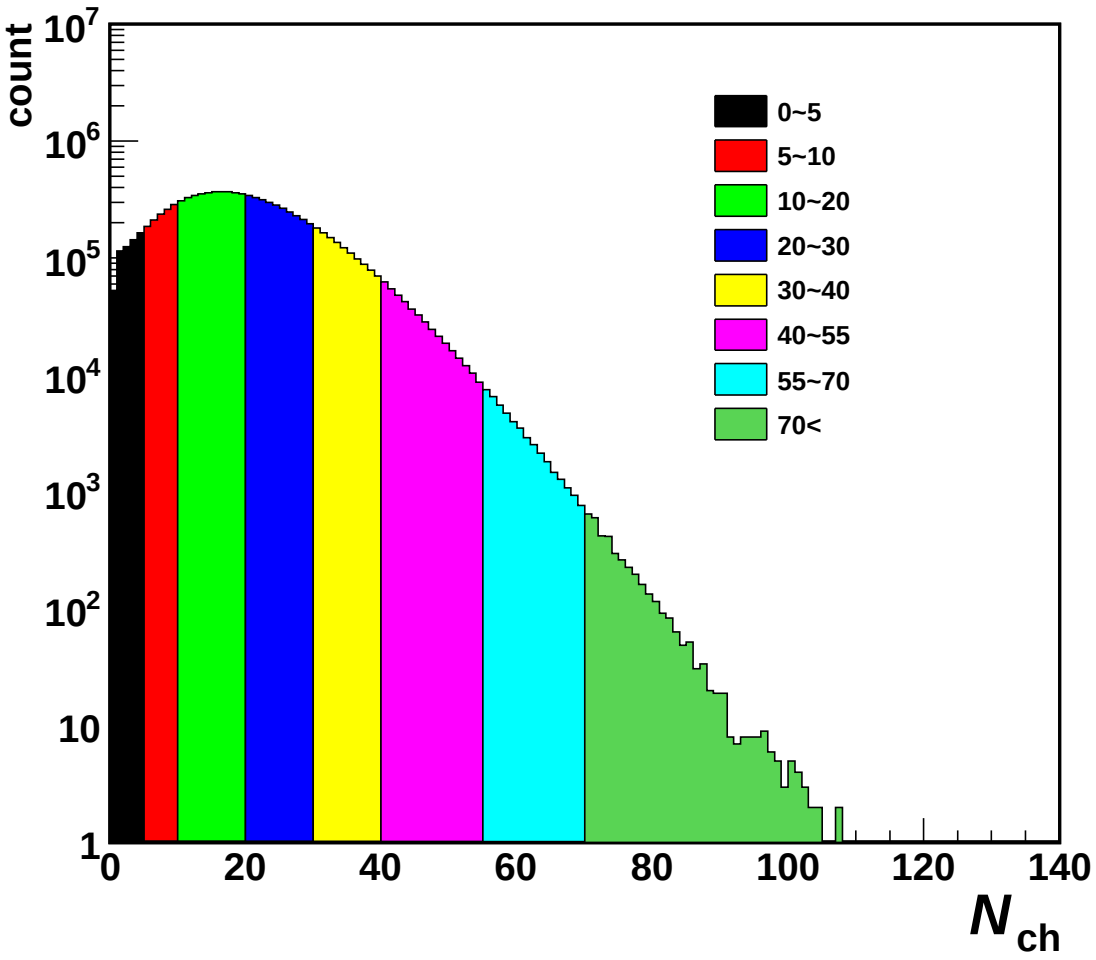

Fig. 4.1.1: Charged track multiplicity distributions with 8 different mixing bins pp collisions at $\sqrt{s}$ = 7 TeV.

$$\frac{1}{N_{trig}^{\pi^0}}\frac{dN^{jet}}{d\Delta\varphi} = \frac{\int N_{pair}^{same}(p_T^{\pi^0},\Delta\varphi)d\Delta\varphi}{N_{trig}^{\pi^0}(p_T^{\pi^0})}\cdot C(\Delta\varphi) \tag{4.1.2}$$

Fig. 4.1.2 shows the azimuthal correlation for real events and mix events and applied event mixing.

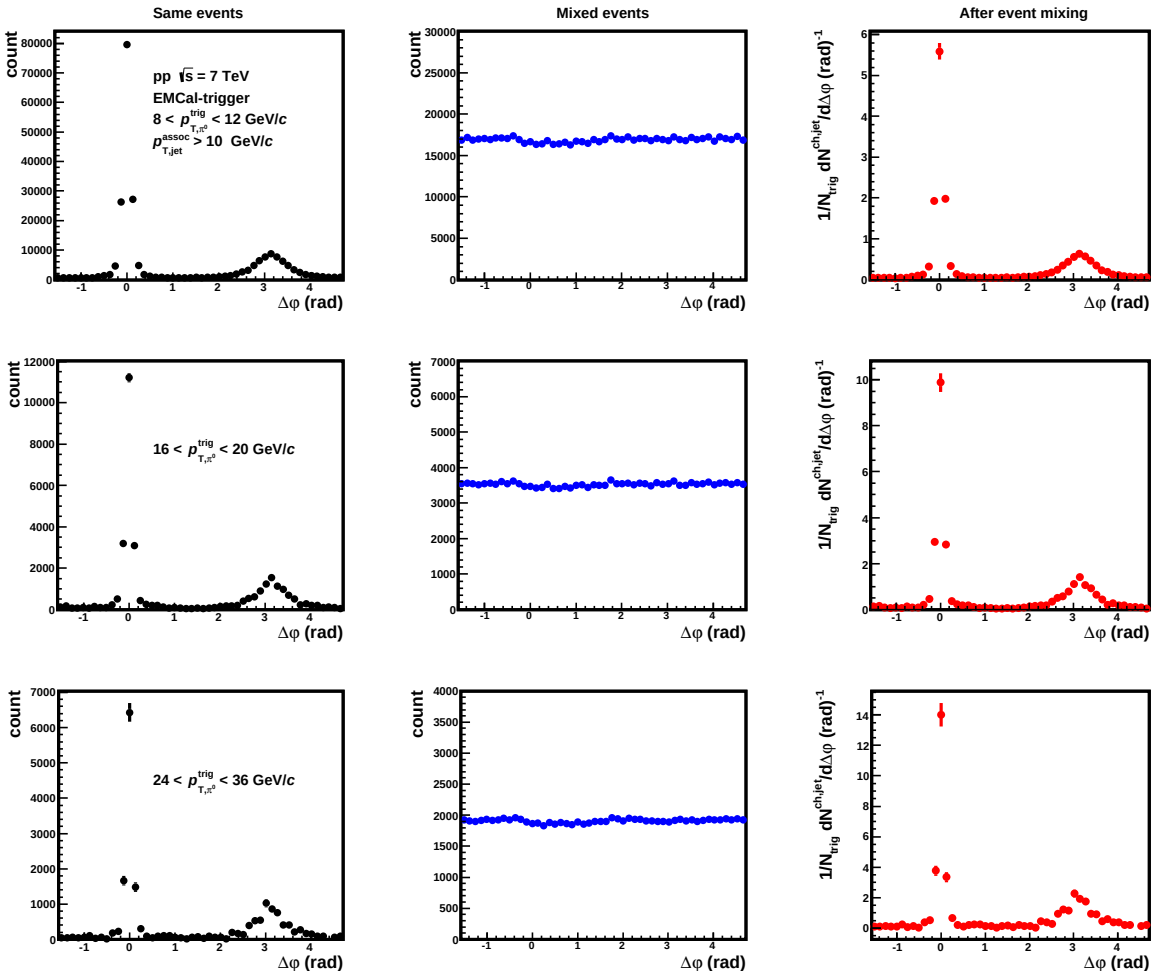

Fig. 4.1.2: The azimuthal distributions of same event without applying event mixing, mixed event and same event with applying event mixing, trigger $\pi^0 p_T$ regions $8 < p_{\mathrm{T}}^{\pi^0} < 12$ (GeV/c), $16 < p_{\mathrm{T}}^{\pi^0} < 20$ (GeV/c), $24 < p_{\mathrm{T}}^{\pi^0} < 36$ (GeV/c) and associated jet $p_{\mathrm{T}} > 10$ (GeV/c) in pp collisions at $\sqrt{s} = 7$ TeV.

4.2 Flat background subtraction

The counting pairs technique is used to extract the correlated and un-correlated yield of charged jets in different $\Delta\phi$ width. Pedestal subtraction is used to extract correlated jet yield. The uncorrelated background is considered as a flat distribution in $\Delta\phi$. The pedestal uncorrelated background is determined in the following two step:

1. Take 4 bins in the valley region on the left and right side from a near side peak region
2. Calculate the average background value from 8 bins in valley regions

Fig.4.2.1 shows the $\Delta\varphi$ distribution between a trigger π^0 and accosiated jets of before (black) and after (red) pedestal background subtraction with the momentum range of the trigger π^0 $8 < p_{\mathrm{T}}^{\pi^0} < 16$ GeV/c in

central Pb-Pb collisions, and the three different momentum ranges of the associated jets and thresholds of the leading particle in a jet. The momentum ranges of the associated jets increase with going from left to right side and the momentum thresholds of the leading particle in a jet increase with going from the top to bottom figures. These results indicate that the amount of pedestal background strongly depends on the momentum of the associated jets and the leading particle in a jet.

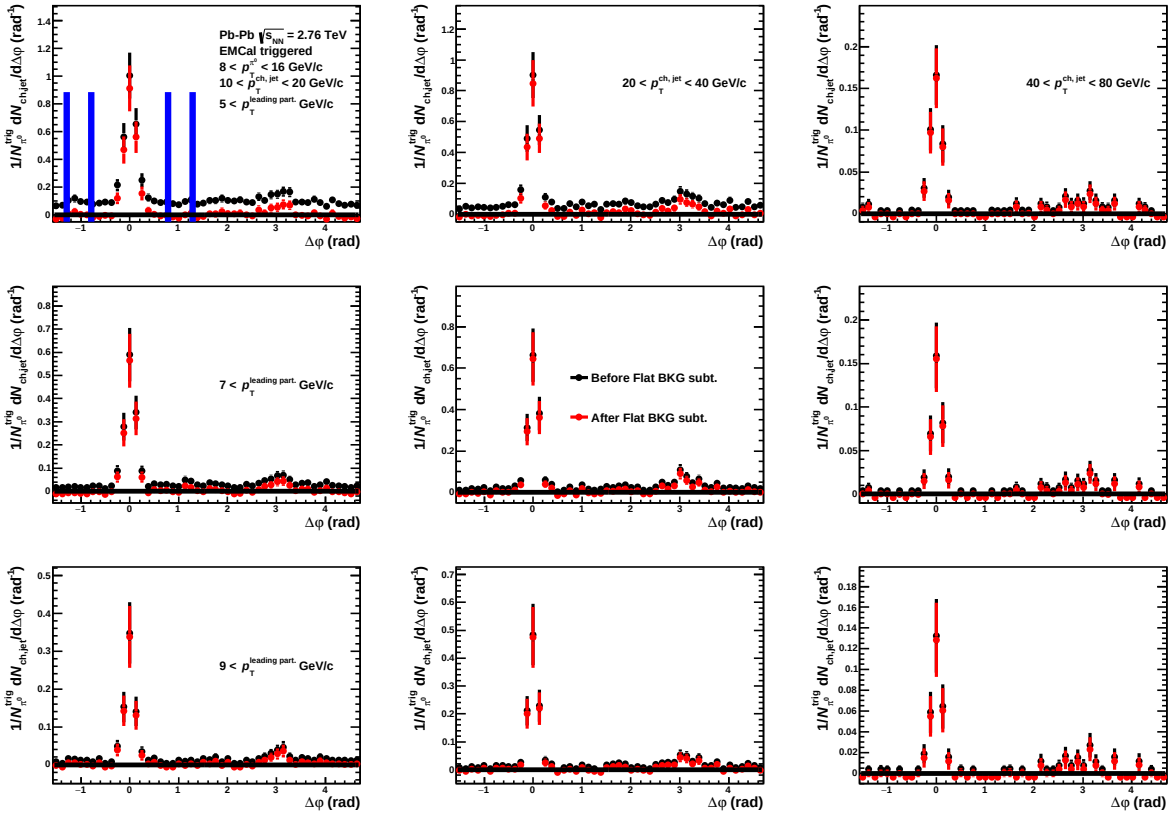

Fig. 4.2.1: $\Delta\varphi$ distribution between a trigger π^0 and accosiated jets of before (black) and after (red) pedestal background subtraction in Pb-Pb collisions with momentum range of the trigger π^0 $8 < p_{\mathrm{T}}^{\pi^0} < 16$ GeV/c, and the associated jets $10 < p_{\mathrm{T,chjet}} < 20$, $20 < p_{\mathrm{T,chjet}} < 40$ and $40 < p_{\mathrm{T,chjet}} < 80$ GeV/c. The thresholds of the leading particle in a jet are 5, 7 and $9 < p_{\mathrm{T}}^{leading part.}$ GeV/c. The two bands around the near side peak defined blue lines show the valley region to determine the flat background.

4.3 π^0 and jet reconstruction efficiencies

In order to correct the effect of the π^0 and jet reconstruction efficiency, we calculated by using Monte Carlo data, as follows:

$$\varepsilon^{\pi^0}(p_T) = \frac{cluster\,generated\,by\,2\gamma\,from\,\pi^0\,decay\,identified\,as\,\pi^0\,for\,NLM = X}{all\,clusters\,generated\,by\,2\gamma\,from\,\pi^0} \tag{4.3.1}$$

$$\varepsilon^{jet}(p_T) = \frac{N_{matched}}{N^{|\eta_{gen}|<0/5}_{particle\,level}} \tag{4.3.2}$$

Fig. 4.3.1 shows the π^0 reconstruction efficiency as function of $p_T^{\pi^0}$, and Fig. 4.3.2 shows the jet finding efficiency as function of p_T^{jet} with generated p_T. In order to correct the effect of π^0 and jet reconstruction

efficiency, we applied the following equation:

$$\frac{1}{N_{trig}^{corrected}}\frac{dN_{pair}^{corrected}}{d\Delta\varphi} = \frac{1}{\Sigma_{\Delta p_{T,(i)}}\frac{1}{\varepsilon_i^{\pi^0}}\cdot N_{trig(i)}^{\pi^0}(\Delta p_T^{trig})}\sum_{\Delta p_{T,(i)}}\frac{1}{\varepsilon_i^{\pi^0}\varepsilon^{jet}}\frac{dN_{pair(i)}^{Raw}}{d\Delta\varphi}(\Delta p_T^{trig}) \tag{4.3.3}$$

Since the π^0 reconstruction efficiency is not flat, in order to correct the effect of π^0 reconstruction efficiency to a p_T bin trigger more exactly, this analysis are used a bin-by-bin correction method with the bin width, $\Delta p_{\mathrm{T}}^{\pi^0}$ = 1 GeV/c. The jet reconstruction efficiency was also corrected with three different p_T bins.($10 < p_{\mathrm{T}}^{jet} < 20$ GeV/c : $\varepsilon^{jet} = 0.93$, $20 < p_{\mathrm{T}}^{jet} < 30$ (GeV/c) : $\varepsilon^{jet} = 0.97$, $30 < p_{\mathrm{T}}^{jet}$ GeV/c : $\varepsilon^{jet} = 0.98$)

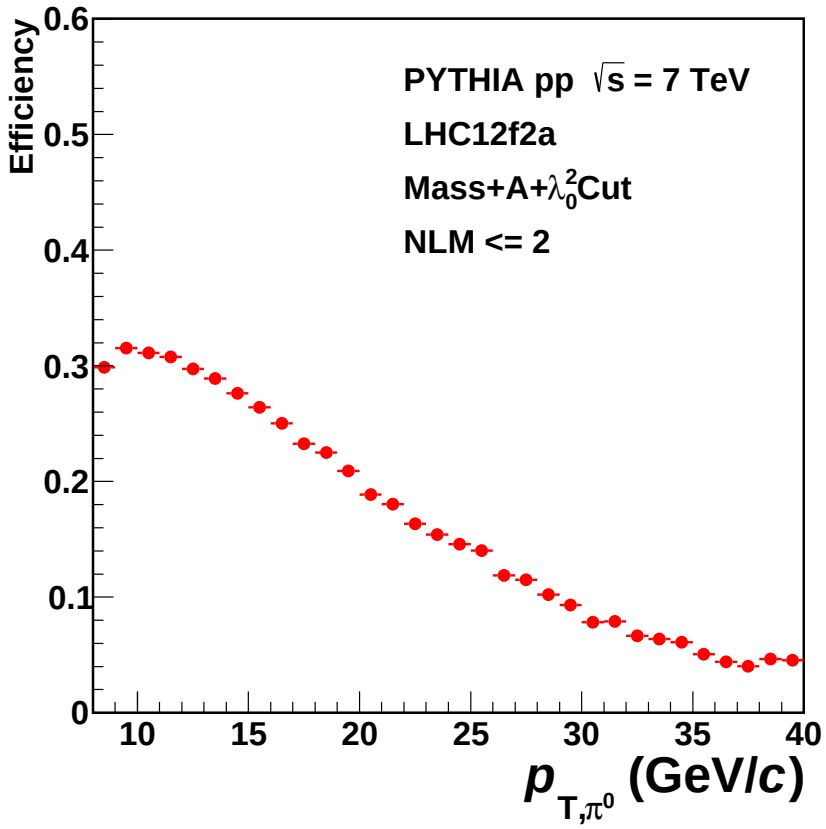

Fig. 4.3.1: π^0 reconstruction efficiency as function of $\pi^0 p_T$ with NLM <= 2.

4.4 Scale down factor calculation

In this section, we explain about the scale down factor calculation to obtain the near and away side jet yields in pp collisions at $\sqrt{s} = 2.76$ TeV from those at $\sqrt{s} = 7$ TeV. This analysis is used the real data of pp 7 TeV (LHC11cd) as pp collision reference, and then we have to scale the near and away side jet yields of pp 7 TeV before comparison to the Pb-Pb 2.76 TeV results (For example the ratio of the trigger yields I_{AA} analysis). In order to obtain the scale down factors, we compare near and away side jet yields between pp 7 TeV and 2.76 TeV which is calculated by the Monte Carlo simulation (PYTHIA simulation). The top figures in Fig.4.4.1, 4.4.2 show the comparison of near and away side jet yields between pp 7 TeV and 2.76 TeV as function of the associated jet $p_{\mathrm{T,ch.jet}}$ in he momentum range of the

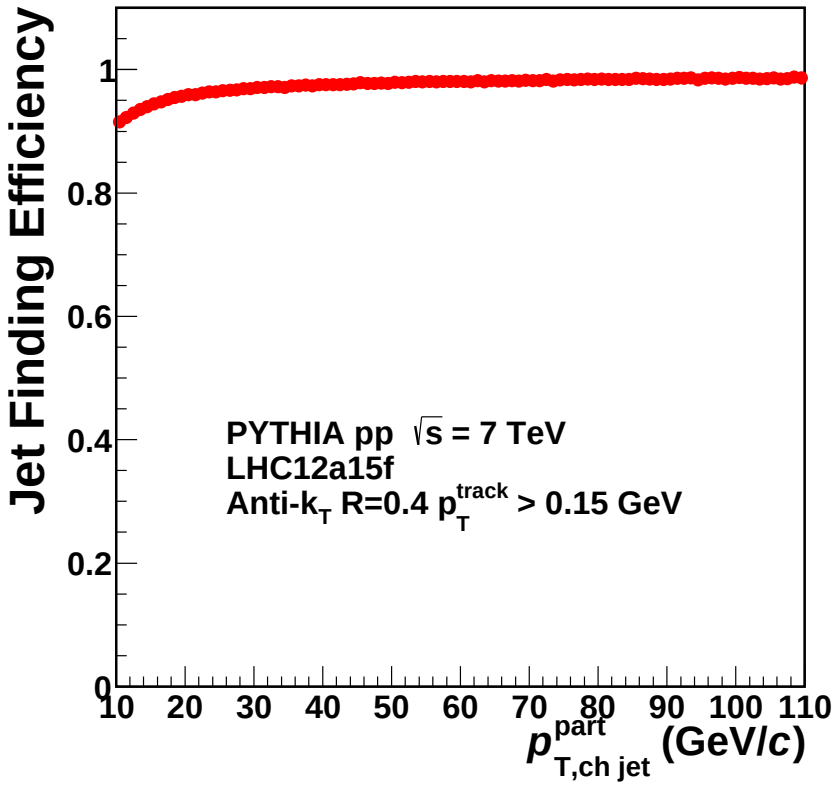

Fig. 4.3.2: Jet reconstruction efficiency as function of jet p_T with particle level.

trigger π^0 $8 < p_{\mathrm{T}}^{\pi^0} < 16$ GeV/c, and the bottom figures show its ratios. These ratios will be used as the bin-by-bin scaling factors to near and away side jet yields in pp 7 TeV.

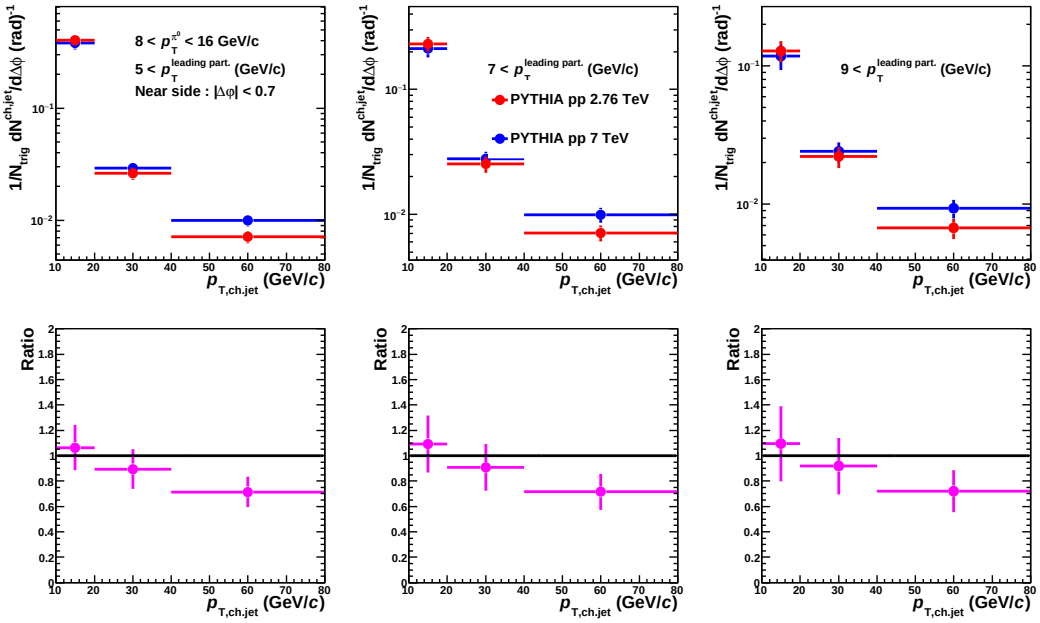

Fig. 4.4.1: Comparison of near side jet yields between pp 7 TeV (blue) and 2.76 TeV (red) which is calculated by the Monte Carlo simulation (PYTHIA simulation) and its ratio as function of the associated jet $p_{\mathrm{T,ch.jet}}$ in the momentum range of the trigger π^0 $8 < p_{\mathrm{T}}^{\pi^0} < 16$ GeV/c. The thresholds of the leading particle in a jet are 5, 7 and $9 < p_{\mathrm{T}}^{leadingpart.}$ GeV/c. The near side region is $|\Delta\varphi| < 0.7$ (rad).

4.5 Unfolding correction

The measured jet spectrum contains the effects of the detector response (pp and Pb-Pb collisions) and the fluctuations in background energy density (Pb-Pb collisions). In order to obtain the true jet spectrum, we have to correct these effects and this analysis is used the unfolding correction method. Mathematically, the measured jet spectrum can be calculate by the following equation,

$$M(p_{\mathrm{T}}^{rec}) = \int G(p_{T}^{\mathrm{rec}}, p_{\mathrm{T}}^{gen}) T(p_{\mathrm{T}}^{gen}) dp_{\mathrm{T}}^{gen} \tag{4.5.1}$$

where $M(p_{\mathrm{T}}^{rec})$ is the measured jet spectrum, $G(p_{\mathrm{T}}^{rec}, p_{\mathrm{T}}^{gen})$ is a functional description of distortions due to background fluctuations and detector effects, $T(p_{\mathrm{T}}^{gen})$ is the true jet spectrum. And, Eq.4.5.1 is changed and can be written in matrix form

$$\mathrm{M_M} = \mathrm{G_{m,t}} \cdot \mathrm{T_t} \tag{4.5.2}$$

where the term $\mathrm{G_{m,t}}$ is the response matrix which is taken into account the effect of background fluctuation and detector response. Solving Eq.4.5.2 is non-trivial as it requires inversion of $\mathrm{G_{m,t}}$ and the exact solution to this problem is usually non-physical as is oscillates wildly due to the statistical errors on the measured distribution[52][53]. We need to regularize the unfolded solution, constraining it to some physical form. This analysis are used the two methods; the Single Value Decomposition (SVD) and iterative Bayesian unfolding for regularized solving of Eq.4.5.2.

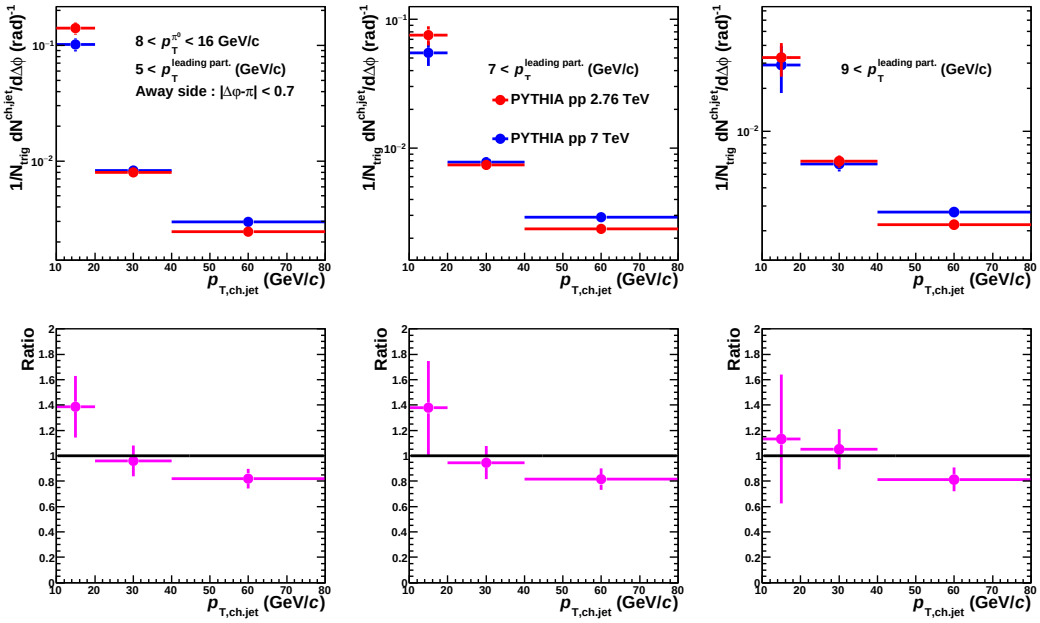

Fig. 4.4.2: Comparison of away side jet yields between pp 7 TeV (blue) and 2.76 TeV (red) which is calculated by the Monte Carlo simulation (PYTHIA simulation) and its ratio as function of the associated jet $p_{\mathrm{T,ch.jet}}$ in the momentum range of the trigger π^0 $8 < p_{\mathrm{T}}^{\pi^0} < 16$ GeV/c. The thresholds of the leading particle in a jet are 5, 7 and $9 < p_{\mathrm{T}}^{leading part.}$ GeV/c. The away side region is $|\Delta\varphi - \pi| < 0.7$ (rad).

4.5.1 Response matrix

The response matrix contains the effects of the detector response and fluctuations of background density which influence to the measured jet spectrum. These effects are determined in two matrices separately, and the full response matrix are produced from the two matrices.

Response matrix for fluctuations of background density

The magnitude of the fluctuations of background density is estimated by embedding rigid random cones into an event and subtracting the expected background from these cones. The random cone procedure are constructed the four steps:

1. A cone with radius R is embedded randomly in φ-η plane limited in detector acceptance.
2. Calculated the total energy within a cone by the following equation,

$$p_{\mathrm{T}} = \sum_i p_{\mathrm{T,i}} \tag{4.5.3}$$

3. The expected background energy density is subtracted from the total energy within a cone by the following equation.

$$\delta p_{\mathrm{T}} = p_{\mathrm{T}} - \rho \times A \tag{4.5.4}$$

   where ρ is background density per unit area which is calculated from local ρ method explained in the previous section.
4. These processes are repeated until the total covered area equals the detector acceptance.

The response matrix for fluctuations of background density is obtained from the $\delta\varphi$ distribution which is converted to a probability distribution by normalizing it to 1. Fig.4.5.1 shows the δp_{T} distribution of random cone analysis with cone radius R = 0.4 and normalizing to 1 and the response

matrix for fluctuation of background density built from the the δp_{T} distribution. The probability of reconstructing a true jet with $p_{\mathrm{T,ch.jet}}^{true}$ at $p_{\mathrm{T,ch.jet}}^{gen}$ is extracted from the δp_{T} distribution. This response matrix uses the assumption that the smearing of measured jet spectrum is the same in all transverse momentum regions.

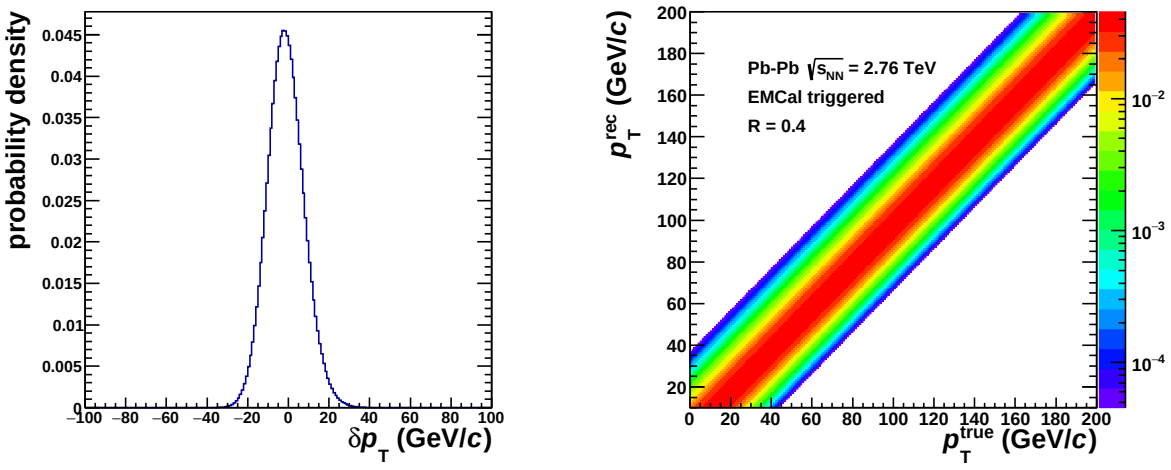

Fig. 4.5.1: Left figure: δp_{T} distribution of random cone analysis with cone radius R = 0.4 and normalizing to 1. Right figure: Response matrix for fluctuation of background density built from the left figure. The x axis is the true jet momentum $p_{\mathrm{T,ch.jet}}^{true}$ and y axis is the reconstructed jet momentum $p_{\mathrm{T,ch.jet}}^{rec}$.

Response matrix for detector response

The second source smearing the measured jet spectrum is the detector response. The measured jet spectrum contains the effect of detector response due to limited efficiency and resolution. This effect is estimated from comparison between generated and reconstructed of Monte Calro simulation. The relation between generated and reconstructed is generally called the detector response matrix. Fig.4.5.2 shows the response matrices for detector response in the momentum thresholds of leading particle with the three different momentum threshold of leading particle in a jet.

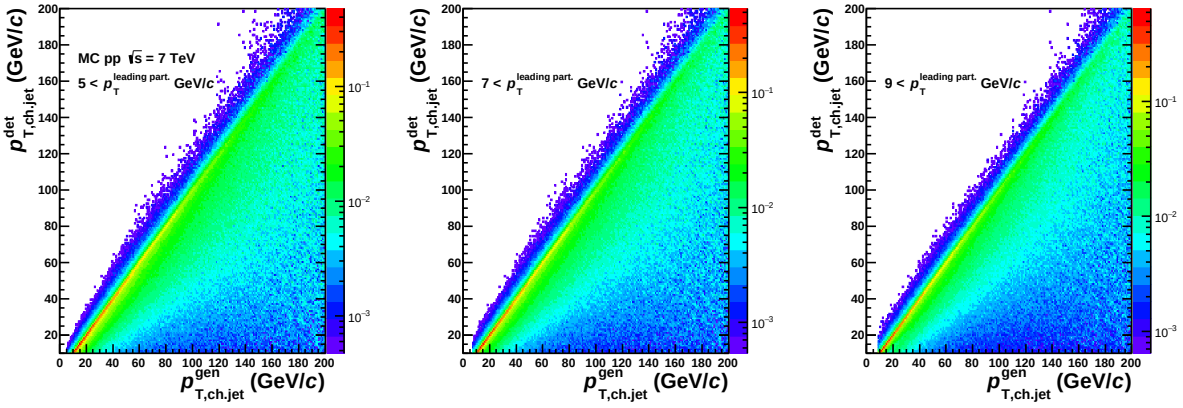

Fig. 4.5.2: Response matrices for detector response in the momentum thresholds of leading particle in a jet 5, 7 and $9 < p_{\mathrm{T}}^{leading part.}$ (GeV/c). The x axis is the true (particle level) spectrum, the y axis is the measured (detector level) spectrum.

Combined response matrix

The measured jet spectrum in this analysis is unfolded by a full response matrix which is combined two response matrices of background fluctuation and detector response. The matrices of background fluctuation and detector response are combined by trivial matrix multiplication

$$M_m = G_{m,d} \cdot G_{d,t} \cdot T_t = G_{m,t} \cdot T_t, \tag{4.5.5}$$

where $G_{m,d}$ is a detector response matrix and $G_{m,t}$ is a response matrix for background fluctuations. The fine binning of the combined response matrix is generally not suitable for unfolding since uncertainties on the measured spectrum are too large to lead to a satisfactory result. Since the jet spectrum itself is steeply falling, a weighted re-binning procedure of the response matrix is used, where as bin weights a Tsallis-fit to a PYTHIA spectrum is used[54].

$$f(p_T) = p_T(1 + \frac{p_T}{7.2})^{-8} \tag{4.5.6}$$

Fig.4.5.3 shows the full response matrix which is combined the matrices of background fluctuation and detector response. The momentum thresholds of leading particle in a jet increase with going to the right side.

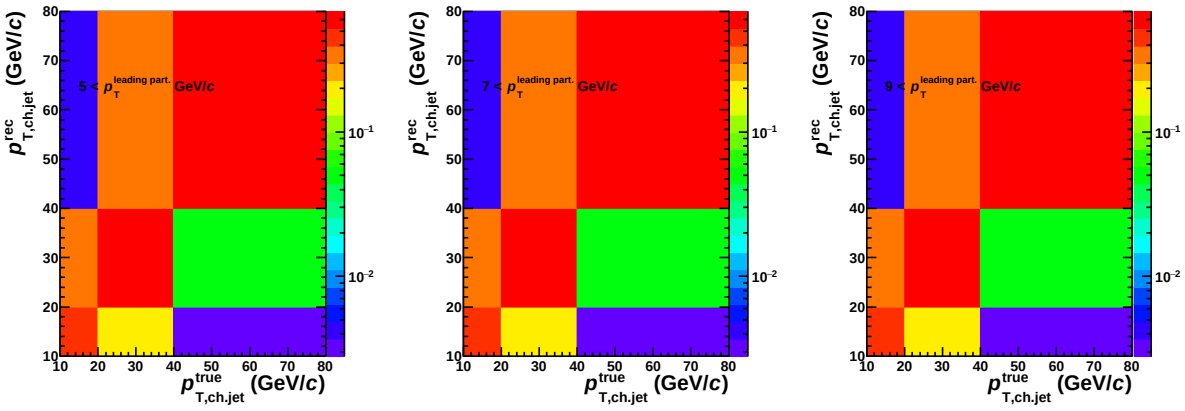

Fig. 4.5.3: Full response matrix which is combined the matrices of background fluctuation and detector response with re-binning and scaling of a Tsallis-fit in the momentum thresholds of leading particle in a jet 5, 7 and 9 $< p_T^{leadingpart.}$ (GeV/c). The x axis is the true (particle level) spectrum, the y axis is the measured (detector level) spectrum.

4.5.2 Unfold near and away side jet spectrum

Fig.4.5.4,4.5.5 show the comparisons of near and away side jet yields in pp and Pb-Pb collisions with three different momentum thresholds of leading particle in a jet. The jet yields in pp collisions are only corrected the effect of detector response, while the jet yields in Pb-Pb collisions are corrected not only detector response, but also fluctuations of background density. The differences of SVD and Bayesian unfolding algorithm are added into the systematic uncertainties.

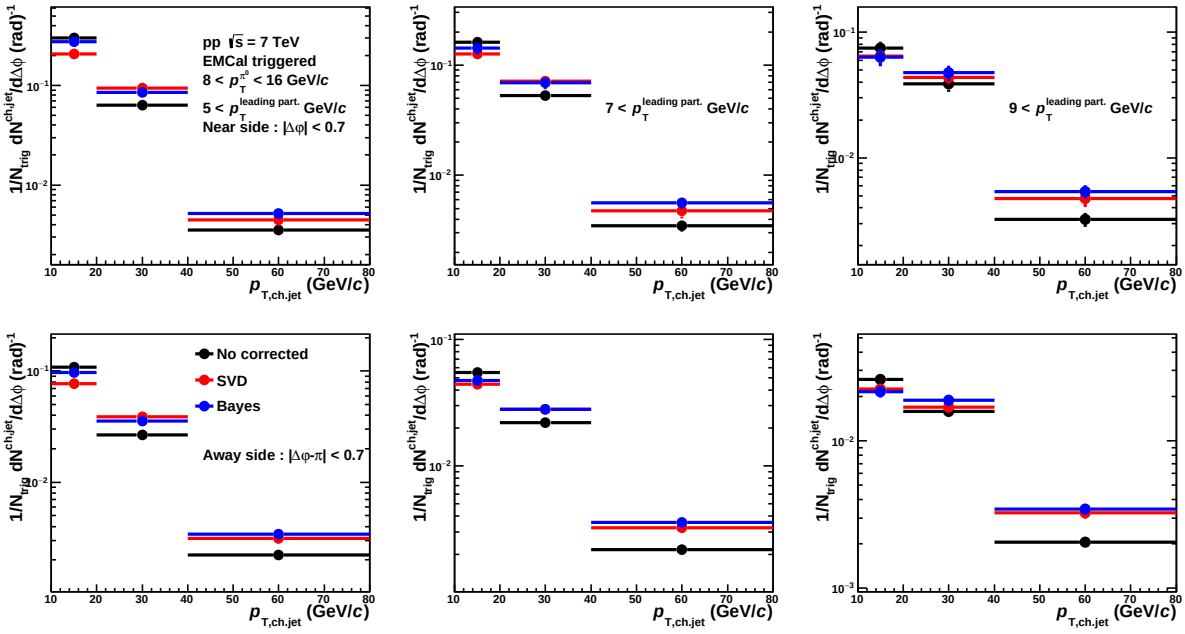

Fig. 4.5.4: Comparisons of near (top) and away (bottom) jet yields of no corrected, SVD unfolding and Bayesian unfolding in pp collisions at $\sqrt{s} = 7$ TeV in momentum range of trigger π^0 $8 < p_{\mathrm{T}}^{\pi^0} < 16$ (GeV/c) and momentum thresholds of leading particle in a jet 5 (left) ,7 (center) and 9 (right) $< p_{\mathrm{T}}^{leadingpart.}$ (GeV/c)

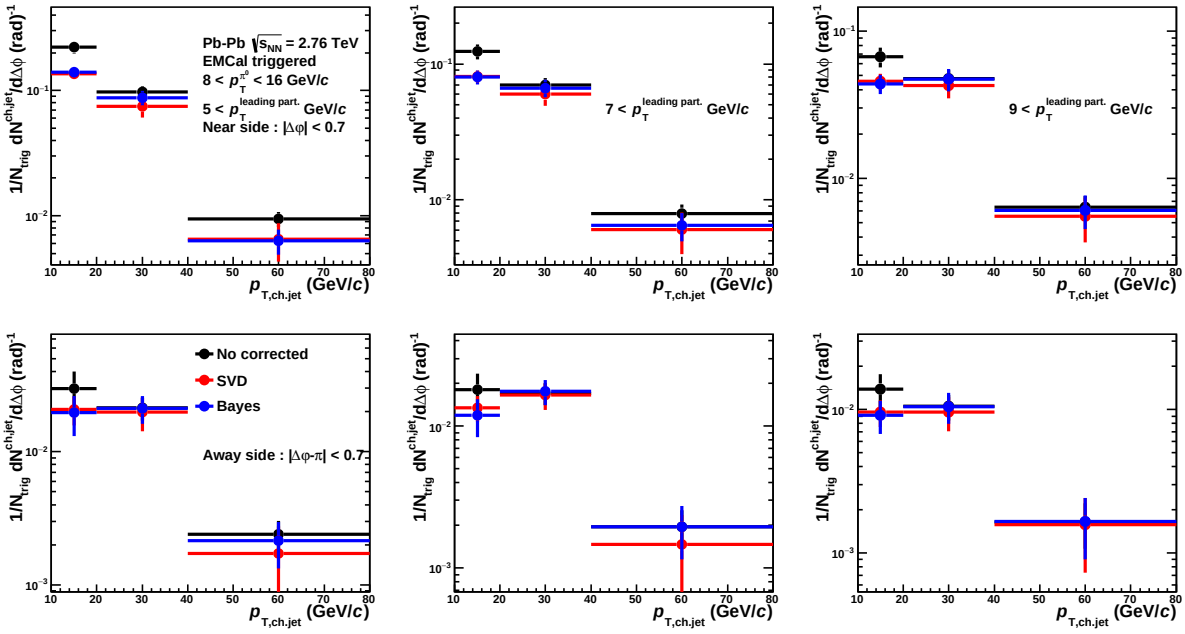

Fig. 4.5.5: Comparisons of near (top) and away (bottom) jet yields of no corrected, SVD unfolding and Bayesian unfolding in Pb-Pb collisions at $\sqrt{s_{\mathrm{NN}}} = 2.76$ TeV in momentum range of trigger π^0 $8 < p_{\mathrm{T}}^{\pi^0} < 16$ (GeV/c) and momentum thresholds of leading particle in a jet 5 (left) ,7 (center) and 9 (right) $< p_{\mathrm{T}}^{leadingpart.}$ (GeV/c)

Chapter 5

Systematic uncertainties

In this analysis, five different systematic uncertainties are considered;

- EMCal shower shape long axis parameter(λ_0^2) cut,
- Invariant mass window,
- π^0 identification purity,
- Flat background subtraction method in azimuthal correlations,
- Unfolding algorithm for near and away side jet yields.

The systematic uncertainty of flat background subtraction method for azimuthal correlations is only applied to pp collisions.

5.1 Systematic uncertainty on shower shape (the major axis parameter λ_0^2)

As mention in the previous section, this analysis used the shower shape long axis cut as function of cluster energy. In order to estimate the systematic uncertainty from shower shape cut, we compare between default cut and modified cuts.

- Default cut : $\lambda^2_{0,min,max}(E) = e^{a+b*E} + c + d*E + e/E$
- Modified cut 1 : $\lambda^2_{0,min,max}(E) = 15*(e^{a+b*E} + c + d*E + e/E)$
- Modified cut 2 : $\lambda^2_{0,min,max}(E) = 0.95*(e^{a+b*E} + c + d*E + e/E)$

Fig.5.1.1,5.1.2 and 5.1.3 show the comparisons of the three kinds of shower shape cuts of azimuthal correlations and its ration in pp collisions with the momentum range of trigger π^0 $8 < p_{\mathrm{T}}^{\pi^0} < 16$ GeV/c and Fig.5.1.4,5.1.5 and 5.1.6 are in Pb-Pb collisions. The uncertainties of azimuthal correlations are determined by the fitting of constant functions on the ratios. Fig.5.1.7,5.1.8 show the comparison of the three kinds of shower shape cuts of near (top) and away (bottom) jet yields and its ratio in pp and Pb-Pb collisions with the momentum range of trigger π^0 $8 < p_{\mathrm{T}}^{\pi^0} < 16$ GeV/c.

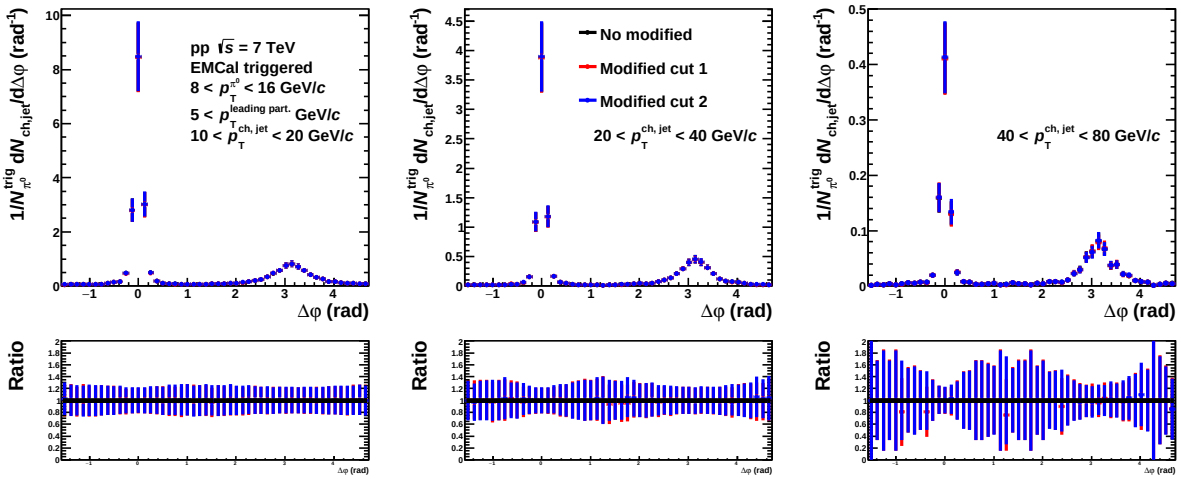

Fig. 5.1.1: Comparison of the three kinds of shower shape cuts of azimuthal correlations (top) and its ratios (bottom) in pp collisions with the momentum range of trigger π^0 $8 < p_{\mathrm{T}}^{\pi^0} < 16$ GeV/c and associated jets $10 < p_{\mathrm{T,ch.jet}} < 20$, $20 < p_{\mathrm{T,ch.jet}} < 40$ and $40 < p_{\mathrm{T,ch.jet}} < 80$ GeV/c. The momentum threshold of leading particle in a jet $5 < p_{\mathrm{T}}^{leading part.}$ GeV/c.

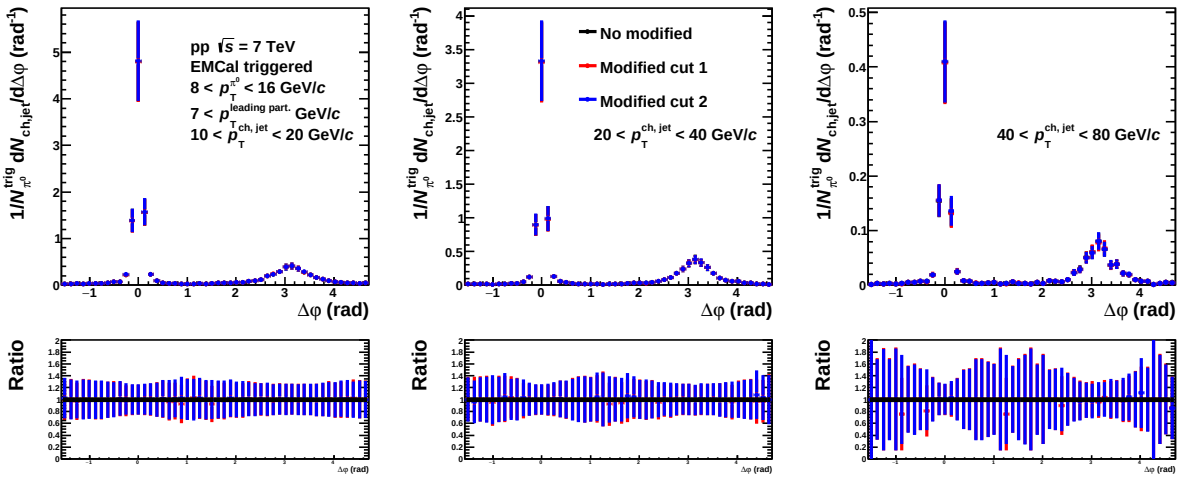

Fig. 5.1.2: Comparison of the three kinds of shower shape cuts of azimuthal correlations (top) and its ratios (bottom) in pp collisions with the momentum range of trigger π^0 $8 < p_{\mathrm{T}}^{\pi^0} < 16$ GeV/c and associated jets $10 < p_{\mathrm{T,ch.jet}} < 20$, $20 < p_{\mathrm{T,ch.jet}} < 40$ and $40 < p_{\mathrm{T,ch.jet}} < 80$ GeV/c. The momentum threshold of leading particle in a jet $7 < p_{\mathrm{T}}^{leading part.}$ GeV/c.

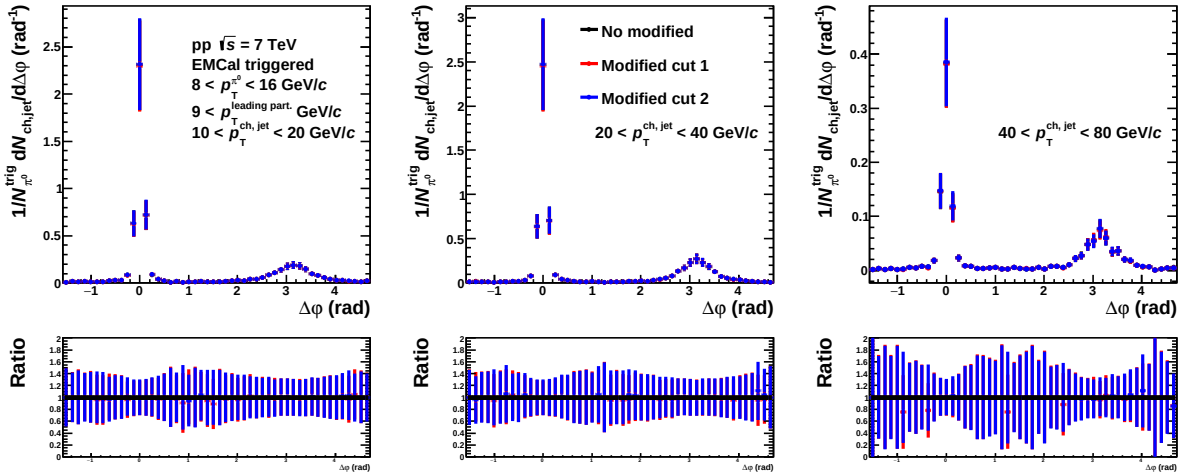

Fig. 5.1.3: Comparison of the three kinds of shower shape cuts of azimuthal correlations (top) and its ratios (bottom) in pp collisions with the momentum range of trigger π^0 $8 < p_{\mathrm{T}}^{\pi^0} < 16$ GeV/c and associated jets $10 < p_{\mathrm{T,ch,jet}} < 20$, $20 < p_{\mathrm{T,ch,jet}} < 40$ and $40 < p_{\mathrm{T,ch,jet}} < 80$ GeV/c. The momentum threshold of leading particle in a jet $9 < p_{\mathrm{T}}^{leadingpart.}$ GeV/c.

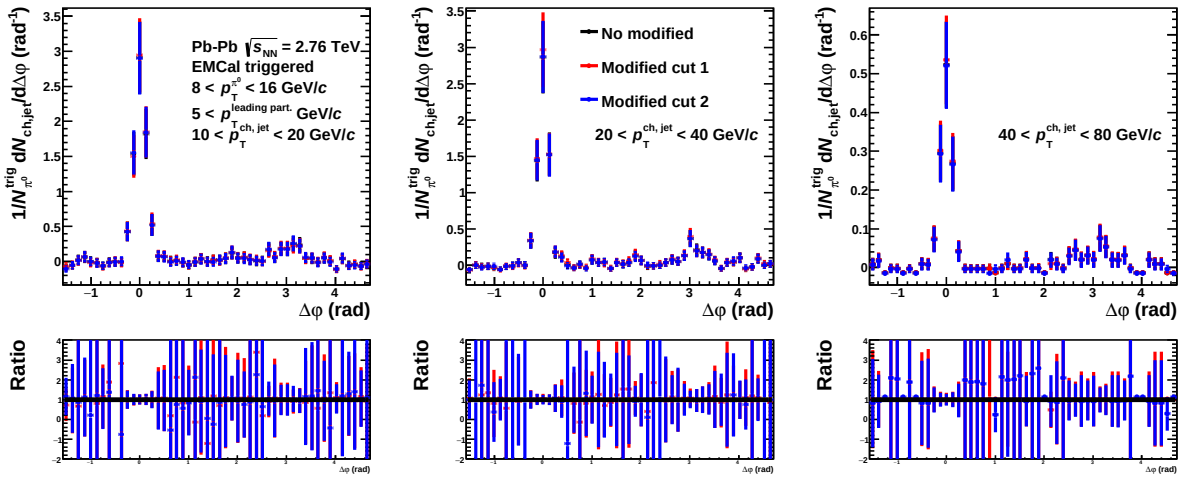

Fig. 5.1.4: Comparison of the three kinds of shower shape cuts of azimuthal correlations (top) and its ratios (bottom) in Pb-Pb collisions with the momentum range of trigger π^0 $8 < p_{\mathrm{T}}^{\pi^0} < 16$ GeV/c and associated jets $10 < p_{\mathrm{T,ch,jet}} < 20$, $20 < p_{\mathrm{T,ch,jet}} < 40$ and $40 < p_{\mathrm{T,ch,jet}} < 80$ GeV/c. The momentum threshold of leading particle in a jet $5 < p_{\mathrm{T}}^{leadingpart.}$ GeV/c.

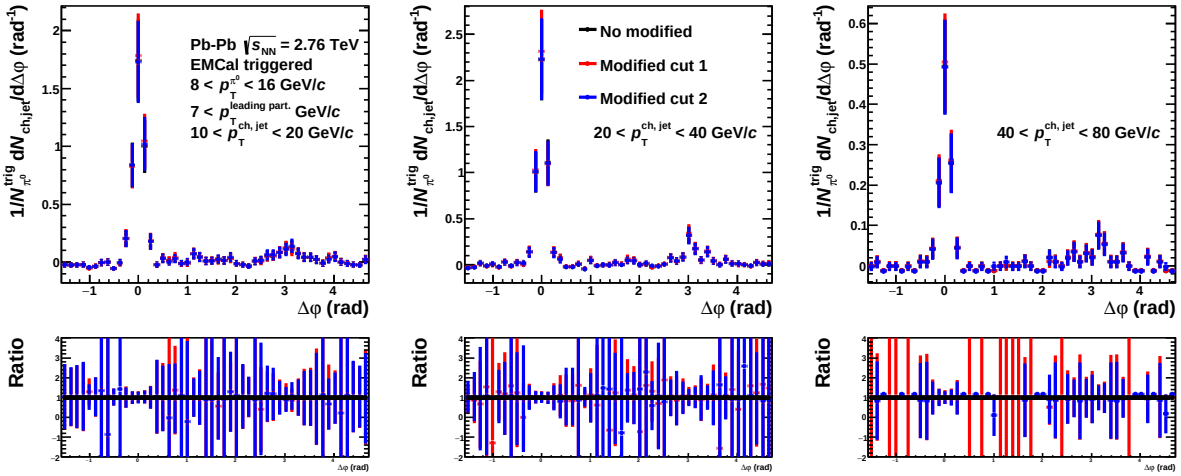

Fig. 5.1.5: Comparison of the three kinds of shower shape cuts of azimuthal correlations (top) and its ratios (bottom) in Pb-Pb collisions with the momentum range of trigger π^0 $8 < p_{\mathrm{T}}^{\pi^0} < 16$ GeV/c and associated jets $10 < p_{\mathrm{T,ch.jet}} < 20$, $20 < p_{\mathrm{T,ch.jet}} < 40$ and $40 < p_{\mathrm{T,ch.jet}} < 80$ GeV/c. The momentum threshold of leading particle in a jet $7 < p_{\mathrm{T}}^{leading part.}$ GeV/c.

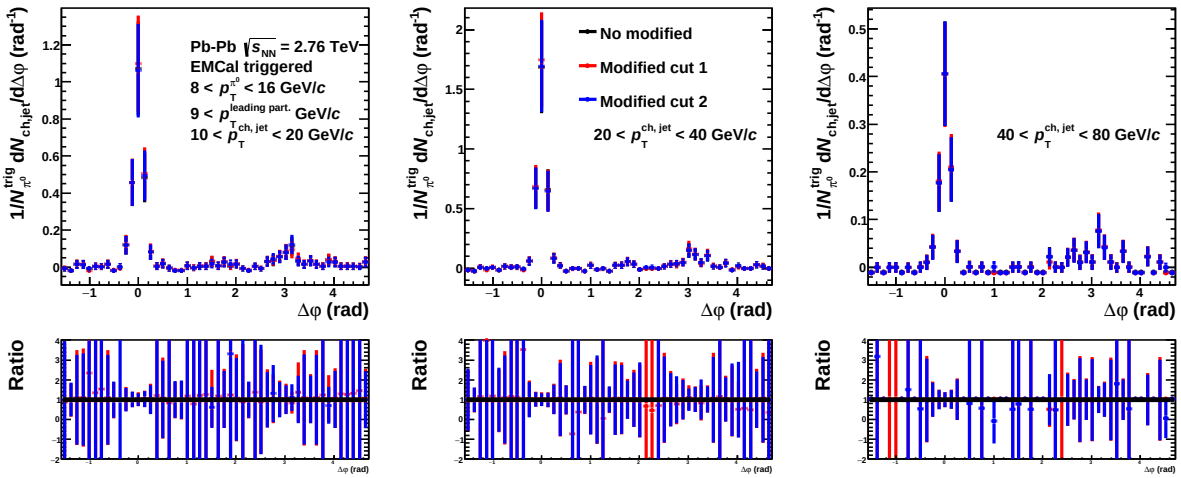

Fig. 5.1.6: Comparison of the three kinds of shower shape cuts of azimuthal correlations (top) and its ratios (bottom) in Pb-Pb collisions with the momentum range of trigger π^0 $8 < p_{\mathrm{T}}^{\pi^0} < 16$ GeV/c and associated jets $10 < p_{\mathrm{T,ch.jet}} < 20$, $20 < p_{\mathrm{T,ch.jet}} < 40$ and $40 < p_{\mathrm{T,ch.jet}} < 80$ GeV/c. The momentum threshold of leading particle in a jet $9 < p_{\mathrm{T}}^{leading part.}$ GeV/c.

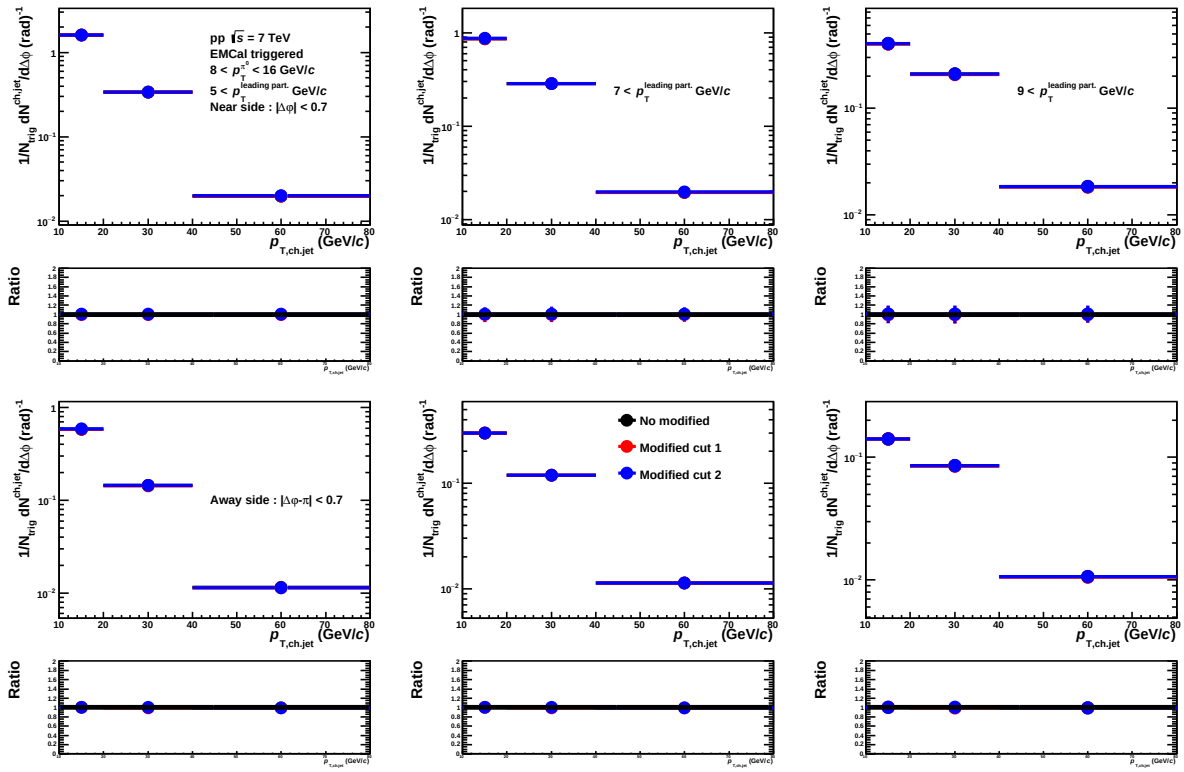

Fig. 5.1.7: Comparison of the three kinds of shower shape cuts of near (top) and away (bottom) jet yields and its ratio in pp collisions with the momentum range of trigger π^0 $8 < p_{\mathrm{T}}^{\pi^0} < 16$ GeV/c. The momentum threshold of leading particle in a jet 5(left), 7(center), 9(right) $< p_{\mathrm{T}}^{leading part.}$ GeV/c.

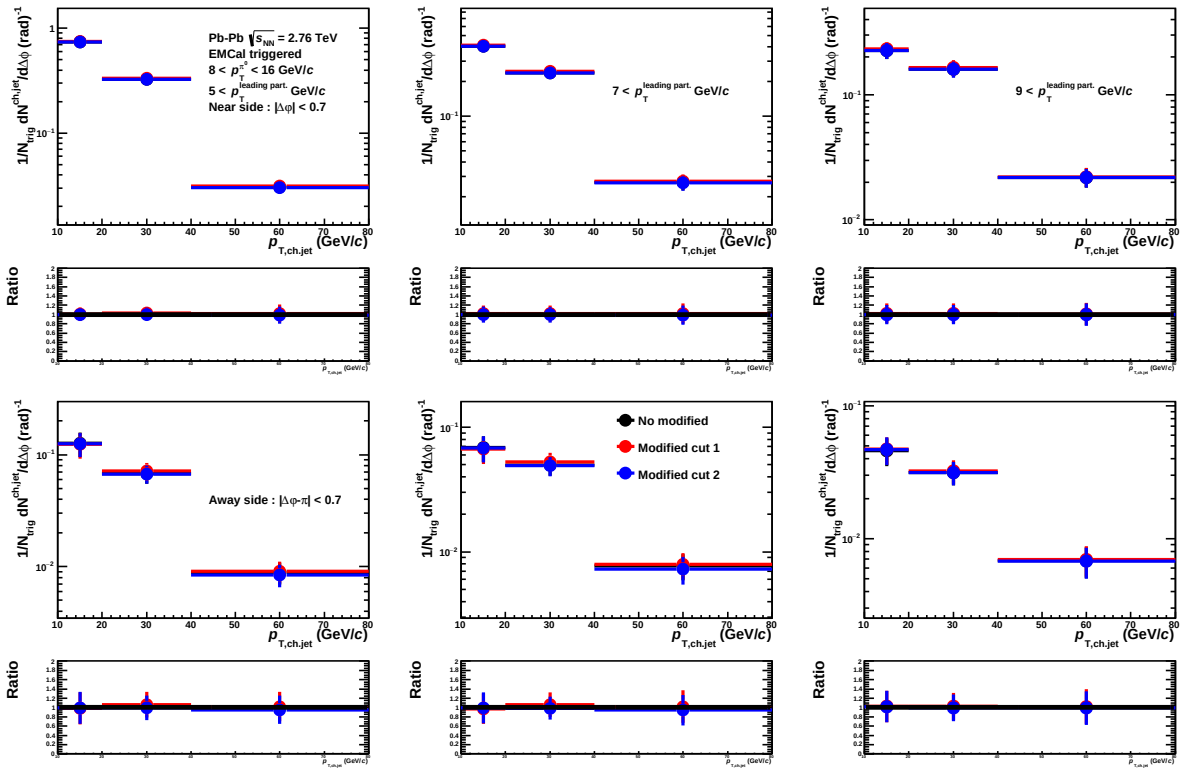

Fig. 5.1.8: Comparison of the three kinds of shower shape cuts of near (top) and away (bottom) jet yields and its ratio in Pb-Pb collisions with the momentum range of trigger π^0 $8 < p_{\mathrm{T}}^{\pi^0} < 16$ GeV/c. The momentum threshold of leading particle in a jet 5(left), 7(center), 9(right) $< p_{\mathrm{T}}^{leading part.}$ GeV/c.

5.2 Systematic uncertainty on invariant mass window

A 3 sigma invariant mass selection window was used in the analysis. In order to estimate the systematic uncertainty from invariant mass window, we compared 3 sigma with 2.5 sigma. Fig.5.2.1, 5.2.2 and 5.2.3 show the comparison of invariant mass cuts between 3 sigma and 2.5 sigma of azimuthal correlations in pp collisions with the momentum range of trigger π^0 $8 < p_{\mathrm{T}}^{\pi^0} < 16$ GeV/c, and Fig.5.2.4, 5.2.5 and 5.2.6 show the results in Pb-Pb collisions. The momentum ranges of associated jets increase with going to the right side. The uncertainties of azimuthal correlations are determined by the fitting of constant functions on the ratios. Fig.5.2.7, 5.2.8 show the comparison of the two kinds of invariant mass cuts between

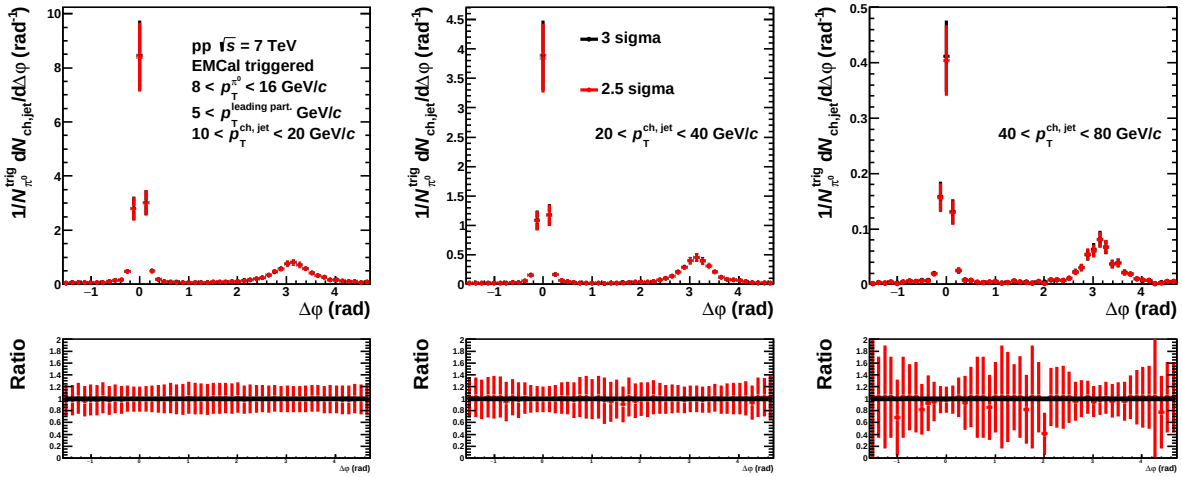

Fig. 5.2.1: Comparison of the two kinds of invariant mass (black:3 sigma, red:2.5 sigma) cuts of azimuthal correlations (top) and its ratios (bottom) in pp collisions with the momentum range of trigger π^0 $8 < p_{\mathrm{T}}^{\pi^0} < 16$ GeV/c and associated jets $10 < p_{\mathrm{T,ch.jet}} < 20$, $20 < p_{\mathrm{T,ch.jet}} < 40$ and $40 < p_{\mathrm{T,ch.jet}} < 80$ GeV/c. The momentum threshold of leading particle in a jet $5 < p_{\mathrm{T}}^{leading part.}$ GeV/c.

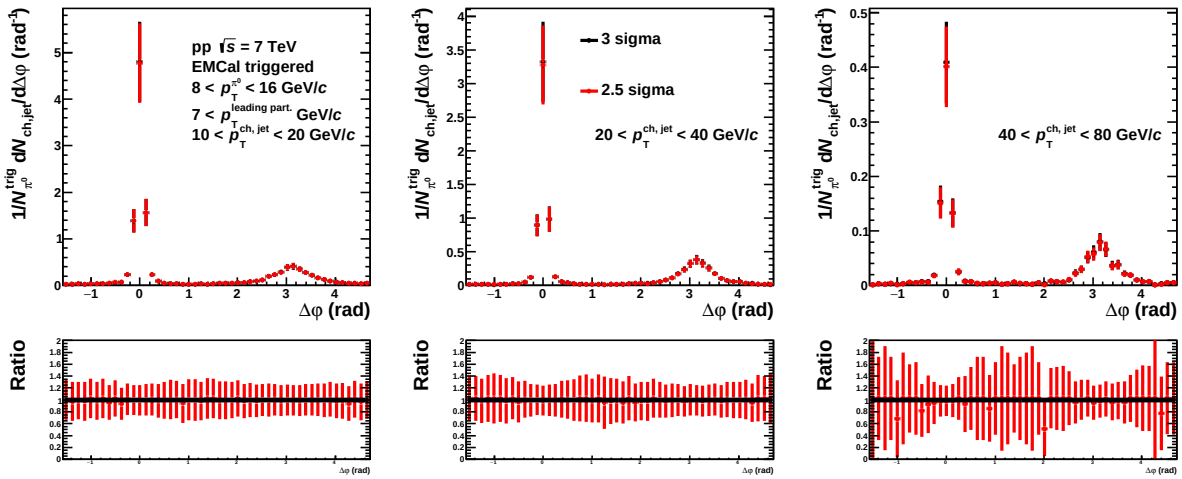

Fig. 5.2.2: Comparison of the two kinds of invariant mass (black:3 sigma, red:2.5 sigma) cuts of azimuthal correlations (top) and its ratios (bottom) in pp collisions with the momentum range of trigger π^0 $8 < p_{\mathrm{T}}^{\pi^0} < 16$ GeV/c and associated jets $10 < p_{\mathrm{T,ch.jet}} < 20$, $20 < p_{\mathrm{T,ch.jet}} < 40$ and $40 < p_{\mathrm{T,ch.jet}} < 80$ GeV/c. The momentum threshold of leading particle in a jet $7 < p_{\mathrm{T}}^{leading part.}$ GeV/c.

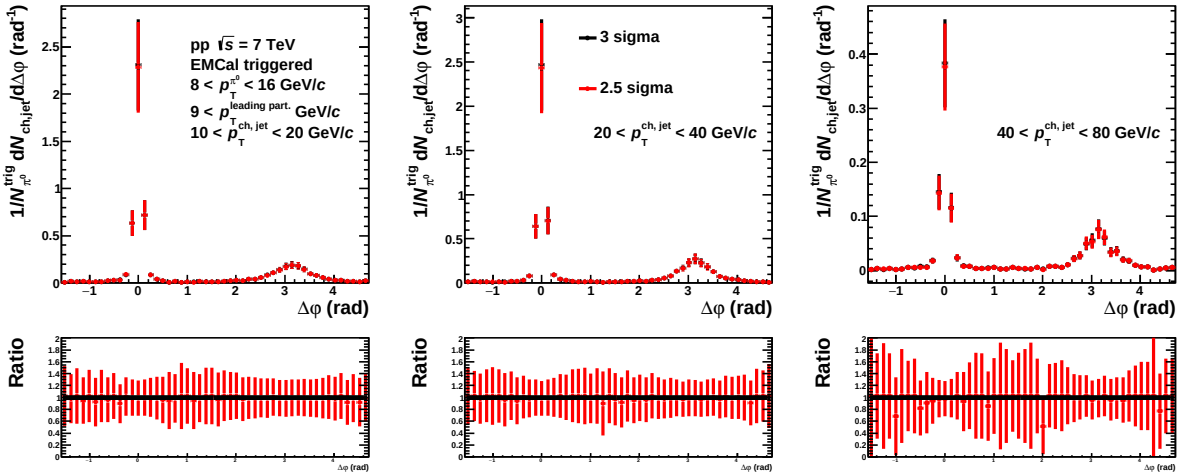

Fig. 5.2.3: Comparison of the two kinds of invariant mass (black:3 sigma, red:2.5 sigma) cuts of azimuthal correlations (top) and its ratios (bottom) in pp collisions with the momentum range of trigger π^0 $8 < p_{\mathrm{T}}^{\pi^0} < 16$ GeV/c and associated jets $10 < p_{\mathrm{T,ch.jet}} < 20$, $20 < p_{\mathrm{T,ch.jet}} < 40$ and $40 < p_{\mathrm{T,ch.jet}} < 80$ GeV/c. The momentum threshold of leading particle in a jet $9 < p_{\mathrm{T}}^{leadingpart.}$ GeV/c.

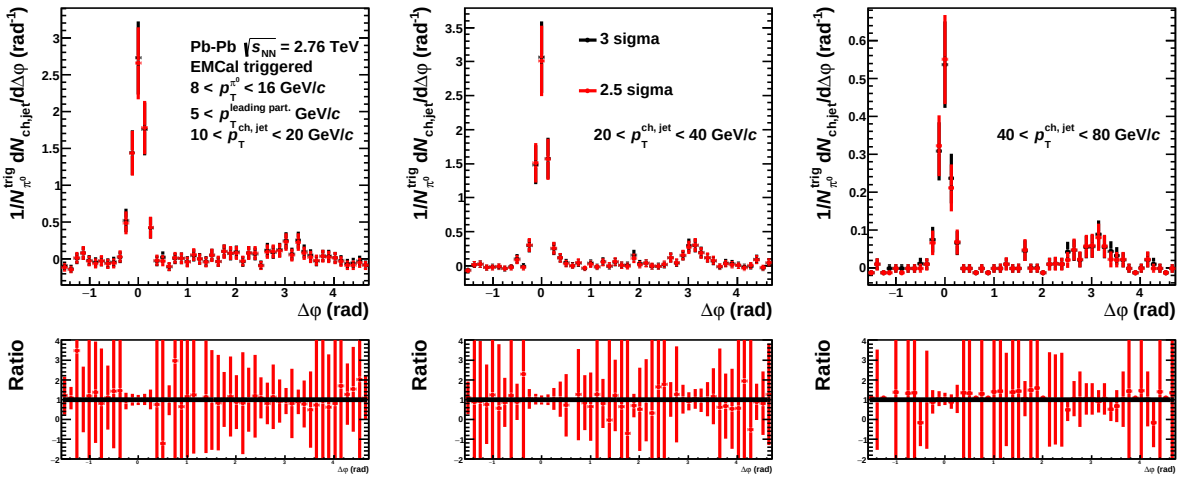

Fig. 5.2.4: Comparison of the two kinds of invariant mass cuts (black:3 sigma, red:2.5 sigma) of azimuthal correlations (top) and its ratios (bottom) in Pb-Pb collisions with the momentum range of trigger π^0 $8 < p_{\mathrm{T}}^{\pi^0} < 16$ GeV/c and associated jets $10 < p_{\mathrm{T,ch.jet}} < 20$, $20 < p_{\mathrm{T,ch.jet}} < 40$ and $40 < p_{\mathrm{T,ch.jet}} < 80$ GeV/c. The momentum threshold of leading particle in a jet $5 < p_{\mathrm{T}}^{leadingpart.}$ GeV/c.

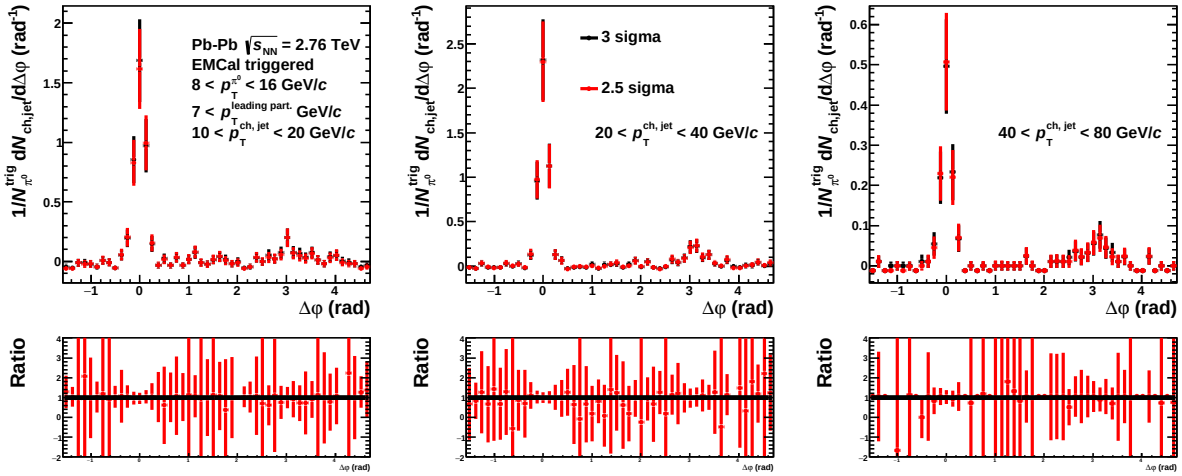

Fig. 5.2.5: Comparison of the two kinds of invariant mass cuts (black:3 sigma, red:2.5 sigma) of azimuthal correlations (top) and its ratios (bottom) in Pb-Pb collisions with the momentum range of trigger π^0 $8 < p_{\mathrm{T}}^{\pi^0} < 16$ GeV/c and associated jets $10 < p_{\mathrm{T,ch.jet}} < 20$, $20 < p_{\mathrm{T,ch.jet}} < 40$ and $40 < p_{\mathrm{T,ch.jet}} < 80$ GeV/c. The momentum threshold of leading particle in a jet $7 < p_{\mathrm{T}}^{leading part.}$ GeV/c.

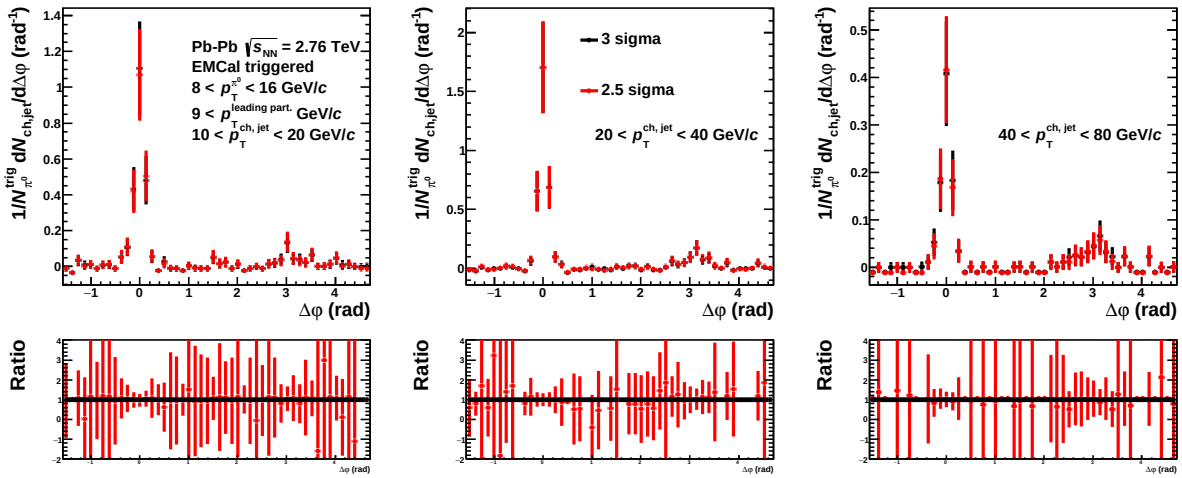

Fig. 5.2.6: Comparison of the two kinds of invariant mass cuts (black:3 sigma, red:2.5 sigma) of azimuthal correlations (top) and its ratios (bottom) in Pb-Pb collisions with the momentum range of trigger π^0 $8 < p_{\mathrm{T}}^{\pi^0} < 16$ GeV/c and associated jets $10 < p_{\mathrm{T,ch.jet}} < 20$, $20 < p_{\mathrm{T,ch.jet}} < 40$ and $40 < p_{\mathrm{T,ch.jet}} < 80$ GeV/c. The momentum threshold of leading particle in a jet $9 < p_{\mathrm{T}}^{leading part.}$ GeV/c.

3 sigma and 2.5 sigma of near and away side jet yields in pp and Pb-Pb collisions wiht the momentum range of trigger π^0 $8 < p_{\mathrm{T}}^{\pi^0} < 16$ GeV/c.

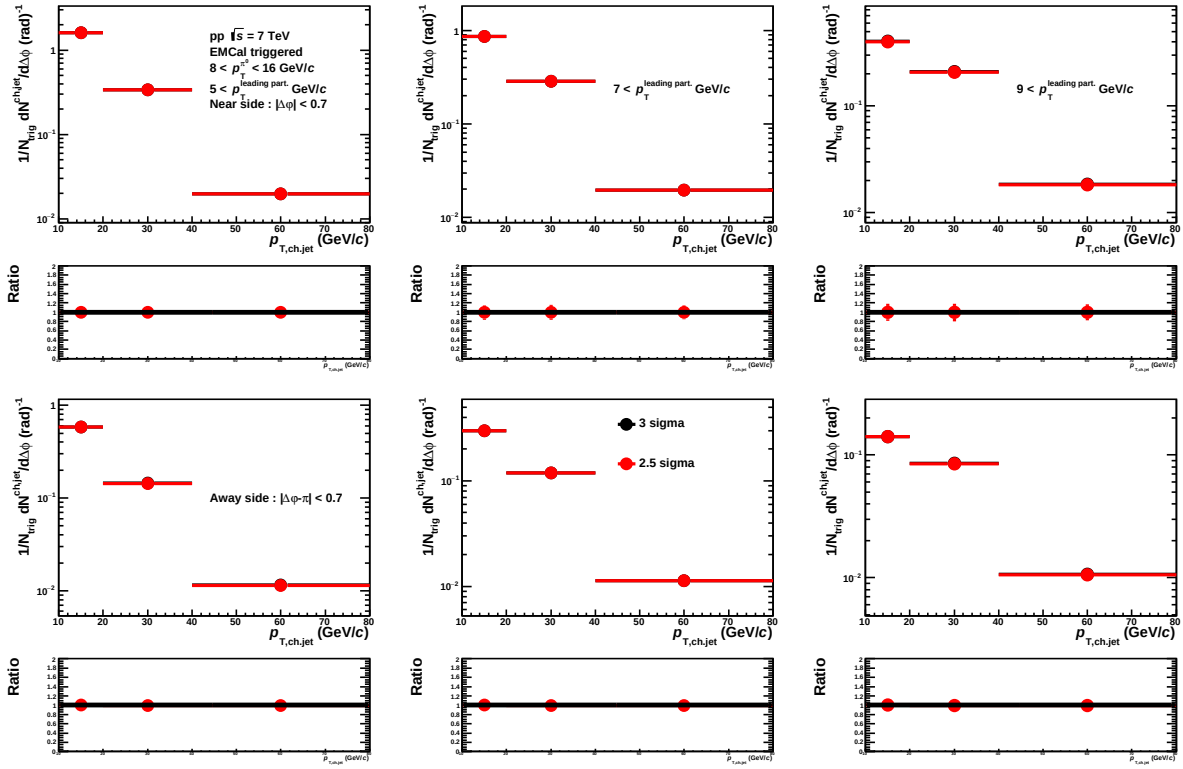

Fig. 5.2.7: Comparison of the two kinds of invariant mass cuts (black:3 sigma, red:2.5 sigma) of near (top) and away (bottom) jet yields and its ratio in pp collisions with the momentum range of trigger π^0 $8 < p_{\mathrm{T}}^{\pi^0} < 16$ GeV/c. The momentum threshold of leading particle in a jet 5(left), 7(center), 9(right) $< p_{\mathrm{T}}^{leadingpart.}$ GeV/c.

5.3 π^0 identification purity

The π^0 identification purity in the cluster splitting method is high, 90 % in pp collisions, 85 % in Pb-Pb collisions. In the π^0-charged hadron analysis in the ALICE experiment, in order to estimate the effect of the π^0 identification purity, a simple ratio of reconstructed candidate π^0-hadron correlations to true π^0-hadron correlations is calculated with generated p_{T} and named pair purity. The pair purity can be given by the following,

$$pair\ purity = \frac{reconstructed\ \pi^0(MC\ matched) - jet(Gen.p_T)}{reconstructed\ \pi^0 - jet(Gen.p_T)} \tag{5.3.1}$$

Fig.5.3.1, 5.3.2 show the pair purity as a function of $\Delta\varphi$ in pp and Pb-Pb collisions of Monte Calro simulation with the two momentum bins of trigger π^0 and associated charged hadron. These results indicate that the effect of π^0 identification purity is very small (few percent) in both collisions systems. Thus, in this analysis, we add 10 % uncertainty in the systematic uncertainties as the effect of π^0 identification purity in pp and Pb-Pb collisions.

5.4 Flat background subtraction method in azimuthal correlation

The flat background comes from combinatorial pairs in Pb-Pb collisions increases with going to the low momentum region and depends on the calculation method due to large statistical fluctuation in this

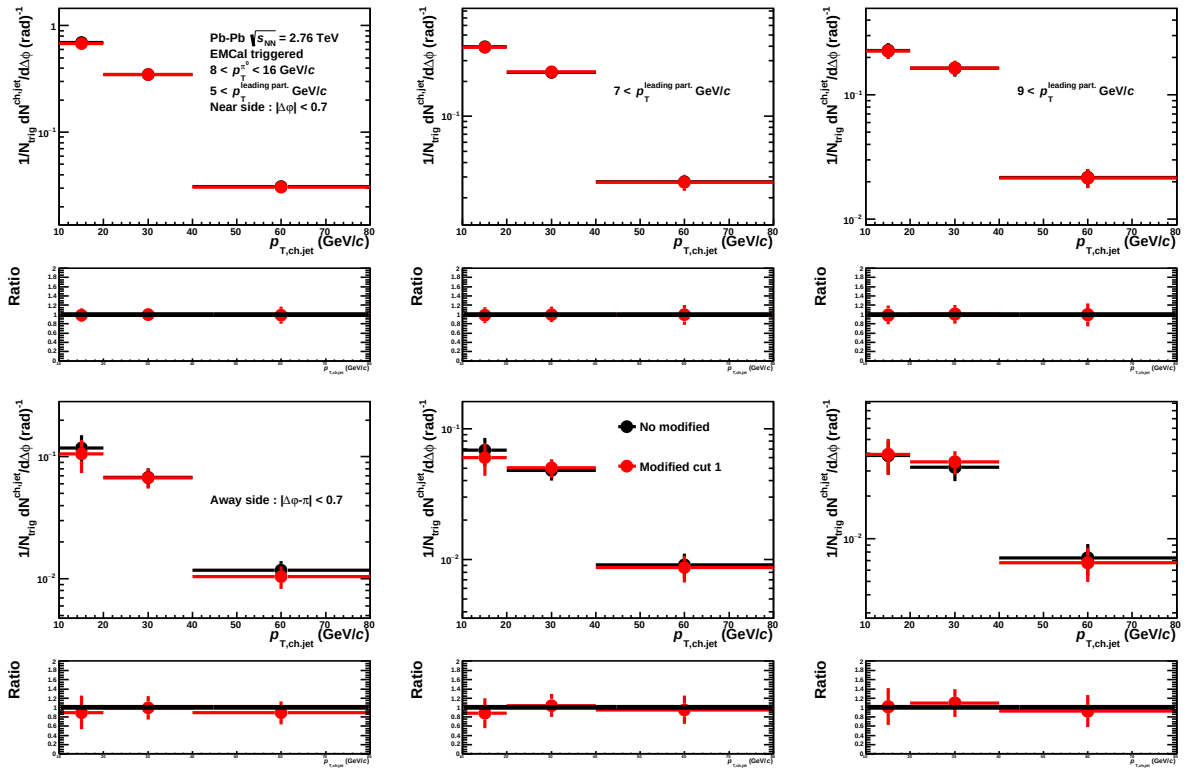

Fig. 5.2.8: Comparison of the two kinds of invariant mass cuts (black:3 sigma, red:2.5 sigma) of near (top) and away (bottom) jet yields and its ratio in Pb-Pb collisions with the momentum range of trigger π^0 $8 < p_{\mathrm{T}}^{\pi^0} < 16$ GeV/c. The momentum threshold of leading particle in a jet 5(left), 7(center), 9(right) $< p_{\mathrm{T}}^{leadingpart.}$ GeV/c.

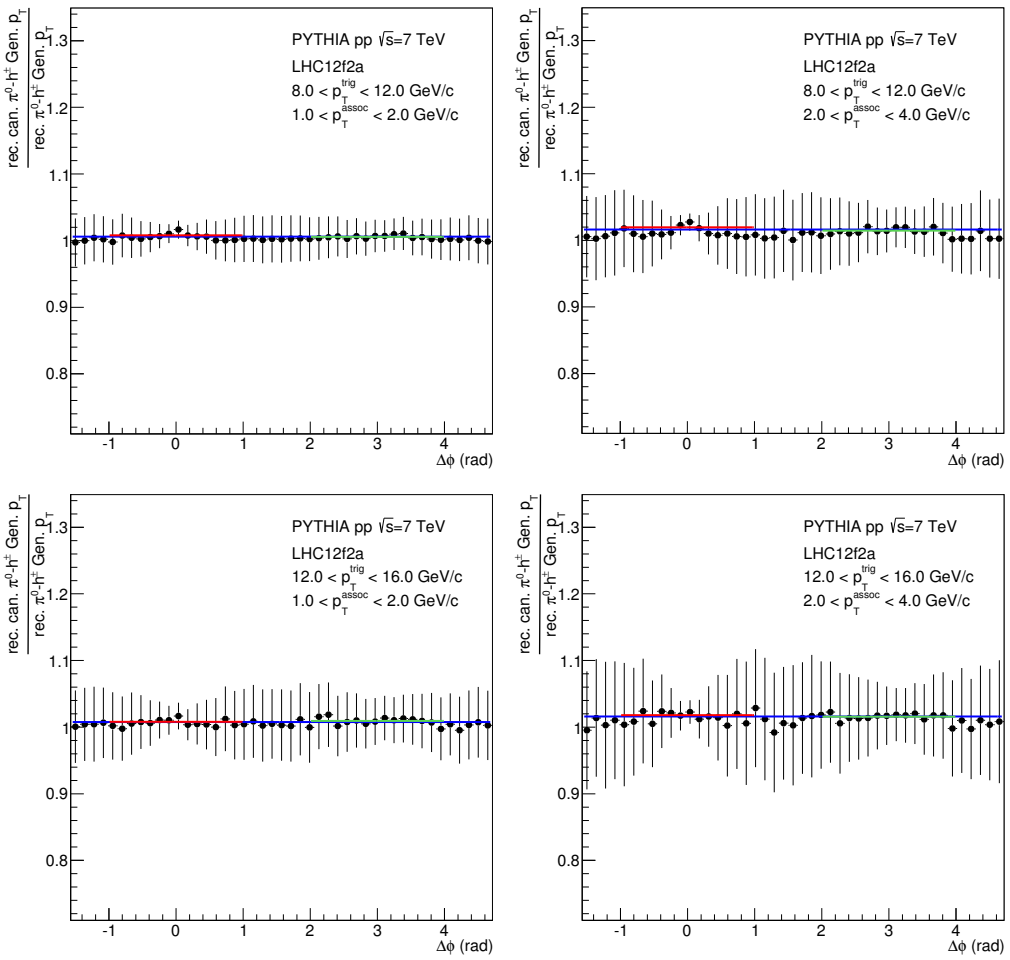

Fig. 5.3.1: Pair purity as a function of $\Delta\varphi$ in pp collisions of Monte Calro simulation with the momentum range of trigger π^0 $8 < p_{\mathrm{T}}^{\pi^0} < 12$ and $12 < p_{\mathrm{T}}^{\pi^0} < 16$ GeV/c, and associated hadron $1.0 < p_{\mathrm{T}}^{assoc} < 2.0$ and $2.0 < p_{\mathrm{T}}^{assoc} < 4.0$ GeV/c[**?**]

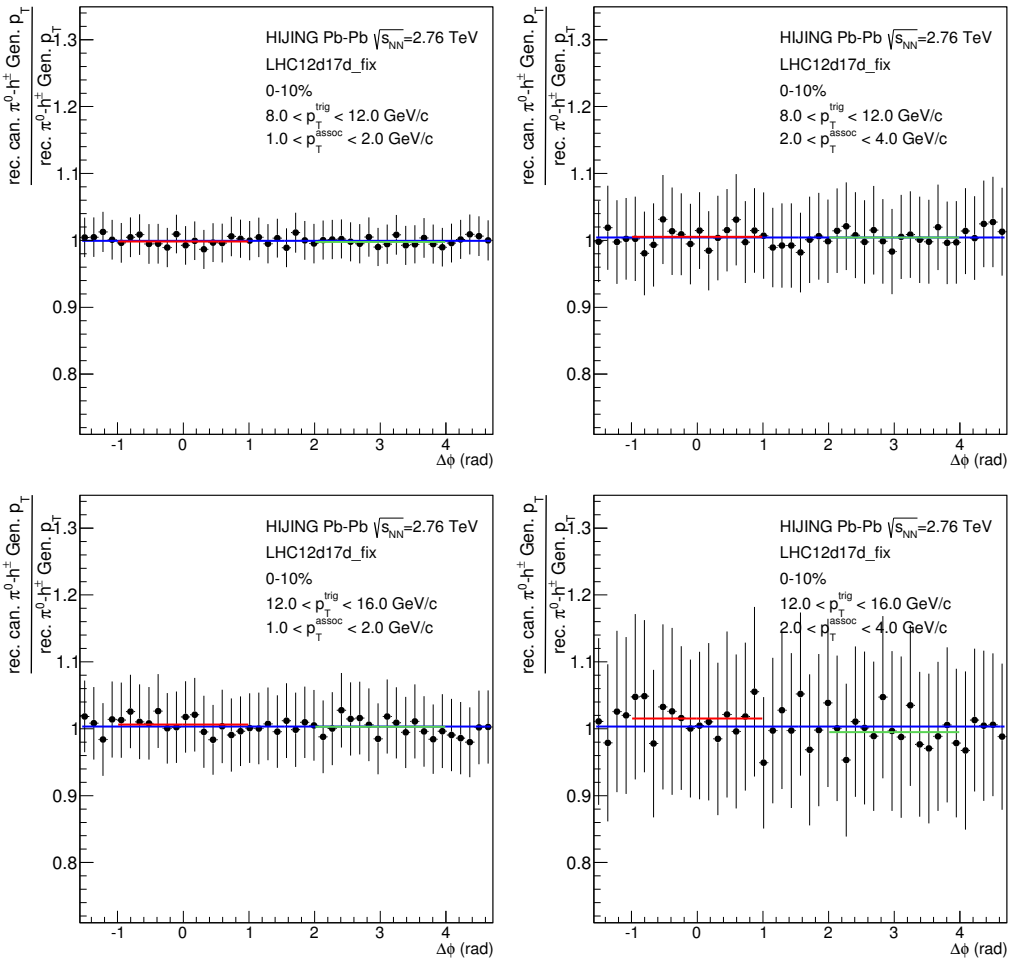

Fig. 5.3.2: Pair purity as a function of $\Delta\varphi$ in Pb-Pb collisions of Monte Calro simulation with the momentum range of trigger π^0 $8 < p_{\mathrm{T}}^{\pi^0} < 12$ and $12 < p_{\mathrm{T}}^{\pi^0} < 16$ GeV/c, and associated hadron $1.0 < p_{\mathrm{T}}^{assoc} < 2.0$ and $2.0 < p_{\mathrm{T}}^{assoc} < 4.0$ GeV/c[**?**].

analysis. This analysis add the differences of the three methods for flat background estimation in the systematic uncertainties:

1. Take 4 bins in the valley region on the left and right side from a near side peak region (as mentioned in the previous section)
2. Constant fit in $1 < |\Delta\varphi| < \pi/2$
3. Average value of the eight smallest points in full $|\Delta\varphi|$ range.

Fig.5.4.1, 5.4.2 and 5.4.3 show the comparison of the three kinds of flat background subtraction methods of azimuthal correlations and its ratios in Pb-Pb collisions with the momentum range of trigger π^0 8 $< p_{\mathrm{T}}^{\pi^0} <$ 16 GeV/c and thresholds of leading particle in a jet 5, 7 and 9 $< p_{\mathrm{T}}^{leadingpart.}$ GeV/c. Fig.5.4.4 shows the comparison of near and away side jet yields. The ratios of the bottom small figure are added in the systematic uncertainties.

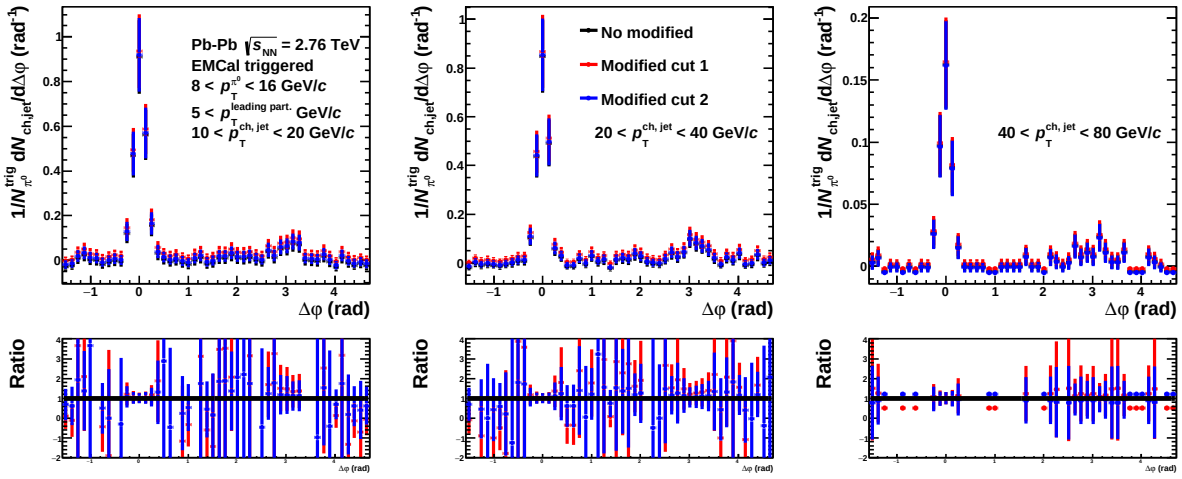

Fig. 5.4.1: Comparison of the three kinds of flat background subtraction methods of azimuthal correlations (top) and its ratios (bottom) in Pb-Pb collisions with the momentum range of trigger π^0 8 $< p_{\mathrm{T}}^{\pi^0} <$ 16 GeV/c and associated jets $10 < p_{\mathrm{T,ch.jet}} < 20$, $20 < p_{\mathrm{T,ch.jet}} < 40$ and $40 < p_{\mathrm{T,ch.jet}} < 80$ GeV/c. The momentum threshold of leading particle in a jet $5 < p_{\mathrm{T}}^{leadingpart.}$ GeV/c.

5.5 Unfolding algorithm

We consider the difference between the two unfolding methods, SVD and Bayesian. Fig.5.5.1, 5.5.2 show the comparison of the two kinds of unfolding algorithm of near (top) and away (bottom) side jet yields in pp and Pb-Pb collisions with the momentum range of trigger π^0 8 $< p_{\mathrm{T}}^{\pi^0} <$ 16 GeV/c. The momentum thresholds of leading particle in a jet increase with going to the right side. The ratios of the bottom small figures are added in the systematic uncertainties.

5.6 Total systematic uncertainty

The total systematic uncertainties of this analysis are calculated by using quadrature sum method. Written as:

$$Total\ systematic\ error = \sqrt{\mathrm{E_{M02}}^2 + \mathrm{E_{IM}}^2 + \mathrm{E_{pair\,purity}}^2 + \mathrm{E^2_{pair\,resolution}} + \mathrm{E_{Flat}}^2 + \mathrm{E_{Unfold}}^2} \qquad (5.6.1)$$

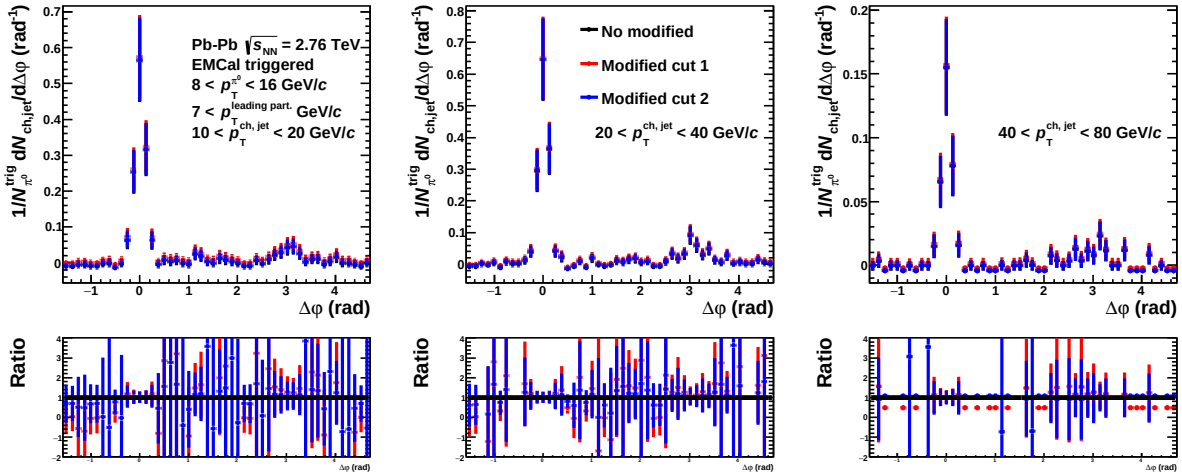

Fig. 5.4.2: Comparison of the three kinds of flat background subtraction methods of azimuthal correlations (top) and its ratios (bottom) in Pb-Pb collisions with the momentum range of trigger π^0 $8 < p_{\mathrm{T}}^{\pi^0} < 16$ GeV/c and associated jets $10 < p_{\mathrm{T,ch.jet}} < 20$, $20 < p_{\mathrm{T,ch.jet}} < 40$ and $40 < p_{\mathrm{T,ch.jet}} < 80$ GeV/c. The momentum threshold of leading particle in a jet $7 < p_{\mathrm{T}}^{leadingpart.}$ GeV/c.

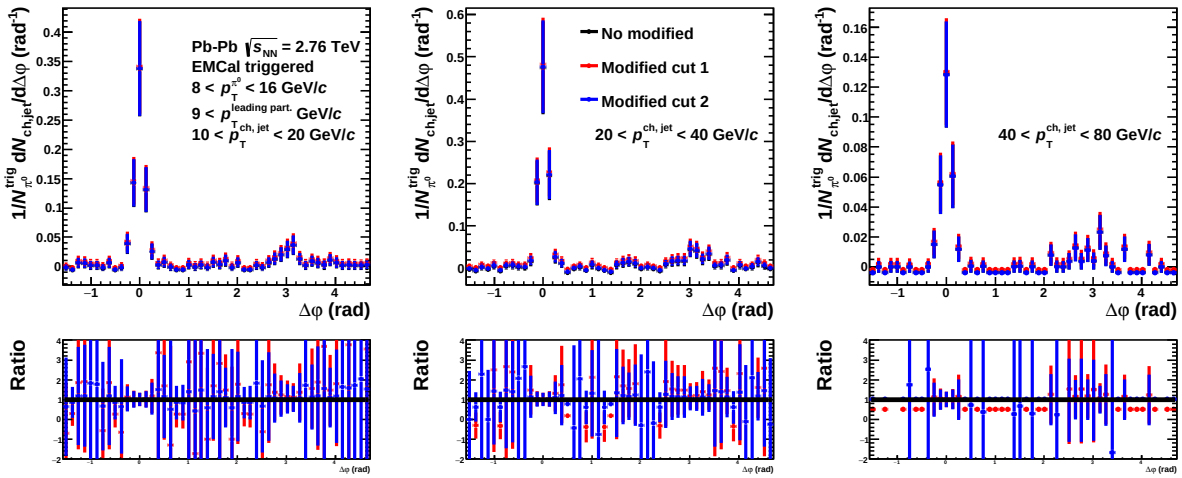

Fig. 5.4.3: Comparison of the three kinds of flat background subtraction methods of azimuthal correlations (top) and its ratios (bottom) in Pb-Pb collisions with the momentum range of trigger π^0 $8 < p_{\mathrm{T}}^{\pi^0} < 16$ GeV/c and associated jets $10 < p_{\mathrm{T,ch.jet}} < 20$, $20 < p_{\mathrm{T,ch.jet}} < 40$ and $40 < p_{\mathrm{T,ch.jet}} < 80$ GeV/c. The momentum threshold of leading particle in a jet $9 < p_{\mathrm{T}}^{leadingpart.}$ GeV/c.

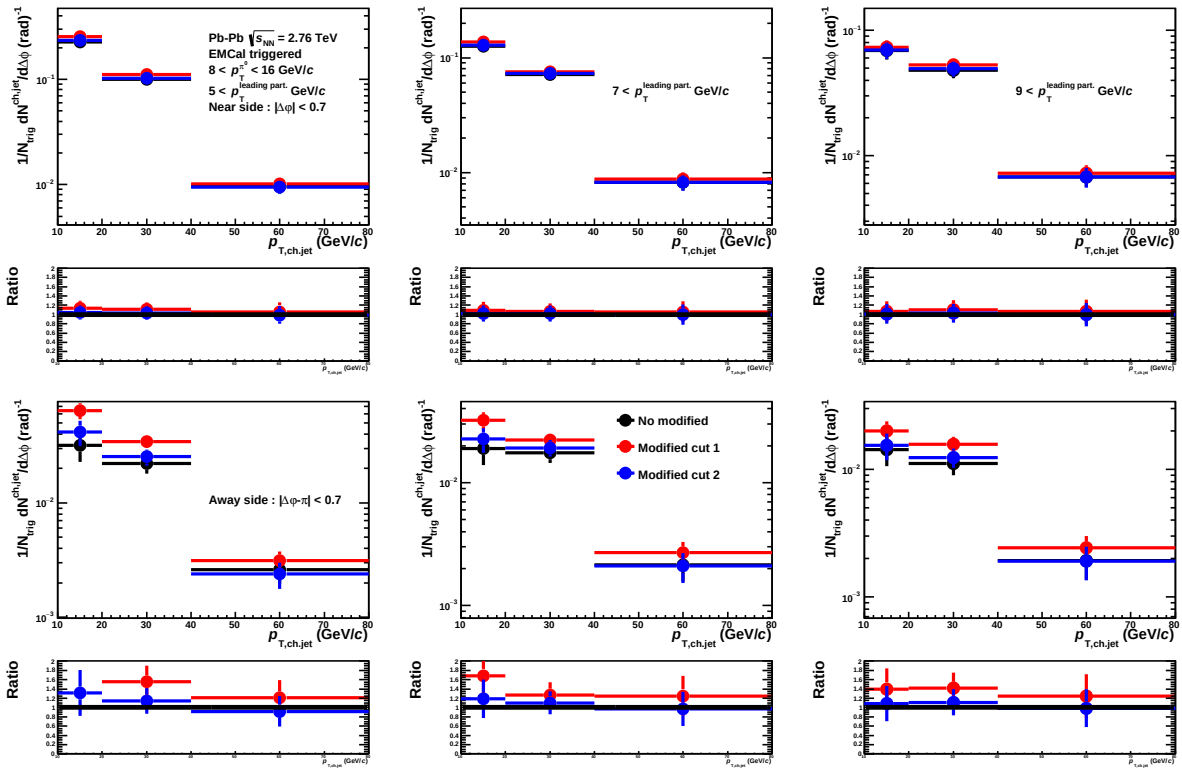

Fig. 5.4.4: Comparison of the three kinds of flat background subtraction methods of near (top) and away (bottom) jet yields and its ratio in Pb-Pb collisions with the momentum range of trigger π^0 $8 < p_{\mathrm{T}}^{\pi^0} < 16$ GeV/c. The momentum threshold of leading particle in a jet 5(left), 7(center), 9(right) $< p_{\mathrm{T}}^{leading part.}$ GeV/c.

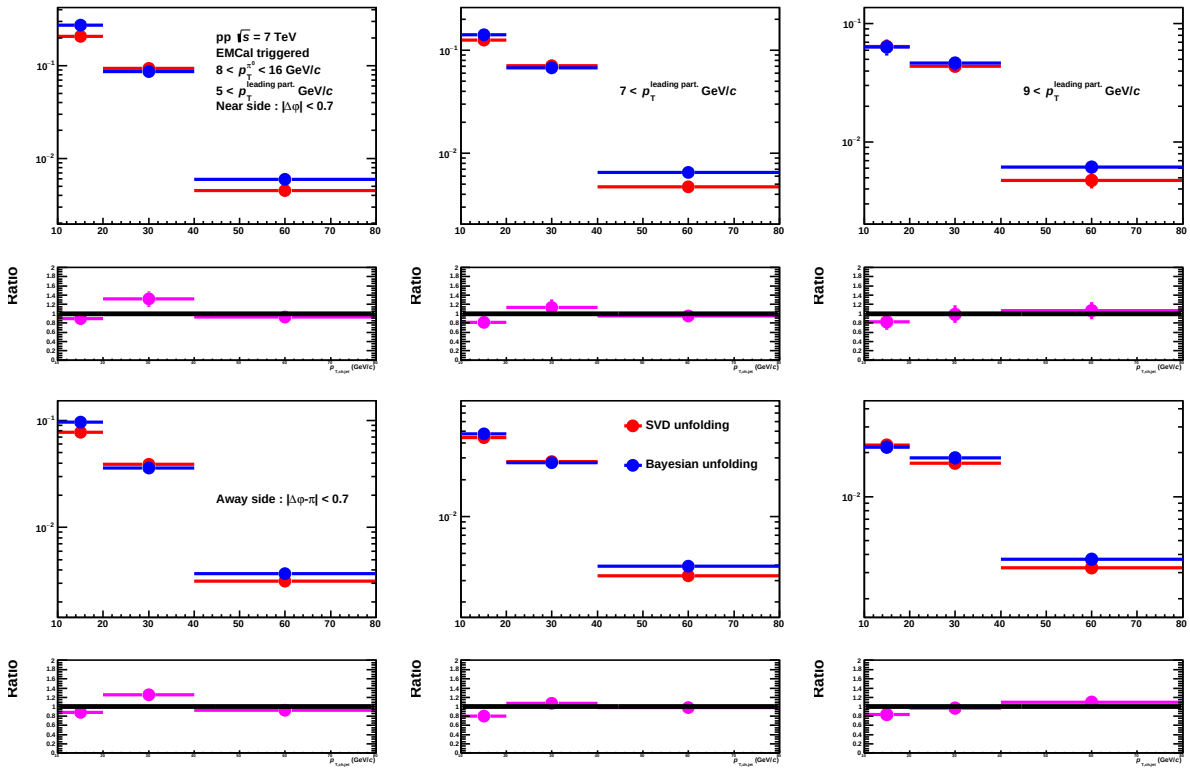

Fig. 5.5.1: Comparison of the two kinds of unfolding algorithm (SVD (red) and Bayesian (blue) unfolding) of near (top) and away (bottom) side jet yields in pp collisions with the momentum range of trigger π^0 $8 < p_{\mathrm{T}}^{\pi^0} < 16$ GeV/c. The momentum thresholds of leading particle in a jet 5(left), 7(center), 9(right) $< p_{\mathrm{T}}^{leading part.}$ GeV/c. The bottom small figures show the ratio of the jet yields of the two kinds of unfolding algorithm.

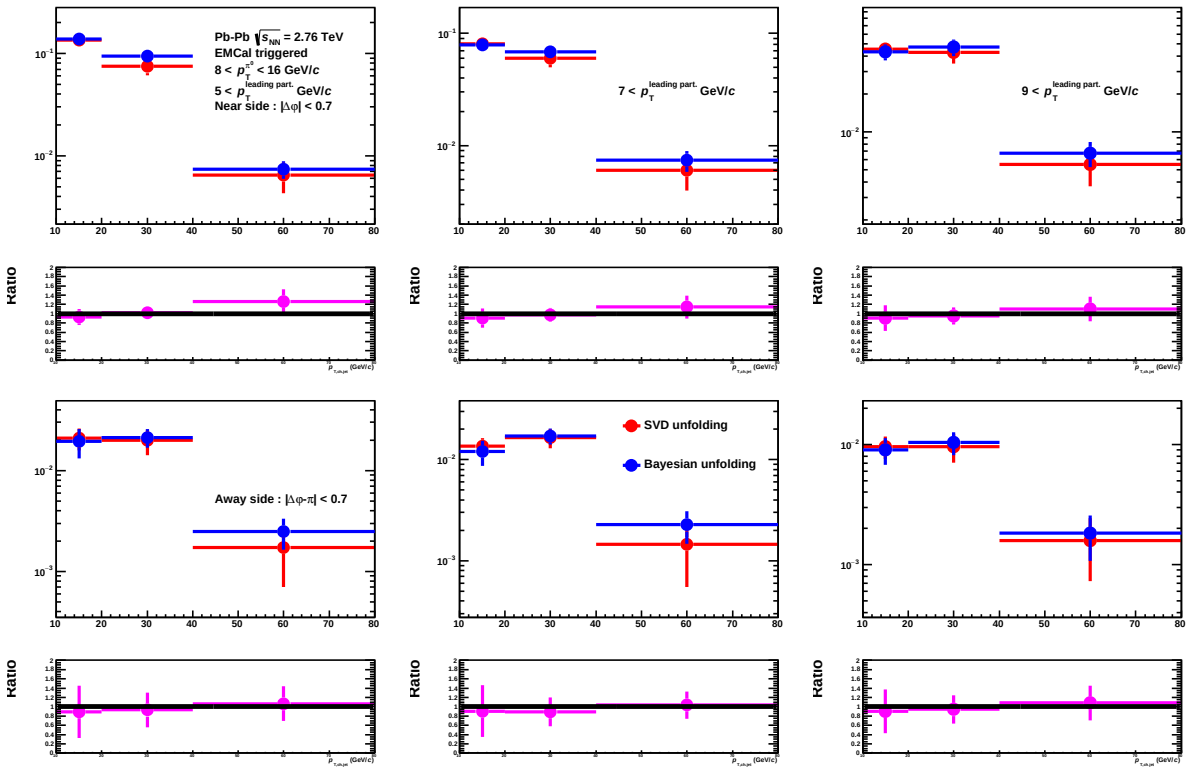

Fig. 5.5.2: Comparison of the two kinds of unfolding algorithm (SVD (red) and Bayesian (blue) unfolding) of near (top) and away (bottom) side jet yields in Pb-Pb collisions with the momentum range of trigger π^0 $8 < p_{\mathrm{T}}^{\pi^0} < 16$ GeV/c. The momentum thresholds of leading particle in a jet 5(left), 7(center), 9(right) $< p_{\mathrm{T}}^{leadingpart.}$ GeV/c. The bottom small figures show the ratio of the jet yields of the two kinds of unfolding algorithm.

Fig.5.6.1, 5.6.2 show the systematic uncertainties as a function of jet $p_{\mathrm{T,ch.jet}}$ for azimuthal correlations in pp and Pb-Pb collisions with the momentum range of trigger π^0 $8 < p_{\mathrm{T}}^{\pi^0} < 16$ GeV/c. Fig.5.6.3, 5.6.4 show the systematic uncertainties as a function of jet $p_{\mathrm{T,ch.jet}}$ for near and away side jet yields in pp and Pb-Pb collisions with the momentum range of trigger π^0 $8 < p_{\mathrm{T}}^{\pi^0} < 16$ GeV/c. Fig.5.6.5, 5.6.6 show the systematic uncertainties as a function of jet $p_{\mathrm{T,ch.jet}}$ for near and away side Widths in pp and Pb-Pb collisions with the momentum range of trigger π^0 $8 < p_{\mathrm{T}}^{\pi^0} < 16$ GeV/c. Fig.5.6.7, 5.6.8 show the systematic uncertainties as a function of jet $p_{\mathrm{T,ch.jet}}$ for near and away side RMSs in pp and Pb-Pb collisions with the momentum range of trigger π^0 $8 < p_{\mathrm{T}}^{\pi^0} < 16$ GeV/c. Table.5.6.1 shows the

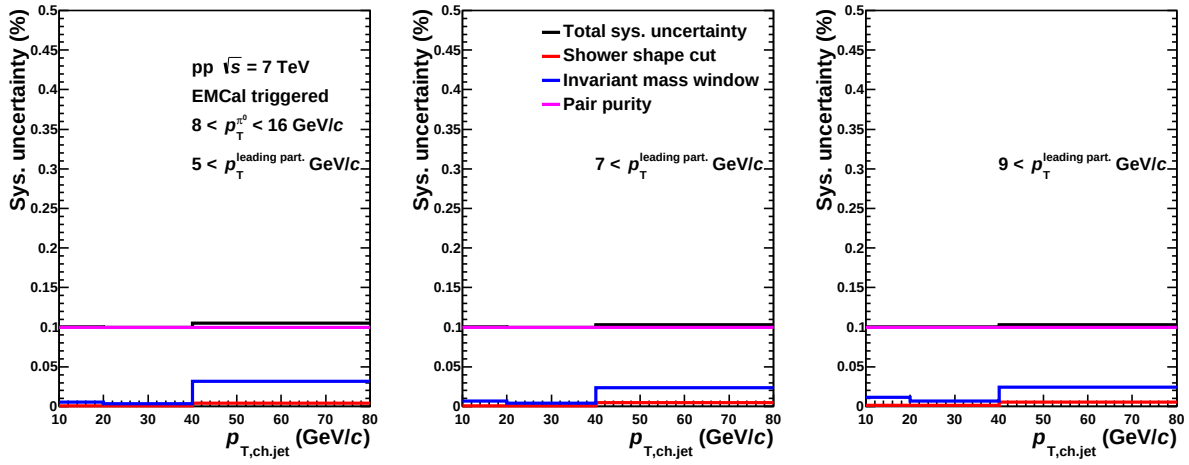

Fig. 5.6.1: The systematic uncertainties as a function of jet $p_{\mathrm{T,ch.jet}}$ for azimuthal correlations in pp collisions with the momentum range of trigger π^0 $8 < p_{\mathrm{T}}^{\pi^0} < 16$ GeV/c. The momentum thresholds of leading particle in a jet 5(left), 7(center), 9(right) $< p_{\mathrm{T}}^{leading part.}$ GeV/c.

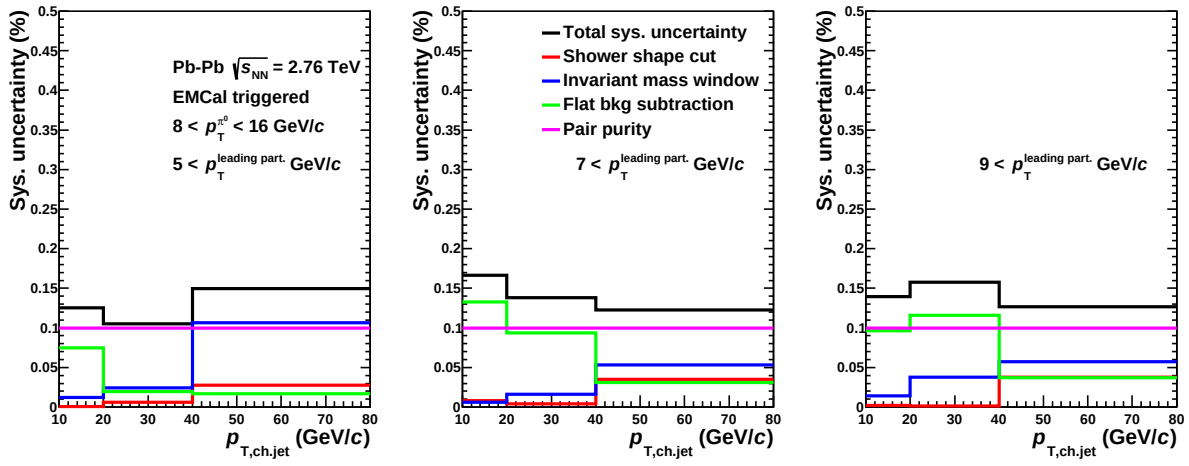

Fig. 5.6.2: The systematic uncertainties as a function of jet $p_{\mathrm{T,ch.jet}}$ for azimuthal correlations in Pb-Pb collisions with the momentum range of trigger π^0 $8 < p_{\mathrm{T}}^{\pi^0} < 16$ GeV/c. The momentum thresholds of leading particle in a jet 5(left), 7(center), 9(right) $< p_{\mathrm{T}}^{leading part.}$ GeV/c.

summary of systematic uncertainties.

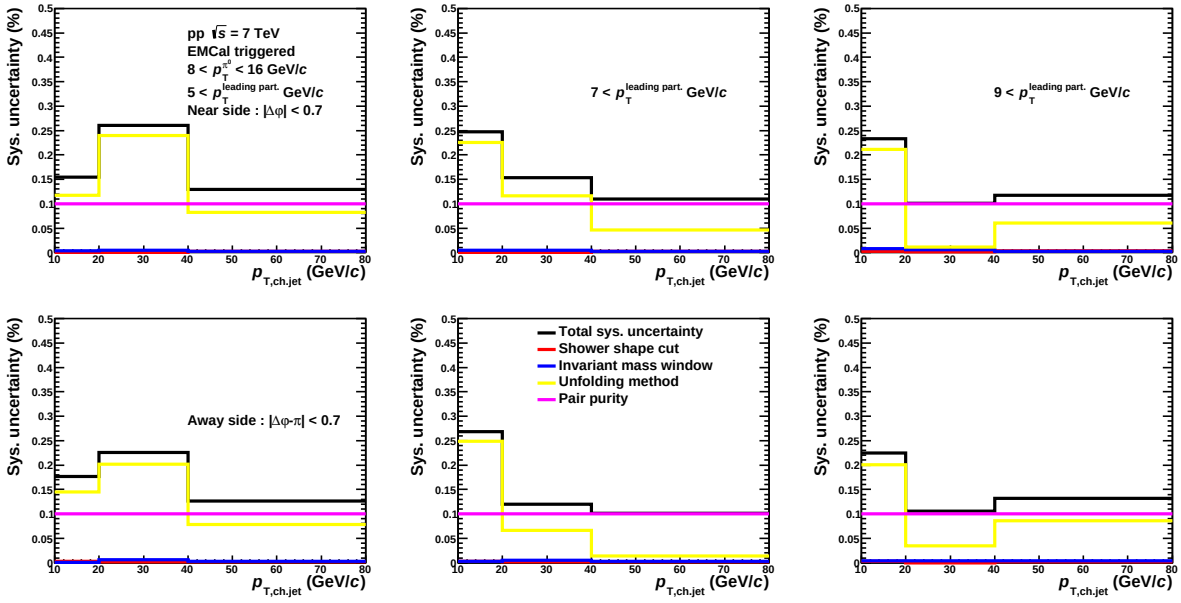

Fig. 5.6.3: The systematic uncertainties as a function of jet $p_{\mathrm{T,ch,jet}}$ for near (top) and away (bottom) side jet yields in pp collisions with the momentum range of trigger π^0 $8 < p_{\mathrm{T}}^{\pi^0} < 16$ GeV/c. The momentum thresholds of leading particle in a jet 5(left), 7(center), 9(right) $< p_{\mathrm{T}}^{leading part.}$ GeV/c.

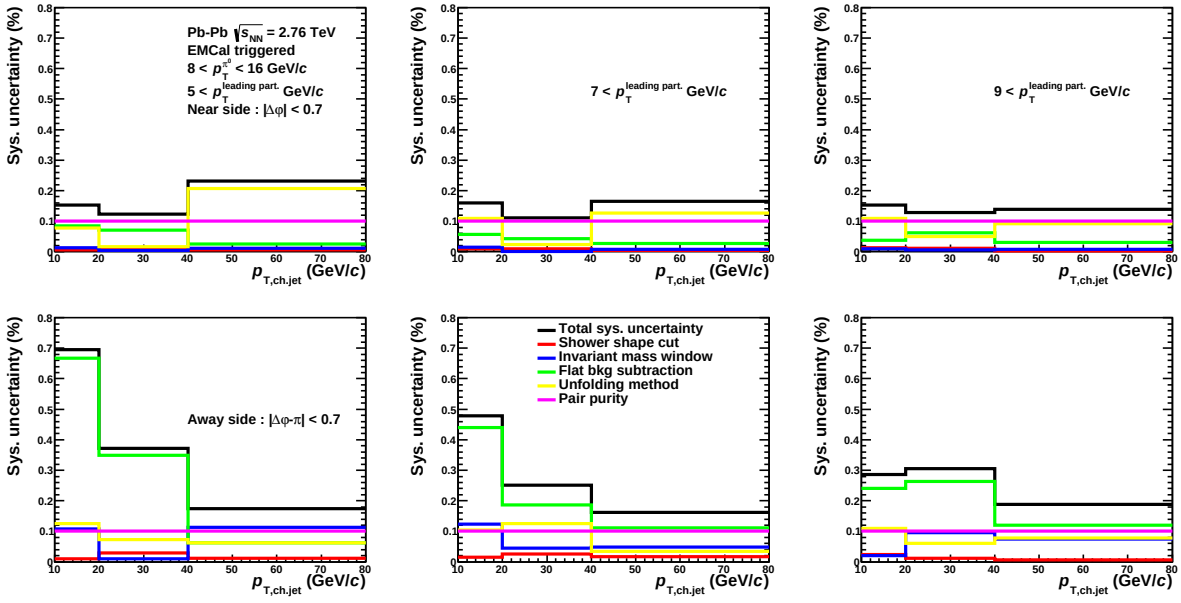

Fig. 5.6.4: The systematic uncertainties as a function of jet $p_{\mathrm{T,ch,jet}}$ for near (top) and away (bottom) side jet yields in PbPb collisions with the momentum range of trigger π^0 $8 < p_{\mathrm{T}}^{\pi^0} < 16$ GeV/c. The momentum thresholds of leading particle in a jet 5(left), 7(center), 9(right) $< p_{\mathrm{T}}^{leading part.}$ GeV/c.

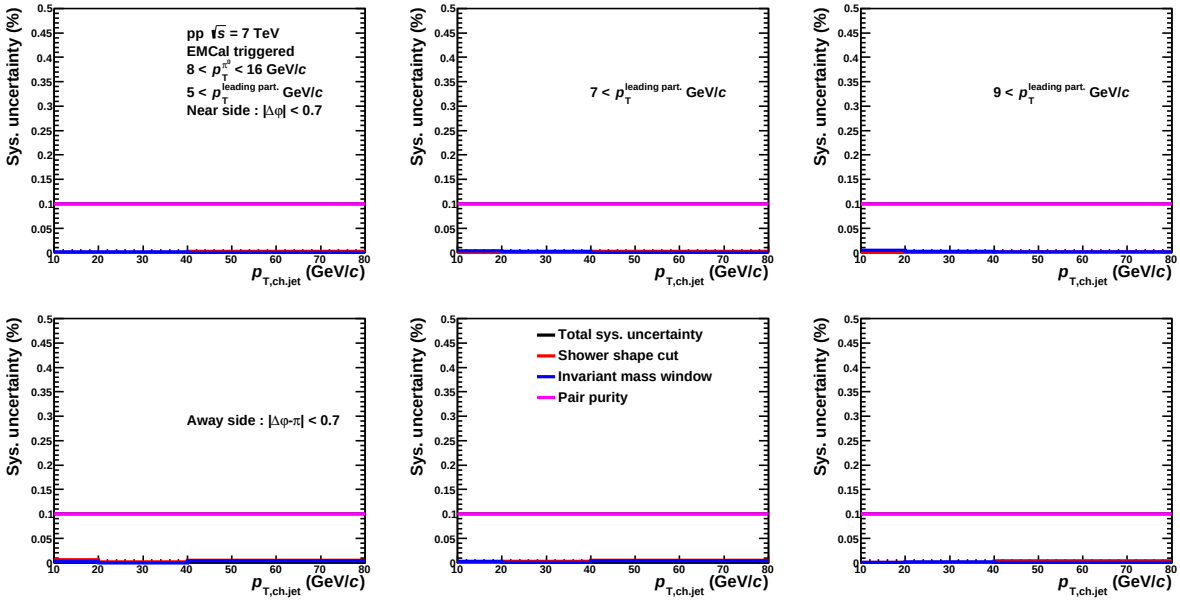

Fig. 5.6.5: The systematic uncertainties as a function of jet $p_{\mathrm{T,ch.jet}}$ for near (top) and away (bottom) side widths in pp collisions with the momentum range of trigger π^0 $8 < p_{\mathrm{T}}^{\pi^0} < 16$ GeV/c. The momentum thresholds of leading particle in a jet 5(left), 7(center), 9(right) $< p_{\mathrm{T}}^{leading part.}$ GeV/c.

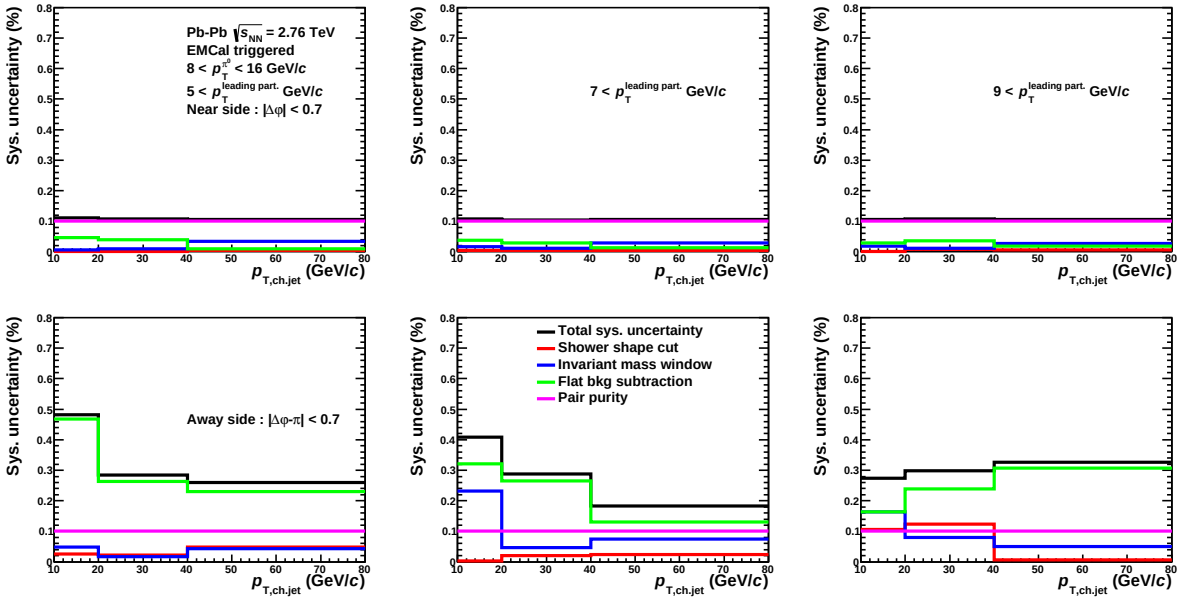

Fig. 5.6.6: The systematic uncertainties as a function of jet $p_{\mathrm{T,ch.jet}}$ for near (top) and away (bottom) side widths in Pb-Pb collisions with the momentum range of trigger π^0 $8 < p_{\mathrm{T}}^{\pi^0} < 16$ GeV/c. The momentum thresholds of leading particle in a jet 5(left), 7(center), 9(right) $< p_{\mathrm{T}}^{leading part.}$ GeV/c.

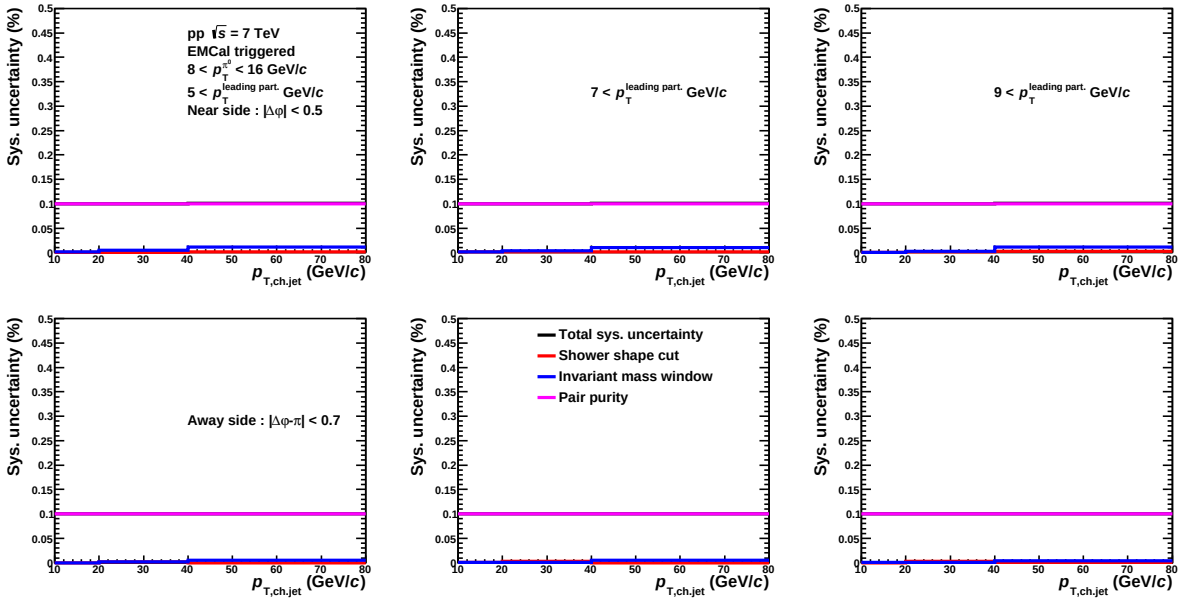

Fig. 5.6.7: The systematic uncertainties as a function of jet $p_{\mathrm{T,ch.jet}}$ for near (top) and away (bottom) side RMSs in pp collisions with the momentum range of trigger π^0 $8 < p_{\mathrm{T}}^{\pi^0} < 16$ GeV/c. The momentum thresholds of leading particle in a jet 5(left), 7(center), 9(right) $< p_{\mathrm{T}}^{leading part.}$ GeV/c.

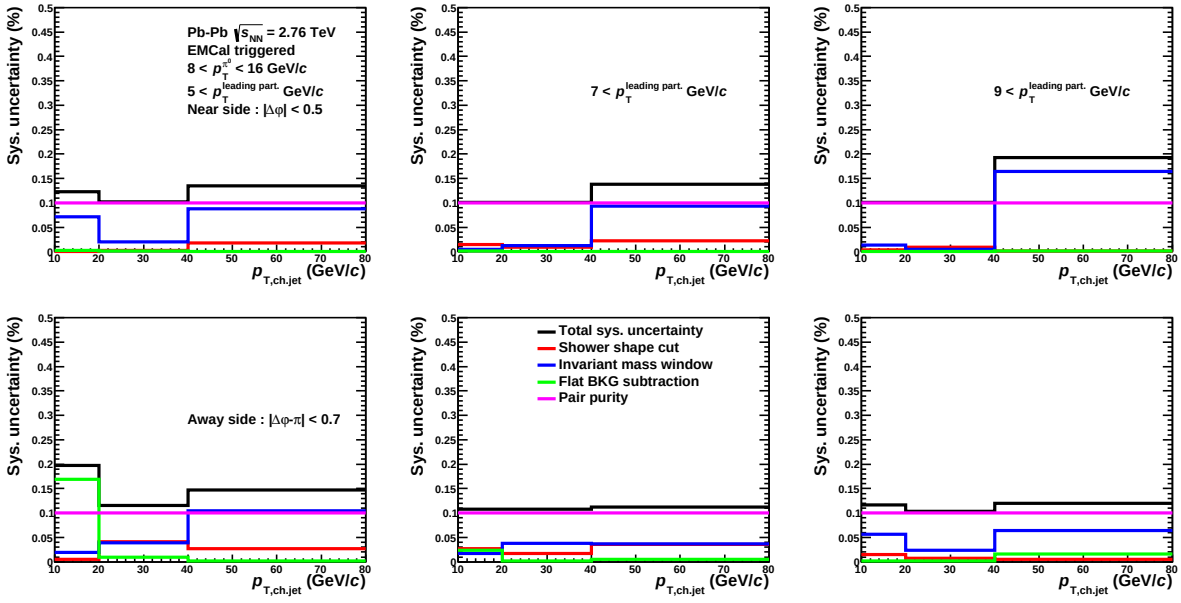

Fig. 5.6.8: The systematic uncertainties as a function of jet $p_{\mathrm{T,ch.jet}}$ for near (top) and away (bottom) side RMSs in Pb-Pb collisions with the momentum range of trigger π^0 $8 < p_{\mathrm{T}}^{\pi^0} < 16$ GeV/c. The momentum thresholds of leading particle in a jet 5(left), 7(center), 9(right) $< p_{\mathrm{T}}^{leading part.}$ GeV/c.

	pp collisions			Pb-Pb collisions		
source	azimuth	yield	width	azimuth	yield	width
Shower shape cut	$< 1\%$	$< 1\%$	$< 1\%$	$< 3\%$	$< 2\%$	$< 12\%$
Invariant mass cut	$< 3\%$	$< 1\%$	$< 1\%$	$< 11\%$	$< 11\%$	$< 14\%$
Flat background subtracktion	-	-	-	$< 13\%$	$< 67\%$	$< 48\%$
Pair purity	$< 10\%$	$< 10\%$	$< 10\%$	$< 10\%$	$< 10\%$	$< 10\%$
Unfolding method	-	$< 25\%$	-	-	$< 21\%$	-
Total	$< 11\%$	$< 26\%$	$< 10\%$	$< 16\%$	$< 70\%$	$< 48\%$

Table 5.6.1: Summary of systematic uncertainties.

Chapter 6

Results and Discussions

In this chapter, we show the results of π^0-jet correlations in pp collisions at $\sqrt{s} = 7$ TeV and Pb-Pb collisions at $\sqrt{s_{\rm NN}} = 2.76$ TeV. The $p_{\rm T}$ range of the π^0 trigger is $8.0 < p_{\rm T}^{\pi^0} < 16.0$ GeV/c, the $p_{\rm T}$ ranges of the associated jets are divided into three bins, the lowest bin of jet $p_{\rm T}$ range is $10 < p_{\rm T,ch.jet} < 20$ GeV/c, the following bin as $20 < p_{\rm T,ch.jet} < 40$ GeV/c and the highest bin as $40 < p_{\rm T,ch.jet} < 80$ GeV/c. We use the three different thresholds for the leading particle in a jet to produce the surface bias and avoid the effects of background fluctuation of jets, fake/combinatorial jets. The $p_{\rm T}$ thresholds for the leading particle in a jet are $p_{\rm T}^{\rm leading\,part.} > 5$, $p_{\rm T}^{\rm leading\,part.} > 7$ and $p_{\rm T}^{\rm leading\,part.} > 9$ GeV/c.

6.1 Azimuthal angle correlation between π^0 and jets

The measurements of azimuthal correlation is very important to find out whether the high $p_{\rm T}$ π^0 production is associated with the jet production. If the high $p_{\rm T}$ π^0 production is independent to the jet production, we can not produce the surface bias by triggering high $p_{\rm T}$ π^0.

Fig.6.1.1, 6.1.2 and 6.1.3 show the azimuthal correlations between the trigger π^0 and the associated jets in pp (top) and Pb-Pb (bottom) with the three $p_{\rm T}$ thresholds for the leading particle in a jet $p_{\rm T}^{\rm leading\,part.} >$ 5 GeV/c (Fig.6.1.1), $p_{\rm T}^{\rm leading\,part.} > 7$ GeV/c (Fig.6.1.2) and $p_{\rm T}^{\rm leading\,part.} > 9$ GeV/c (Fig.6.1.3). The jet-like peaks at both near and away-side in pp collisions and at near side in Pb-Pb collisions are observed, although barely see some away-side peak like structure in Pb-Pb. As shown in Fig.6.1.1, 6.1.2 and 6.1.3, we observe similar jet-like peak structures for all $p_{\rm T}$ ranges of the associated jets and thresholds of the leading particle in a jets. These results indicate that the high $p_{\rm T}$ π^0 production is associated with the jet production in the both collision systems, and then we can use π^0's as trigger particle to make the surface bias.

In Pb-Pb collisions, the peaks in away-side ($|\Delta\varphi - \pi| < 0.7$) are smaller and broader than pp collisions. As mentioned in Chapter 1, these results suggest that the path-length of the away-side jets is longer than the near-side jets due to the surface bias, and the jet yields are strongly suppressed.

6.2 Near and away-side jet yields

The near and away-side jet yields in pp and Pb-Pb collisions are extracted from Fig.6.1.1, 6.1.2 and 6.1.3 by counting the values in bins within in the region of $|\Delta\varphi| < 0.7$ for the near side and $|\Delta\varphi - \pi| < 0.7$ for the away side. Fig.6.2.1 shows the near (left) and away-side jet yields (right) as a function of $p_{\rm T,ch.jet}$ in pp collisions (top) and Pb-Pb collisions (bottom) with the different thresholds of the leading particle in a jet $p_{\rm T}^{\rm leading\,part.} > 5$ GeV/c (red), $p_{\rm T}^{\rm leading\,part.} > 7$ GeV/c (blue) and $p_{\rm T}^{\rm leading\,part.} > 9$ GeV/c (magenta). The jet yields in the low $p_{\rm T}$ regions $10 < p_{\rm T,ch.jet} < 20$ GeV/c and $20 < p_{\rm T,ch.jet} < 40$ GeV/c decrease with increasing the thresholds of the leading particle $p_{\rm T}$ in a jet, because the contribution of background

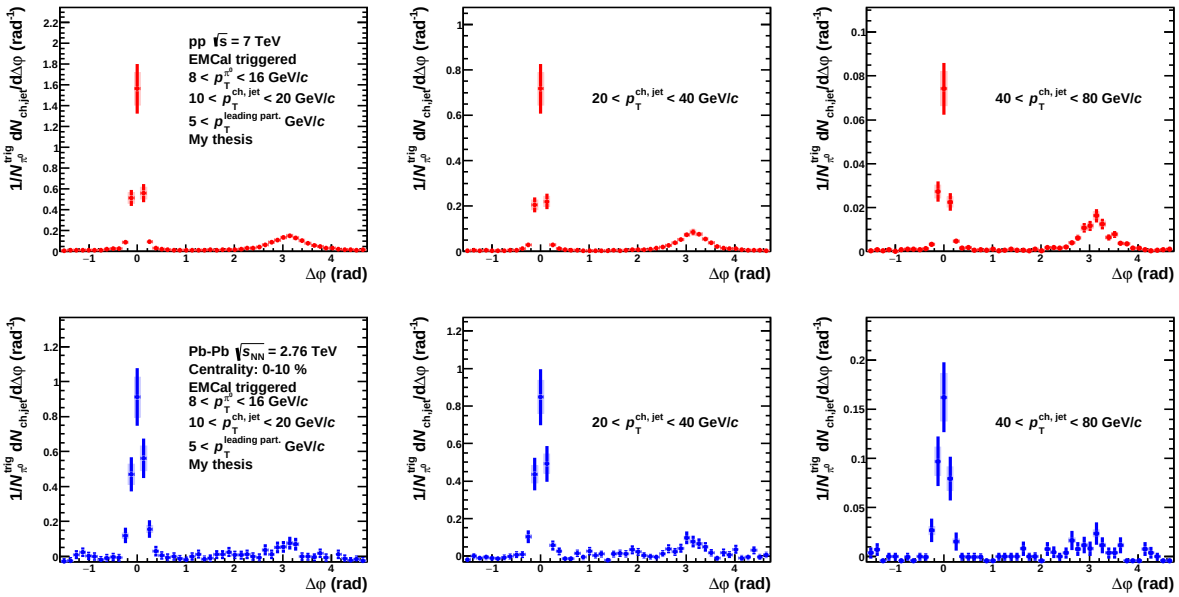

Fig. 6.1.1: Azimuthal correlations between the trigger π^0 and the associated jets in pp (top) and Pb-Pb (bottom) collisions with p_{T} range of trigger for π^0 in $8 < p_{\mathrm{T}}^{\pi^0} < 16$ GeV/c and the associated jet in $10 < p_{\mathrm{T,ch.jet}} < 20$ GeV/c, $20 < p_{\mathrm{T,ch.jet}} < 40$ GeV/c and $40 < p_{\mathrm{T,ch.jet}} < 80$ GeV/c. The p_{T} threshold of the leading particle in a jet is $p_{\mathrm{T}}^{\mathrm{leading\,part.}} > 5$ GeV/c. These results are normalized by number of trigger π^0.

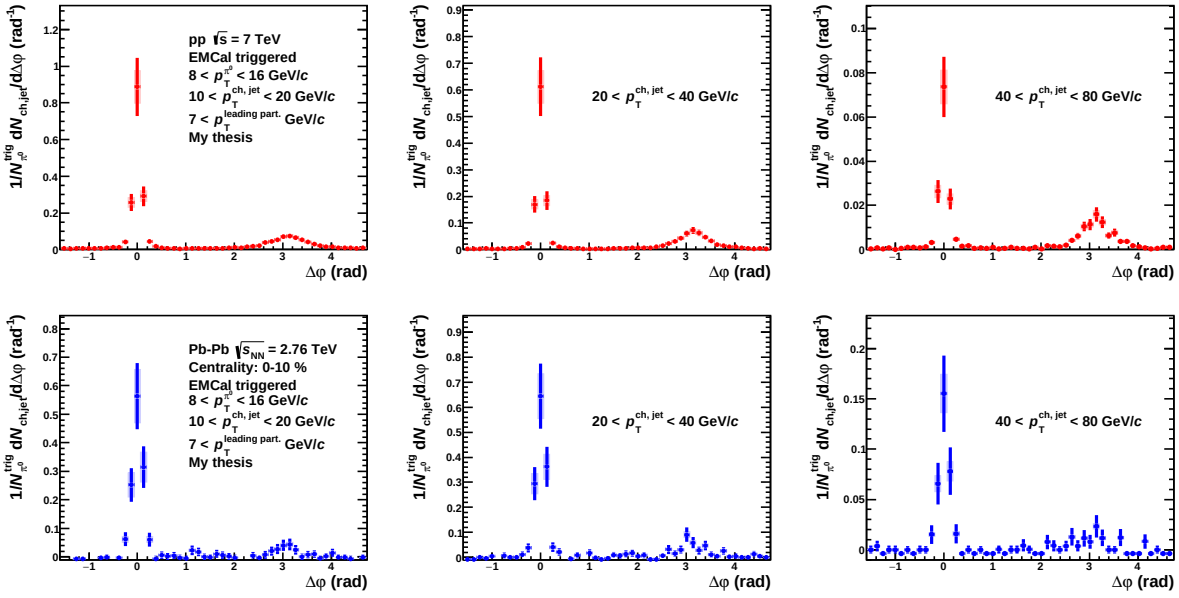

Fig. 6.1.2: Azimuthal correlations between the trigger π^0 and the associated jets in pp (top) and Pb-Pb (bottom) collisions with p_{T} range of trigger for π^0 in $8 < p_{\mathrm{T}}^{\pi^0} < 16$ GeV/c and the associated jet in $10 < p_{\mathrm{T,ch.jet}} < 20$ GeV/c, $20 < p_{\mathrm{T,ch.jet}} < 40$ GeV/c and $40 < p_{\mathrm{T,ch.jet}} < 80$ GeV/c. The p_{T} threshold of the leading particle in a jet is $p_{\mathrm{T}}^{\mathrm{leading\,part.}} > 7$ GeV/c. These results are normalized by number of trigger π^0.

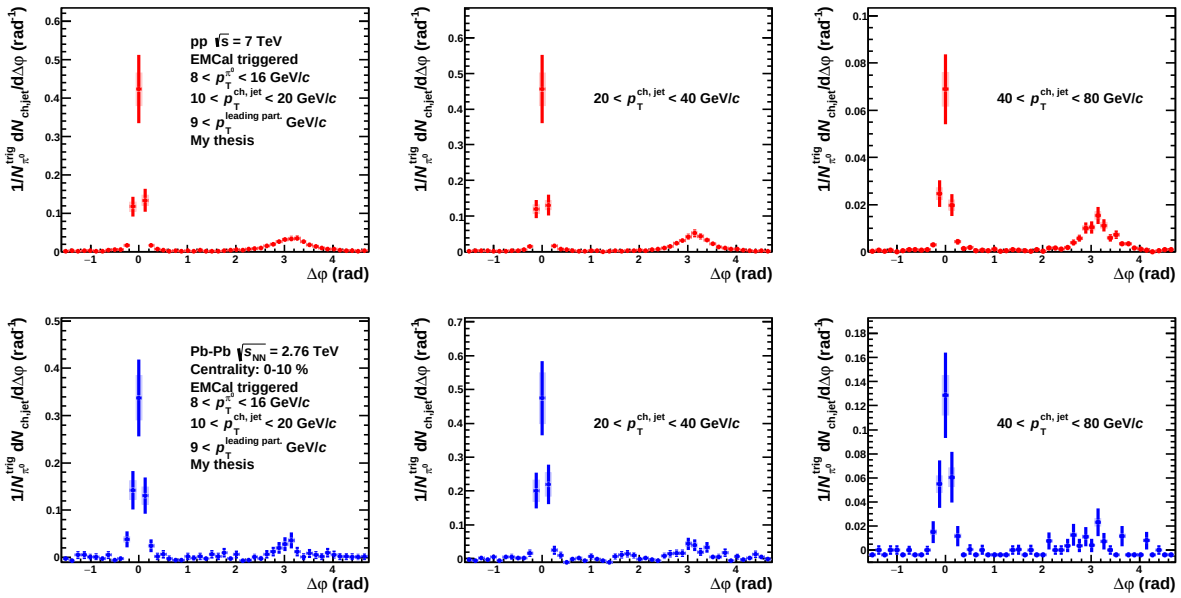

Fig. 6.1.3: Azimuthal correlations between the trigger π^0 and the associated jets in pp (top) and Pb-Pb (bottom) collisions with $p_{\rm T}$ range of trigger for π^0 in $8 < p_{\rm T}^{\pi^0} < 16$ GeV/c and the associated jet in $10 < p_{\rm T,ch.jet} < 20$ GeV/c, $20 < p_{\rm T,ch.jet} < 40$ GeV/c and $40 < p_{\rm T,ch.jet} < 80$ GeV/c. The $p_{\rm T}$ threshold of the leading particle in a jet is $p_{\rm T}^{\rm leading\,part.} > 9$ GeV/c. These results are normalized by number of trigger π^0.

fluctuation and combinatorial jets can be removed by requiring higher $p_{\rm T}$ for the leading particle in a jet (see Fig.3.4.13)[24], and requiring the high $p_{\rm T}$ leading particle in a jet increases the average of the jet $p_{\rm T}$.

6.3 Ratio of per trigger yield I_{AA}

In this section, we show the results of $I_{\rm AA}$, the ratios of per trigger jet yields between pp collisions and Pb-Pb collisions to know the effect of surface bias by requiring high $p_{\rm T}$ trigger π^0, and to measure the modification in jet yield in Pb-Pb collisions at high $p_{\rm T}$ regions. The ratio of per trigger yields $I_{\rm AA}$ is defined as;

$$I_{\rm AA}(p_{\rm T}^{\pi^0}, p_{\rm T,ch.jet}) = \frac{Y^{\rm Pb-Pb}(p_{\rm T}^{\pi^0}, p_{\rm T,ch.jet})}{Y^{\rm pp}(p_{\rm T}^{\pi^0}, p_{\rm T,ch.jet})}, \tag{6.3.1}$$

where $Y^{\rm Pb-Pb}$ is a per trigger jet yield in Pb-Pb collisions and $Y^{\rm pp}$ is a per trigger yield in pp collisions. The $I_{\rm AA}$ represents the effect of enhancement (> 1) or, suppression (< 1), or absence of modification ($= 1$).

Fig.6.3.1 shows the ratios of per trigger yields $I_{\rm AA}$ of near (left) and away-side (right) as a function of $p_{\rm T,ch.jet}$ with the three thresholds of the leading particle in a jet $p_{\rm T}^{\rm leading\,part.} > 5$ (red), $p_{\rm T}^{\rm leading\,part.} > 7$ (blue) and $p_{\rm T}^{\rm leading\,part.} > 9$ GeV/c (magenta).
In order to evaluate the effect of integration region, we compare the results by changing near and away-side bin counting regions; region of $|\Delta\varphi| < 0.7$ to $|\Delta\varphi| < 0.5$ and also $|\Delta\varphi| < 0.9$, and the differences between 0.7 and 0.5, 0.9 are ≈ 6 %. In the near-side, we observe around 0.6 for $p_{\rm T,ch.jet} = 10 - 20$ GeV/c, a unity for $20-40$ GeV/c, and above 1 (enhancement) for $40-80$ GeV/c jet $p_{\rm T}$ bin. This effect can be seen for all $p_{\rm T}$ thresholds for a leading particle in a jet. In the away-side, there is a clear suppression pattern in measured jet $p_{\rm T}$ range, and for all leading particle $p_{\rm T}$ thresholds. These results indicate that triggering a high $p_{\rm T}$ π^0 selects jets in near-side which is produced mostly on a surface in a medium

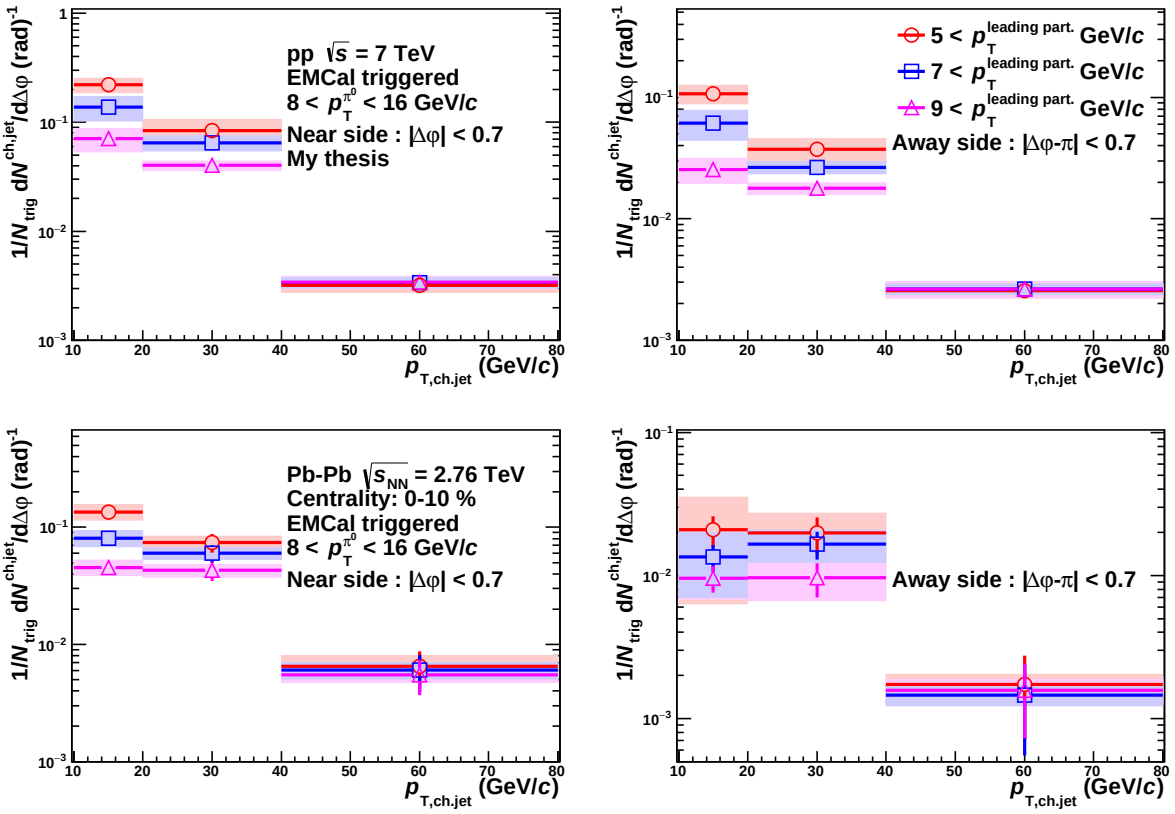

Fig. 6.2.1: Near (left) and away (right) jet yields with normalized number of trigger π^0's of pp collisions at $\sqrt{s} = 7$ TeV and Pb-Pb collisions at $\sqrt{s_{\rm NN}} = 2.76$ TeV with the three thresholds of the leading particle in a jet $p_{\rm T}^{\rm leading\,part.} > 5$ GeV/c (red), $p_{\rm T}^{\rm leading\,part.} > 7$ GeV/c (blue) and $p_{\rm T}^{\rm leading\,part.} > 9$ GeV/c (magenta).

due to the surface bias effect, while the path-length of the away-side jets become longer than those for near-side jets. On the other hand, as mentioned in Chapter 1, we can also bias near and away-side jets to the surface in a medium by requiring high p_{T} of leading particle in a jet. However, the dependence of the thresholds of the leading particles in a jet is not seen in the both sides and all p_{T} ranges of the associated jets due to large statistical fluctuation and/or too strong surface bias of trigger π^0. It is likely that we need to require lower p_{T} of trigger π^0, e.g. around 5 GeV/c in order to reduce the surface bias from triggering π^0 and to see the effect of path-length dependence for jets, as we mentioned in Chapter 1.

Fig.6.3.2 shows the comparison of I_{AA} as a function of the associated jet $p_{\mathrm{T,ch.jet}}$ between π^0-charged

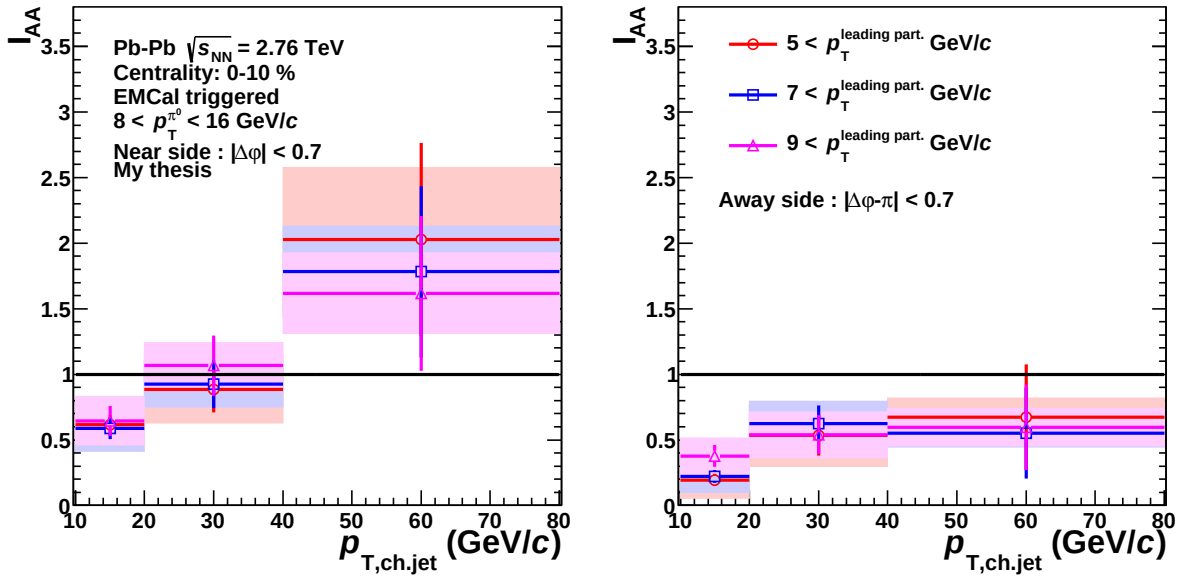

Fig. 6.3.1: Ratios of per trigger yields I_{AA} of near (left) and away-side (right) as a function of $p_{\mathrm{T,ch.jet}}$ with the three thresholds of the leading particle in a jet $p_{\mathrm{T}}^{\text{leading part.}} > 5$ GeV/c (red), $p_{\mathrm{T}}^{\text{leading part.}} > 7$ GeV/c (blue) and $p_{\mathrm{T}}^{\text{leading part.}} > 9$ GeV/c (magenta).

hadron analysis (black markers) in the associated charged hadron p_{T} region $3 < p_{\mathrm{T,ch.}} < 10$ GeV/c and π^0-charged jet analysis (magenta) in the associated jet p_{T} region $10 < p_{\mathrm{T,ch.jet}} < 80$ GeV/c. We only show the results of the π^0-jet analysis with the p_{T} threshold of the leading particle in a jet $p_{\mathrm{T}}^{\text{leadingpart.}} > 9$ GeV/c in order to compare both results in the same p_{T} threshold for leading particle. In the near-side, the result of the π^0-jet analysis in the p_{T} range of the associated jets $p_{\mathrm{T,ch.jet}} > 20$ GeV/c has good agreement with the results of π^0-hadron analysis, and in the away-side, the result of the π^0-jet analysis also agree with the the π^0-hadron analysis for the all p_{T} ranges of the associated jets. These results indicate that triggering high p_{T} π^0 provide the surface bias in the high p_{T} regions for jets similar to those at low p_{T} region (< 10 GeV/c) for hadrons and jets.

6.4 Near and away-side widths

In this section, we show the results of the widths of near and away-side peaks in the azimuthal correlations in Fig.6.1.1, 6.1.2 and 6.1.3 to extract the property of jet shape modification in Pb-Pb collisions. The near-side widths are estimated by a Gaussian function fit in the region of $|\Delta\varphi| < 0.5$ (rad), and the away-side widths are estimated by the same way for the near side in the region of $|\Delta\varphi - \pi| < 0.7$ (rad). Fig.4.1, 4.2, 4.3 show the near and away side peaks by fitting Gaussian functions in pp and the near-side peaks by fitting Gaussian function in Pb-Pb collisions. The near-side peaks in pp and Pb-Pb collisions and the

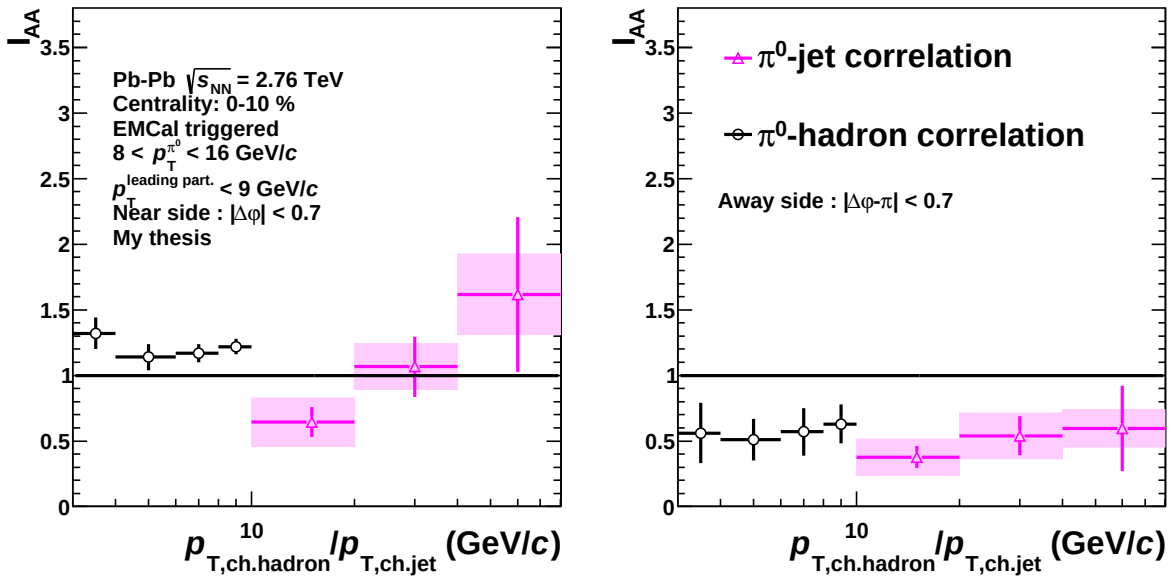

Fig. 6.3.2: Comparison of the ratio of per trigger yields $I_{\rm AA}$ as a function of the associated jet $p_{\rm T,ch.jet}$ between π^0-charged hadron analysis (black) in the associated charged hadron $p_{\rm T}$ region $3 < p_{\rm T,ch.} < 10$ GeV/c and π^0-charged jet analysis (magenta) in the associated jet $p_{\rm T}$ region $10 < p_{\rm T,ch.jet} < 80$ GeV/c with the $p_{\rm T}$ threshold of the leading particle in a jet $p_{\rm T}^{\rm leadingpart.} > 9$ GeV/c.

away-side peaks in pp collisions are fitted for all $p_{\rm T}$ ranges of the associated jets and thresholds of the leading particle in a jet. However, the away side peaks in Pb-Pb collisions are not so clearly visible due to statistical fluctuations. Thus, we do not fit the away-side peaks in Pb-Pb and not discuss the widths in this thesis.

Fig.6.4.1 shows comparison of the near and away-side widths as a function of the associated jet $p_{\rm T}$ between pp collisions (top) and Pb-Pb collisions (bottom) with the three thresholds of the leading particle in a jet $p_{\rm T}^{\rm leading\,part.} > 5$ (red), $p_{\rm T}^{\rm leading\,part.} > 7$ (blue) and $p_{\rm T}^{\rm leading\,part.} > 9$ GeV/c (magenta). The near-side widths in pp and Pb-Pb collisions are constants with all $p_{\rm T}$ ranges of the associated jets, while the away-side widths in pp collisions decrease with increasing $p_{\rm T}$ ranges of the associated jets due to the di-jet kinematics.

We also check the potential surface bias by changing trigger $p_{\rm T}$ for π^0 and leading particle $p_{\rm T}$ region. Fig.6.4.2 shows the comparisons of near-side widths between pp and Pb-Pb collisions as a function of the associated jet $p_{\rm T,ch.jet}$ with the two different $p_{\rm T}$ ranges of trigger π^0 in $8 < p_{\rm T}^{\pi^0} < 12$ GeV/c, $12 < p_{\rm T}^{\pi^0} < 36$ GeV/c. The $p_{\rm T}$ thresholds of the leading particle in a jet increase with going from the left to right side in Fig.6.4.2. The widths with $8 < p_{\rm T}^{\pi^0} < 12$ GeV/c and $p_{\rm T}^{\rm leading\,part.} > 5$ GeV/c in Pb-Pb collisions become broader than that in pp collisions, and the differences between pp and Pb-Pb collisions decreases with increasing the $p_{\rm T}$ of the trigger π^0 or the leading particle in a jet.

Fig.6.4.3 shows the comparisons of near-side widths between the two different $p_{\rm T}$ ranges of the trigger π^0 in pp (top) and Pb-Pb (bottom) collisions. The $p_{\rm T}$ thresholds of the leading particle in a jet increase with going from the left to right side in Fig.6.4.3. In pp collisions, the differences of widths between the two $p_{\rm T}$ ranges of the trigger π^0 are constant for the all $p_{\rm T}$ thresholds of the leading particle in a jet, while its differences in Pb-Pb collisions decrease with increasing the $p_{\rm T}$ of leading particle in a jet, especially for the higher $p_{\rm T}$ associated jets. These results suggest that the jet production points is strongly biased towards the surface in a medium by requiring the high $p_{\rm T}$ trigger π^0 and leading particle in a jet compared with requiring the low $p_{\rm T}$ trigger π^0 and leading particle in a jet (mentioned in Chapter 1).

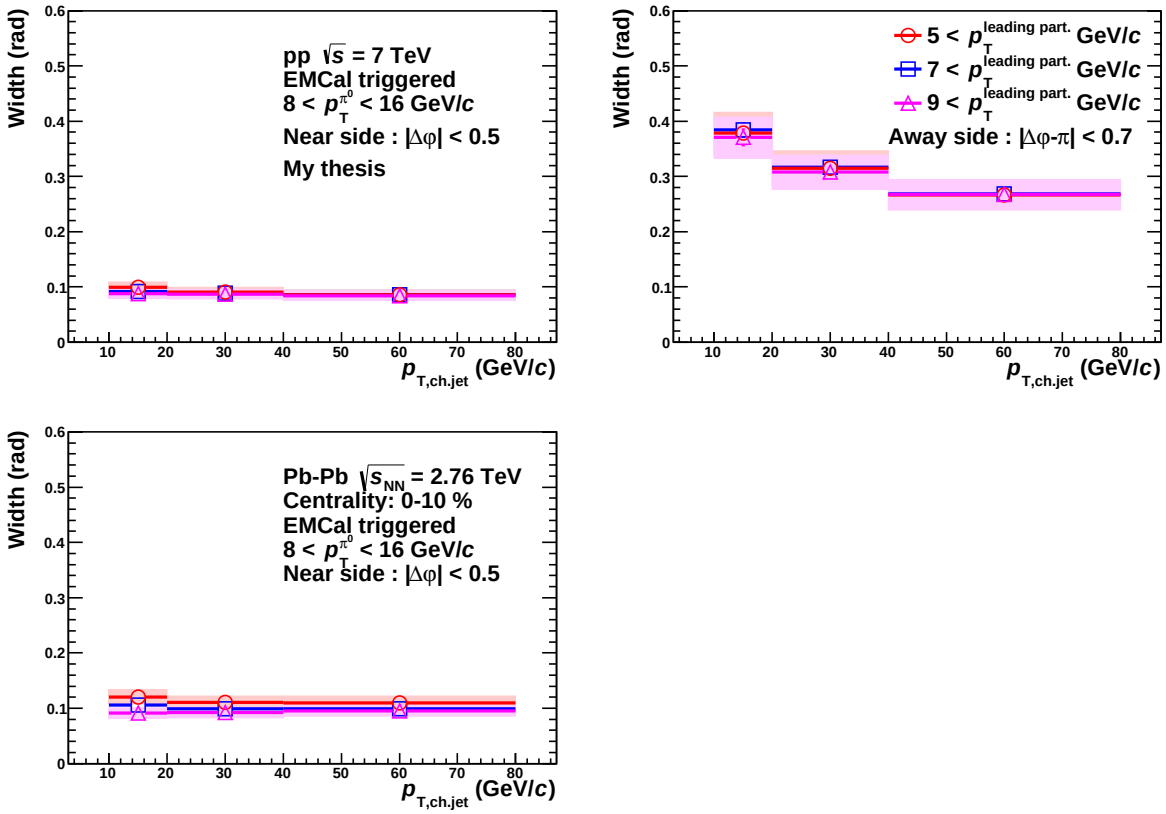

Fig. 6.4.1: Near and away-side widths as a function of the associated jet pT,ch.jet in pp collisions at $\sqrt{s} = 7$ TeV (upper two figures) and Pb-Pb collisions at $\sqrt{s_{\rm NN}} = 2.76$ TeV with trigger π^0 $p_{\rm T}$ region $8 < p_{\rm T}^{\pi^0} < 16$ GeV/c. The $p_{\rm T}$ thresholds of the leading particle in a jet are $p_{\rm T}^{\rm leading\,part.} > 5$ GeV/c (red), $p_{\rm T}^{\rm leading\,part.} > 7$ GeV/c (blue) and $p_{\rm T}^{\rm leading\,part.} > 9$ GeV/c (magenta).

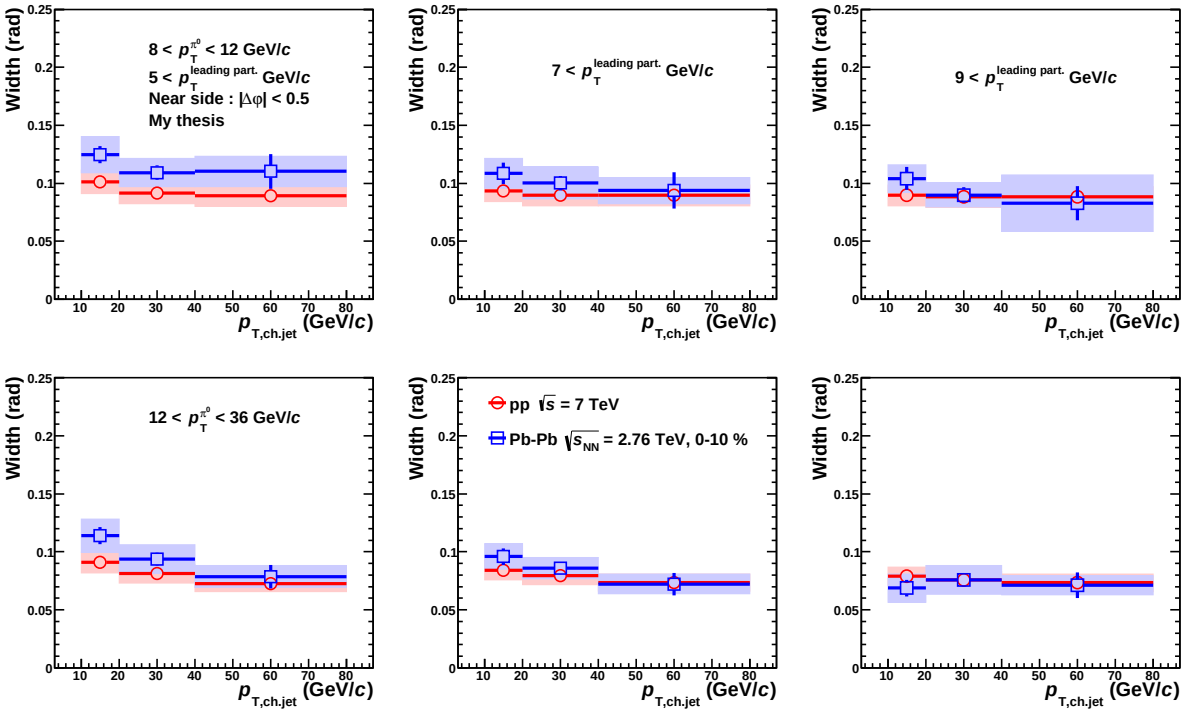

Fig. 6.4.2: Comparisons of near-side widths between pp (red) and Pb-Pb (blue) collisions as a function of the associated jet $p_{\mathrm{T,ch.jet}}$ with the two different p_{T} ranges of trigger π^0 in $8 < p_{\mathrm{T}}^{\pi^0} < 12$ GeV/c (top), $12 < p_{\mathrm{T}}^{\pi^0} < 36$ GeV/c (bottom). The p_{T} thresholds of the leading particle in a jet increase with going to the right side.

6.5 Summary of the surface bias

We see the azimuthal correlations, jet yields and widths in near and away-sides by using π^0-jet correlation in pp collisions and Pb-Pb collisions. In particular, we focus here away-side suppression, near-side enhancement and near-side width broadening by the surface bias with respect to p_{T} of trigger π^0 and leading particle in a jet.

6.5.1 Suppression of away-side jet yields

We observe suppression of away-side jet yields in Pb-Pb collisions by triggering high p_{T} π^0 in the all p_{T} regions of the associated jets and the leading particle in a jet, while the path-length dependence of suppression of away-side jet yields by changing p_{T} ranges of the trigger π^0 and leading particle in a jet are not seen in this analysis (see in Fig.6.3.1). In order to interpret the results in this analysis, we compare these with two other experimental results of jet suppression in Pb-Pb collisions at $\sqrt{s_{NN}} = 2.76$ TeV.

Fig.6.5.1 shows the R_{AA} for $R = 0.2$ jets with leading particle requirement of 5 GeV/c in 0-10 % and 10-30 % most central Pb-Pb collisions compared with the two different models of YaJEM[56] and JEWEL[57]. This result indicate that the jet yields in central Pb-Pb collisions are strongly suppressed in the p_{T} range of jets in $40 < p_{\mathrm{T,jet}} < 120$ GeV/c, and is qualitatively in good agreement with the results of suppression of away-side jet yields in this analysis.

Fig.6.5.2 shows the second-order harmonic coefficient $v_2^{\mathrm{ch.jet}}$ as a function of $p_{\mathrm{T,ch.jet}}$ in 0-5 % and 30-50 % collision centrality in Pb-Pb collisions6.5.2. A positive v_2 is observed in semi-central collisions, and this results indicates the jet suppression depends on the path-length of initial parton in a medium. However, this effect are not observed in this analysis. In order to observe the path-length dependence of jet suppression by triggering high p_{T} hadrons, we need to take a larger interval between two trigger p_{T} regions. In this analysis, we can not take a large enough lever arm for trigger π^0 p_{T} dependence due to

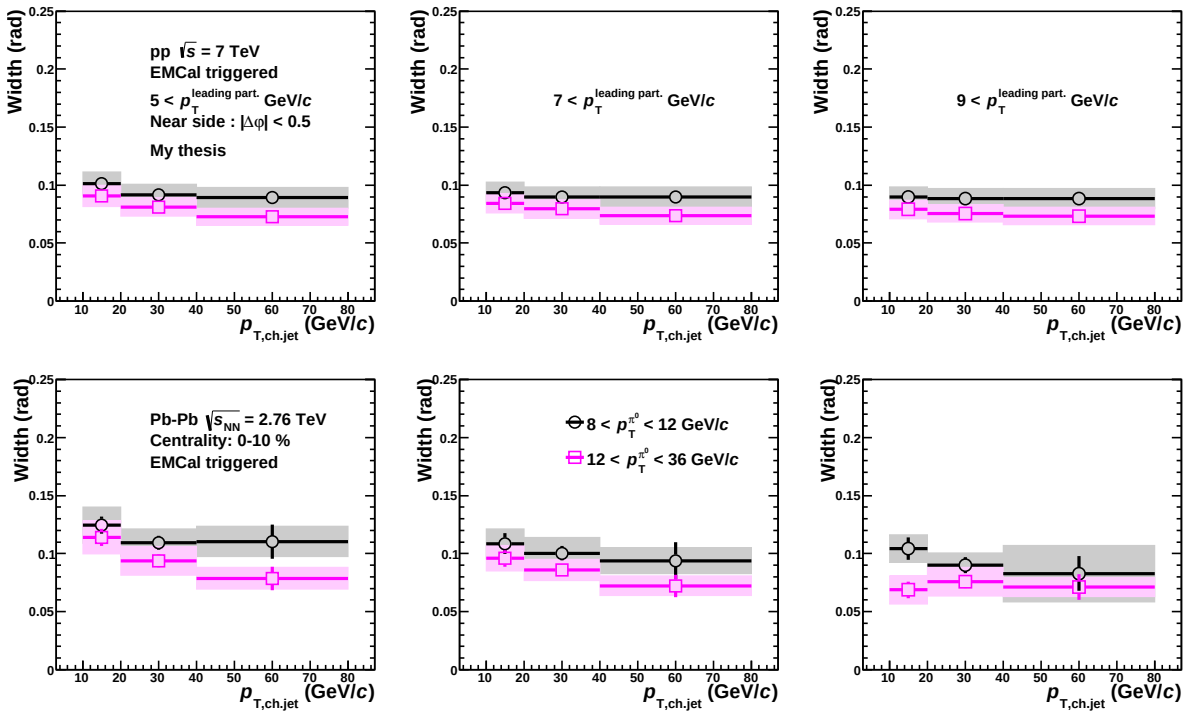

Fig. 6.4.3: Comparisons of near-side widths between the two different p_{T} ranges (glay and magenta) of the trigger π^0 in pp (top) and Pb-Pb (bottom) collisions. The p_{T} thresholds of the leading particle in a jet increase with going to the right side.

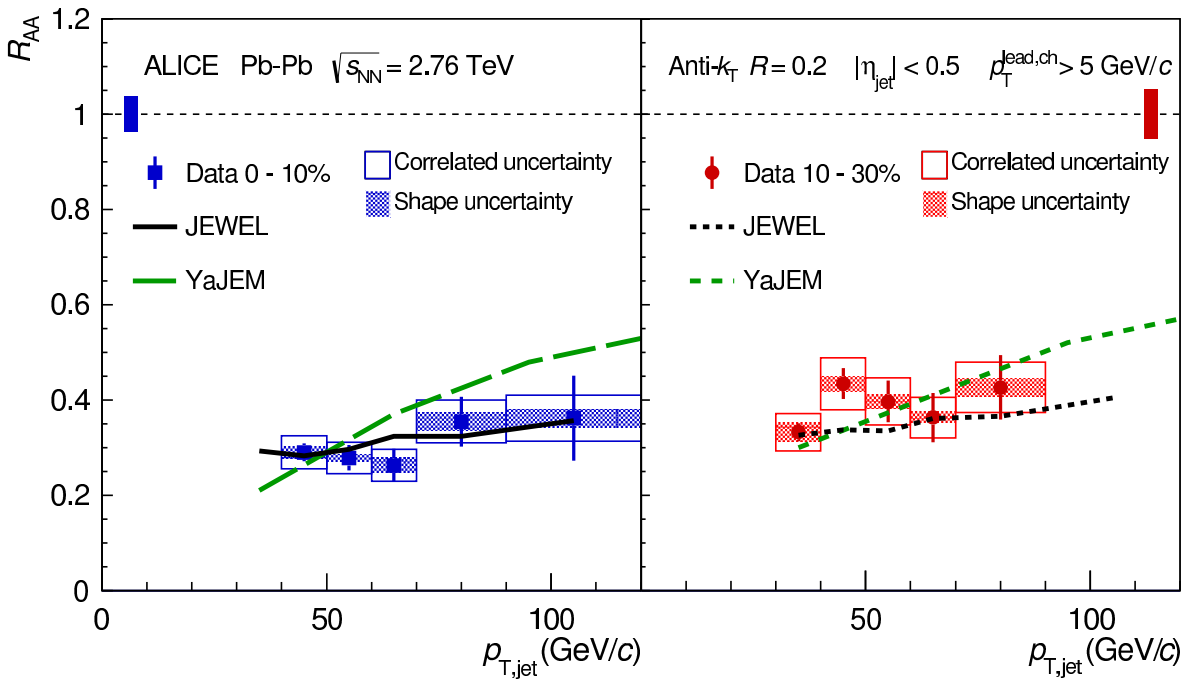

Fig. 6.5.1: R_{AA} for $R = 0.2$ jets with leading particle requirement of 5 GeV/c in 0-10 (left) % and 10-30 % (right) most central Pb-Pb collisions from the LHC-ALICE[55] experiment compared to calculations from YaJEM[56] and JEWEL[57].

low statistics in high p_{T} regions and small signal to noise ratio of π^0 identification in low p_{T} regions.

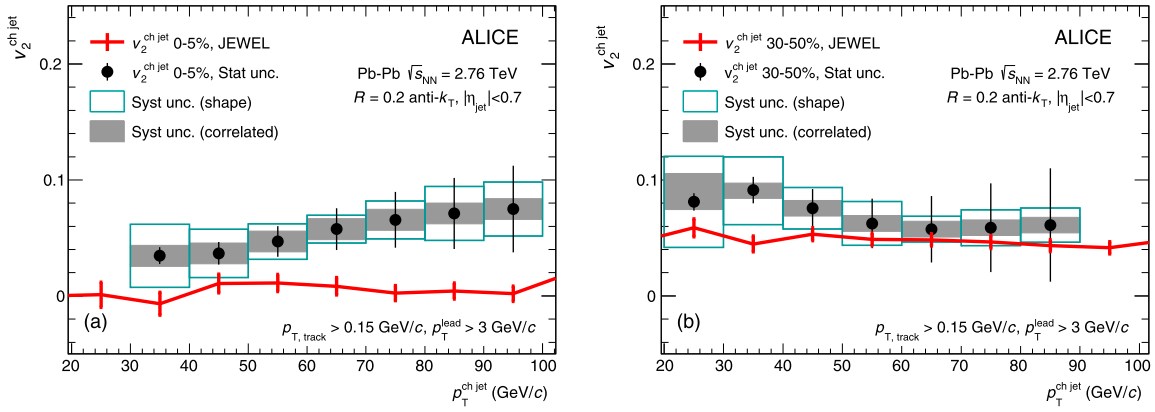

Fig. 6.5.2: Second-order harmonic coefficient $v_2^{\mathrm{ch.jet}}$ as a function of $p_{\mathrm{T,ch.jet}}$ in 0-5 (left) % and 30-50 % (right) collision centrality in Pb-Pb collisions from the LHC-ALICE experiment[58].

6.5.2 Enhancement of near-side jet yields

In this analysis, we observe enhancement of near-side jet yields in Pb-Pb collisions by triggering high p_{T} π^0 in the highest p_{T} region of the associated jets. Enhancement of jet yields in near-side are observed by I_{AA} of the di-hadron correlation in the LHC-ALICE experiment (Fig.1.8.4) and also observed by the π^0-hadron correlation in the LHC-ALICE experiment. The possible explanations for this yield enhancement are;

- a change of the fragmentation function,
- a possible change of the quark/gluon jet ratio in the final state due to the different coupling to the medium,
- a bias on the parton p_{T} spectrum after energy loss due to the trigger particle selection.

6.5.3 Broadening effect of near-side widths

In the theoretical approach, the jet shape modification in heavy-ion collisions are expected to depend on the properties of a medium and its dynamics. Fig.6.5.3 shows the jet shape modification with the three kinds of medium types in vacuum, static medium and flowing medium. One is a static medium, if jets go through a static medium, the jet shapes are broadened like the middle figure in Fig.6.5.3. Second is a flowing medium, if jets go through a flowing medium, the asymmetrical jet shape can be observed like the right figure in Fig.6.5.3.

In this analysis, we observe that the jet shape in near-side of Pb-Pb collisions become broader than that pp collisions. The potential jet broadening in Pb-Pb collisions become stronger in low p_{T} regions of trigger π^0 and/or leading particle. This fact suggests that we can provide the surface bias by selecting the high p_{T} trigger π^0 and/or leading particle in a jet and these results don't conflict with the expectation of jet shape modification in a static medium.

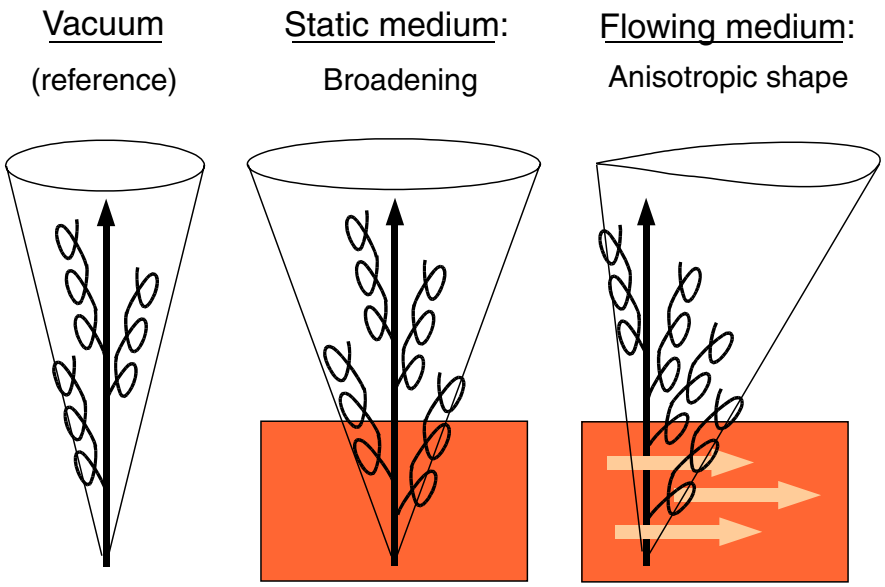

Fig. 6.5.3: Sketch of jet shape with assuming the three kinds of medium types in vacuum (left), static medium (center) and flowing medium (right).

Chapter 7

Conclusion

We study the jet modifications in near and away-side by using the correlation between high p_{T} π^0 (trigger particle) and charged jet in pp collisions at $\sqrt{s} = 7$ TeV and in central Pb-Pb collisions at $\sqrt{s_{\mathrm{NN}}} = 2.76$ TeV from the LHC-ALICE experiment.

To identify and measure π^0 in high p_{T} regions, a new method "cluster splitting method" has been implemented. This method identifies high p_{T} π^0s via a shower shape with long axis parameter λ_0 of the elliptic shape of two overlapping shower. We can reconstruct high p_{T} π^0 up to 40 GeV/c by this method. We also measured charged jets from 10 to 80 GeV/c in p_{T} with anti-k_{T} algorithm and resolution parameter R = 0.4. The contamination of reconstructed jets in Pb-Pb collisions are subtracted by considering the event plane dependence of underlying events density.

In the azimuthal correlations between π^0's and charged jets measurement, we observe two jet-like peaks in pp collisions at $\sqrt{s} = 7$ TeV and also in central Pb-Pb collisions at $\sqrt{s_{\mathrm{NN}}} = 2.76$ TeV. Thus, it is confirmed that high p_{T} π^0 production is strongly associated with jet production.

In the ratio of per trigger yields (I_{AA}) measurements, we observe the enhancement of near-side jets in $p_{\mathrm{T,ch.jet}} > 20$ GeV/c while the suppression of jets in away side by triggering high p_{T} π^0 ($8 < p_{\mathrm{T}}^{\pi^0} < 16$ GeV/c). This result indicates that we select jets produced near at the surface of the QGP by triggering high p_{T} hadron, so that the path-length of away side jets get longer than that of near side jets. In the comparisons to the results of low p_{T} regions (π^0-charged hadron correlation), the I_{AA} values in the near-side with the p_{T} range of the associated jets $p_{\mathrm{T,ch.jet}} > 20$ GeV/c are in good agreement with the present data. The I_{AA} values in the away-side with the all p_{T} ranges of the associated jets ($10 < p_{\mathrm{T,ch.jet}} < 80$ GeV/c) are also consistent each other. Thus, triggering high p_{T} π^0 provides the surface bias in high p_{T} regions in the similar to the low p_{T} associated hadrons.

In the near and away-side width measurements, we observe an indication of jet broadening effect in the near-side by requiring the low p_{T} triggering π^0 and low p_{T} leading particle in a jet in central Pb-Pb collisions. This effect decreases with increasing p_{T} of the trigger π^0 or the leading particle in a jet. These results suggest a possible jet broadening effect in central Pb-Pb collision depending on the path-length of a initial parton in a medium.

In order to extract more detailed information of path-length, we need larger data samples to take a large enough lever arm between different the trigger π^0 momenta. The Di-jet calorimeter has been installed in opposite azimuthal direction of the EMCal in the ALICE experiment. This new apparatus allows us to study of the path-length dependence of parton energy loss in QGP in more detail through the high statistics correlation measurements during the LHC Run-2.

Appendix

A Quantum Chromo Dynamix (QCD)

The QCD is the theory to describe fundamental force in strong interaction between quarks and gluons with three color symmetry SU(3). Quarks have not only the flavor degrees of freedom (up, down, strange, charm, bottom, tor), but also the color degrees of freedom (red, blue, and green) and are always bound together to form color-white composite in hadrons. Gluons is spin 1 gauge bosons that mediate the strong force between quarks. QCD permit gluons to interact by themselves.

The classical Lagrangian density for a quark with mass m given by

$$\mathscr{L}_{cl} = \sum_{f}^{N_f} \overline{q}_f (i\gamma^\mu D_\mu - m_f) q_f - \frac{1}{4} F^a_{\mu\nu} F^{\mu\nu}_a \tag{1.1}$$

Quark (gluon) field q_f belong to the SU(3) triplet (octet). Therefore, f runs 1 to 3, while a runs 1 to 8. The covariant derivative, D_μ is

$$D_\mu \equiv \partial_\mu + ig\frac{\lambda^a}{2} A^a_\mu \tag{1.2}$$

where λ^a is the eight Gell-Mann matrices. The strength tensor of gluon field $F^a_{\mu\nu}$ is defended as

$$F^a_{\mu\nu} = \partial_\mu A^a_\nu - \partial_\nu A^a_\mu + g f_{abc} A^b_\mu A^c_\nu \tag{1.3}$$

where A^a_ν is the gluon fields, and f_{abc} is the structure constants of the SU(3) group. g is defined using coupling constant α as,

$$g \equiv \sqrt{4\pi\alpha_s} \tag{1.4}$$

β function can be calculated in perturbation theory if g is small enough. And the function can be expanded in series of g

$$Q\frac{\partial g}{\partial Q} = \beta_0 \beta(g) = -\beta_0 g^3 - \beta_1^5 + \ldots \tag{1.5}$$

$$\beta_0 = \frac{1}{(4\pi)^2}(11 - \frac{2}{3}N_f), \beta_1 = \frac{1}{(4\pi)^4}(102 - \frac{38}{3}N_f) \tag{1.6}$$

Running coupling constant can be described as function of momentum transfer Q,

$$\alpha_s(Q) = \frac{1}{4\pi\beta_0 \ln(Q^2/\Lambda^2_{QCD})}\left(1 - \frac{\beta_1}{\beta_0^2}\frac{\ln(\ln(Q^2/\Lambda^2_{QCD}))}{\ln(Q^2/\Lambda^2_{QCD})}\right) \tag{1.7}$$

Λ_{QCD} is called QCD scale parameter, to be determined from experiments.

According to Eq.1.7, running coupling constant of strong force α_s should be smaller at large momentum transfer Q (or smaller distance). This property in large momentum transfer region is called asymptotic freedom. The effect decreasing coupling constant with the increasing energy comes from

anti-screening of color charge. The decreasing coupling constant with increasing energy is caused by the effect of anti-screening of color charge. It can be to calculate in perturbative calculations by DGLAP[8][9][10] of cross sections in deep inelastic processes.

Fig.1.1 illustrates that the coupling constants measured by several experiments are good agreement with the calculations by perturbative QCD. On the other hands, in smaller Q region (or larger distance), α_s gets increase rapidly. We call the property "confinement of quarks". Even if we try to draw quark away from hadron, strong force generate energy to produce a new $q\bar{q}$ pair from the vacuum. Therefore, we can not let quark be alone in vacuum.

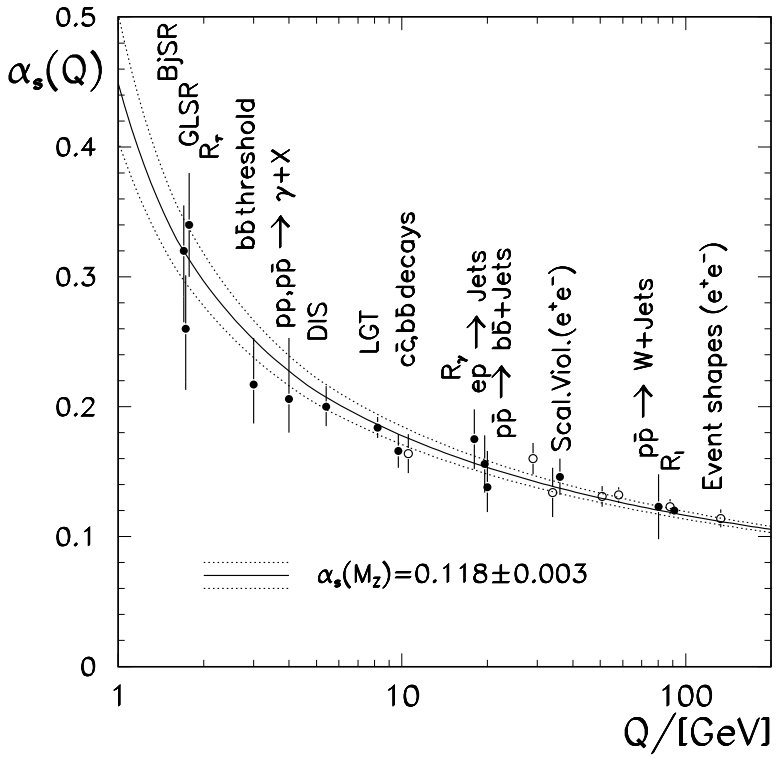

Fig. 1.1: Running of the strong coupling constant established by various types of measurements at different scales, compared to the QCD prediction for $\alpha_s(M_z) = 0.118 \pm 0.003$.[11]

B Run list

2.1 Data set in pp collisions at $\sqrt{s}$ =7 TeV

– LHC11c, full EMCal, L0 trigger at 5.5 GeV: 154808, 154796, 154793, 154789, 154787, 154786, 154783, 154780, 154773 154763.

– LHC11c, full EMCal except super-module 5, L0 trigger at 5.5 GeV: 154495, 154485, 154483, 154480, 154478, 154383, 154385 , 154382, 154289, 154286, 154283, 154281,154273, 154270, 154269, 154266, 154264, 154261, 154257, 154252, 154222, 154221, 154219, 154211, 154207, 154143, 154141, 154136, 154132, 154130, 154126.

– LHC11c, full EMCal, L0 trigger at 4.5 GeV: 53566, 153560, 153558, 153552, 153548, 153544, 153542, 153541, 153539, 153536, 153533, 153373, 153371, 153369, 153296, 153362, 153232,153223.

– LHC11c full EMCal except super-module 5, L0 trigger at 4.5 GeV: 53738, 153733, 153728, 153727, 153726, 153725, 153718, 153709, 153702, 153594, 153589, 153591 , 153587, 153571, 153570.

– LHC11d, full EMCal, L0 trigger at 5.5 GeV: 59582, 159581, 159580, 159577, 159575, 159538, 159535, 159532, 159286, 159260, 159258,159254, 157976, 157975, 157819, 157818, 157569, 157567, 157564, 157562, 157560, 157496, 157475, 157277, 157275, 157262, 157261, 157257, 157227, 157220, 157203, 156896, 156891, 156889.

2.2 Data set in Pb-Pb collisions at $\sqrt{s_{NN}}$ =2.76 TeV

– LHC11h, good TPC runs, full EMCal, L1-Gamma+Central+SemiCentral trigger: 167813, 167988, 168066, 168068, 168069, 168076, 168104, 168212, 168311, 168322, 168325, 168341, 168361, 168362, 168458, 168460, 168461, 168992, 169091, 169094, 169138, 169143, 169167, 169417, 169835, 169837, 169838, 169846, 169855, 169858, 169859, 169923, 169956, 170027, 170036, 170081, 169415, 169411, 169035, 168988, 168984, 168826, 168777, 168512, 168511, 168467, 168464, 168342, 168310, 168115, 168108, 168107, 167987, 167915, 167903

– LHC11h, semi-good TPC runs, full EMCal, L1-Gamma+Central+SemiCentral trigger: 169975, 169981, 170038, 170040, 170083, 170084, 170085, 170088, 170089, 170091, 170152, 170155, 170159, 170163, 170193, 170195, 170203, 170204, 170205, 170228, 170230, 170264, 170268, 170269, 170270, 170306, 170308, 170309

C Comparison with Monte Carlo

The MC data (LHC12a15f) used in this analysis is PYTHIA pp collisions at $\sqrt{s}$ = 7 TeV with unbiased jet-jet events and doesn't include the information of EMCal trigger. This analysis are used the two kinds of MC data to compare with real data. The first one is the MC data without EMCal trigger bias, and the next one is the MC data which is reproduced EMCal trigger by using a sliding window algorithm [**?**]. We compare the p_T distributions (charged track, jet, π^0) and π^0-jet azimuthal distributions between real and MC data.

Fig. 3.1 shows the comparison of charged track, jet and π^0 pt distribution with two different MC samples. The Results of MC data used in this analysis are normalized by the number of events generated, and the average cross section given by PYTHIA. When we combine various p_T-hard bins after normalized by the average cross section, there are outliers in $\pi^0 p_T$ distributions and azimuthal correlations in away side. In order to avoid the effect of outliers, we removed outliers of $\pi^0 p_T$ distributions and azimuthal correlations in away side. In case of removed outliers of $\pi^0 p_T$ distributions, I fitted $\pi^0 p_T$ distributions by exponential functions at the regions of $\pm$ 5 bins from the outlier, and then scaled down outliers to the fit functions. Fig. 3.2 show the $\pi^0 p_T$ distributions before and after removed outliers.

Fig. 3.3 shows the comparison of azimuthal yields between uncorrected MC and real data. Fig. 3.4 shows the comparison of azimuthal yields between particle level MC and corrected real data. Fig. 3.5 shows the comparison of near and away side width between MC and real data.

3.1 Comparison of away-side jet yields between π^0-jet analysis and $h^{\pm}$-jet analysis

Ass mention in the previous section, we could not exactly compare the away-side jet yields with the results of MC due to large fluctuations which are caused by low statistics of MC. In order to avoild the effect of large fluctuations, we compared with the away-side jet yields of $h^{\pm}$-jet analysis(Filip's analysis) [**?**]. The away-side jet yields of $h^{\pm}$-jet analysis are consistent with the results of MC.

Fig. 3.6 shows the away-side jet yields of $h^{\pm}$-jet and π^0-jet analysis, and fig. 3.7 shows the ratios of the away-side jet yields of π^0-jet to the away-side jet yields of $h^{\pm}$-jet. The results of $h^{\pm}$-jet analysis

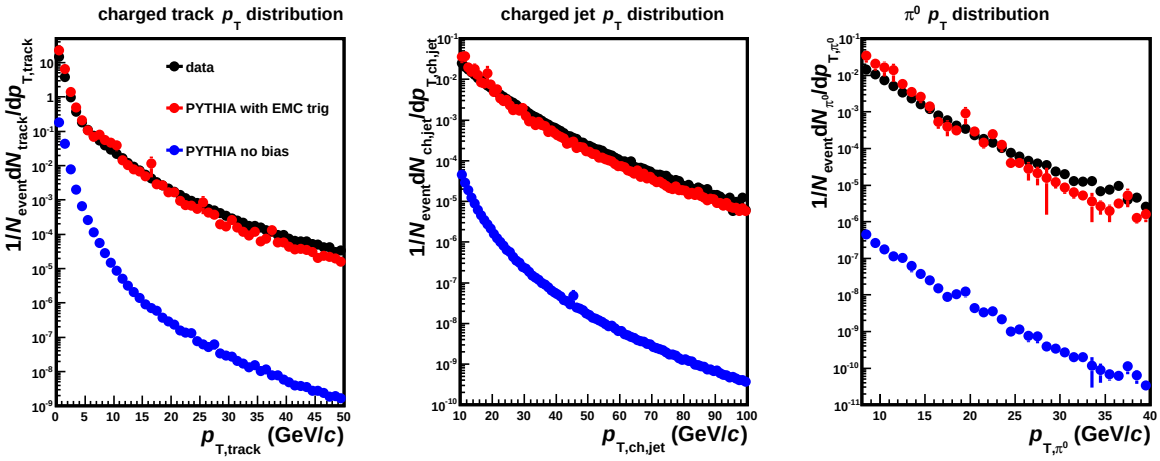

Fig. 3.1: The comparison to the simulation data of charged track and jet, π^0. The black points are the real data (LHC11d), the red points are the simulation data (LHC12a15f) with reproduced EMCal trigger and the blue points are the simulation data with no bias.

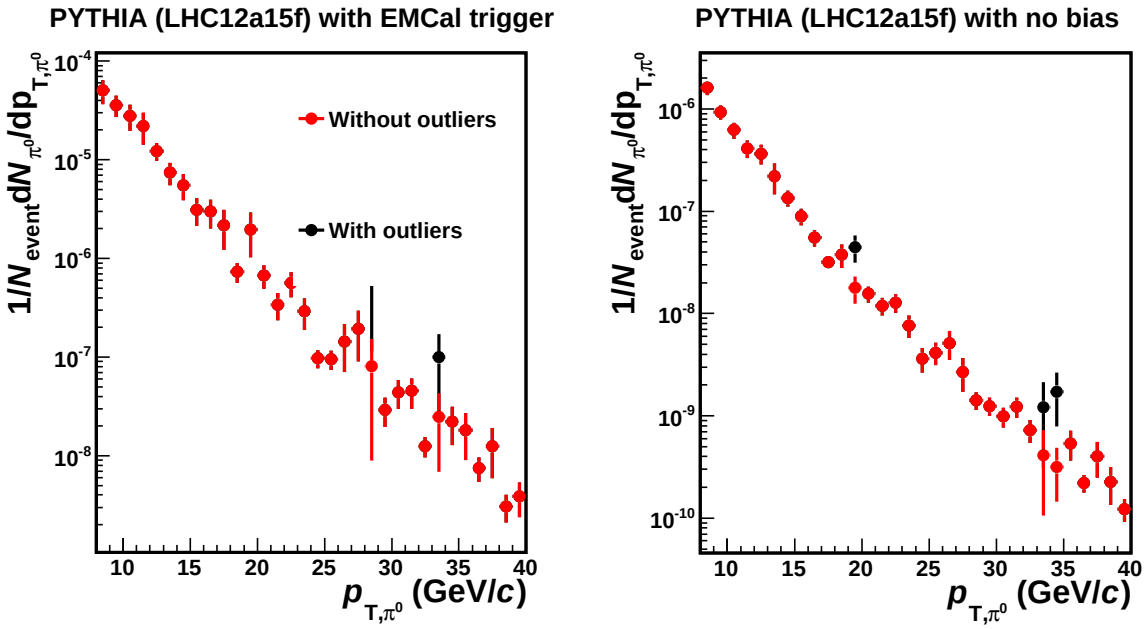

Fig. 3.2: The $\pi^0 p_T$ distributions before (black points) and after (red points) removed outlier with two different MC data.

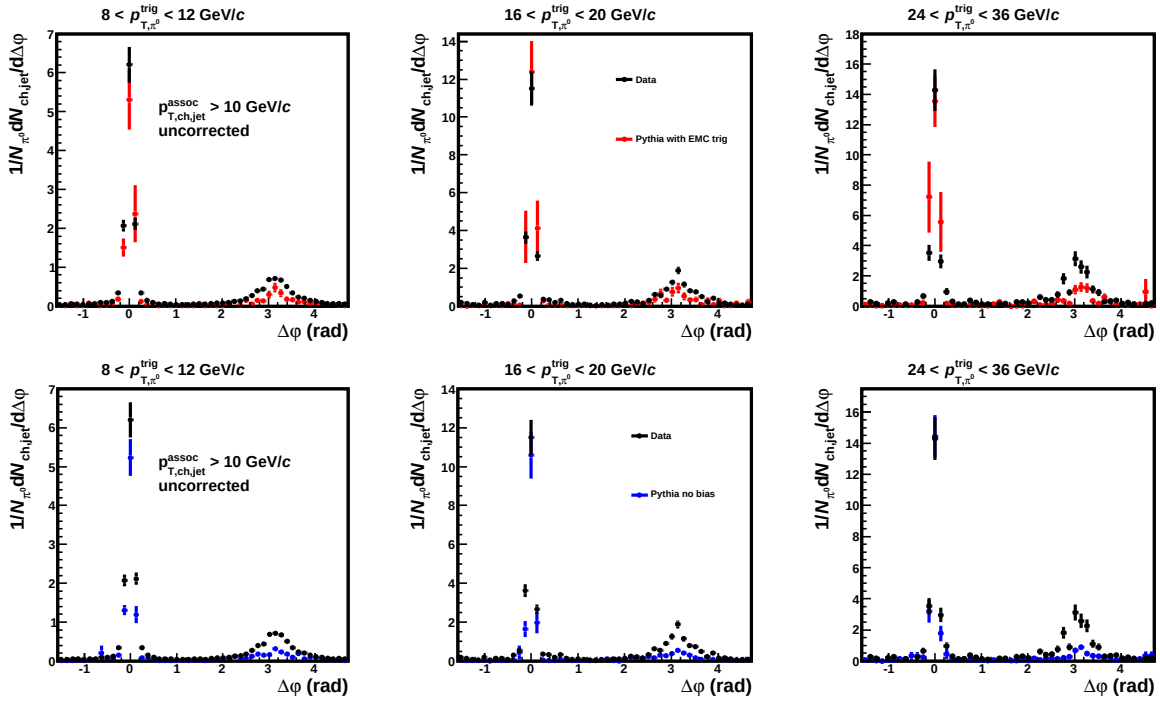

Fig. 3.3: The comparison to the simulation data of the uncorrected azimuthal correlations, trigger $\pi^0 p_T$ regions at $8 < p^{trig}_{T,\pi^0} < 12$ (GeV/c), $16 < p^{trig}_{T,\pi^0} < 20$ (GeV/c) and $24 < p^{trig}_{T,\pi^0} < 36$ (GeV/c), associated jet p_T threshold $p^{assoc}_{T,ch,jet} > 10$ (GeV/c). The black markers are the real data (LHC11d), the red markers are the simulation data (LHC12a15f) with reproduced EMCal trigger and the blue markers are the simulation data with no bias.

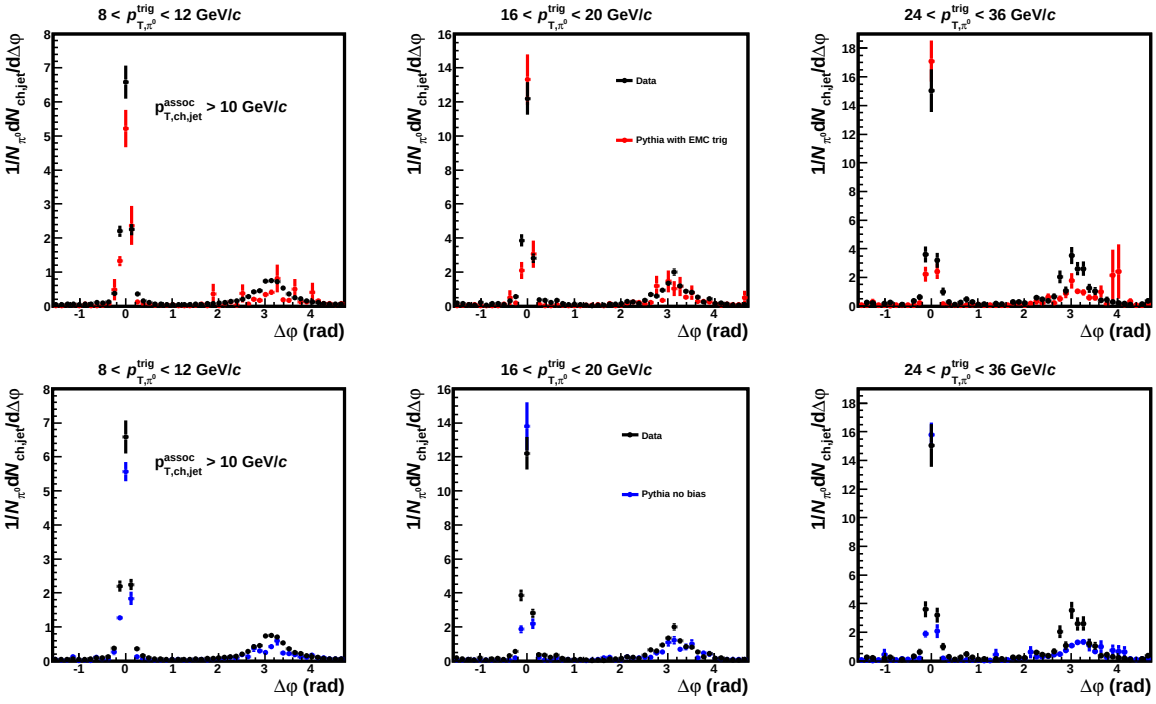

Fig. 3.4: The comparison of azimuthal yields between the particle level MC and corrected real data, trigger π^0 p_T regions at $8 < p_{T,\pi^0}^{trig} < 12$ (GeV/c), $16 < p_{T,\pi^0}^{trig} < 20$ (GeV/c) and $24 < p_{T,\pi^0}^{trig} < 36$ (GeV/c), associated jet p_T threshold $p_{T,ch,jet}^{assoc} > 10$ (GeV/c). The black markers are the real data (LHC11d), the red markers are the simulation data (LHC12a15f) with reproduced EMCal trigger and the blue markers are the simulation data with no bias.

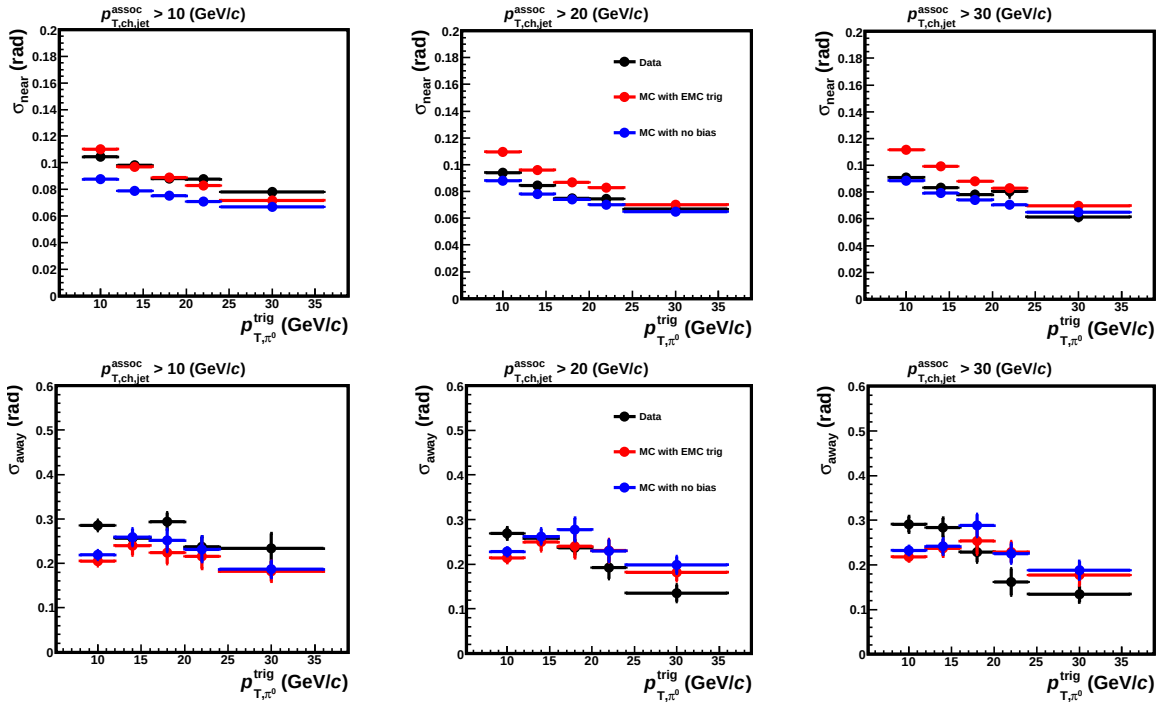

Fig. 3.5: The comparison of near (upper plots) and away (bottom plots) side width as function of trigger $\pi^0 p_T$ between the uncorrected MC and real data, trigger $\pi^0 p_T$ regions at $8 < p_{T,\pi^0}^{trig} < 12$ (GeV/c), $16 < p_{T,\pi^0}^{trig} < 20$ (GeV/c) and $24 < p_{T,\pi^0}^{trig} < 36$ (GeV/c), associated jet p_T threshold $p_{T,ch,jet}^{assoc} > 10$ (GeV/c). The black markers are the real data (LHC11d), the red markers are the simulation data (LHC12a15f) with reproduced EMCal trigger and the blue markers are the simulation data with no bias.

were applied the unfolding method to correct the detector effect, while the results of π^0-jet analysis were applied the bin-by-bin correction.

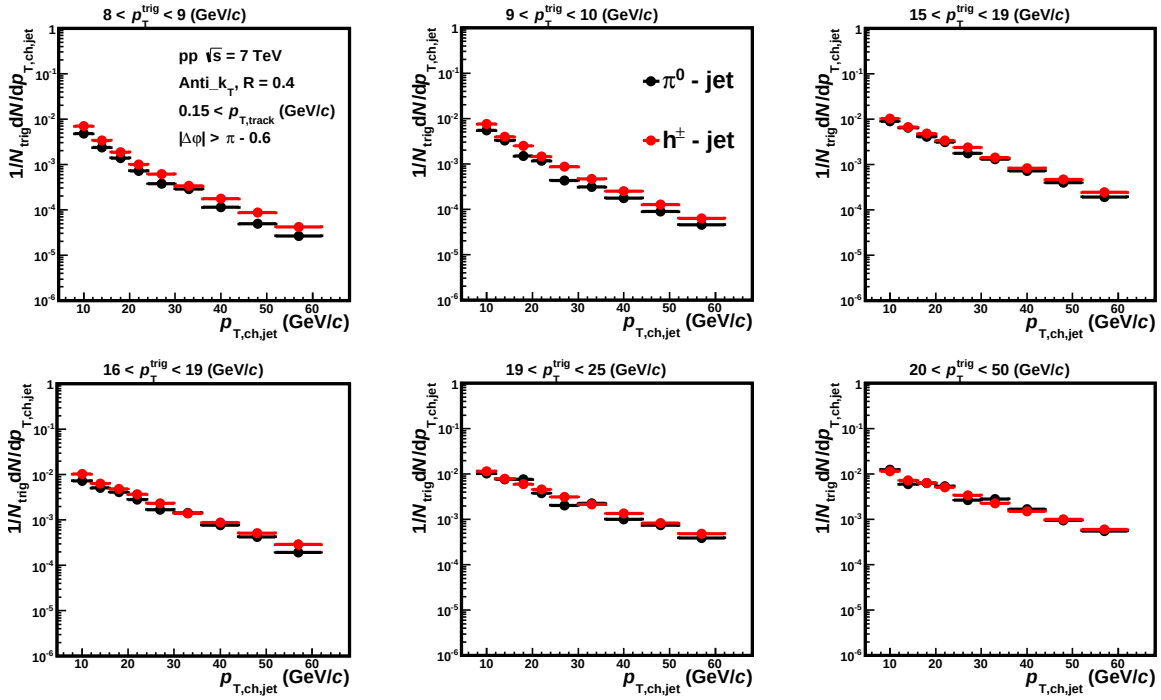

Fig. 3.6: The away-side jet p_T distribution of π^0-jet and $h^{\pm}$-jet analysis with six different trigger p_T regions, $8 < p_T^{trig} < 9$ (GeV/c), $9 < p_T^{trig} < 10$ (GeV/c), $15 < p_T^{trig} < 19$ (GeV/c), $16 < p_T^{trig} < 19$ (GeV/c), $19 < p_T^{trig} < 25$ (GeV/c), $20 < p_T^{trig} < 50$ (GeV/c). The black points are the results of π^0-jet analysis, The red points are the results of $h^{\pm}$-jet analysis.

D Gaussian fitting of the near and away-side peaks in azimuthal correlations

Fig.4.1, 4.2, 4.3 show the near and away side peaks by fitting Gaussian functions in pp and the near-side peaks by fitting Gaussian function in Pb-Pb collisions.

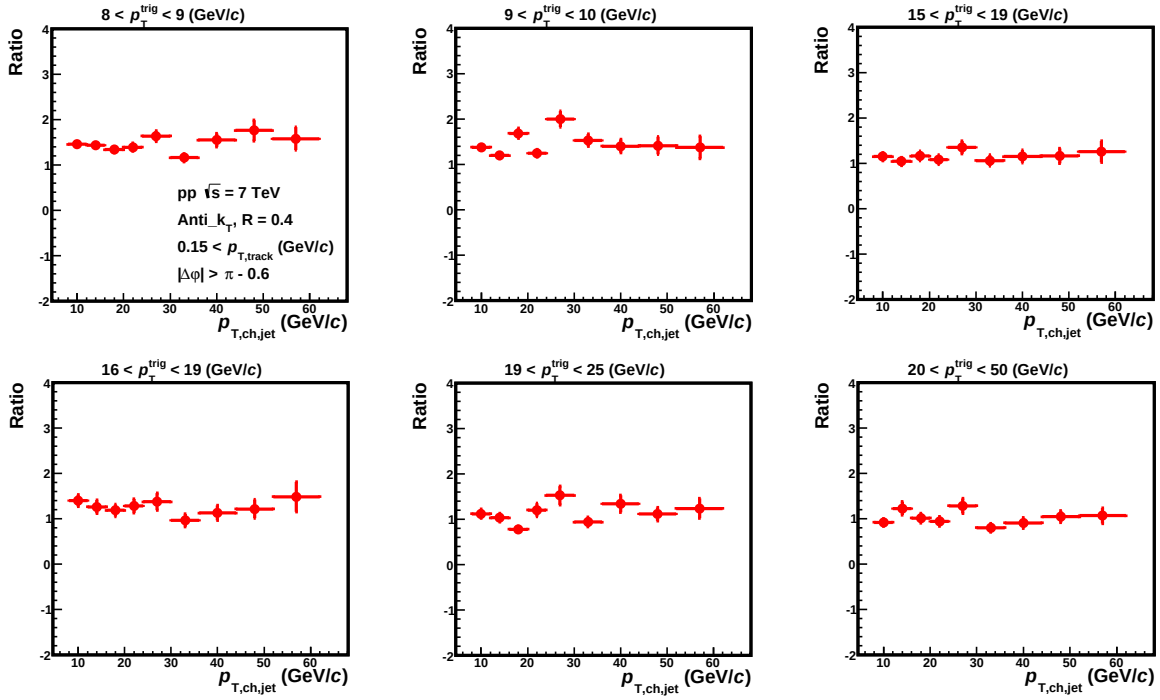

Fig. 3.7: The ratios of the away-side jet yields of π^0-jet to the away-side jet yields of $h^{\pm}$-jet with six different trigger p_T regions.

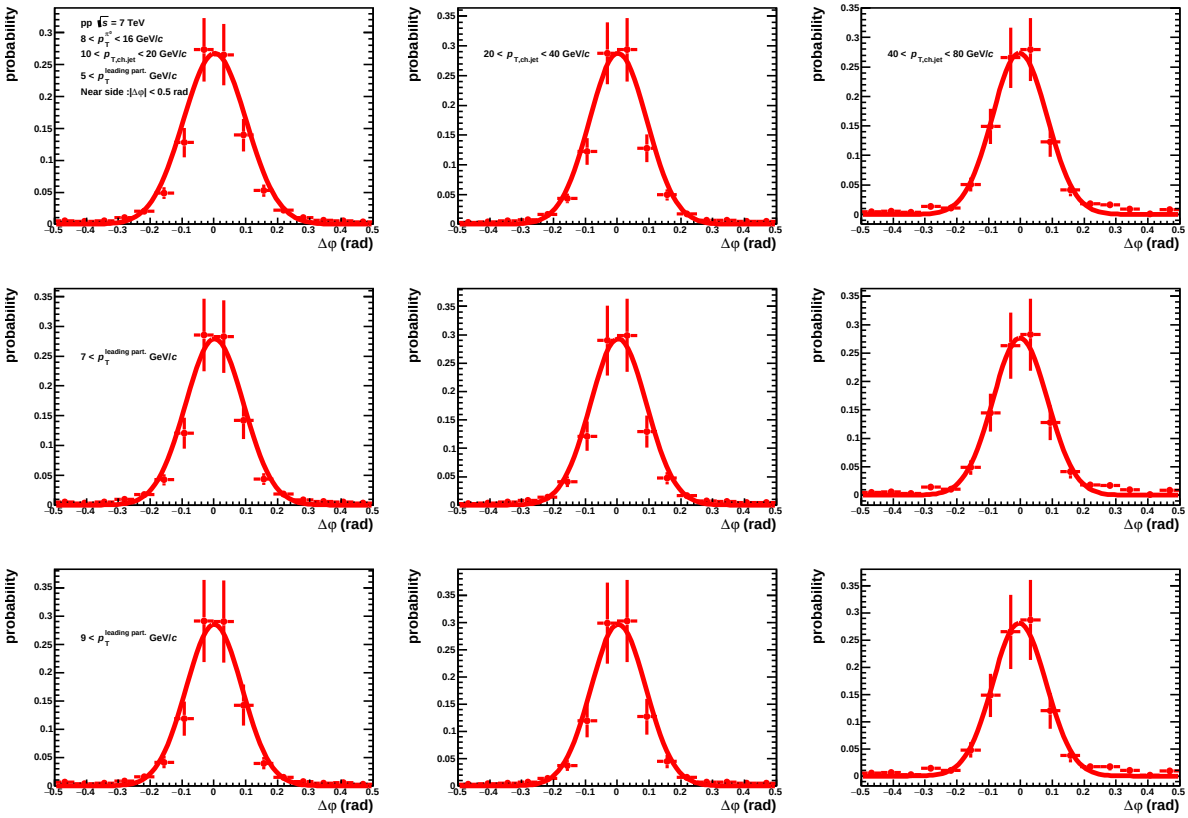

Fig. 4.1: Near side peaks in $|\Delta\varphi| < 0.5$ (rad) fitted by Gaussian functions in pp collisions at $\sqrt{s} = 7$ TeV with trigger π^0 momentum region $8 < p_{\mathrm{T}}^{\pi^0} < 16$ GeV/c. The momentum ranges of the associated jets increase with going to right sides and the momentum thresholds of the leading particle in a jet increase with going bottom sides.

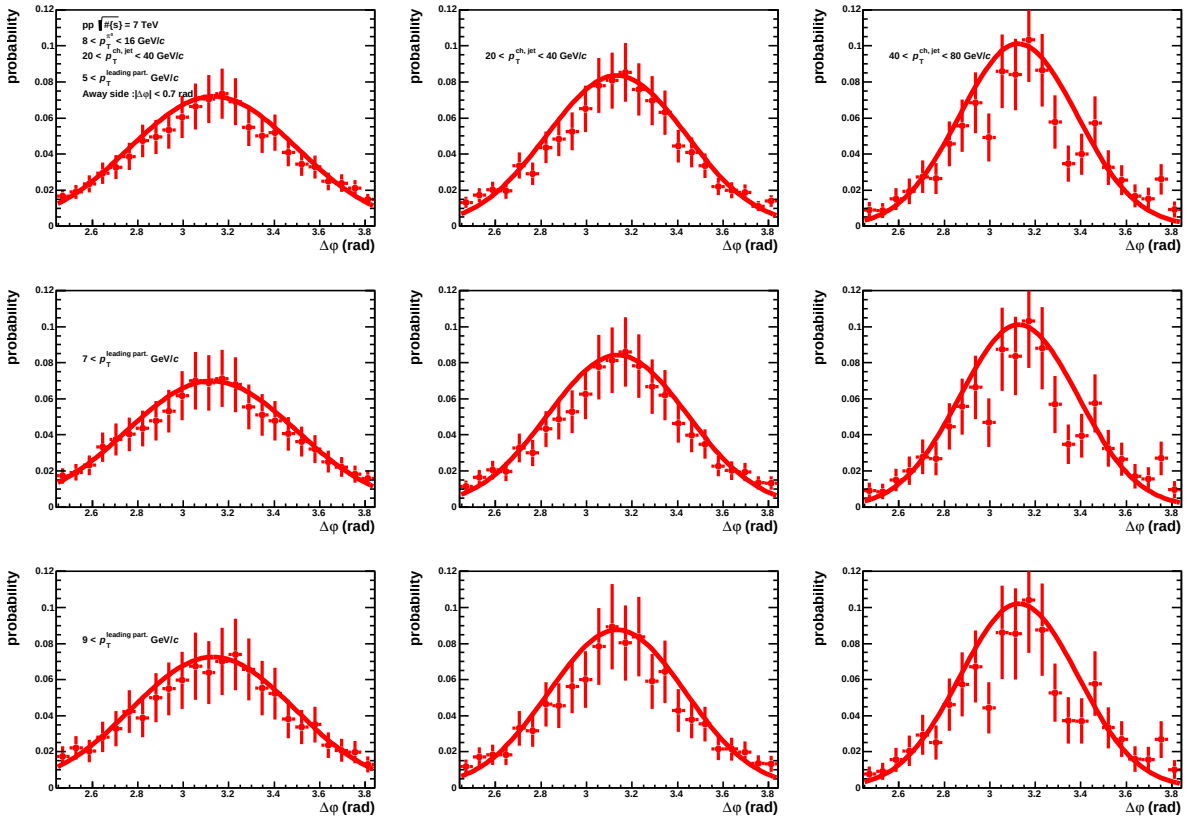

Fig. 4.2: Away side peaks in $|\Delta\varphi - \pi| < 0.7$ (rad) fitted by Gaussian functions in pp collisions at $\sqrt{s} = 7$ TeV with trigger π^0 momentum region $8 < p_{\mathrm{T}}^{\pi^0} < 16$ GeV/c. The momentum ranges of the associated jets increase with going to right sides and the momentum thresholds of the leading particle in a jet increase with going bottom sides.

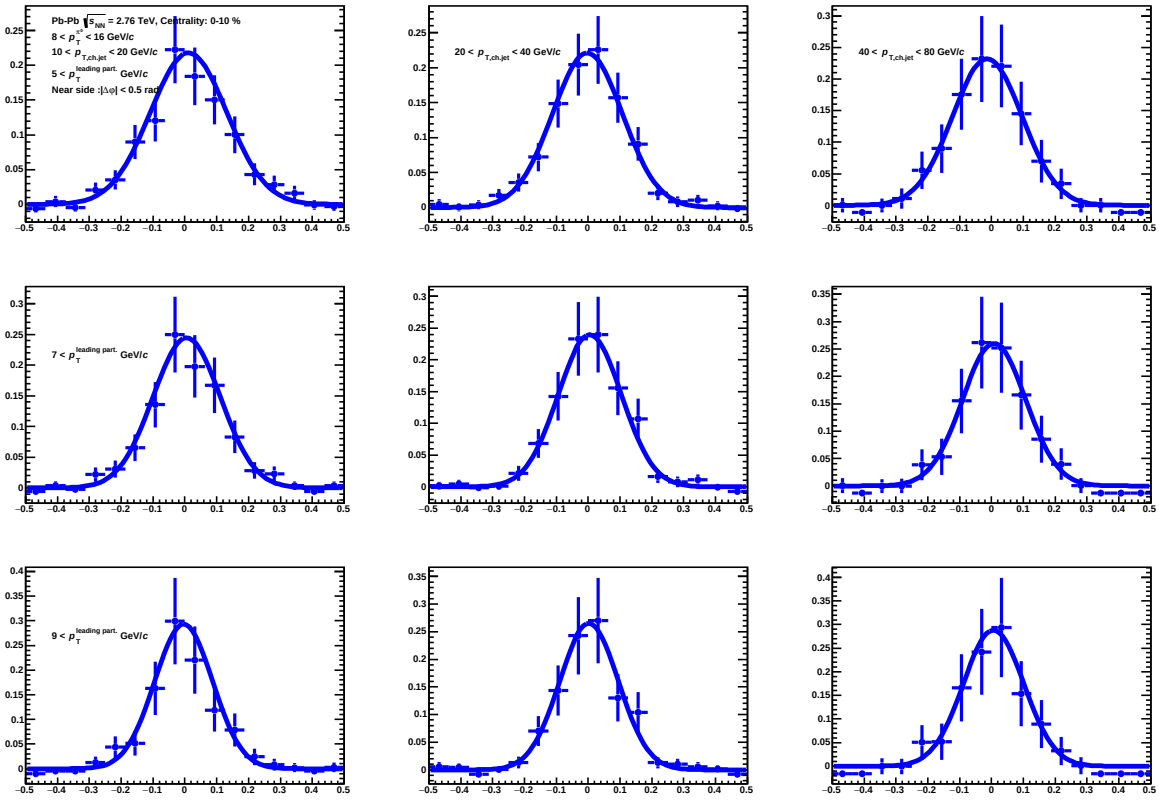

Fig. 4.3: Near side peaks in $|\Delta\varphi| < 0.5$ (rad) fitted by Gaussian functions in Pb-Pb collisions at $\sqrt{s_{\mathrm{NN}}} = 2.76$ TeV with trigger π^0 momentum region $8 < p_{\mathrm{T}}^{\pi^0} < 16$ GeV/c. The momentum ranges of the associated jets increase with going to right sides and the momentum thresholds of the leading particle in a jet increase with going bottom sides.

References

[1] K. Fukushima and T. Hatsuda, The phase diagram of dense QCD, Rept.Prog.Phys.74:014001,2011

[2] S. Borsanyi, G. Endrodi et al, The QCD equation of state with dynamical quarks, JHEP 1011 (2010)77

[3] J. D. Bjorken, High relativistic nucleus-nucleus collisions: The central rapidity region, Phys. Rev. D27, 140 (1983)

[4] K. Yagi,T. Hatsuda and Y. Miake et al, Quark Gluon Plasma, Cambridge Monographs on Particle Physics, Nuclear Physics and Cosmology

[5] Tomas D. Cohen, David A. McGady, The Schwinger mechanism revisited, Phys.Rev.D78:036008,2008

[6] I.P. Lokhtin, A.M. Snigirev et al, A model of jet quenching in ultrarelativistic heavy ion collisions and high-pt hadron spectra at RHIC hep-ph/0506189 (2005)

[7] Szabolcs Borsanyi et al, The QCD equation of state with dynamical quarks, JHEP 1011:077,2010

[8] V.N. Gribov, L.N. Lipatov et al, Deep inelastic electron scattering in perturbation theory, Sov.J.Nucl.Phys. 15:438 (1972)

[9] G. Altarelli and G. Parisi et al, Asymptotic Freedom in Parton Language Nucl.Phys. B126:298 (1977)

[10] Y.L. Dokshitzeret al, Calculation of the Structure Functions for Deep Inelastic Scattering and e+ e Annihilation by Perturbation Theory in Quantum Chromodynamics Sov.Phys.JET 46:641 (1977)

[11] Michael Schmellinget al, Status of the Strong Coupling Constant, arXiv:hep-ex/9701002 (1997)

[12] M.L. Miller, K. Reygers, S.J. Sanders, P. Steinberget al, Glauber Modeling in High Energy Nuclear Collisions, arXiv:nucl-ex/0701025 (2007)

[13] I.P. Lokhtin, A.M. Snigirev et al, Angular structure of energy losses of hard jet in dense QCD-matter Phys. Lett. B 440 (1998)163

[14] M. Gyulassy, P. Levai, I. Vitev et al, Reaction operator approach to nonAbelian energy loss. Nucl. Phys. B594 (2001) 371

[15] R. Baier, Y. L. Dokshitzer, A.H. Mueller, D. Schiff et al, Angular dependence of the radiative gluon spectrum Phys. Rev. C 64, 057902 (2001)

[16] J. Bjorken, Phys. Rev. D27, (1983) 140.

[17] K. Krajczar (for the CMS Collaboration), J. Phys. G38, (2011) 124041.

[18] M. Wilde [ALICE Collaboration], QM 2012 Proceedings to be published in Nucl. Phys. A.

[19] A.M. Adare et al. [PHENIX Collaboration], Phys. Rev. Lett. 104, 132301 (2010).

[20] ALICE Collaboration Collaboration, B. Abelev et al., Anisotropic flow of charged hadrons, pions and (anti-)protons measured at high transverse momentum in Pb-Pb collisions at sNN=2.76 TeV, Phys.Lett.B 719 (2013) 1828, arXiv:1205.5761 [nucl-ex].

[21] P. Huovinen, P. F. Kolb, U. W. Heinz, P. V. Ruuskanen, S. A. Voloshin, Phys. Lett. B 503, 58 (2001).

[22] PHENIX Collaboration, Common Suppression Pattern of and 0 Mesons at High Trans- verse Momentum in Au+Au Collisions at sNN = 200 GeV, PhysRevLett.96.202301 (2006).

[23] ALICE Collaboration, B. Abelev et al., arXiv:1208.2711 [hep-ex].

[24] ALICE Collaboration, M. Verwij, Nucl. Phys. A, (2012) 1.

[25] STAR Collaboration, Evidence from d+Au measurements for final-state suppression of high pT hadrons in Au+Au collisions at RHIC, PhysRevLett.91.072304 (2003)

[26] CMS Collaboration, Observation and studies of jet quenching in PbPb collisions at sNN = 2.76 TeV, Phys. Rev. C 84, 024906 (2011)

[27] ALICE Collaboration, Measurement of jet quenching with semi-inclusive hadron-jet distributions in central Pb-Pb collisions at sNN = 2.76 TeV, arXiv:nucl-ex/1506.03984 (2015)

[28] ALICE Collaboration, J. Allen, et al, CERN-LHCC-2010-011, ALICE-TDR-014-ADD-1

[29] ALICE Collaboration, Xiangrong Zhu, TWO-PARTICLE CORRELATIONS IN pp AND Pb-Pb COLLISIONS WITH ALICE, arXiv:1311.2395,v2 (2013)

[30] O.S.Bruning, P.Collie, P.Lebrun, S.Myers, R.Ostojic, J.Poole, P.Proudlock et al, LHC De- sign Report, CERN-2004-003-V-1

[31] ATLAS experiment, http://atlas.ch/

[32] CMS experiment, http://cms.web.cern.ch/

[33] ALICE experiment, http://aliceinfo.cern.ch/

[34] LHCb experiment, http://lhcb.web.cern.ch/lhcb/

[35] ALICE Collaboration, B. Abelev, et al, Int. J. Mod. Phys. A 29 (2014) 1430044

[36] ALICE Collaboration, ALICE Technical Designe Report Forward Detectors: *FMD*, T0 and V0, CERN-LHCC-2004-025

[37] ALICE Collaboration, ALICE Technical Designe Report Inner Tracking System(ITS), CERN-LHCC 99-12

[38] ALICE Collaboration, ALICE Technical Design Report Time Projection Chamber(TPC), CERN-LHCC-2000-001

[39] ALICE Collaboration, ALICE The Electromagnetic Calorimeter Addendum to the Technical Proposal, CERN-LHCC-2006-014

[40] ALICE Collaboration, The ALICE EMCal L1 trigger first year of operation experience, arXiv:1210.8078

[41] CMS Collaboration, Modification of jet shapes in PbPb collisions at $\sqrt{s_{NN}} = 2.76$ TeV, arXiv:1310.0878 [nucl-ex]

[42] ALICE Aanalysis Note 589, Gustavo Conesa Balbastre, "π^0identification with EMCAL in ALICE in 2011 data via cluster splitting: pp and Pb-Pb collisions", `https://aliceinfo.cern.ch/Notes/node/145`.

[43] ALICE Aanalysis Note 875, Xiangrong Zhu, "Neutral pion-hadron correlations in pp and Pb-Pb collisions with EMCal in ALICE", `https://aliceinfo.cern.ch/Notes/node/191`.

[44] ALICE Aanalysis Note 1480, Filip Krizek, "Analysis of p_T spectra of jet associated to a high-p_T trigger in pp at $\sqrt{s}$ = 7 TeV", `https://aliceinfo.cern.ch/Notes/node/276`.

[45] "Rejection of exotic clusters in EMCAal (in preparetion)", `https://aliceinfo.cern.ch/Notes/node/XXX`.

[46] Jiri Kral, Terry Awes, Hans Muller, Jan Rak, Joachim Schambach, "L0 trigger for the EMCal detector of the ALICE experiment", Physics Research A 693 (2012) 261-267.

[47] "Full jets reconstructed with TPC+EMCal in 0-10 % Pb-Pb at 2.76 TeV" `https://aliceinfo.cern.ch/Notes/node/100`.

[48] "M. Cacciari and G. P. Salam, Pileup subtraction using jet areas," Phys.Lett.B, vol. 659, pp. 119126, 2008.

[49] "M. Cacciari, J. Rojo, G. P. Salam, and G. Soyez, Jet reconstruction in heavy ion colli-sions," Eur.Phys.J.C, vol. 71, p. 1539, Oct. 2010.

[50] ALICE Collaboration, Measurement of charged jet suppression in Pb-Pb collisions at $\sqrt{s_{NN}} = 2.76$ TeV, JHEP03(2014)013

[51] ALICE Collaboration, Elliptic Flow of Charged Particles in Pb-Pb Collisions at $\sqrt{s_{\rm NN}} = 2.76$ TeV, Phys. Rev. Lett. 105, 252302

[52] V. Blobel, An Unfolding method for high-energy physics experiments, in Advanced statistical techniques in particle physics. Proceedings, Conference, Durham, UK, March 18-22, 2002, pp. 258267. 2002. arXiv:hep-ex/0208022 [hep-ex].

[53] M. Schmelling, The Method of reduced cross entropy: A General approach to unfold probability distributions, Nucl. Instrum. Meth. A340 (1994) 400412.

[54] ALICE Collaboration, B. Abelev et al., Measurement of Event Background Fluctuations for Charged Particle Jet Reconstruction in Pb-Pb collisions at psNN = 2.76 TeV, JHEP 1203 (2012) 053, arXiv:1201.2423 [hep-ex].

[55] ALICE Collaboration, Measurement of jet suppression in central PbPb collisions at $\sqrt{s_{\mathrm{NN}}} = 2.76$ TeV, Phys. Lett. B 746 (2015) 1

[56] T. Renk, Physics probed by the PT dependence of the nuclear suppression factor, Phys.Rev. C88 no. 1, (2013) 014905, arXiv:1302.3710 [hep-ph].

[57] K. C. Zapp, F. Krauss, and U. A. Wiedemann, A perturbative framework for jet quenching, JHEP 1303 (2013) 080, arXiv:1212.1599 [hep-ph].

[58] ALICE Collaboration, Azimuthal anisotropy of charged jet production in sNN = 2.76 TeV PbPb collisions, Physics Letters B 753 (2016) 511525